

USE OF MONTE CARLO TECHNIQUES IN EXTERNAL BEAM THERAPY OF  
LUNG CANCER



by  
Türkey Toklu

Submitted to Graduate School of Natural and Applied Sciences  
in Partial Fulfillment of the Requirements  
for the Degree of Doctor of Philosophy in  
Physics

Yeditepe University  
2016


USE OF MONTE CARLO TECHNIQUES IN EXTERNAL BEAM THERAPY OF  
LUNG CANCER

APPROVED BY:

Prof. Dr. Necdet Aslan  
(Thesis Supervisor)



Assoc. Prof. Dr. Bahar Dirican  
(Thesis Co-Supervisor)



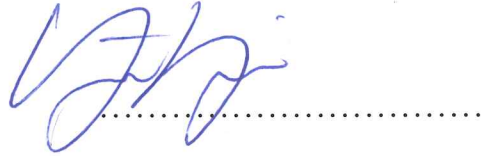
Prof. Dr. Hatice Bilge Becerir



Prof. Dr. Rıza Gürcan Oraltay



Prof. Dr. Uğur Yahşi



Assoc. Prof. Dr. Şerife İpek Karaaslan



Assist. Prof. Dr. Ercüment Akat



DATE OF APPROVAL: 16.06/2016



*To my wife and  
my sons Doruk and Toprak...*

## ACKNOWLEDGEMENTS

I would like to thank Prof. Necdet ASLAN and Assoc. Prof. Bahar DİRİCAN for supervising this thesis and for their great discussion and guidance of my research.

I would like to thank Yelda ELÇİM, medical physicist at Gülhane Military Medical School, Department of Radiation Oncology, for her supports of my thesis. I would also like to thank the other medical physicist friends at the department for their kind welcome.

I am grateful to Assoc. Prof. Nalan ALAN SELÇUK for her support and enthusiasm during the years of my research. I would also like to thank my colleague Zeynep FIRAT, Tech. Alper GÜLER, Tech. Sema ÇELİK, Tech. Ayşe DURA KEFELİ, Elif GÖREN and Ebru AYYILDIZ.

I thank Prof. Uğur YAHŞI and Assist. Prof. Ercüment AKAT who acts in my dissertation committee for their thoughtful insights and guidance.

I would like to thank Assoc. Prof. İpek KARAASLAN for her support of my study. I would also like to thank Ayçin BORA for her support.

I would also like to thank Assoc. Prof. Altay Burak DALAN for encouraging me to finish my thesis.

Finally, I am grateful to my parents and my wife Aslı TOKLU for their endless support.

## **ABSTRACT**

### **USE OF MONTE CARLO TECHNIQUES IN EXTERNAL BEAM THERAPY OF LUNG CANCER**

The dose calculation models implemented in clinical radiation therapy has increased gradually in the last few decades. Monte Carlo (MC) simulations of the radiotherapy dose delivery has the highest dose calculation accuracy. Implementation of MC techniques to the intensity modulated radiation therapy (IMRT) of lung cancer was the main purpose of this thesis. Elekta Synergy MLCi linear accelerator was modelled using EGSnrc/BEAMnrc Monte Carlo code system in the thesis. Model verification was performed with ionization chamber measurements in water phantom. After model verification, dose distributions obtained from two different treatment planning systems (TPSs) and MC simulation in virtual slab phantoms that include tissue inhomogeneity were compared. Finally, dose distributions were compared in a real patient situation of IMRT of lung cancer. A good agreement was observed between ionization chamber measurements and MC calculations. Huge calculation errors in both virtual phantom and real patient situations were observed with TPS with pencil-beam calculation algorithm in comparison with MC calculations. Better results were obtained with TPS with collapse cone convolution/superposition calculation algorithm in both cases. In conclusion, the MC model of the linac produced in this study can be used for both radiotherapy plan verification and dose calculation in the situations of small fields and tissue inhomogeneities where TPSs fail.

## ÖZET

### MONTE CARLO TEKNİKLERİNİN AKCİĞER KANSERİNİN EKSTERNAL DEMET RADYOTERAPİSİNDE KULLANIMI

Klinik radyoterapide, doz hesaplama modellerinin uygulanması son birkaç on yılda artmaktadır. Radyoterapideki doz uygulamasının Monte Carlo (MC) simülasyonu en yüksek doz hesaplama doğruluğuna sahiptir. Akciğer kanserinin yoğunluk ayarlı radyasyon terapisine (YART) MC tekniklerinin uygulanması, bu tez çalışmasının ana amacıdır. Bu tezde, Elekta Synergy MLCi lineer hızlandırıcı sistemi EGSnrc/BEAMnrc Monte Carlo kod sistemi kullanılarak modellenmiştir. Model doğrulaması, su fantomunda alınmış iyon odası ölçümleri ile gerçekleştirilmiştir. Model doğrulamasının ardından doku inhomojenitesi içeren sanal katmanlı fantomlarda, iki farklı tedavi planlama sistemi (TPS) ve MC simülasyonlarından elde edilen doz dağılımları karşılaştırıldı. Son olarak akciğer kanserli hastaların YART'sinde doz dağılımları karşılaştırıldı. MC hesaplamaları ile iyon odası ölçümleri arasında iyi bir korelasyon gözlemlendi. Pencil-beam hesaplama algoritmaları TPS'ninde MC hesaplamaları ile karşılaştırıldığında büyük hesaplama hataları tespit edildi. Konik yığılımlı konvolüsyon/süperpozisyon algoritmaları TPS'nde ise her iki durumda da daha iyi sonuçlar elde edilmiştir. Sonuç olarak, bu çalışmada ortaya çıkartılan MC modeli, radyoterapi plan doğrulamasında ve TPS'lerinin hata yaptığı küçük alan ve doku inhomojenitesi içeren durumlarda doz hesaplamasında kullanılabilir.

## TABLE OF CONTENTS

ACKNOWLEDGEMENTS.....	iv
ABSTRACT.....	v
ÖZET .....	vi
LIST OF FIGURES .....	x
LIST OF TABLES.....	xv
LIST OF SYMBOLS/ABBREVIATIONS.....	xvi
1. INTRODUCTION .....	1
2. THEORETICAL BACKGROUND.....	5
2.1. THE MONTE CARLO SIMULATION OF RADIATION TRANSPORT .....	5
2.1.1. Photon Interaction Processes .....	5
2.1.2. Electron Interaction Processes .....	7
2.1.3. Coupled Electron–Photon Transport .....	9
2.1.4. Sampling Theory.....	10
2.1.5. EGSnrc Monte Carlo Code .....	12
2.1.6. Modelling Radiotherapy Beams .....	16
2.2. MEDICAL LINEAR ACCELERATORS .....	17
2.3. PATIENT DOSE CALCULATIONS.....	21
2.3.1. Isodose Curves.....	21
2.3.2. Conventional Radiotherapy .....	22
2.3.3. Three-Dimensional Conformal Radiation Therapy .....	23
2.3.4. Definition of Treatment Volumes.....	24
2.3.4.1. <i>Gross Tumor Volume</i> .....	24
2.3.4.2. <i>Clinical Target Volume</i> .....	24
2.3.4.3. <i>Internal Target Volume</i> .....	24
2.3.4.4. <i>Planning Target Volume</i> .....	25
2.3.4.5. <i>Planning Organ at Risk Volume</i> .....	25
2.3.5. Intensity Modulated Radiation Therapy (IMRT).....	25
2.3.6. Treatment Planning Systems .....	26
2.3.7. Dose Evaluation of Treatment Plans .....	26

2.3.8. Biological Evaluation of Treatment Plans .....	29
3. MATERIALS AND METHODS.....	32
3.1. MONTE CARLO MODEL OF ELEKTA SYNERGY MLC <sub>i</sub> LINAC .....	32
3.1.1. Monte Carlo Modelling .....	32
3.1.2. Monte Carlo Radiation Transport Parameters .....	40
3.1.3. Measurements on Linac .....	43
3.1.4. Accelerator Simulation Validation .....	46
3.1.5. Absolute Dose Calculation .....	50
3.2. COMPARISON OF TREATMENT PLANNING SYSTEMS WITH MONTE CARLO SIMULATION UNDER CONDITIONS OF TISSUE INHOMOGENITIES ..	50
3.2.1. Treatment Planning Systems .....	50
3.2.2. Conversation of Hounsfield Unit (HU) to Relative Electron Density or Physical Density .....	51
3.2.3. Construction of Slab Phantoms.....	55
3.2.4. Open Field Plans and Dose Distributions .....	56
3.2.5. Dose Distribution Calculations with MC.....	56
3.2.6. Comparisons .....	57
3.3. COMPARISON OF TREATMENT PLANNING SYSTEMS WITH MONTE CARLO SIMULATION IN IMRT OF NON-SMALL CELL LUNG CANCER.....	58
3.3.1. Patients.....	58
3.3.2. Target and OAR Delineation and Volumes.....	59
3.3.3. Treatment Plans and Planning Objectives .....	60
3.3.4. Dose Distribution Calculations in TPSs .....	60
3.3.5. Dose Distribution Calculations in MC.....	61
3.3.6. Comparison of Dose Distributions .....	62
4. RESULTS AND DISCUSSION .....	64
4.1. MONTE CARLO MODELLING OF ELEKTA SYNERGY MLC <sub>i</sub> TREATMENT HEAD .....	64
4.1.1. Monte Carlo Modelling .....	64
4.1.2. Monte Carlo Radiation Transport Parameters .....	65
4.1.3. Initial Electron Beam Energy Selection.....	68
4.1.4. Validation of the Simulation.....	72



4.1.5. Concluding Remarks.....	77
4.2. COMPARISON OF TREATMENT PLANNING SYSTEMS WITH MONTE CARLO SIMULATION UNDER CONDITIONS OF TISSUE INHOMOGENITIES..	78
4.2.1. Lung Phantom.....	78
4.2.2. Bone Phantom.....	81
4.2.3. Water Phantom .....	85
4.2.4. Concluding Remarks.....	87
4.3. COMPARISON OF TREATMENT PLANNING SYSTEMS WITH MONTE CARLO SIMULATION IN IMRT OF NON-SMALL CELL LUNG CANCER.....	88
4.3.1. IMRT Dose Distributions .....	88
4.3.2. Comparison of MC <sub>H2O</sub> with TPSs.....	90
4.3.3. Comparison of MC <sub>H2O</sub> with the Other MC calculations.....	97
4.3.4. Concluding Remarks.....	98
5. CONCLUSION.....	100
REFERENCES .....	102
APPENDIX A.....	117
APPENDIX B .....	143
APPENDIX C .....	169
APPENDIX D.....	171
APPENDIX E .....	176
APPENDIX F .....	184
APPENDIX G.....	192
APPENDIX H.....	207

## LIST OF FIGURES

Figure 2.1. A schematic illustration of a Monte Carlo photon history .....	6
Figure 2.2. Electron elastic, ionization, excitation, and bremsstrahlung mean-free path in oxygen.....	8
Figure 2.3. (a) Global picture of electron transport. Photons are represented by straight dashed lines; electrons and positrons by solid curves (I, insertion; E, escape; P, pair production; B, bremsstrahlung; M, Møller; X, end-of-range; C, Compton; R, Rayleigh; Ph, photoelectric; Bh, Bhabha; A, annihilation). (b) Expanded version of the dashed box in (a). .....	9
Figure 2.4. The structure of the EGSnrc code system when used with a user-code.....	15
Figure 2.5. Schematic diagram of a linear accelerator designed for radiotherapy and used in x-ray mode .....	18
Figure 2.6. Schematic illustration of spatial distribution of x-rays around a thin target .....	19
Figure 2.7. Schematic diagram of a linear accelerator.....	19
Figure 2.8. Overlapped leaf sections from different manufacturers .....	21
Figure 2.9. Example isodose curves for (a) 4 MV, (b) 10 MV photon beams .....	22
Figure 2.10. Treatment planning using two or more radiation fields .....	23
Figure 2.11. PTV and isodose curves .....	27
Figure 2.12. Dose volume histograms: (a) differential, (b) cumulative .....	28
Figure 3.1. Technical drawing of Elekta Synergy MLCi treatment head.....	32

Figure 3.2. (a) The graphical user interface of the BEAMnrc code, (b) the linac component list in order, (c) PEGS4: the cross section file selecting window .....	33
Figure 3.3. (a) The SLABS component module (CM) schematics. The CM is assumed to have a square boundary shape. (b) GUI of the SLABS CM.....	34
Figure 3.4. (a) The CONS3R CM schematics. The outer boundary of the CM is assumed to be a cylinder. (b) GUI of the CONS3R CM. ....	34
Figure 3.5. (a) The FLATFILT CM schematics. (b) GUI of the FLATFILT CM. ....	35
Figure 3.6. (a) The CHAMBER CM schematics. (b) GUI of the CHAMBER CM.....	36
Figure 3.7. (a) The JAWS CM schematics. (b) GUI of the JAWS CM. ....	37
Figure 3.8. (a) The MIRROR CM schematics. (b) GUI of the MIRROR CM.....	38
Figure 3.9. The MLCE CM schematics .....	39
Figure 3.10. (a) Tongue-and-groove arrangement of MLCs, (b-d) MLC model in three orthogonal planes of $10 \times 10 \text{ cm}^2$ open field size.....	39
Figure 3.11. The MLCQ CM schematics .....	40
Figure 3.12. EGSnrc simulation parameters selection window .....	41
Figure 3.13. Main inputs window of BEAMnrc .....	42
Figure 3.14. (a) IBA Blue Water Phantom, (b) IBA CC13 $0.13 \text{ cm}^3$ ionization chamber, (c) a measurement output on OmniPro-Accept software.....	44
Figure 3.15. Scanned film for measuring MLC transmission and interleaf leakage. The black line represents the profile drawn on the film. ....	45

Figure 3.16. One of the scanned film to determine absolute dose-grey level relationship. The black box represents region of interest placed on the film. ....	45
Figure 3.17. Sigmoidal fit .....	46
Figure 3.18. Window for BEAMnrc source number 19 .....	47
Figure 3.19. Graphical user interface of the DOSXYZnrc code's input parameters .....	48
Figure 3.20. Window for DOSXYZnrc source number 19.....	48
Figure 3.21. HU to relative electron density to water conversions for (a) TPS <sub>PB</sub> (b) TPS <sub>CCC</sub> and BEAMnrc MC code .....	52
Figure 3.22. Bi-linear transformation used to convert relative electron density to physical density .....	53
Figure 3.23. HU to physical density conversion used for TPS <sub>CCC</sub> and Monte Carlo .....	54
Figure 3.24. Virtual slab phantoms: (a) Geometry, (b) Lung Phantom, (c) Bone Phantom, (d) Water Phantom .....	55
Figure 3.25. An example of Boltzmann fit to ascending side of a dose profile .....	58
Figure 4.1. Monte Carlo model of Elekta Synergy MLC <sub>i</sub> treatment head using EGSnrc/BEAMnrc code system .....	64
Figure 4.2. Percent depth dose curves of MC simulation with default transport parameters versus MC simulation with (a) electron impact ionisation ON, (b) bound Compton scattering ON, (c) photoelectron angular sampling ON, (d) Rayleigh scattering ON, (e) atomic relaxations ON and (f) E <sub>CUT</sub> =521 keV .....	65
Figure 4.3. Effect of MC transport parameters on CPU time .....	66

Figure 4.4. Percent depth dose curves of MC simulation with ESAVE_GLOBAL is equals to 2.0 MeV in comparison with MC simulation with ESAVE_GLOBAL is equals to (a) 1.0 MeV, (b) 1.5 MeV, (c) 2.5 MeV, (d) 3.0 MeV .....	67
Figure 4.5. Effect of different cross sections on PDD curves.....	68
Figure 4.6. (a) PDD curves obtained with different initial electron energies in comparison with ionisation chamber measurements, (b) differences of curves from measurement ( $10 \times 10$ cm <sup>2</sup> open field and SSD=100 cm).....	69
Figure 4.7. (a) Dose profiles at 10 cm depth obtained with different initial electron energies in comparison with ionisation chamber measurements, (b) differences of curves from measurement ( $10 \times 10$ cm <sup>2</sup> open field and SSD=100 cm).....	70
Figure 4.8. Dose profile measurements made by Haryanto et al. [84] .....	71
Figure 4.9. Percent depth dose comparison of MC simulation and ionisation chamber measurement for $10 \times 10$ cm <sup>2</sup> open field and SSD=100 cm.....	73
Figure 4.10. Some selected PDD curve comparisons for (a) open fields (b) wedged fields (SSD=100 cm) .....	74
Figure 4.11. Dose profile comparisons for (a) open fields at 10 cm depth (b) $30W \times 40$ cm <sup>2</sup> wedged field at different depths (SSD=100 cm) .....	75
Figure 4.12. MLC transmission and interleaf leakage comparison (SSD=100 cm).....	76
Figure 4.13. Comparison of output factors (SSD=100 cm).....	77
Figure 4.14. PDD curves in Lung Phantom for field sizes of (a) $3 \times 3$ cm <sup>2</sup> , (b) $10 \times 10$ cm <sup>2</sup> , (c) $20 \times 20$ cm <sup>2</sup> (SSD=100 cm) .....	79
Figure 4.15. Dose profiles at 4.5 cm depth (in the middle of lung region) for field sizes of (a) $3 \times 3$ cm <sup>2</sup> , (b) $10 \times 10$ cm <sup>2</sup> , (c) $20 \times 20$ cm <sup>2</sup> (SSD=100 cm) .....	80

Figure 4.16. Penumbra widths (80%-20%) for Lung Phantom .....	81
Figure 4.17. PDD curves in Bone Phantom for field sizes of (a) $3 \times 3 \text{ cm}^2$ , (b) $10 \times 10 \text{ cm}^2$ , (c) $20 \times 20 \text{ cm}^2$ (SSD=100 cm) .....	82
Figure 4.18. Dose profiles at 4.5 cm depth (in the middle of bone region) for field sizes of (a) $3 \times 3 \text{ cm}^2$ , (b) $10 \times 10 \text{ cm}^2$ , (c) $20 \times 20 \text{ cm}^2$ (SSD=100 cm) .....	83
Figure 4.19. Penumbra widths (80%-20%) for Bone Phantom .....	84
Figure 4.20. PDD curves in Water Phantom for field sizes of (a) $3 \times 3 \text{ cm}^2$ , (b) $10 \times 10 \text{ cm}^2$ , (c) $20 \times 20 \text{ cm}^2$ (SSD=100 cm) .....	85
Figure 4.21. Dose profiles at 4.5 cm depth for field sizes of (a) $3 \times 3 \text{ cm}^2$ , (b) $10 \times 10 \text{ cm}^2$ , (c) $20 \times 20 \text{ cm}^2$ (SSD=100 cm) .....	86
Figure 4.22. Penumbra widths (80%-20%) for Water Phantom.....	87
Figure 4.23. Dose distribution of the Patient-9 from TPS <sub>PB</sub> .....	88
Figure 4.24. DVHs from TPS <sub>PB</sub> for targets and OARs of the Patient-9 .....	89
Figure 4.25. Dose distributions of the same patient from different calculation methods: (a) TPS <sub>PB</sub> , (b) TPS <sub>CCC</sub> , (c) MC <sub>DM</sub> , (d) MC <sub>H<sub>2</sub>O</sub> , (e) MC <sub>DW</sub> .....	89
Figure 4.26. DVHs from different dose distributions for PTV and spinal cord .....	90
Figure 4.27. Graphical comparisons of the DVH parameters for PTV .....	91
Figure 4.28. Maximum doses for heart, esophagus and spinal cord.....	93
Figure 4.29. Comparisons between MC <sub>H<sub>2</sub>O</sub> and TPSs for Lungs: (a) $V_{20\text{Gy}}$ , (b) $V_{30\text{Gy}}$ , (c) MLD.....	94
Figure 4.30. Comparisons between MC <sub>H<sub>2</sub>O</sub> and TPSs for EUD (a) Heart, (b) Esophagus, (c) Spinal Cord, (d) Lungs.....	95

## LIST OF TABLES

Table 3.1. Density ranges and atomic compositions of the material or tissues used in MC simulation.....	54
Table 3.2. Target volumes for each patient .....	59
Table 3.3. Model parameters for NTCP and EUD .....	62
Table 4.1. $\chi^2$ results against initial electron beam energy.....	72
Table 4.2. Paired-samples T-Test comparison results between MC <sub>H2O</sub> and TPSs for target volumes.....	92
Table 4.3. Paired-samples T-Test comparison results between MC <sub>H2O</sub> and TPSs for OARs .....	96
Table 4.4. Paired-samples T-Test comparison results between MC <sub>H2O</sub> and the other MC calculations for target volumes .....	97
Table 4.5. Paired-samples T-Test comparison results between MC <sub>H2O</sub> and the other MC calculations for OARs.....	99

## LIST OF SYMBOLS/ABBREVIATIONS

$A$	Mass number
$A_{plan}$	Arbitrary field size in patient plan
$A_{ref}$	Reference field size
$b$	Distance of closest approach
$c$	Speed of light
$c(x)$	Cumulative probability distribution
$D$	Dose
$d$	Depth
$d_{eff}$	Effective depth
$D_{max}$	Maximum dose
$d_{max}$	Reference depth of maximum dose
$D_{mean}$	Mean dose
$D_{min}$	Minimum dose
$D_{ref}$	Dose at reference depth
$E$	Energy
$F_Q$	Calibration factor to convert MC dose to absolute dose
$f_Q$	Cavity theory factor
$g$	Fraction of the initial kinetic energy of the electrons that is reradiated as bremsstrahlung
$h$	Planck's constant
$I$	Intensity
$IF_{HT}(D)$	Irradiation factor of the healthy tissue
$IF_{PTV}(D)$	Irradiation factor of the PTV
$k$	Constant equals to $8.9875 \times 10^9 \text{ Nm}^2\text{C}^{-2}$
$K$	Kerma
$L$	Mean excitation energy
$l$	Distance
$m$	A parameter representing the steepness of the dose–response curve
$m_e$	Mass of the electron



$n$	The exponent of volume in the power law that relates the tolerance doses for uniform whole and uniform partial organ irradiation.
$N_A$	Avogadro's number
$p(x)$	Probability function
$Q$	Energy transfer
$r_0$	Continuous-slowng-down-approximation range
$r_e$	Electron radius
$S_{col}$	Collision stopping power
$S_{rad}$	Radiation stopping power
$t$	Thickness
$TD_{50}$	Dose to an organ which would lead to complication in 50% of the population
$v$	Velocity of the primary particle
$V$	Velocity
$V_{eff}$	Effective volume
$V_{ref}$	Reference volume
$V_T$	Total organ volume
$V_x$	Fractional volume
$W$	Mean energy required to produce one ion pair
$X$	Exposure
$Z$	Atomic number
$z$	Charge on the primary particle
$\alpha$	Fine structure constant
$\beta$	$v/c$
$\delta$	Density-effect correction
$\Sigma_t$	Macroscopic total cross section of interaction
$\varepsilon$	Energy imparted
$\lambda$	Mean free path
$\mu$	Linear attenuation coefficient
$\nu$	Frequency
$\xi$	Random variable
$\rho$	Physical density
$\sigma$	Cross-section

$\Upsilon$	Radiation yield
$\Phi$	Fluence
$\psi$	Energy fluence
$\Omega$	Solid angle
3-D	Three-dimensional
AAA	Analytic anisotropic dose calculation algorithm
AAPM	American Association of Physicists in Medicine
CAX	Central axis
CCC	Collapsed cone convolution/superposition dose calculation algorithm
CERR	Computational Environment for Radiotherapy Research
CHM	Condensed history method
CI	Conformity index
CM	Component module
CPE	Charged particle equilibrium
CPU	Central processing unit
CRT	Conformal radiotherapy
CSDA	Continuous slowing down approximation
CT	Computed tomography
CTV	Clinical target volume
DBS	Directional Bremsstrahlung splitting
DICOM	Digital Imaging and Communication in Medicine
DVH	Dose-volume histogram
EGS	Electron Gamma Shower
EUD	Equivalent uniform dose
FWHM	Full-width at half-maximum
GTV	Gross tumor volume
GUI	Graphical user interface
HI	Homogeneity index
HU	Hounsfield Unit
ICRP	International Commission on Radiological Protection
ICRU	International Commission on Radiation Units and Measurements
IMRT	Intensity modulated radiation therapy

ITV	Internal target volume
Kerma	Kinetic energy released per unit mass
Linac	Linear accelerator
LKB	Lyman–Kutcher–Burman
MC	Monte Carlo
MLC	Multi leaf collimator
MLD	Mean lung dose
MRI	Magnetic resonance imaging
MU	Monitor Unit
NIST	National Institute of Standards and Technology
NSCLC	Non-small cell lung cancer
NTCP	Normal tissue complication probability
OAR	Organ at risk
PB	Pencil beam dose calculation algorithm
PDD	Percent depth dose
PEGS	Preprocessor for Electron Gamma Shower
PET	Positron emission tomography
PRV	Planning organ at risk volume
PTV	Planning target volume
RTOG	Radiation Therapy Oncology Group
SAD	Source to axis (isocenter) distance
SPECT	Single photon emission tomography
SSD	Source to skin distance
TAR	Tissue air ratio
TCPE	Transient charged particle equilibrium
TMR	Tissue maximum ratio
TPR	Tissue phantom ratio
TPS	Treatment planning systems
TV	Treated volume
US	Ultrasound

## 1. INTRODUCTION

The dose calculation models implemented in clinical radiation therapy or radiotherapy treatment planning systems (TPSs) has increased gradually in the last few decades. This is mainly due to the available computer power in hospitals. This evolution, going from rather simple inhomogeneity corrections to pencil beam (PB) algorithms, has resulted in continuous improvements in the accuracy of predicted patient doses [1].

Dose calculation algorithms in treatment planning systems can be separated into two categories based on modelling of energy deposition [2]. In the first category, it is assumed that the charged particle equilibrium is always maintained. Besides, energy deposition occurs at the point of photon interaction and there is no secondary electron transport modelling. The Modified Batho [3] and equivalent tissue-to-air ratio [4] techniques are two examples of this category. In the second category, electron transport is applied and there is no assumption of local energy deposition. An example of this category is superposition/convolution method [5] such as the collapsed cone convolution (CCC) [6] or the analytic anisotropic algorithm (AAA) [7]. They model the electron transport analytically. Another example of this category is Monte Carlo (MC) technique [8] that explicitly tracks electron transport. The MC approach is generally considered to be the gold standard for determining dose distributions for circumstances of electron disequilibrium, and where interpretations of dosimetric measurements are challenging [9]. As such, it has been used by many authors to benchmark the accuracy of different dose calculation techniques [10-16].

Under the conditions of lateral electronic disequilibrium, it has been shown that dose algorithms fall into the first category overestimate the amount of dose deposited in lung as well as tumour tissues [10,15-19]. For instance, Engelsman et al. [18] compared the dose calculating accuracy of pencil beam, modified Batho, and equivalent path length methods with film dosimetry and ion chamber measurements. In their study, they irradiated a polystyrene target centrally contained a lung slab, simulated by cork. They used beam energies of 6, 8, 15, and 18 MV. Their results show that the algorithms calculate up to 20 per cent higher doses in the lung and tumour in comparison with the actual delivered dose

values measured by ion chamber or film. Besides, the error in dose calculation raised with photon beam energy.

The second category algorithms' ability of accurately computing dose in lung tissue has been evaluated by multiple authors. Most studies suggest that AAA and CCC algorithms are superior to pencil beam, modified Batho, and equivalent path length methods for calculating dose under the conditions of electronic disequilibrium [10,12,13,15,16,20]. However, a recent comparison of CCC and MC by Chow et al. [14] suggests that the CCC algorithm produced significant dose deviations in lung phantoms and patients for treatment parameters using high-energy beams, small field sizes, and low lung density ( $<0.3 \text{ g/cm}^3$ ).

Summarizing the literature in the frame of dose calculating algorithms used in TPSs, it is evident that the first category algorithms are inadequate for prediction of a correct dose in IMRT of lung cancer patients. The second category algorithms perform generally better, but may still be challenged to produce accurate dose distributions under extreme lateral electronic disequilibrium due to oversimplification and assumptions in modelling of electron transport [14].

The full Monte Carlo simulations of the radiotherapy dose delivery has the highest dose calculation accuracy [8,21-23]. The demand for a reliable calculation of the absorbed dose distribution with a therapy planning system depends on the accuracy of modelling the simulated system. Thus, accurate knowledge of the characteristics of incident electron beam on the target, such as the mean energy, radial intensity distribution and energy distribution, are important parameters, in careful modelling the linac head by a MC code. The determination of these initial beam parameters is a challenging part in linac modelling with the MC method, and is an important issue for implementing MC dose calculation in treatment planning [24,25].

Besides the calculation accuracy, how the dose reporting carried out is important for MC calculations. Conventional dose calculations for photon beam radiotherapy typically report the absorbed dose to water. This is because the input data used for treatment planning algorithms are generally measured in water phantoms [26], since it is easy to be constructed in laboratories. These data are then manipulated in various ways by TPS algorithms to

compute dose distributions in a patient. They assume the human body is composed of water with different densities. On the other hand, MC calculation reports absorbed dose to medium defined by the user of code. The defined medium can be made of any compositions of elements or compounds. Because of these, the direct comparison of dose distributions of TPSs and MC is not logical. For comparison, one should convert MC dose distribution to the dose in water equivalent.

There are several methods defined to convert MC dose distributions to dose in water. A conversion method based on the Bragg–Gray cavity theory is proposed in the work of Siebers et al. [27] which also recommended by American Association of Physicists in Medicine (AAPM) Task Group No. 105 [28]. In their study, the conversion factors are the unrestricted water-to-medium mass collision stopping power ratios averaged over the energy spectrum of the electrons. With MC calculations, they determined the conversion factors as a function of depth in a phantom for 6 and 18MV photon beams of a linear accelerator. A depth dependence was only found for air. Upon conversion, the dose may change by about 1% for soft tissues and lung, and by up to 12% for bone, depending on the beam quality.

Another method for calculating dose to water with MC is proposed by Ma et al. [26]. In their study, they made MC calculations with only the water material with variable electron density. They conclude that direct computation of dose distribution with MC using the all materials of water with variable electron density is produce more accurate results than the method suggested by AAPM Task Group No. 105.

The widespread use of MC techniques in field of radiotherapy is the main source of motivation of this thesis work. Surveying the literature, the first aim of the thesis was determined as to perform an accurate MC simulation of a clinical linac. This would give the ability of MC plan verification to the clinic. According to our best knowledge, it was the first attempt to MC simulate a real clinical linac in our country. The detailed simulation and commissioning steps were given in the thesis.

Following the linac simulation, comparison MC dose distribution calculation with the clinical TPS that used with the simulated linac was proposed in virtual phantoms where tissue inhomogeneities were modelled. The algorithm of the TPS used with the linac was

fallen into the first category. Another TPS with CCC calculation algorithm was also included in the comparisons. MC simulations used in comparisons were performed as the method described by Ma et al. [26] to produce dose to water. Dose to water calculations according to the method suggested by AAPM Task Group No. 105 [28] and dose to medium calculations were also compared with the first MC calculations.

MC with dose to water calculation methodology using different water densities was proposed for this thesis as described by the study of Ma et al. [26]. Ma et al. used the methodology only for high density materials such as bone. In this thesis work, the idea was used not only high density materials but also low density materials such as lung tissue. This was the most innovative idea in this thesis study. Besides, most of the comparisons in the literature were made with the real phantoms that include lung or bone equivalent materials in it [15,16,18,26]. The virtual phantoms used in this thesis were very uncommon in this type of comparisons [11].

Finally, similar comparisons were performed in the real patient situations. For this purpose, intensity modulated radiation therapy (IMRT) of lung cancer was selected. Fifteen patients were included in the study. Graphical and statistical comparisons of dose-volume histogram (DVH) parameters were performed between MC calculations and TPS calculations. Additionally, MC calculations with dose to water and dose to medium were compared.

## **2. THEORETICAL BACKGROUND**

### **2.1. THE MONTE CARLO SIMULATION OF RADIATION TRANSPORT**

The Monte Carlo method provides approximate solutions to a variety of mathematical problems by performing statistical sampling experiments on a computer. The method applies to problems with no probabilistic content as well as to those with inherent probabilistic structure. It represents an attempt to model nature through direct simulation of the essential dynamics of the system in question. In this sense the Monte Carlo method is a solution to a macroscopic system through simulation of its microscopic interactions.

For radiation transport problems, it simulates the tracks of individual particles by sampling appropriate quantities from the probability distributions governing the individual physical processes using machine-generated (pseudo-) random numbers. Average values of macroscopic quantities such as particle fluence, energy spectrum and absorbed dose distribution can be calculated by simulating a large number of particle histories. The Monte Carlo method and its application in medical radiation physics, especially in radiation therapy physics, have been discussed in a number of publications [29-33].

#### **2.1.1. Photon Interaction Processes**

The photon interaction processes that should be modelled by a Monte Carlo code designed for applications in radiotherapy and dosimetry are:

- Pair production in the nuclear and atomic fields
- Compton scattering from atomic electrons (incoherent scattering)
- Photoelectric absorption and photoelectron production
- Rayleigh scattering from atomic and molecular fields (coherent scattering)

Detailed information about interactions of photons with matter can be found on Appendix A.



Figure 2.1 is a schematic illustration of an actual photon history that includes the tracks of the secondary particles [34]. The history begins at position 1 in a vacuum; photons are indicated by sinusoidal tracks and the secondary electrons by straight lines.

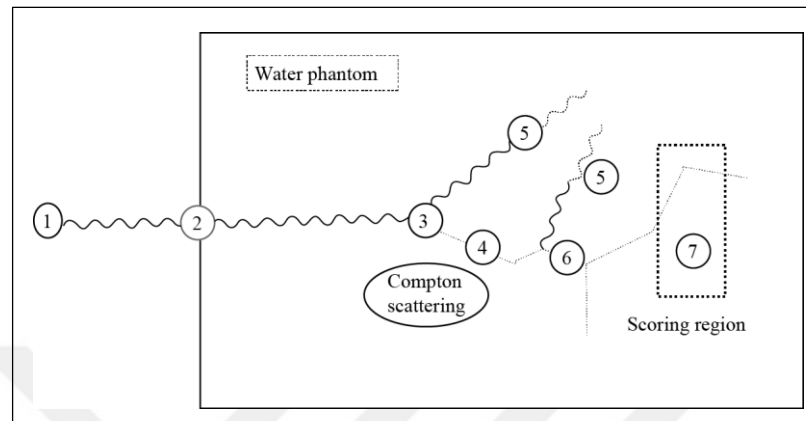


Figure 2.1. A schematic illustration of a Monte Carlo photon history

The simulation consists of the following steps 1 to 7 labelled in Figure 2.1:

1. Choose photon energy, direction, and starting position based on sampling from distribution of incident photons, and transport photon to first boundary
2. Choose distance to first interaction and transport photon to this interaction point
3. Choose the type of interaction (Compton scatter, photo-electric, pair-production, Rayleigh scatter)
4. Choose direction, energy, etc. of new particles (such as Compton electrons by sampling from the Klein–Nishina differential cross-section; characteristic photons; Auger electrons). Put them on the stack (i.e. a list of secondary particles to be followed later)
5. Transport scattered photon until it either leaves the geometry, or it reaches some predetermined energy cut-off
6. Transport secondary electron. Keep track of any  $\delta$  electrons and bremsstrahlung photons produced
7. Score deposited energy, fluence spectra, etc. in region of interest
8. Repeat steps 1–7 for many more particles until scored quantities reach a sufficiently low statistical uncertainty

### 2.1.2. Electron Interaction Processes

The electron and positron interaction processes that should be modelled by a Monte Carlo code designed for applications in radiotherapy and dosimetry are:

- Møller scattering of electrons from atomic electrons
- Bhabha scattering of positrons from atomic electrons
- Bremsstrahlung photon creation in the nuclear and atomic fields
- Positron annihilation with atomic electrons
- Elastic scattering of electrons and positrons from nuclei
- Excitation of atoms and molecules by electrons and positrons

Detailed information about interactions of charged particles with matter can be found on Appendix A.

Figure 2.2 presents the electron mean-free paths for the elastic, ionisation, excitation, and bremsstrahlung interactions in oxygen. The distance to an interaction in the relativistic region (greater than, 1 MeV) is noted as between  $10^5$  and  $10^4$  g/cm<sup>2</sup>. The range of a 10 MeV electron in oxygen is 5.6 g/cm<sup>2</sup>. This means, for example, that a relativistic electron must undergo  $10^5$  to  $10^6$  interactions before slowing down. A typical electron is completely slowed down in a typical simulation geometry. This means that each one of the  $10^5$  to  $10^6$  interactions would have to be simulated for each electron history. This form of calculation is called analogue simulation, and it is always done for photons. However, it requires Teraflop computational resources for most practical problems involving electron transport.

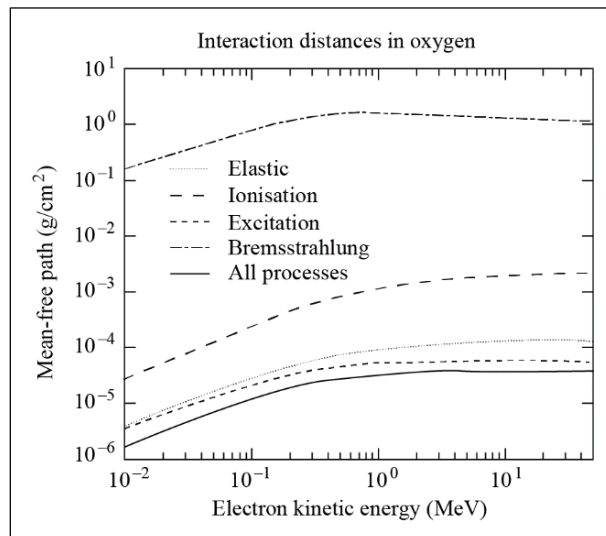


Figure 2.2. Electron elastic, ionization, excitation, and bremsstrahlung mean-free path in oxygen

Fortunately, there is a practical solution to this problem that was pioneered by Berger [35]. Berger called his technique Condensed History Electron Transport. It is based on the realisation that, whereas electrons undergo many interactions, relatively few of these interactions cause a great deal of energy loss or directional change. Therefore, the effect of most of these interactions is small, involving little energy loss or small angular deflections. Therefore, one can combine the effect of these small-effect interactions into single virtual large-effect interactions. These large-effect interactions can be theoretically predicted through cumulative-event theories. For energy losses, there is the continuous slowing down approximation (CSDA) method with the energy loss being characterised by the stopping power [36-40] or by distributions that are a function of the length of the electron path [41,42]. The effect of cumulative elastic scattering events is predicted by several small-angle theories [43-46]; although, these are being superseded by the any-angle theory of Goudsmit and Saunderson [47,48]. All of these theories require single-event elastic scattering models. The Goudsmit–Saunderson approach is favoured because it can be employed to use any cross-section. In particular, elastic cross-section calculations using partial-wave analysis are becoming quite sophisticated [49] and are being adopted in advanced Monte Carlo algorithms. Fortunately, the elastic scattering that produces the angular deflections produces no energy loss. Additionally, the energy-loss process produces very little angular deflection. Therefore, these two processes nearly decouple, making the theoretical development somewhat simpler and the construction of algorithms somewhat easier.

The Condensed History Method (CHM) has been put on a stronger theoretical footing by Larsen [50] who showed that the CHM converges at the exact solution of the Boltzmann transport equation in the limit of small electron path-lengths. This has led to the development of high-accuracy CHM [51-54]. Research in this area remains quite active. Nahum [55] has provided a review of the breadth of applications of the CHM in medical physics.

### 2.1.3. Coupled Electron–Photon Transport

The process by which coupled electron–photon transport is carried out is described in Figure 2.3.

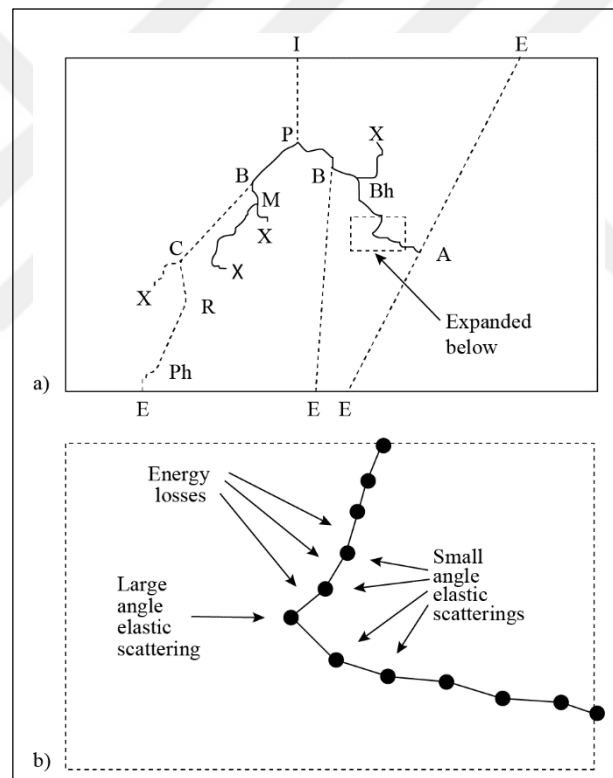


Figure 2.3. (a) Global picture of electron transport. Photons are represented by straight dashed lines; electrons and positrons by solid curves (I, insertion; E, escape; P, pair production; B, bremsstrahlung; M, Møller; X, end-of-range; C, Compton; R, Rayleigh; Ph, photoelectric; Bh, Bhabha; A, annihilation). (b) Expanded version of the dashed box in (a).

Figure 2.3.a, the simulation geometry is depicted by the outer rectangular box. Photons are represented by straight dashed lines; electrons and positrons by solid curves. A photon starts

the simulation by insertion, I, into the simulation geometry. It undergoes a pair interaction, P, producing an  $e^- e^+$  pair. The electron track (on the left) undergoes a bremsstrahlung interaction at B. Following the photon, it can be seen that there is a Compton interaction at C. The resulting electron is then transported until it runs out of energy at X. The photon undergoes a Rayleigh interaction at R, and it is then absorbed in a photoelectric event at Ph. The photoelectron escapes the simulation geometry at E. Returning to the initial electron, it undergoes a Møller interaction at M. Both the electron and its knock-on are then transported until their end-of-range at the X's. The positron that was born in the pair interaction at P undergoes a bremsstrahlung interaction at B, followed by a Bhabha interaction at Bh. The electron from B reaches its end-of-range at X. The positron eventually annihilates, producing two back-to-back annihilation quanta that escape the simulation geometry at their respective Es. The details of the CHM depicted in Figure 2.3.b are now the focus. At each one of the vertices, represented by a solid circle, the positron changes direction. (Electron and positron transport in the CHM are essentially the same.) The deposition of energy according to the CSD or other models can be considered to happen anywhere along the track segments.

#### 2.1.4. Sampling Theory

There are a number of sampling techniques well-known to all constructors of Monte Carlo codes. Only the Cumulative Probability Distribution Function Method is dealt with here. Assume that a probability function  $p(x)$  that is normalised over some range between  $a$  and  $b$  is used; that is:

$$\int_a^b p(x')dx' = 1 \quad (2.1)$$

Its cumulative probability distribution function is now constructed:

$$c(x) = \int_a^x p(x')dx' \quad (2.2)$$

that is monotonically increasing and bounded between 0 and 1. If random variable  $\xi$  is uniformly distributed on  $0 < \xi < 1$ , one can set  $\xi = c(x)$ . Therefore:

$$\xi = \int_0^x p(x') dx' \quad (2.3)$$

Using this expression, for example, distance to an interaction can be calculated as follows:

For mono-energetic photons, macroscopic total cross section of interaction ( $\Sigma_t$ ) remains the same in the same medium. This ensures that mean free path ( $\lambda = 1/\Sigma_t$ ) remains the same. Using Beer-Lambert law:

$$I = I_0 e^{-\frac{x}{\lambda}} \Rightarrow I = I_0 e^{-\Sigma_t x} \quad (2.4)$$

Therefore, probability of transportation of a mono-energetic photon in thickness  $x$  is  $I/I_0 = e^{-\Sigma_t x}$  and probability of absorption  $1 - e^{-\Sigma_t x}$ . Hence, probability of collision (or absorption) between  $x$  and  $x+dx$  can be written as:

$$p(x)dx = d(1 - e^{-\Sigma_t x}) = \Sigma_t e^{-\Sigma_t x} dx \quad (2.5)$$

Using the Equation (2.3),

$$\begin{aligned} \xi &= \int_0^x \Sigma_t e^{-\Sigma_t x'} dx' \\ &= 1 - e^{-\Sigma_t x} \end{aligned} \quad (2.6)$$

$$\Rightarrow x = -\frac{1}{\Sigma_t} \ln(1 - \xi) \quad (2.7)$$

One can change  $(1 - \xi)$  with  $\xi$ , therefore, distance to an interaction can be written as:

$$x = -\frac{1}{\Sigma_t} \ln \xi \quad (2.8)$$

### 2.1.5. EGSnrc Monte Carlo Code

The Electron Gamma Shower (EGS) Code System (EGS3 and later EGS4) was designed to simulate the flow of electrons and photons through matter at energies ranging from just below one MeV to several thousand. EGS uses a statistical game-playing approach to solve the difficult mathematical problem posed by electron transport through matter. The program uses Monte Carlo methods to simulate the statistical outcome of each interaction. All possible outcomes of an interaction are identified and assigned to an imaginary roulette wheel and the wheel is weighted to reflect predicted outcomes of an interaction. The wheel is spun and particles are created and transported in a random-walk process.

This version of EGS proved valuable in detector design, radiation shielding analysis, determining accelerator component temperature rises, and other accelerator problems. EGS, which was well documented, user-friendly, versatile, upwardly compatible and supported by technical experts, was licensed free of charge to the scientific community. The program soon became very popular and a large user community developed.

EGSnrc is an updated and developed EGS code at the National Research Center of Canada. The EGSnrc capabilities and features are [56]:

- The radiation transport of electrons (+ or -) or photons can be simulated in any element, compound, or mixture.
- Both photons and charged particles are transported in steps of random length rather than in discrete steps.
- The dynamic range of charged particle kinetic energies goes from a few tens of keV up to a few hundred GeV.
- The dynamic range of photon energies lies between 1 keV and several hundred GeV.
- The following physics processes are taken into account by the EGSnrc Code System:
  - Bremsstrahlung production using either Bethe-Heitler cross sections or the National Institute of Standards and Technology (NIST) cross sections.
  - Positron annihilation in flight and at rest.
  - Multiple scattering of charged particles by coulomb scattering from nuclei is handled using a new multiple scattering theory that overcomes the shortcomings of Moliere multiple scattering theory. It allows for steps of any size and moves seamlessly from a single scattering model for short steps to an accurate multiple scattering model at large steps. The

user has the option of scattering based on Rutherford scattering or scattering accounting for relativistic and spin effects.

- Møller ( $e^-e^-$ ) and Bhabha ( $e^+e^-$ ) scattering.
- Continuous energy loss applied to charged particle tracks between discrete interactions.
  - Total restricted charged particle stopping power consists of soft bremsstrahlung and collision loss terms.
  - Collision loss determined by the restricted Bethe-Bloch stopping power with Sternheimer treatment of the density effect in the general case but with provision of using an arbitrary density effect correction and data supplied to use the density effect recommended by the ICRU in Report 37 [40].
- Pair production.
- Compton scattering, either Klein-Nishina or bound Compton.
- Coherent (Rayleigh) scattering can be included by means of an option.
- Photoelectric effect.
- Relaxation of excited atoms after vacancies are created (eg after photoelectric or Compton scattering events) to create fluorescent photons (K, L, M shells) and Auger and Coster-Kronig electrons may be produced and tracked if requested.
- PEGS4 is a stand-alone data preprocessing code consisting of 12 subroutines and 85 functions. The output is in a form for direct use by EGS4.
  - PEGS4 constructs piecewise-linear fits over a large number of energy intervals of the cross section and branching ratio data.
  - In general, the user need only use PEGS4 once to obtain the media data files required by EGSnrc.
  - In addition to the material specific data files produced by PEGS4, EGSnrc uses a variety of other data files as input for the calculations.
- EGSnrc is a package of subroutines plus block data with a flexible user interface.
  - This allows for greater flexibility without requiring one to be overly familiar with the internal details of the code.
  - Together with the macro facility capabilities of the Mortran3 language, this reduces the likelihood that user edits will introduce bugs into the code.
  - EGSnrc uses material cross section and branching ratio data created and fit by the companion code, PEGS4.
  - The geometry for any given problem is specified by a user-written subroutine called HOWFAR, which, in turn, can make use of auxiliary subprograms.
  - Auxiliary geometry routines for planes, cylinders, cones, spheres, etc., are provided with the EGSnrc Code System.
  - Macro versions of these routines are also provided in the set of defining macros (i.e., in the `egsnrc.macros` file) which, if used, generally result in a faster running simulation.



- Transport can take place in a magnetic field by writing a specially designed HOWFAR subprogram, or in a more general manner (eg., including electric field) by making use of Mortran3 macro templates that have been appropriately placed for that purpose in subroutine ELECTR.
- The user scores and outputs information in the user-written subroutine called AUSGAB.
  - By setting various AUSFLG flags, the user can arrange to have access to the simulation parameters under many different situations to allow scoring of almost any parameter of interest without delving into the code itself.
  - Auxiliary subprogram WATCH is provided in order to allow an event-by-event or step-by-step tracking of the simulation, either to the terminal or for 3-D graphics display using the program EGS\_Windows.
- EGSnrc allows for the implementation of importance sampling and other variance reduction techniques (eg., leading particle biasing, splitting, path length biasing, Russian roulette, etc.).
  - EGSnrc introduces options to allow for efficient bremsstrahlung splitting and Russian Roulette of secondary charged-particles, but only if “turned on” by the user.
  - EGSnrc calculates the range and distance of the particle to the nearest boundary on every step as part of the electron transport algorithm and there is an option to do range rejection on any particle that cannot get out of the current region.
- Initiation of the radiation transport:
  - An option exists for initiating a shower with two photons from pi-zero decay.
  - The user has the choice of initiating the transport by means of a monoenergetic particle, or by sampling from a known distribution (eg., a synchrotron radiation spectrum).
  - Transport can also be initiated from sources that have spatial and/or angular distributions.

The EGS code itself consists of two User-Callable subroutines, HATCH and SHOWER, which in turn call the other subroutines in the EGS code, some of which call three User-written subroutines, HOWFAR, HOWNEAR and AUSGAB. This is best illustrated with the aid of Figure 2.4.

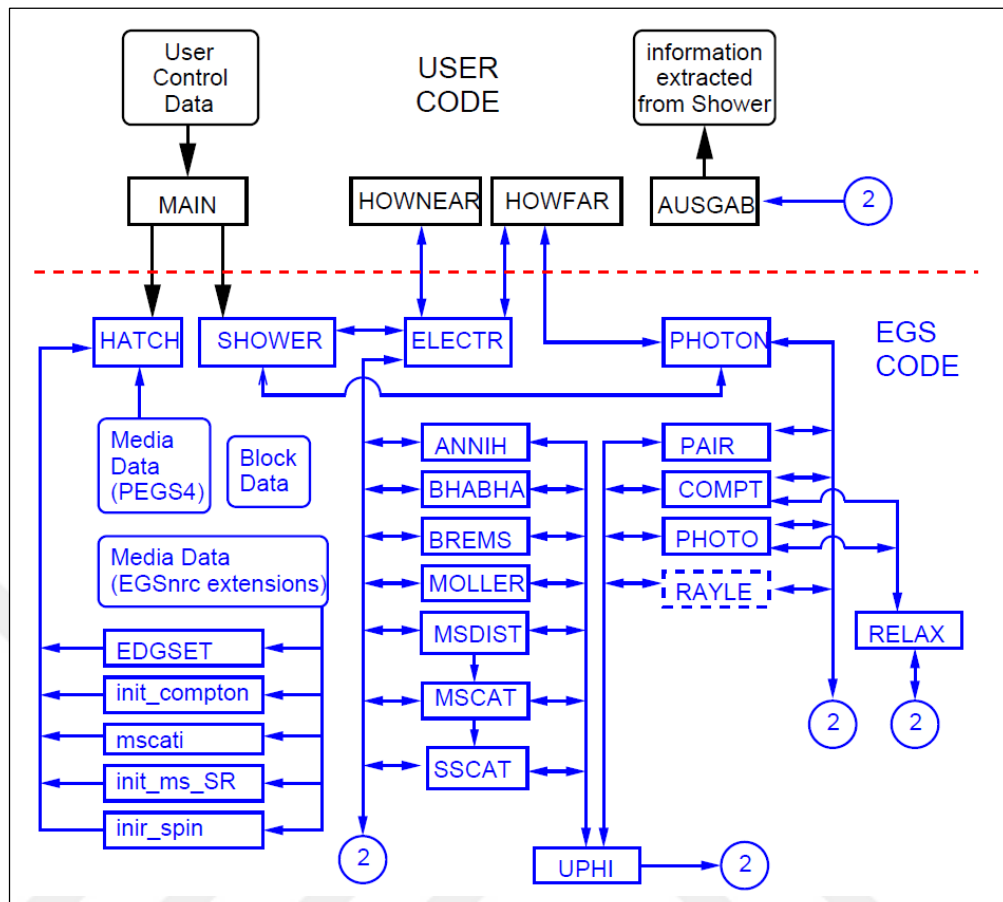


Figure 2.4. The structure of the EGSnrc code system when used with a user-code

To use EGS the user must write a “User Code”. This consists of a MAIN program and the subroutines HOWFAR, HOWNEAR and AUSGAB, the latter three determining the geometry and output (scoring), respectively. Additional auxiliary subprograms might be included in the User Code to facilitate matters. The user can communicate with EGS by means of various COMMON variables. Usually MAIN will perform any initialization needed for the geometry routines, HOWFAR and HOWNEAR, and sets the values of certain EGS COMMON variables which specify such things as names of the media to be used, the desired cutoff energies, and the distance unit to be used (e.g., inches, centimeters, radiation lengths, etc.). MAIN then calls the HATCH subroutine which “hatches EGS” by doing necessary once-only initialization and by reading material data for the media from a data set that had been previously created by PEGS. This initialization completed, MAIN may then call SHOWER when desired. Each call to SHOWER results in the generation of one history (often referred to as a “case”). The arguments to SHOWER specify the parameters of the incident particle initiating the cascade.

In addition, macro definitions can be included in MAIN in order to control or override various functions in EGS as well as in the User-Written codes.

### **2.1.6. Modelling Radiotherapy Beams**

Radiotherapy beams from linear accelerators are very complex. Some are high-energy electron beams, made uniform by one or two thin scattering foils and shaped by thick metal devices called applicators. More commonly they are high energy x-ray or photon beams created as Bremsstrahlung as the electrons are stopped in thick high-Z targets and then made uniform across the field by a flattening filter designed to attenuate the center of the beam much more than the edges and shaped by thick jaws or multi-leaf collimators. In 1995, the BEAM code was released for general use [57]. BEAM was designed to model all types of radiotherapy accelerators. The model of an accelerator is built from a series of component modules (CMs), each of which can be re-used several times in the accelerator and each of which has two surfaces perpendicular to the axis of the accelerator.

When the BEAM code was developed in the early nineties, it was within the larger OMEGA project (a collaboration between NRC, the University of Wisconsin and the Ottawa Cancer Clinic), which was to develop a 3-D dose calculation engine for use in clinical treatment planning systems for electron beam therapy. The OMEGA project's goal was to develop electron beam dose calculation capabilities, although the resulting codes work equally well for electron and photon beam therapy. The project developed a code, called DOSXYZ [58], which calculates the dose distribution in a patient defined by a computed tomography (CT) data set. The program handles the complexities of the accelerator beam coming in at an arbitrary angle and the problem of defining the materials and densities to be used in the Monte Carlo simulation based on the CT data, but otherwise is a relatively simple Monte Carlo code that only needs to simulate rectangular parallelepipeds with different materials. While BEAM and DOSXYZ are still used to define the gold standard for many Monte Carlo calculations, there have been some truly remarkable developments in the last few years, which have taken the concept of using Monte Carlo for clinical treatment planning out of the research lab and into commercial implementations.

Other codes of the OMEGA are the STATDOSE, CTCREATE, and BEAMDP for the analysis of the dose distributions, creation of patient phantoms from CT images and analysis of the phase space files. The DOSXYZ\_SHOW code can also, be considered as part of the OMEGA project, and it is used for the representation of the isodose curves of the dose distribution.

Detailed information about dosimetric concepts in radiation therapy can be found on Appendix B.

## **2.2. MEDICAL LINEAR ACCELERATORS**

Radiation therapy, also referred to as radiotherapy, is one of the three principal modalities used in treatment of malignant disease (cancer), the other two being surgery and chemotherapy. In contrast to other medical specialties that rely mainly on the clinical knowledge and experience of medical specialists, radiotherapy, with its use of ionizing radiation in treatment of cancer, relies heavily on modern technology and collaborative efforts of several professionals whose coordinated team approach greatly influences the outcome of the treatment.

Today radiotherapy techniques have been improved with an aim to kill all cancer cells while preserving as many normal surrounding cells as possible. Wherever possible a cure for cancer is sought. If a cure is not possible, the aim is to relieve the symptoms of cancer (palliation), thereby improving the quality or extending the person's life. Radiotherapy can be used alone or with chemotherapy or surgery as a combined treatment.

In radiation therapy, high energy x-rays in the megavoltage range are commonly used for cancer treatments. These high energy x-rays are generally produced by a linear accelerator (linac).

In a linear accelerator (linac) designed for radiotherapy, electrons gain energy by interacting with a synchronised radio-frequency electromagnetic field rather than by acceleration by direct potential. In free air, electromagnetic waves travel at the speed of light, but in a suitably designed waveguide, the speed of propagation of the waves can be substantially

reduced. The accelerating waveguide (or accelerator structure) consists of a long cylindrical tube, containing a series of circular baffles (Figure 2.5). These are designed so that speed of propagation of the microwaves increases in the first part of the accelerating tube until it eventually reaches velocities close to the speed of light. Bunches of electrons generated in the gun are injected into the guide in synchronism with pulsed microwave radiation and are carried down the guide in a manner analogous to riding the crest of a wave [59].

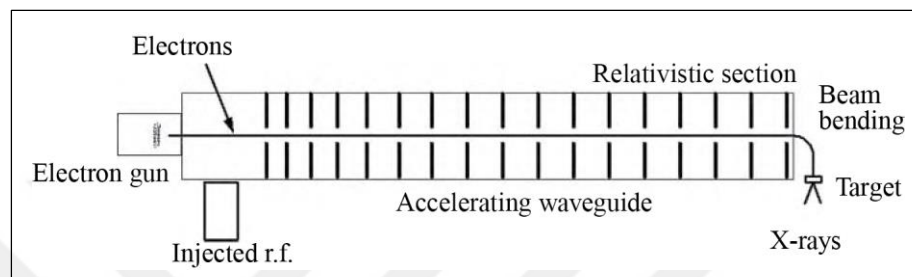


Figure 2.5. Schematic diagram of a linear accelerator designed for radiotherapy and used in x-ray mode

The high-energy electron beams, typically 6 MeV or above, can be directly used for therapy. Electron beams from linear accelerators are useful for treatment of superficial tumors, but for more deep-seated tumours, it is better to use photon beams. If the electron beam is to be used for therapy, the originally narrow beam of electrons must be broadened by scattering the electrons.

In photon mode, megavoltage x-rays are generated by bremsstrahlung from a high-energy electron beam striking a high atomic number metal target, usually tungsten or a copper-tungsten laminate. However, as the energy is increased, the bremsstrahlung emission becomes increasingly directed forward (Figure 2.6), so that at megavoltage energies, the target acts as a transmission target. The target is water cooled, but because of the higher efficiency of x-ray production, the target assembly is sufficiently compact so that it can be moved out of the beam to enable an electron beam to be delivered.

In the simplest accelerators, the target is fixed and the accelerating structure is coaxial with the emerging x-ray beam (i.e. it is parallel to the direction of travel of the electrons so that no bending of the electrons takes place) and is perpendicular to the cranio-caudal axis of the

patient. However, for energies above 6 MeV, the length of the accelerator tube is such that it makes this impracticable. In order for the radiation beam to be brought in to irradiate the patient from any angle, it becomes necessary to bend the beam. Electrons are easily deflected in a magnetic field, and it is convenient to bend them through about 90 or 270 degree (Figure 2.7).

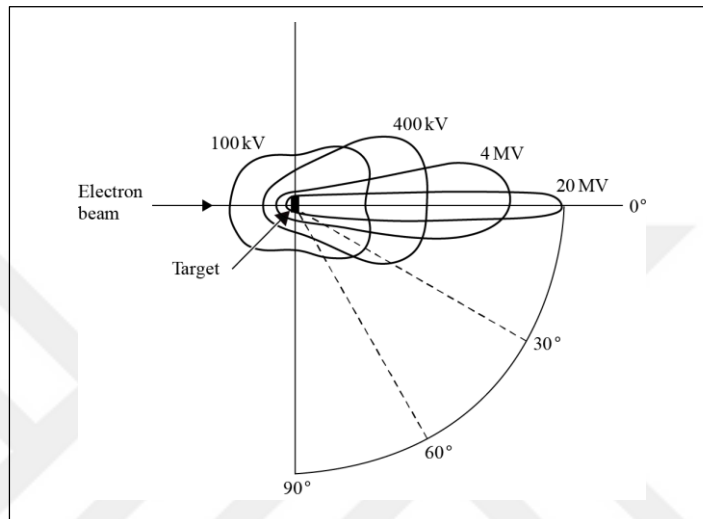


Figure 2.6. Schematic illustration of spatial distribution of x-rays around a thin target

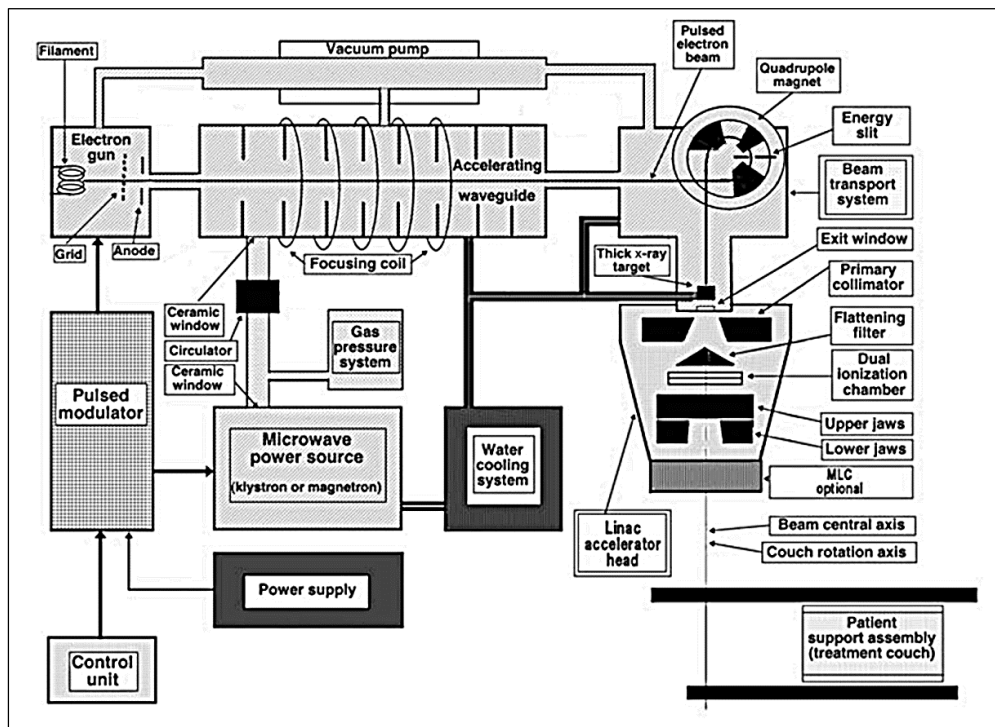


Figure 2.7. Schematic diagram of a linear accelerator

The radiation beam must be constrained in some way to ensure that only the required part of the patient is irradiated. In order to meet the requirements for very low dose rates at a large distance beyond the edge of the radiation field, accelerators have a circular primary collimator close to the source. This limits the field to a circular shape.

The bremsstrahlung generated when a high-energy electron beam strikes a target is primarily directed forward and Gaussian shape. The use of a flattening filter (Figure 2.7) makes it possible to compensate for the lack of scatter at the edge of the field by deliberately designing a profile that increases toward the edges. The flattening filter is generally circularly symmetric.

The secondary collimators (sometimes also called diaphragms or jaws) is usually made of flat-faced blocks of lead that move in an arc in order that the face of the block shall be aligned with the field's divergent edge. Some of them may have curved edges. They collimate the beam as square fields in both direction. The maximum field size of square field in a linac is generally  $40\text{ cm} \times 40\text{ cm}$  at 100 cm source to skin distance (SSD) (i.e., the distance between target to center of rotation of the gantry).

Conventional collimators are only able to constrain the radiation to a rectangular shape. In order to provide more flexibility, multileaf collimators have been introduced. Instead of a single block of metal, these have up to 80 pairs of leaves that can move independently, allowing any beam shape to be produced subject to the width of the leaves. The leaf thickness of about 7 cm is sufficient to reduce the intensity of the primary beam to one per cent. There has to be a mechanical clearance between the leaves to permit easy movement, and this results in leakage between adjacent leaves that is minimised by the use of stepped and overlapped leaf sections as shown in Figure 2.8. As long as the overlap is maintained, the maximum leakage between leaves will be approximately 10 per cent, but in practice, lower leakage is achieved.

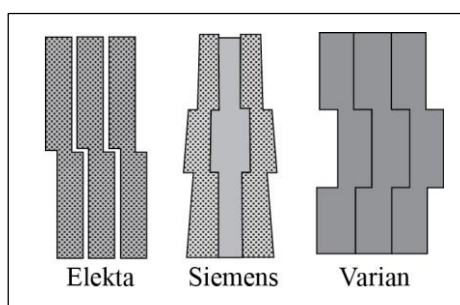


Figure 2.8. Overlapped leaf sections from different manufacturers

Most of the linear accelerators currently produced are so constructed that the source of radiation can rotate about a horizontal axis. As the gantry rotates, the collimator axis (supposedly coincident with the central axis of the beam) moves in a vertical plane. The point of intersection of the collimator axis and the axis of rotation of the gantry is known as the isocenter.

## 2.3. PATIENT DOSE CALCULATIONS

### 2.3.1. Isodose Curves

The central axis depth dose distribution by itself is not sufficient to characterize a radiation beam that produces a dose distribution in a three-dimensional volume. In order to represent volumetric or planar variations in absorbed dose, distributions are depicted by means of isodose curves, which are lines passing through points of equal dose (Figure 2.9). An isodose chart for a given beam consists of a family of isodose curves usually drawn at equal increments of percent depth dose, representing the variation in dose as a function of depth and transverse distance from the central axis. The depth dose values of the curves are normalized either at the reference point of maximum dose on the central axis or at a fixed distance along the central axis in the irradiated medium.

Detailed information on characteristics of megavoltage photon beams can be found on Appendix B.



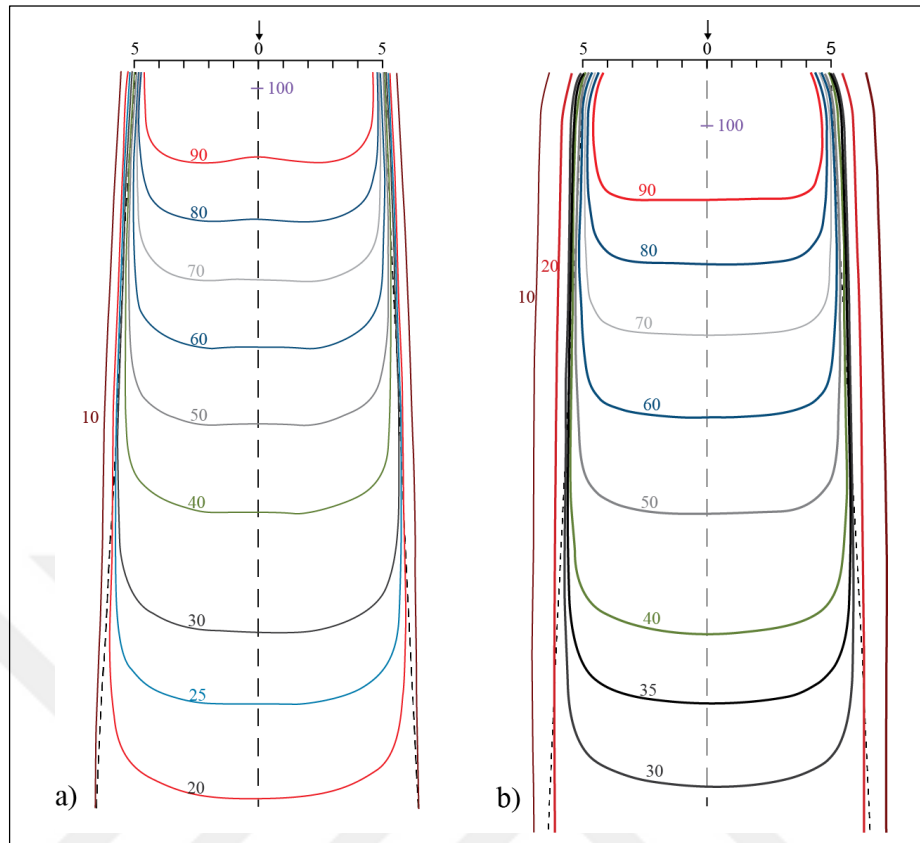


Figure 2.9. Example isodose curves for (a) 4 MV, (b) 10 MV photon beams

### 2.3.2. Conventional Radiotherapy

In conventional radiotherapy, realistic body thickness of the patient is used and the localization of the target volume is determined. It is assumed that the whole body consist of water. For treatment planning, most commonly two or more radiation fields is used. Using intersection points of isodose curves of the fields, total isodose curves are determined (Figure 2.10) [60]. Using percent dose of the curve which covers most of the target volume (115% for this example), irradiation time (for  $^{60}\text{Co}$  machines) or Monitor Units (MUs) (for linacs) are calculated.

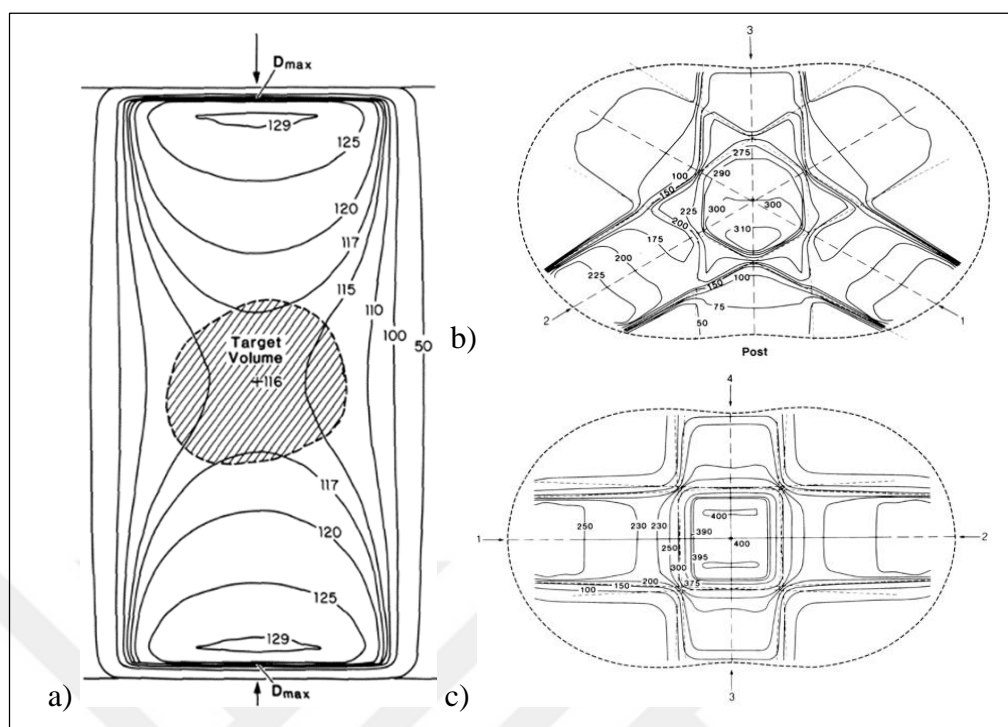


Figure 2.10. Treatment planning using two or more radiation fields

### 2.3.3. Three-Dimensional Conformal Radiation Therapy

In three-dimensional conformal radiotherapy (3D-CRT), treatments that are based on 3D anatomic information and use treatment fields that conform as closely as possible to the tumor volume in order to deliver adequate dose to the tumor and minimum possible dose to normal tissue. The main difference between treatment planning of 3D-CRT and conventional radiation therapy is that the former requires the availability of 3D anatomic information and a Treatment Planning System (TPS) that is capable of calculating 3D dose distributions and dose-volume statistics for contoured structures.

Anatomic images of high quality are required to accurately delineate target volumes and normal structures. Modern imaging modalities for treatment planning include computed tomography (CT), magnetic resonance imaging (MRI), ultrasound (US), single photon emission tomography (SPECT), and positron emission tomography (PET). Depending on the imaging modality, visible tumor, critical structures, and other relevant landmarks are outlined slice by slice by the planner. The radiation oncologist draws the target volumes in each slice with appropriate margins to include visible tumor, the suspected tumor spread,

and patient motion uncertainties. This process of delineating targets and relevant anatomic structures is called segmentation.

#### **2.3.4. Definition of Treatment Volumes**

International Commission on Radiation Units and Measurements (ICRU) recognized the need for a general dose-specification system that could be adopted universally. Although the system proposed by the ICRU has not been universally implemented, there is a substantial advantage in adopting a common method of dose specification. Various volumes that the ICRU Report 50 [61] recommends to be identified in a treatment plan. These volumes are as follows:

##### ***2.3.4.1. Gross Tumor Volume***

The gross tumor volume (GTV) is the gross demonstrable extent and location of the tumor. It may consist of primary tumor, metastatic lymphadenopathy, or other metastases.

##### ***2.3.4.2. Clinical Target Volume***

The clinical target volume (CTV) consists of the demonstrated tumor(s) if present and any other tissue with presumed tumor. It represents therefore the true extent and location of the tumor.

##### ***2.3.4.3. Internal Target Volume***

ICRU Report 62 [62] recommends that an internal margin (IM) be added to CTV to compensate for internal physiologic movements and variation in size, shape, and position of the CTV during therapy in relation to an internal reference point and its corresponding coordinate system. The volume that includes CTV with these margins is called the internal target volume (ITV).

#### ***2.3.4.4. Planning Target Volume***

The volume that includes CTV with an IM as well as a setup margin (SM) for patient movement and setup uncertainties is called the planning target volume (PTV).

#### ***2.3.4.5. Planning Organ at Risk Volume***

The organ(s) at risk (OAR) needs adequate protection just as CTV needs adequate treatment. Once the OAR is identified, margins need to be added to compensate for its movements, internal as well as setup. Thus, in analogy to the PTV, one needs to outline planning organ at risk volume (PRV) to protect OAR effectively.

#### **2.3.5. Intensity Modulated Radiation Therapy (IMRT)**

In the traditional external beam photon radiation therapy, most treatments are delivered with radiation beams that are of uniform intensity across the field (within the flatness specification limits). Occasionally, wedges or compensators are used to modify the intensity profile to offset contour irregularities and/or produce more uniform composite dose distributions. This process of changing beam intensity profiles to meet the goals of a composite plan is called intensity modulation. Thus, the compensators and wedges may be called intensity modulators, albeit much simpler than the modern computer-controlled intensity modulation systems such as dynamic multileaf collimators.

The principle of IMRT is to treat a patient from a number of different directions (or continuous arcs) with beams of nonuniform fluences, which have been optimized to deliver a high dose to the target volume and an acceptably low dose to the surrounding normal structures. The treatment planning program divides each beam into a large number of beamlets and determines optimum setting of their fluences or weights. The optimization process involves inverse planning in which beamlet weights or intensities are adjusted to satisfy predefined dose criteria for the composite plan.

### **2.3.6. Treatment Planning Systems**

The Treatment Planning Systems (TPSs) are responsible for predicting the dose distribution inside the patient given the anatomy of the patient and the beam arrangement. There are two major components in the TPSs that are required in order to get the desired result. The first one is non-patient specific data, which includes the machine model and measured dosimetric data etc. The second one is the patient specific data, which includes beam settings and patient anatomy, etc.

After supplying the non-patient specific and patient specific data, the dose calculation can be achieved. The dose computation “engine” is the major component of a TPS. The dose calculation method should be as accurate as possible and fast enough to provide results in short time for any desired treatment arrangement.

The patient representation is required for the dose calculation algorithm to accurately predict the dose distribution in the presence of inhomogeneities. The classical approach for dose calculations to a heterogeneous geometry is to correct the dose acquired for a similar but homogeneous geometry. That is the dose to the inhomogeneous medium is corrected by applying a multiplicative factor to the dose to homogeneous medium at the same point. More recent methods calculate the dose directly by including effects from heterogeneities directly into the models. The situation for modeling of volume scattering effects is similar; a number of methods estimate scatter variations while newer models make calculations based on particle or energy transport directly.

Detailed information on dose calculation algorithms used in TPSs can be found on Appendix B.

### **2.3.7. Dose Evaluation of Treatment Plans**

Traditionally, treatment plans are optimized iteratively by using multiple fields, beam modifiers (e.g., wedges and compensators, etc.), beam weights, and appropriate beam directions. Dose distributions of competing plans are evaluated by viewing isodose curves in individual slices, orthogonal planes (e.g., transverse, sagittal, and coronal) [60]. Figure 2.11 is an example of isodose curves displayed in transverse plane. One of the major

advantages of 3-D treatment planning is the display of dose distribution, which can be manipulated with ease to show volumetric dose coverage in individual slices, in orthogonal planes.

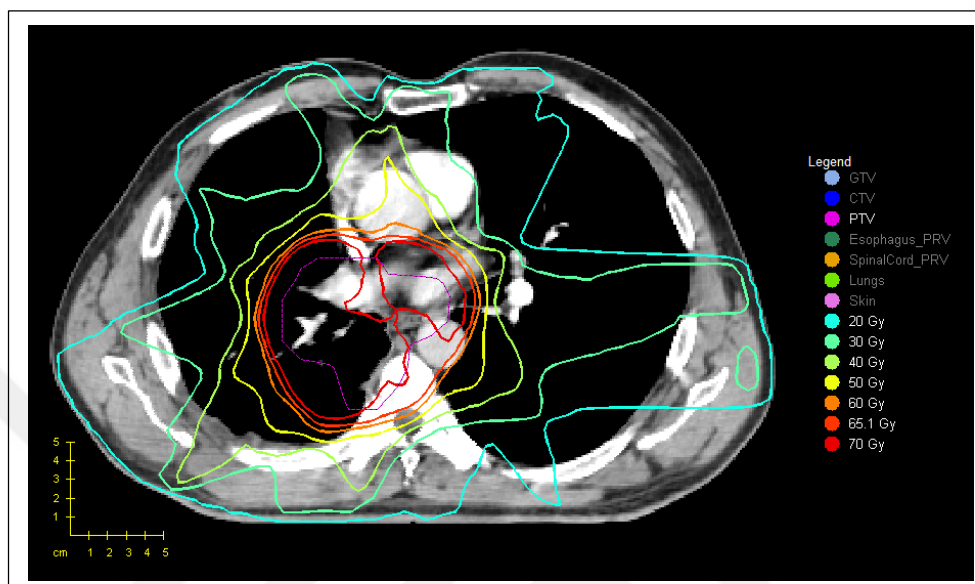


Figure 2.11. PTV and isodose curves

The dose distribution is usually normalized to be 100% at the point of dose prescription so that the isodose curves represent lines of equal dose as a percentage of the prescribed dose.

Display of dose distribution in the form of isodose curves or surfaces is useful because it shows not only regions of uniform dose, high dose, or low dose, but also their anatomic location and extent. In 3D treatment planning, this information is essential but should be supplemented by dose volume histograms (DVHs) for the segmented structures, for example, targets and critical structures. A DVH not only provides quantitative information with regard to how much dose is absorbed in how much volume, but also summarizes the entire dose distribution into a single curve for each anatomic structure of interest. It is, therefore, a great tool for evaluating a given plan or comparing competing plans [63].

The DVH can be expressed as the summed volume of elements receiving dose in a specified dose interval, against a set of equally spaced dose intervals. This is a differential DVH and shows the absolute or relative volume in each dose interval (bin) directly Figure 2.12. More frequently used, however are cumulative dose volume frequency distributions, which are

plots of the volume receiving a dose greater than, or equal to, a given dose, against dose. The volume accumulates starting at the highest dose bin continuing towards zero dose, eventually reaching 100 per cent of the total volume. Normally volumes are expressed as a percentage of the total volume; however, in some situations the absolute volume may be more appropriate.

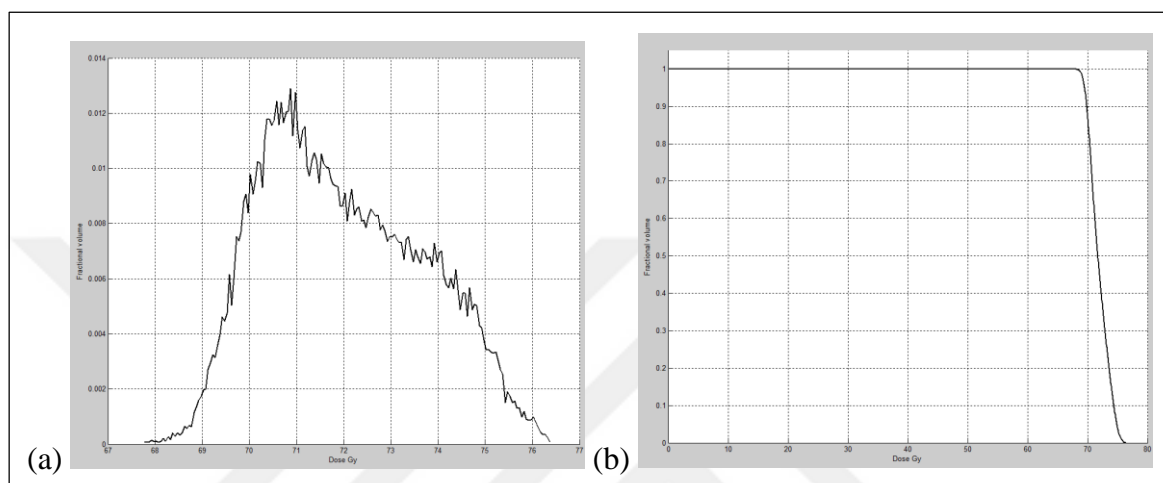


Figure 2.12. Dose volume histograms: (a) differential, (b) cumulative

DVHs can be used during the planning process to check whether the dose is adequate and uniform throughout the target volume, and the extent and value of any hot spots in adjacent normal tissue. However, because they do not display positional information, they should not be the only method used. Their main use is as a plan evaluation tool. They can be used as a method of comparing different treatment plans on a single graph, for specifically identified structures and target volumes. For the PTV, DVHs should show a uniformly high dose throughout the volume. The shape approximates to a step function and a steep slope shows that a large percentage of the volume has a similar dose.

A number of parameters can be derived from a DVH. The simplest form of reporting the dose in a structure, either a target volume or an organ at risk, consists of choosing a point meant to be representative of the dose distribution within the structure. This was the approach chosen by ICRU [61] as a means to obtain a uniform method for dose reporting in a given center or amongst several centers. These parameters include, minimum, maximum and mean doses, dose at reference fractional volume ( $D_{V_{ref}}$ ), volume of reference dose ( $V_{D_{ref}}$ ), etc.

It is possible to derive combination of these parameters, such as, homogeneity index that is defined as:

$$HI(\%) = 100 \cdot \frac{D_{\max} - D_{\min}}{D_{\text{mean}}} \quad (2.9)$$

Another parameter defined by ICRU [62] is conformity index. The conformity index (CI) is defined as the ratio of the treated volume (TV) and the PTV. This definition implies that the TV totally encompasses the PTV. In cases where a fraction of the PTV lies outside of the TV, a CI equal to 1 could still be obtained even though the conformity of the dose distribution was very poor. To overcome this problem a more general definition of the CI for a given dose level D is the following [63]:

$$CI(D) = IF_{PTV}(D) \times [1 - IF_{HT}(D)] \quad (2.10)$$

where  $IF_{PTV}(D)$  is the irradiation factor of the PTV, defined as the fraction of the PTV receiving a dose higher than D;  $IF_{HT}(D)$  is the irradiation factor of healthy tissue, defined as the ratio of the volume of tissue outside the PTV receiving a dose greater than D to the volume of isodose D.

### 2.3.8. Biological Evaluation of Treatment Plans

To evaluate or compare treatment plans a radiobiological parameter called normal tissue complication probability (NTCP) can be used. It reduces the large amount of data characterizing a three-dimensional dose distribution to a limited number of numerical indices, thus making the comparison of a number of rival plans more efficient. In addition, NTCP nominally represents an endpoint, which often determines the acceptability of a treatment plan, that is, whether the tolerance of normal tissues has been respected or exceeded.

Lyman [64] argued that normal tissue complication probabilities depend upon volume as well as dose, and that they could be conveniently represented by an error function in dose



and volume. For organs that are irradiated by a uniform dose to part of the volume and no dose to the rest, the probability of a complication can be represented by:

$$NTCP = \frac{1}{\sqrt{2\pi}} \int_{-\infty}^t e^{-t^2/2} dt \quad (2.11)$$

$$t = \frac{D - TD_{50}(V/V_{ref})}{m \cdot TD_{50}(V/V_{ref})} \quad (2.12)$$

$$TD_{50}(1) = TD_{50}(V/V_{ref})(V/V_{ref})^n \quad (2.13)$$

The parameters in this model:

- $TD_{50}(1)$ , the dose to the whole organ which would lead to complication in 50% of the population
- $TD_{50}(V/V_{ref})$ , the  $TD_{50}$  at partial volume  $V/V_{ref}$  ;
- $V_{ref}$ , a reference volume, which in many cases will be the (whole) organ volume;
- $m$ , a parameter representing the steepness of the dose–response curve;
- $n$ , the exponent of volume in the power law that relates the tolerance doses for uniform whole and uniform partial organ irradiation.

In many cases, uniform organ irradiation is not possible. Therefore, a way of using the Lyman model in the more general case of inhomogeneous dose in the organ or tissue of interest is necessary. One way of doing this is to convert the organ's DVH into an equivalent uniform one using effective volume method [65]. In this method, the DVH for the organ in question is transformed into one in which the volume  $V_{eff}$  (which is equal to or less than the whole organ volume) receives a dose equal to the maximum dose in the organ ( $D_{max}$ ). One operates on each dose-bin of the differential DVH in turn, multiplying the fractional volume  $\Delta V_i$  in that bin; of (mean) dose  $D_i$ , by  $(D_i / D_{max})^{1/n}$  to yield the effective volume for that bin,  $\Delta V_{eff}$ . Thus the effective volume is given by:

$$V_{eff} = \sum_{i=1}^k \Delta V_i (D_i / D_{max})^{1/n} \quad (2.14)$$

There is a family of equivalent uniform DVHs with effective volume and dose related through the defining power-law relationship. Thus, there is an effective dose ( $D_{eff}$ ) or equivalent uniform dose ( $EUD$ ) that, if applied to the whole organ ( $V_T$ ), would yield the same NTCP:

$$EUD = \sum_i \left[ D_i^{1/n} \frac{V_i}{V_T} \right]^n \quad (2.15)$$



### 3. MATERIALS AND METHODS

#### 3.1. MONTE CARLO MODEL OF ELEKTA SYNERGY MLCi LINAC

##### 3.1.1. Monte Carlo Modelling

The Monte Carlo model of the 6-MV photon beam of the Elekta Synergy MLCi linac (Elekta Oncology Systems, Crawley, UK) installed at Gülhane Military Medical Academy, Department of Radiation Oncology was modelled by taking into consideration of the technical specifications provided by the manufacturer (Figure 3.1) [66]. The Monte Carlo code used in this study was the 2010 version of EGSnrc/BEAMnrc code system [67,68]. This code is not able to simulate electromagnetic waves. Because of this, the simulation started with the electron beam that is accelerated and directed to the vacuum window of the linac.

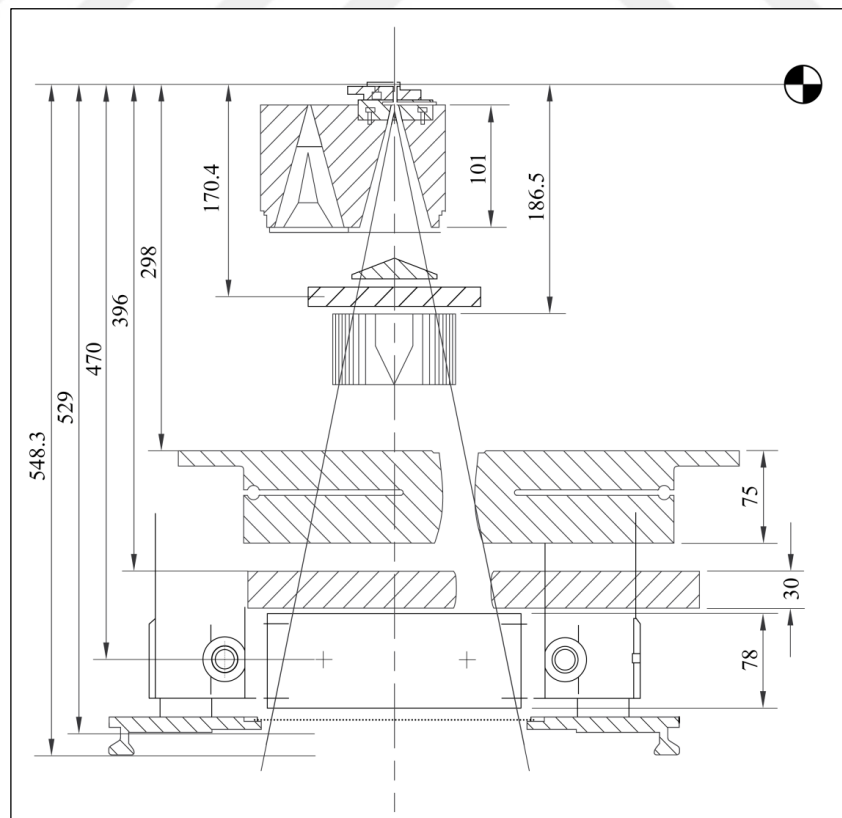


Figure 3.1. Technical drawing of Elekta Synergy MLCi treatment head

The components of the linac simulated here were defined by means of the graphical user interface (GUI) of the code: BEAMnrc (Figure 3.2.a). In the definition of each part, the components should be ordered in a list (Figure 3.2.b). After these definitions, the PEGS4 file that contains cross section data of the elements, molecules and compounds used in the simulation should be selected. (Figure 3.2.c). The next step is to specify the details of the components by using “Edit...” buttons next to their names (Figure 3.2.b).

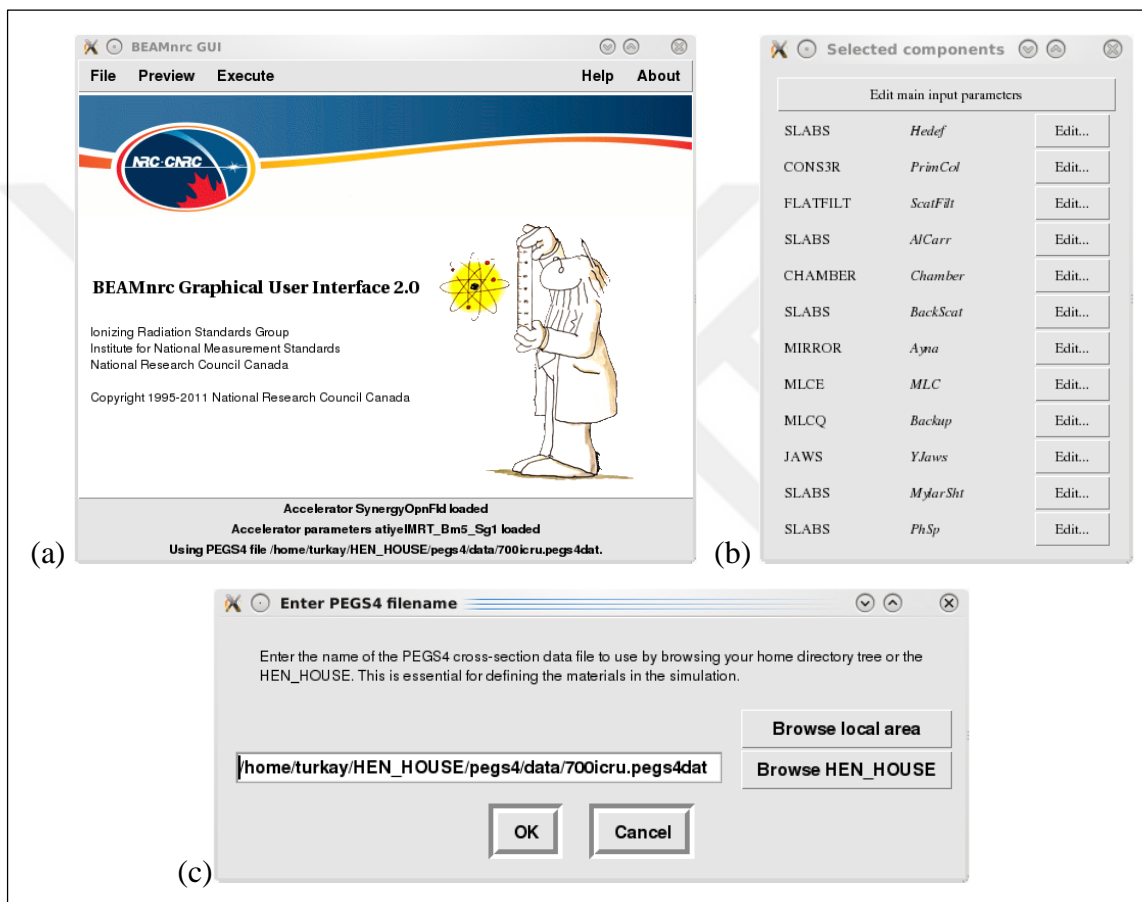


Figure 3.2. (a) The graphical user interface of the BEAMnrc code, (b) the linac component list in order, (c) PEGS4: the cross section file selecting window

The initial component that electron beam interacts is the target that used to produce Bremsstrahlung X-rays. In case of electron beam treatment, this target is removed from the way of the electron beam automatically. SLABS component module (CM) (Figure 3.3.a) was used to model tungsten target that has 6.0 mm thickness (Figure 3.3.b).

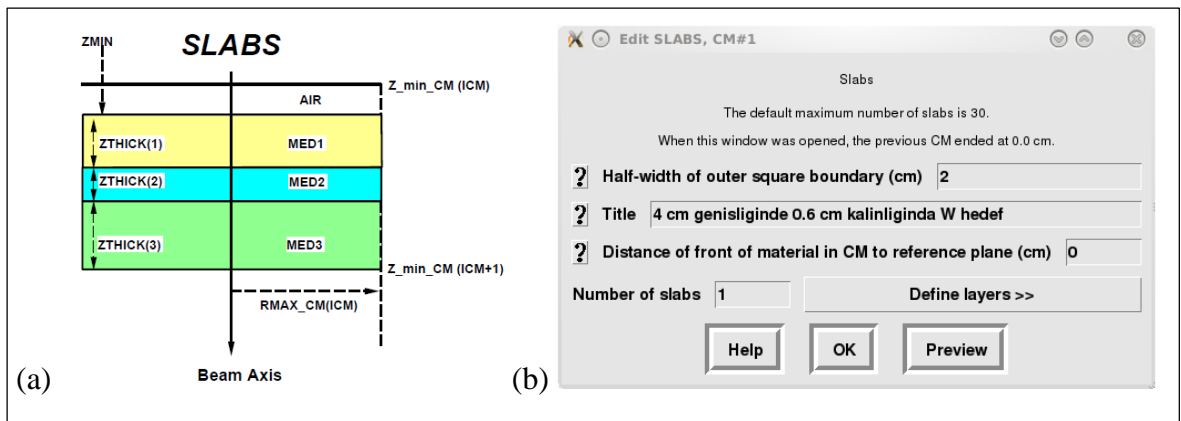


Figure 3.3. (a) The SLABS component module (CM) schematics. The CM is assumed to have a square boundary shape. (b) GUI of the SLABS CM.

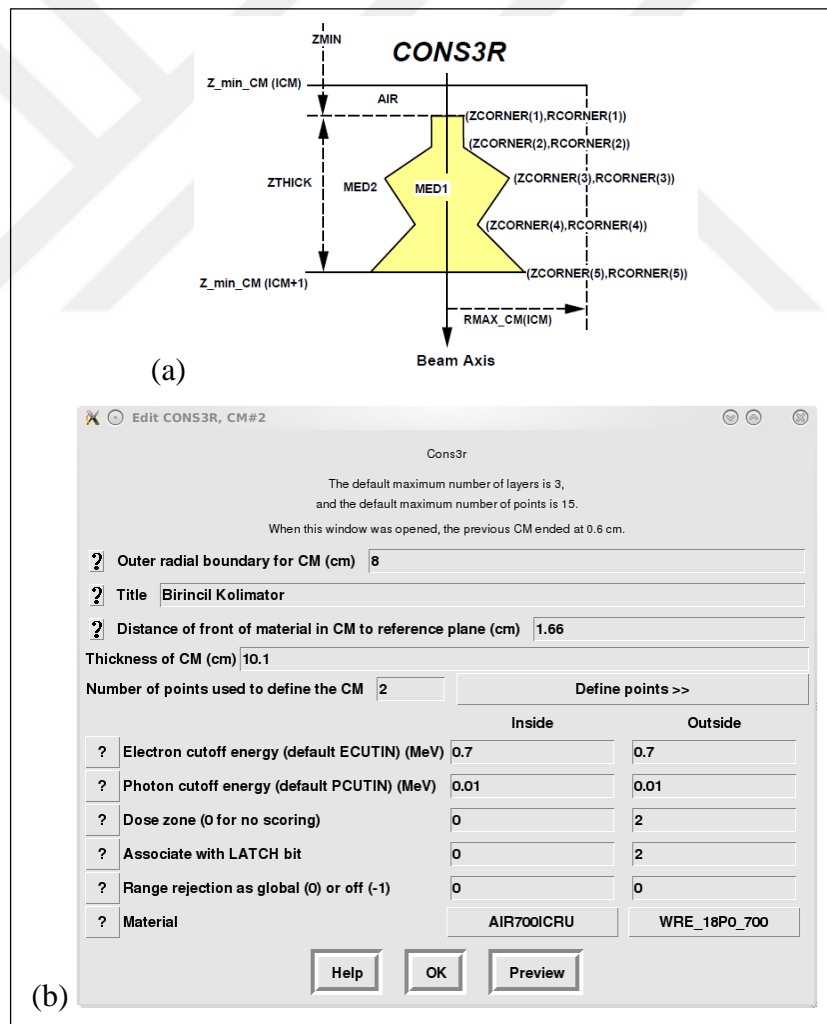


Figure 3.4. (a) The CONS3R CM schematics. The outer boundary of the CM is assumed to be a cylinder. (b) GUI of the CONS3R CM.

The component selected next is the primary collimator that includes two cones (see the top part of Figure 3.1). The empty cone used for 6 MV photon beam and electron beams modelled in this study. The other (unused) cone includes a difference filter and is used only for 18 MV photon beam production. The material of the primary collimator modelled by CONS3R CM is a tungsten-rhenium alloy, which has  $18 \text{ g/cm}^3$  density (Figure 3.4). The physical dimensions of the cone are selected to have a curvature of  $27^\circ 48'$  with 12.9 mm aperture at the upper part.

The linac has a number of flattening filters that selected automatically by the linac according to the selection of the beam energy. For 6 MV photon beam, the flattening filter has six layers that made from stainless steel. The filter has a 2 mm thickness of Al alloy carrier at the bottom of the filter with density of  $2.73 \text{ g/cm}^3$ . The design of the filter and its carrier were done using FLATFILT (Figure 3.5) and SLABS CMs, respectively.

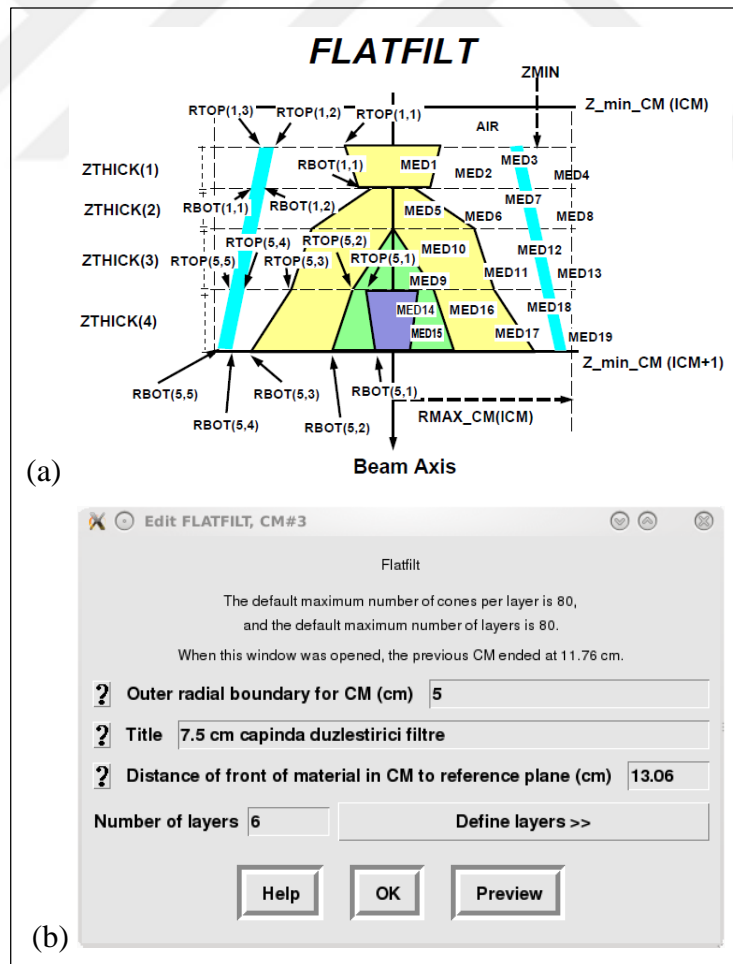


Figure 3.5. (a) The FLATFILT CM schematics. (b) GUI of the FLATFILT CM.

Due to the inexistence of the details of the ionization chamber (IC), the sample chamber provided by the MC code [69] was used. This IC model included very thin Al and Mylar layers of about 0.01 mm thickness, and relatively large air cavities. Because of this, the design of the ionization chamber had negligible effects on dose distributions. The ionization chamber was modelled using CHAMBER CM (Figure 3.6).

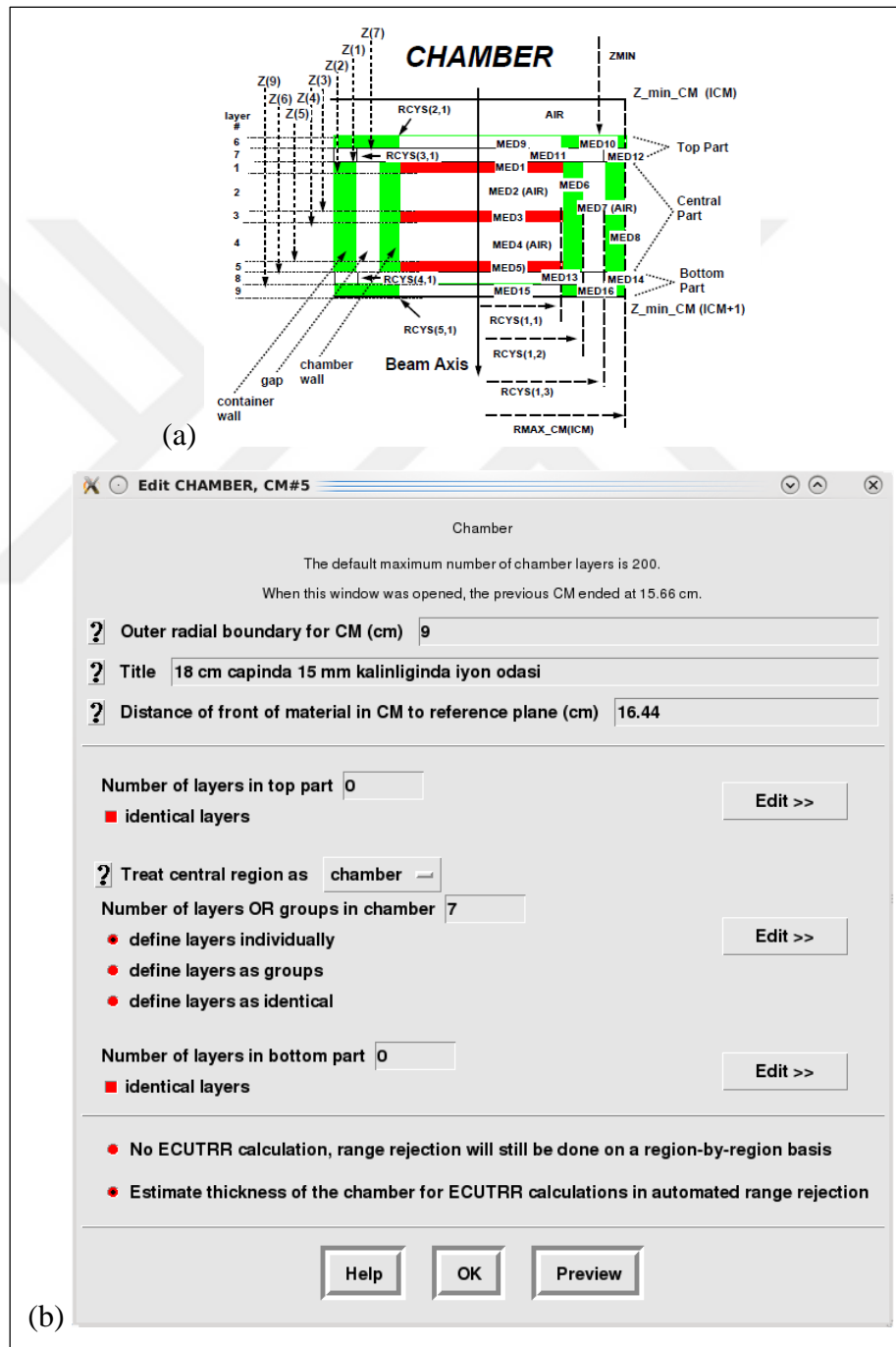


Figure 3.6. (a) The CHAMBER CM schematics. (b) GUI of the CHAMBER CM.

After the IC, Al backscatter plate of 3.0 mm thickness with  $2.73 \text{ g/cm}^3$  density was considered using SLABS CM.

The motorized wedge filter made of lead and antimony alloy (96 per cent Pb, 4 per cent Sb) with a density of  $11.1 \text{ g/cm}^3$  is the filter used in the simulations. The filter was modelled with JAWS CM (Figure 3.7) including a jaw to serve as wedge and the other jaw serve a medium of air.

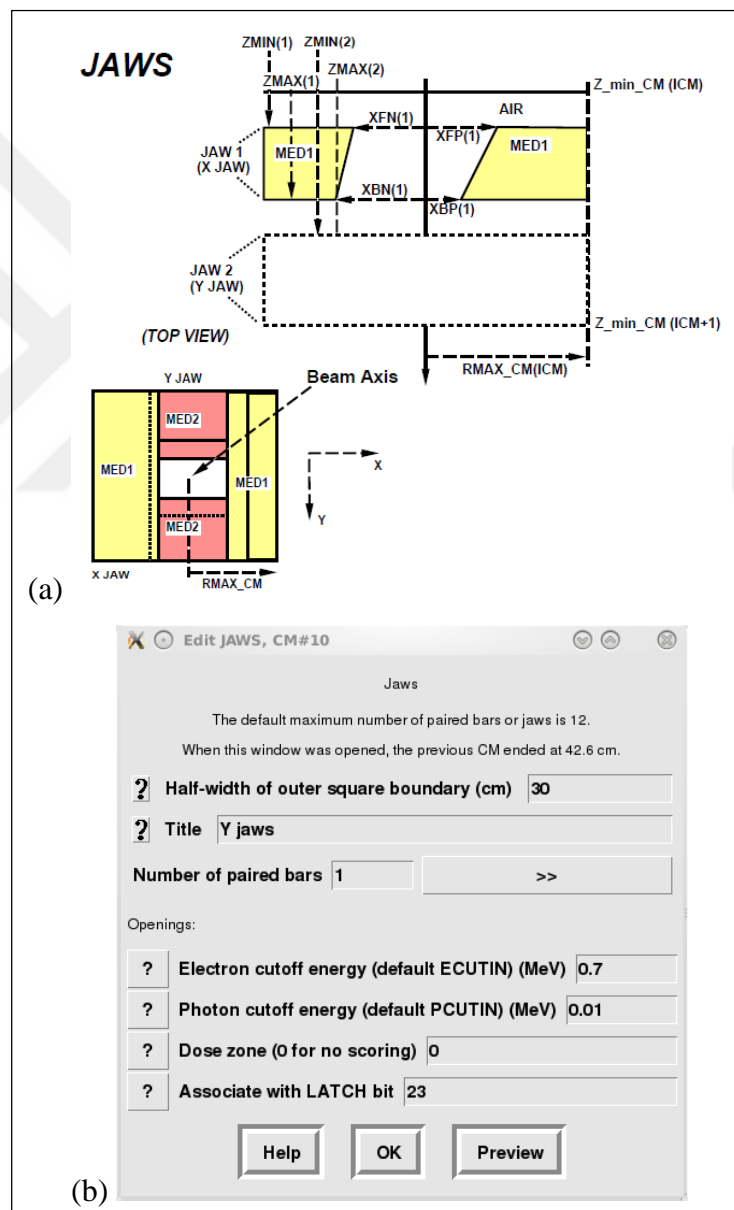


Figure 3.7. (a) The JAWS CM schematics. (b) GUI of the JAWS CM.



The mirror was modelled using MIRROR CM (Figure 3.8). Since they are not allowed to overlap CMs in BEAMnrc code, the mirror has to be removed for wedged fields.

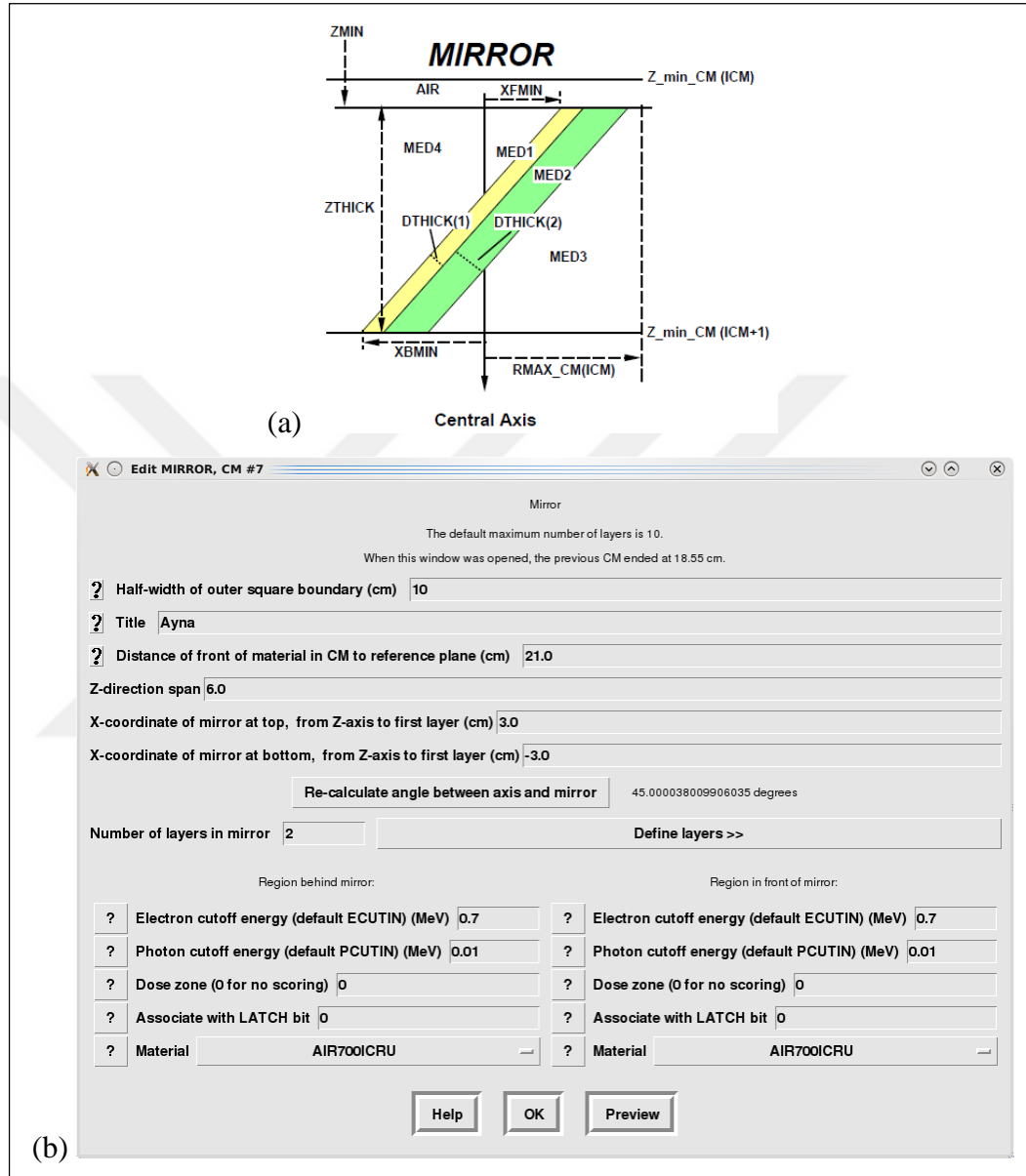


Figure 3.8. (a) The MIRROR CM schematics. (b) GUI of the MIRROR CM.

The multi leaf collimator (MLC) assembly includes 40 curved-end leaves of two banks. These leaves (made of tungsten alloy,  $\rho=18 \text{ g/cm}^3$ , leaf end radius: 150 mm) are mounted perpendicular to the radiation direction and aligned linearly along the beam path. These MLCs were modelled by the MLCE CM part of the code (Figure 3.9), which is used to simulate MLCs of Elekta linacs. The leaves can be arranged according to tongue-and-groove

shapes (Figure 3.10.a). The MLC design used in this study in the three orthogonal planes of  $10 \times 10 \text{ cm}^2$  open field size is shown in Figure 3.10.b-d.

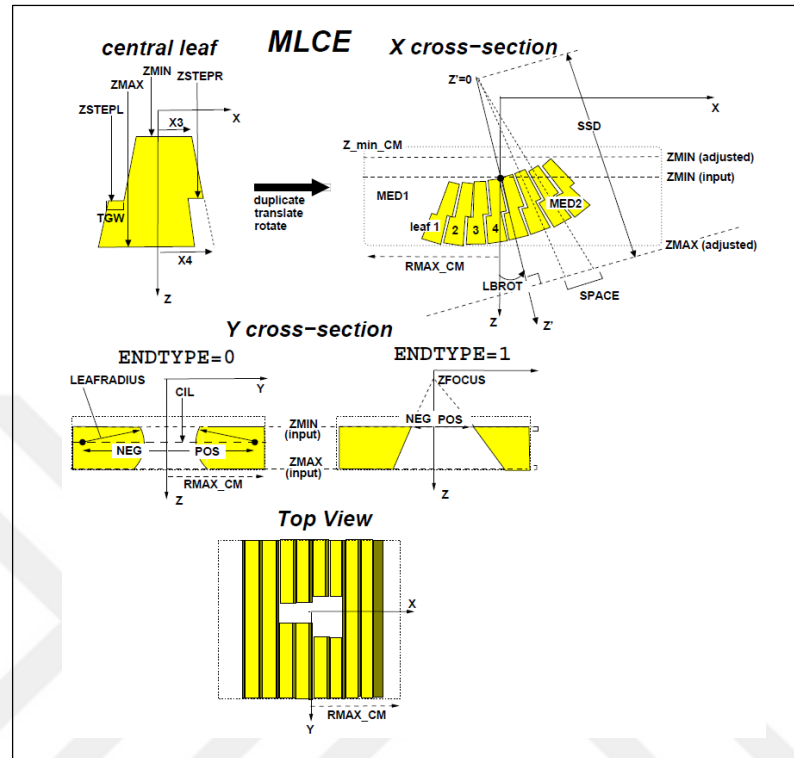


Figure 3.9. The MLCE CM schematics

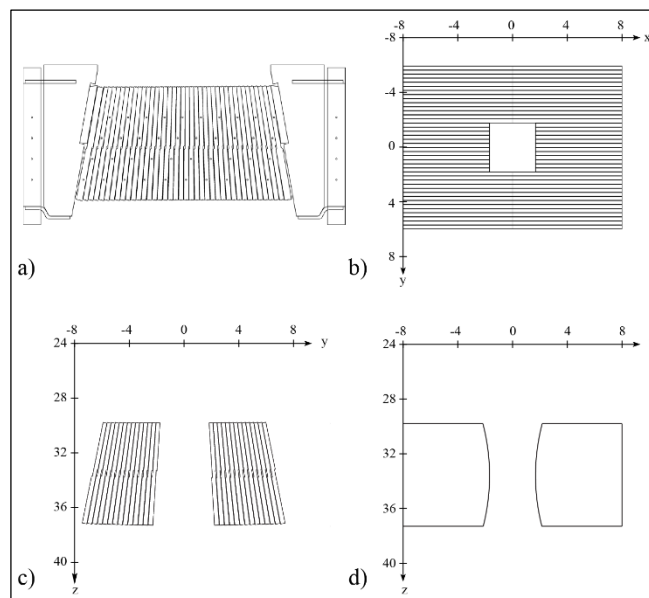


Figure 3.10. (a) Tongue-and-groove arrangement of MLCs, (b-d) MLC model in three orthogonal planes of  $10 \times 10 \text{ cm}^2$  open field size

Two X back-up jaws (made of tungsten alloy with a density of  $18 \text{ g/cm}^3$ ) that have thickness of 3 cm and curved-end with a radius of 7 cm modelled with JAWS CM. Because the CM does not include simulating curved-end jaws, it was simulated by MLCQ CM (Figure 3.11), since it has simpler geometry than MLCE. Because of minimum allowed leaf pair number, two-pair of leaves were used.

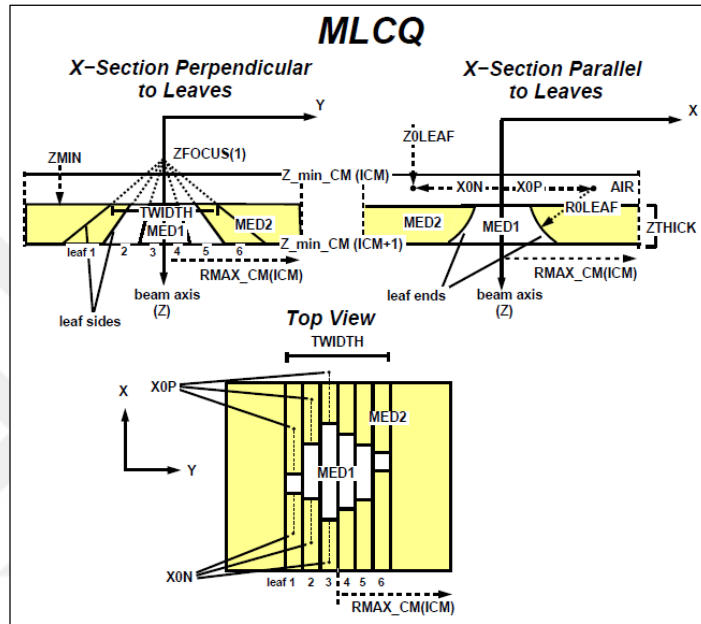


Figure 3.11. The MLCQ CM schematics

Y jaws made of the same tungsten alloy were also simulated by JAWS CM.

After these jaws, a crosswire sheet of Mylar is followed by an air slab with 1 mm thickness at 70 cm from the target in order to produce Phase-Space (PhSp) files of the simulation.

### 3.1.2. Monte Carlo Radiation Transport Parameters

The interactions included in the MC simulation are bremsstrahlung production, electron impact ionization, electron-positron scattering, positron annihilation, continuous energy loss of charged particles, photoelectric effect, pair production, Compton scattering, Rayleigh scattering and atomic relaxations. All these interactions have some probability related to their interaction cross section. The effects of interactions of electron impact ionization,

bound Compton scattering, photoelectron angular sampling, Rayleigh scattering and atomic relaxations on percent depth dose (PDD) curves are theoretically negligible for megavoltage photon beams. Effects of these interactions on PDD curves and central processing unit (CPU) time were investigated by turning them on respectively.

To run the code, default values were chosen for boundary crossing algorithm (EXACT), electron-step algorithm (PRESTA-II), bremsstrahlung angular sampling (Simple), bremsstrahlung cross sections (Bethe-Heitler [BH]), pair production angular sampling (Simple), pair production cross sections (BH) and photon cross sections (Storm-Israel) (Figure 3.12). Spin effects were kept as “ON” status as it is strongly recommended by the authors of the code system [69].

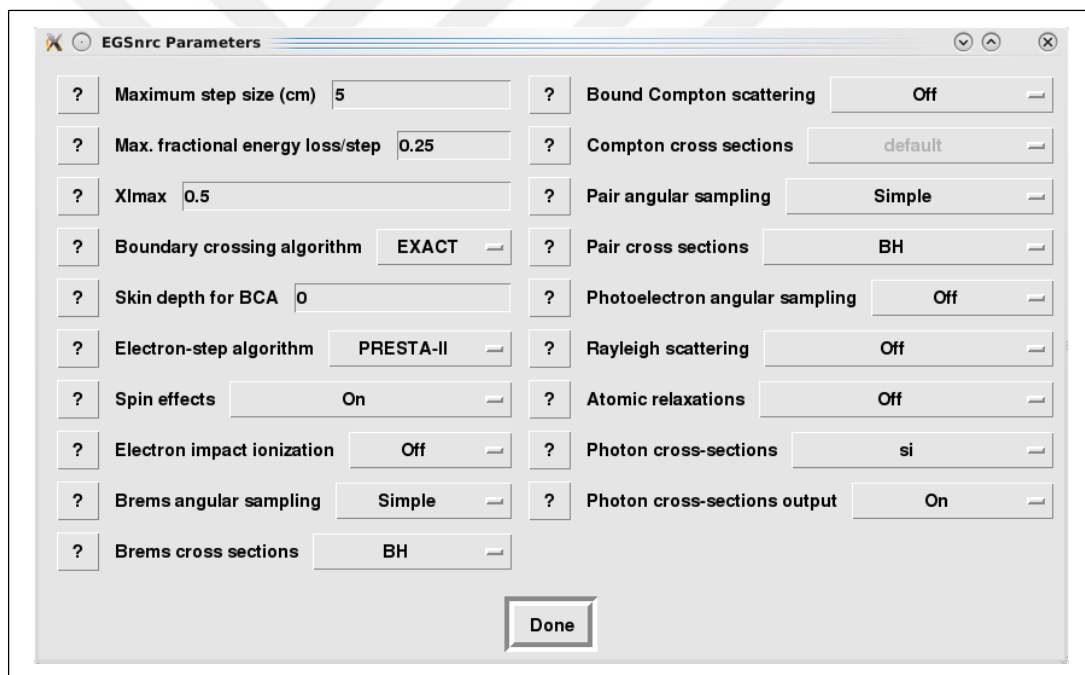


Figure 3.12. EGSnrc simulation parameters selection window

For the simulations, electron and photon cut-off energies were chosen as  $ECUT=700$  keV (including electron’s rest mass energy) and  $PCUT=10$  keV, respectively [69] (Figure 3.13). Effects of the electron cut-off energy on PDD curves and CPU time were also investigated. For this purpose, the same simulation was performed with  $ECUT$  equals to 521 keV.

Variance reduction techniques including directional Bremsstrahlung splitting (DBS) with a splitting number of 1000, electron splitting at flattening filter and range rejection with constant cut-off energy of 2 MeV were used [70]. Effects of global electron cut-off energy for range rejection (ESAVE\_GLOBAL) on PDD curves were investigated. Electrons with the energy larger than this value are not considered for range rejection since their energy may be enough to leave the region. In contrast, electrons with lower energy from this value are not transported anymore and considered as absorbed. The ECUT was chosen as 700 keV and the parameter was adjusted from 1.0 MeV to 3.0 MeV with steps of 0.5 MeV. Effects of the ESAVE\_GLOBAL values and usage of DBS on the CPU time were also investigated.

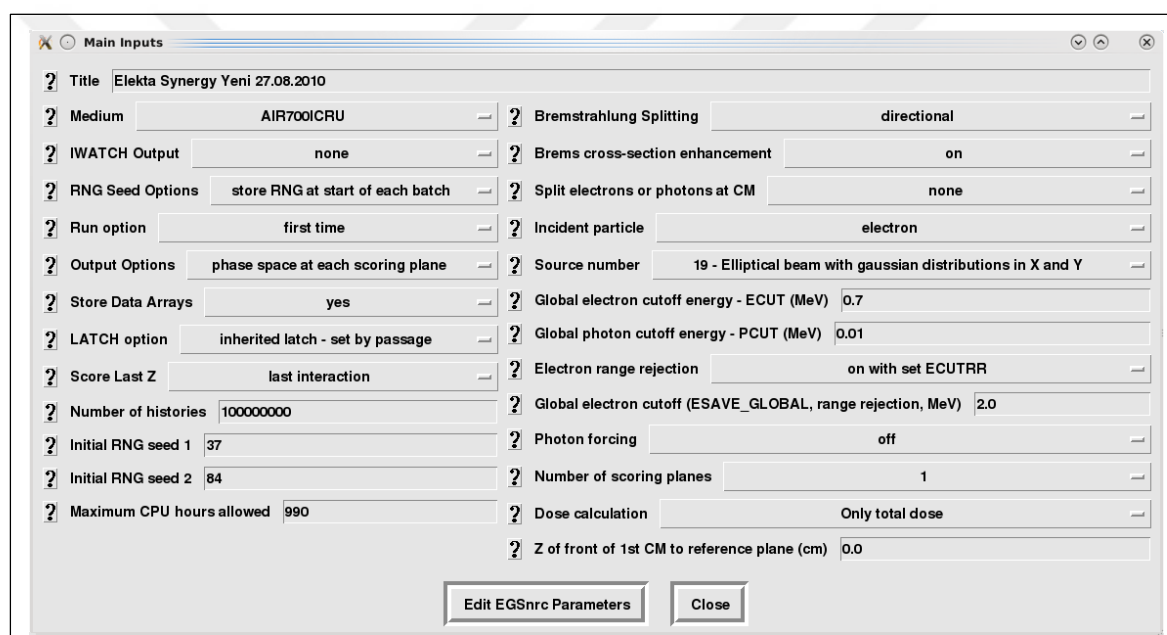


Figure 3.13. Main inputs window of BEAMnrc

Additionally, effects of eligible bremsstrahlung, pair production and photon cross sections on PDD curves were investigated by changing each cross section once in a time. The independent CPU time for each cross section was also evaluated.

The mono-energetic electron beam with 6 MeV having 1 mm diameter was considered in the simulations.  $2 \times 10^8$  initial electrons were used for each simulation. To calculate PDD curves, 100 cylindrical virtual detectors made up of water with 0.3 cm thickness and 0.3 cm radius were placed starting 1 m away the target. Detectors were covered from sides and the bottom with 20 cm thick water to establish electronic equilibrium. A square open field with

edge width of 10 cm and source to skin distance (SSD) 100 cm was used for all of the simulations.

### 3.1.3. Measurements on Linac

PDD curves and dose profiles were measured in IBA Blue Water Phantom with IBA CC13 0.13 cm<sup>3</sup> ionization chamber (IBA dosimetry, Schwarzenbruck, Germany) (Figure 3.14.a,b). The phantom has three computer-controlled servomotors to position ionization chamber in water. It provides  $\pm 0.1$  mm position accuracy and reproducibility. Reference chamber used for normalization of measurements was also IBA CC13 ionization chamber.

PDD curves from central axis (CAX) were measured for open fields from 3×3 cm<sup>2</sup> to 40×40 cm<sup>2</sup> and for wedged fields of 4×4, 10×10, 20×20 and 30×40 cm<sup>2</sup>. Dose profiles at 10 and 20 cm depth were also measured for 3×3, 10×10 and 20×20 cm<sup>2</sup> open fields. Dose profiles at 1.5, 5, 10 and 20 cm depth were measured only for 30×40 cm<sup>2</sup> wedged field. All the profiles were measured in the direction of the perpendicular to the direction of MLCs' motion. PDD curves and profiles were obtained with OmniPro-Accept software (IBA dosimetry, Schwarzenbruck, Germany), a part of IBA Blue Water Phantom (Figure 3.14.c).

Water equivalent solid phantoms composed of RW3 material (PTW Freiburg, Freiburg, Germany), which is a kind of polystyrene with density of 1.045 g/cm<sup>3</sup>, and IBA FC65-P 0.65 cm<sup>3</sup> ionization chamber (IBA dosimetry, Schwarzenbruck, Germany) were used for TPR<sub>20,10</sub> and output measurements. Outputs were measured at 5 cm depth from the surface and expressed at 1.5 cm using PDD curves for each field size.

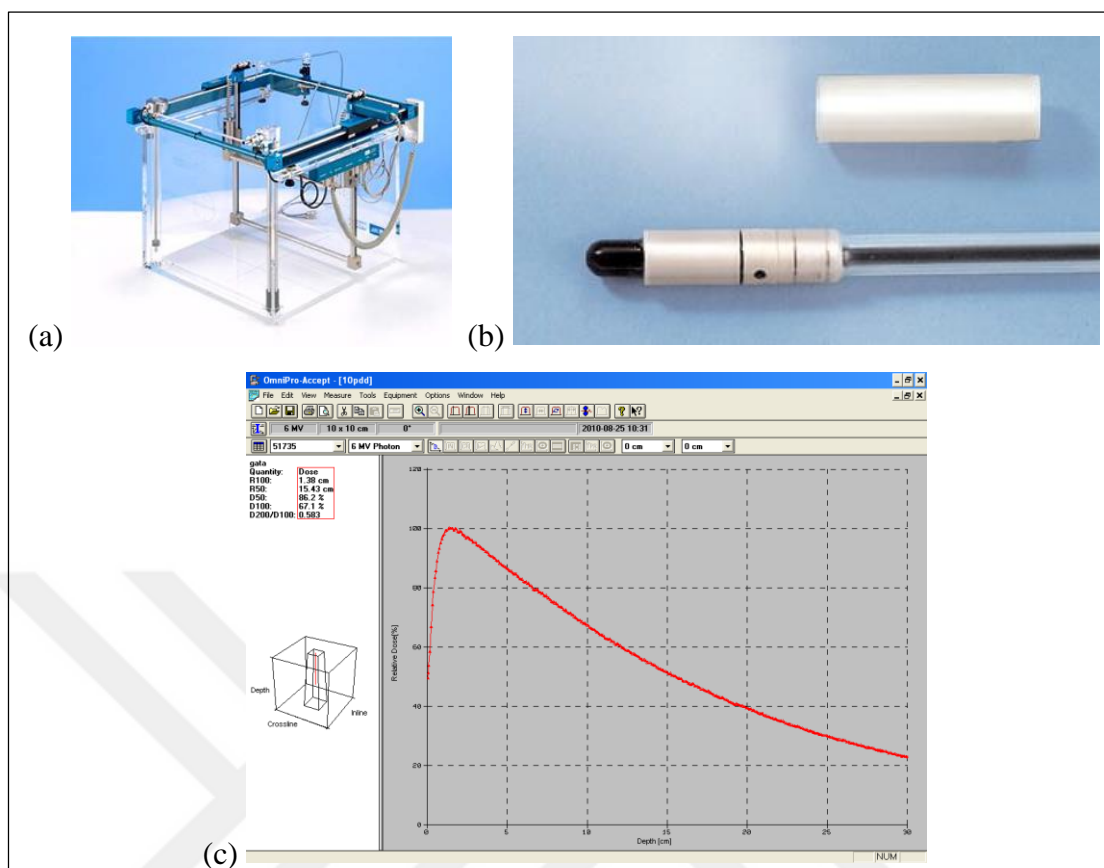


Figure 3.14. (a) IBA Blue Water Phantom, (b) IBA CC13 0.13 cm<sup>3</sup> ionization chamber, (c) a measurement output on OmniPro-Accept software

MLC transmission and interleaf leakage were measured with Kodak X-OMAT V (Kodak Inc., Rochester, NY) film for 20×20 cm<sup>2</sup> field size and SSD=100 cm (opened with jaws only, MLCs are closed) at 1.5 cm depth in water equivalent solid phantoms. The film was exposed with 1000 MU to darken the film sufficiently. Developed films were scanned with Vidar DiagnosticPRO Advantage (Vidar Systems Corp. Herndon, VA) medical grade film digitizer. Scanning resolution was selected to be 300 dpi and bit depth was 12 bits per pixel. A profile was drawn as shown in Figure 3.15 along the direction perpendicular to leaf movement direction to determine MLC transmission and interleaf leakage. Readings were corrected for field size difference using output factors.

To evaluate dose profiles in terms of absolute dose, absolute dose-grey level relationship was determined for dose range from 1 to 200 cGy with irradiation films with at 1.5 cm depth 10×10 cm<sup>2</sup> field size and SSD=100 cm (Figure 3.16). Regions of interests were drawn over

the exposed areas and the data fitted to a sigmoidal curve (Figure 3.17). Each point on the profile was then converted to absolute dose using inverse of the sigmoidal function.

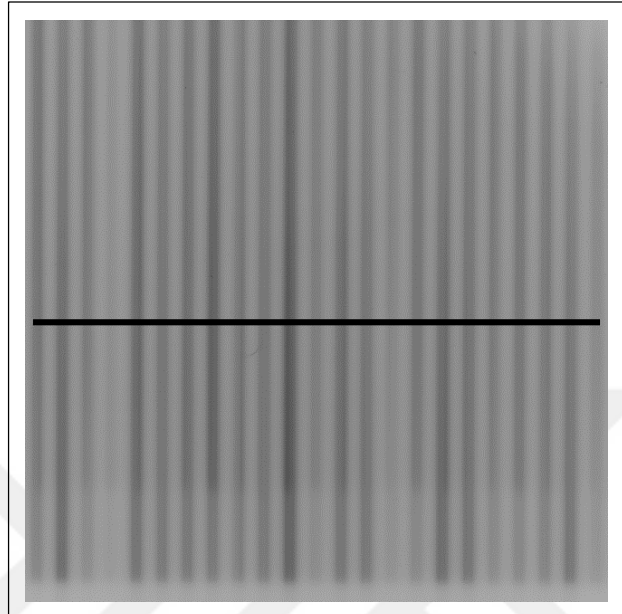


Figure 3.15. Scanned film for measuring MLC transmission and interleaf leakage. The black line represents the profile drawn on the film.

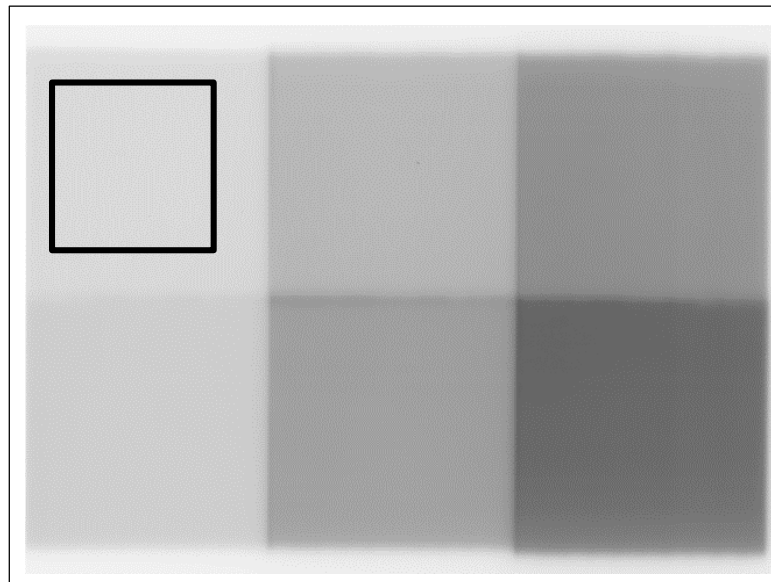


Figure 3.16. One of the scanned film to determine absolute dose-grey level relationship. The black box represents region of interest placed on the film.



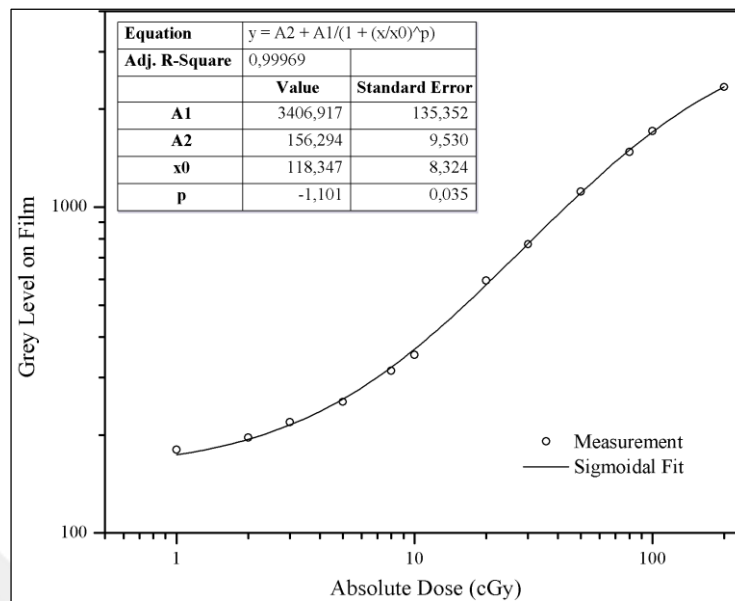


Figure 3.17. Sigmoidal fit

### 3.1.4. Accelerator Simulation Validation

Determining initial electron beam characteristics is the most important step of simulating a linac. Following the work of Sheikh-Bagheri and Rogers [71], only the mean energy of initial electron beam was considered to be the adjustable parameter while radial intensity distribution and energy distribution of the beam were kept constant. Circular electron beam source with 1 mm full-width at half-maximum (FWHM) Gaussian radial intensity distribution in both x and y directions and 1 MeV FWHM Gaussian energy distribution were set using source number 19 of BEAMnrc (Figure 3.18).

To determine the correct initial electron mean energy, electron beams with mean energy from 5.4 to 6.6 MeV were selected with 0.2 MeV increments. SSD was chosen to be 100 cm, field size was set to  $10 \times 10 \text{ cm}^2$ , and the number of initial electrons was chosen to be  $10^8$  for each simulation. PhSp files 70 cm from the target were created after each simulation using BEAMnrc.

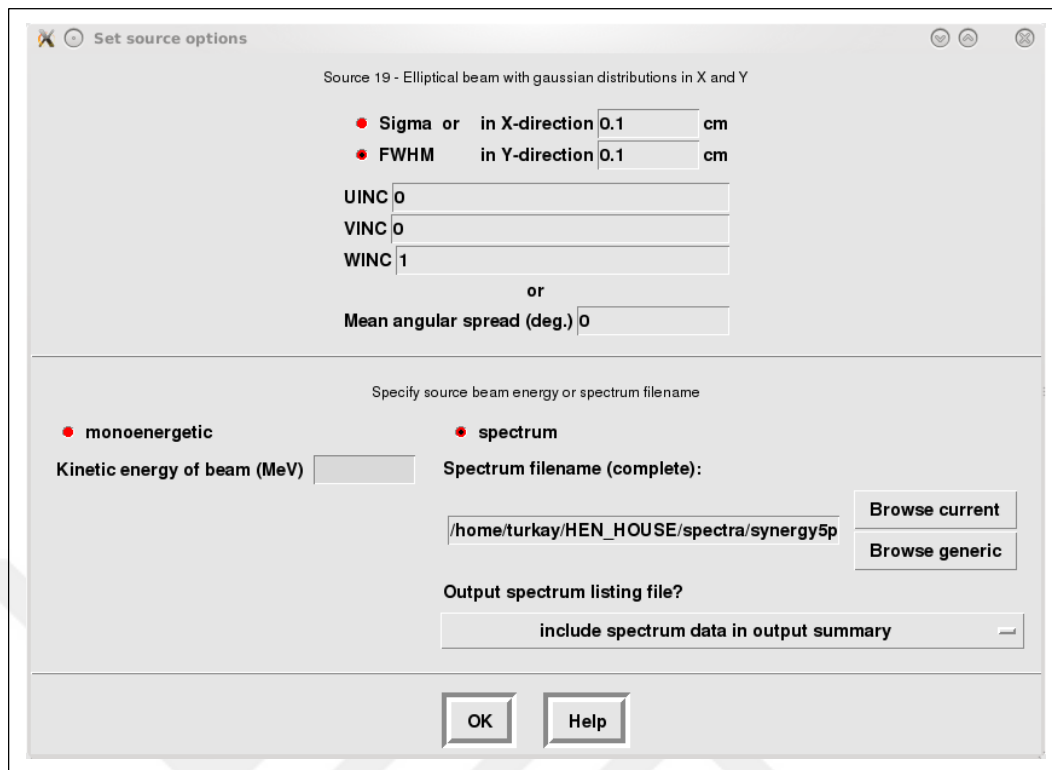


Figure 3.18. Window for BEAMnrc source number 19

Simulations were run on single PC with AMD Phenom II X6 with 3.3 GHz (run at 4.0 GHz) multi-core processor with Scientific Linux V6.0 operating system. Since it is not possible to perform parallel processing of the BEAMnrc simulation on single CPU, the same simulation was run six times simultaneously on different CPU cores of the PC by using different initial seed numbers of random number generator. By this procedure, the number of initial electron entering the media could be increased six times so that the total simulation time is reduced. After all the simulations for were completed, the produced PhSp files were combined into a single file using BEAMDP utility [72].

In order to obtain 3-dimensional dose distribution in water,  $40 \times 40 \times 40 \text{ cm}^3$  water phantom with voxel size of  $0.2 \times 0.2 \times 0.2 \text{ cm}^3$  created in DOSXYZnrc GUI (Figure 3.19) [73]. PhSp files created in BEAMnrc were used as initial particles (both electrons ( $e^+$ ,  $e^-$ ) and photons) in DOSXYZnrc via source number 2 of DOSXYZnrc (Figure 3.20) [58]. It must be noted that parallel process with in a single CPU is not possible for a DOSXYZnrc simulation.

The 'Inputs' window is titled '4x4x4 mm3 su fantomu'. It is divided into three main sections: Phantom definition, Source parameters, and Simulation parameters.

**Phantom definition:**

- Global electron cutoff energy - ECUT (MeV): 0.7
- Global photon cutoff energy - PCUT (MeV): 0.01
- Print summary of highest 20 doses: yes
- Define phantom using ...:
  - non-CT data input
  - phantom created from CT data

**Source parameters:**

- Incident particle: all
- Source type: 2 - Full phase-space source file

**Simulation parameters:**

- Number of histories: 100000000
- Thickness of region outside phantom is: uniform
- IWATCH Output: none
- Medium of region outside phantom: AIR700ICRU
- Maximum CPU time (hours): 990
- Output restart data: at end of run only
- RNG seed 1: 21
- Range rejection: on
- RNG seed 2: 73
- ESAVE: range rejection done only below this energy (MeV): 2
- Incident beam size (source 2, 4 or 8): 100.0
- Photon splitting number: 40
- Run option: first time
- # times to recycle each particle in phase space source: 0
- 'HOWFARLESS': on
- Run job in parallel: no

Buttons at the bottom: Edit EGSnrc Parameters, Close.

Figure 3.19. Graphical user interface of the DOSXYZnrc code's input parameters

The 'Set source options' window is titled 'Source 2 - Full phase-space source file'. It contains the following fields and options:

- x-coordinate of the isocenter: 0
- y-coordinate of the isocenter: 0
- z-coordinate of the isocenter: 100
- Theta (degrees): 180
- Phi (degrees): 90
- Distance from source to isocenter (cm): 30
- Collimator angle (degrees): 180
- DBS used to generate source
- DBS splitting field radius (cm): 20
- SSD of splitting field (cm): 100
- Z where source scored (cm): 70
- Phase space beam input (with no LATCH filter)
- Phase space beam input + dose component (with LATCH filter)
- File containing phase space data: /home/turkay/egsnrc\_mp/BEAM\_SynergyOpnf
- Browse current directory
- Phase space data redistribution: redistribute
- Phase space file format: with ZLAST
- LATCH Bit filter
- no. of times to split e+/e-: 40

Buttons at the bottom: OK, Help.

Figure 3.20. Window for DOSXYZnrc source number 19

Three-dimensional dose files produced by DOSXYZnrc in “\*.3ddose” format were read with the DICOM-RT toolbox [74] supplied by the Computational Environment for Radiotherapy Research (CERR version 4.0beta2) from University of Washington, St Louis [75]. PDD curves and dose profiles were extracted from these files by MATLAB version 7.6 (The MathWorks, Inc., Natick, MA).

For  $10 \times 10 \text{ cm}^2$  open field and SSD=100 cm, PDD curves and dose profiles were compared with water phantom measurements by simple subtraction for each electron beam energy. To obtain statistically correct results, further comparisons were made by performing  $\chi^2$  analysis defined as,

$$\chi^2 = \frac{1}{n} \sum_{i=1}^n (D_i^{(m)} - D_i^{(s)})^2 \quad (3.16)$$

where  $n$  is the number of data points of comparison,  $D^{(m)}$  is measured local dose value and  $D^{(s)}$  is corresponding dose value obtained from simulation [76]. The mean energy value that minimizes  $\chi^2$  was selected as the most appropriate value for initial energy of the electron beam. At this energy the beam quality parameter, TPR<sub>20,10</sub> value, was also evaluated.

Selecting appropriate initial electron energy was followed by the comparison of MC simulations with ionization chamber measurements for field sizes other than  $10 \times 10 \text{ cm}^2$ . For each field size (where ionization chamber measurements were made) the MC simulations were performed with the same water phantom. Sufficient initial number of electrons ( $10^8$  to  $5 \times 10^8$ ) depending on the field size was used to keep statistical uncertainty under 0.5 per cent. Comparisons were made again by simple subtraction.

MLC transmission and interleaf leakage were evaluated for  $20 \times 20 \text{ cm}^2$  field. Water phantom with  $0.4 \times 0.1 \times 0.4 \text{ cm}^3$  voxel size was used in DOSXYZnrc. The dimension with 0.1 mm wide was perpendicular to MLC's motion direction.

Output factors were measured using a  $0.5 \times 0.5 \times 0.2 \text{ cm}^3$  sized single voxel at 5 cm depth of water. The voxel surrounded by 20 cm thick water from each side and bottom.

### 3.1.5. Absolute Dose Calculation

Absolute dose calculations were made by using the calibration factor, which has unit of particles per MU [77]:

$$F_Q = \frac{D_{ref}(A_{ref}) / MU}{D_{ref,MC/hist}(A_{ref})} \quad (3.17)$$

where  $D_{ref}$  is dose measured with ionization chamber at reference depth for reference field size:  $A_{ref}$ ,  $D_{ref,MC/hist}$  is dose calculated with MC simulation per initial particle at reference depth for the same  $A_{ref}$ . Absolute dose at a point of interest,  $P$ , in patient for an arbitrary field size,  $A_{plan}$  calculated by formula:

$$D_P(A_{plan}) / MU = F_Q \times D_P(A_{plan})_{MC/hist} \quad (3.18)$$

## 3.2. COMPARISON OF TREATMENT PLANNING SYSTEMS WITH MONTE CARLO SIMULATION UNDER CONDITIONS OF TISSUE INHOMOGENITIES

### 3.2.1. Treatment Planning Systems

In order to compare with the MC simulations two treatment planning systems (TPSs) were used. The first TPS was PrecisePLAN v2.10 (Elekta Oncology Systems, Crawley, UK) that is used with the linac installed at Gülhane Military Medical Academy, Department of Radiation Oncology. The other one was Pinnacle3 v8.0 (Philips Medical Systems, Andover, MA).

PrecisePLAN system utilizes Pencil Beam (PB) algorithm with TAR Ratio Method for tissue inhomogeneity correction for calculation patient dose distributions. The TPS will be specified by  $TPS_{PB}$  from now on.

Pinnacle3 uses 3D Adaptive Collapse Cone Convolution-Superposition (CCC) algorithm for calculation patient dose distributions. The TPS will be specified by  $TPS_{CCC}$  from now on.

Both TPSs were commissioned with the same set of PDD and dose profile measurements. The acceptance criteria for commissioning are in accordance with the recommendations of Van Dyk et al. [78].

### **3.2.2. Conversation of Hounsfield Unit (HU) to Relative Electron Density or Physical Density**

TPSs require physical density or relative electron density of the medium in which dose calculation will be performed. How much photons and electrons in the medium are absorbed is calculated using this information. Thus, for correct and accurate treatment planning density or relative electron density of the medium must be accurately provided to the TPS.

One can reach this information by analyzing the computerized tomography (CT) images of the patient. Pixel values or Hounsfield Unit (HU) values in each pixel is obtained by normalizing the measured linear attenuation coefficient in that pixel to that of water. In other words, CT image is nothing but the linear attenuation map of the patient. Thus, using appropriate transformations, physical density or relative electron density values of the medium can be obtained from HU values in CT images.

In all calculations, the HU-Relative electron density transformation of TPS<sub>PB</sub> utilized in clinical routine was used as reference transformation. This transformation was obtained from CT images of the phantom that includes tissue-equivalent materials. CT images acquired from the CT scanner that routinely used in the clinic with constant tube voltage of 120 kVp. Measured HU values from the CT images and corresponding relative electron density values known from the phantom then fitted to a third-order polynomial function (Figure 3.21.a).

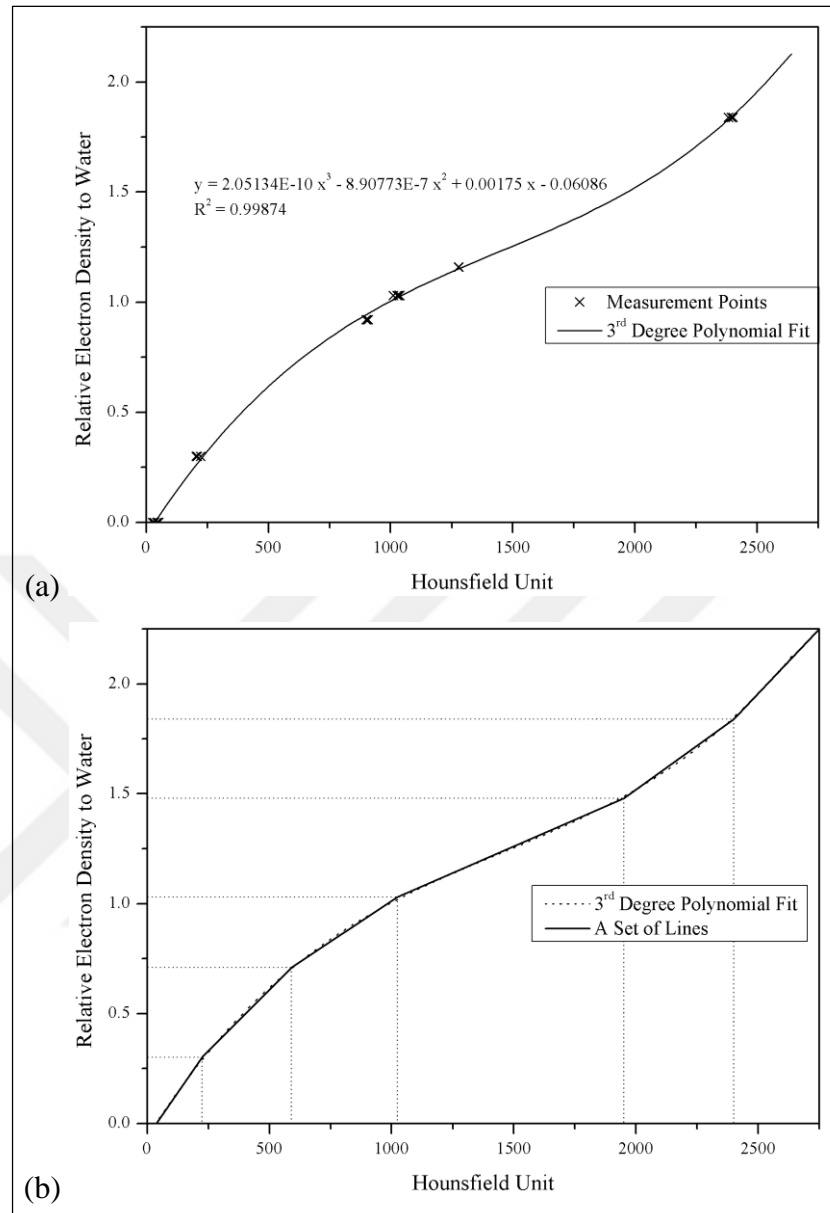


Figure 3.21. HU to relative electron density to water conversions for (a) TPS<sub>PB</sub>  
(b) TPS<sub>CCC</sub> and BEAMnrc MC code

TPS<sub>CCC</sub> and BEAMnrc MC code system, however, need physical density values of the medium that dose distribution will be calculated instead of relative electron density. In addition, this must be done by a set of linear equations instead of a third-order polynomial. For this reason, HU-Relative electron density transformation of TPS<sub>PB</sub> represented with a set of linear equations (Figure 3.21.b). The bi-linear transformation shown in Figure 3.22 was then used to convert relative electron density to physical density. The bi-linear transformation in Figure 3.22 was obtained from the measured physical density and relative

electron density values of the materials included in two different phantoms: Gammex Tissue Characterisation Phantom Model 467, CIRS Electron Density Phantom Model 062M.

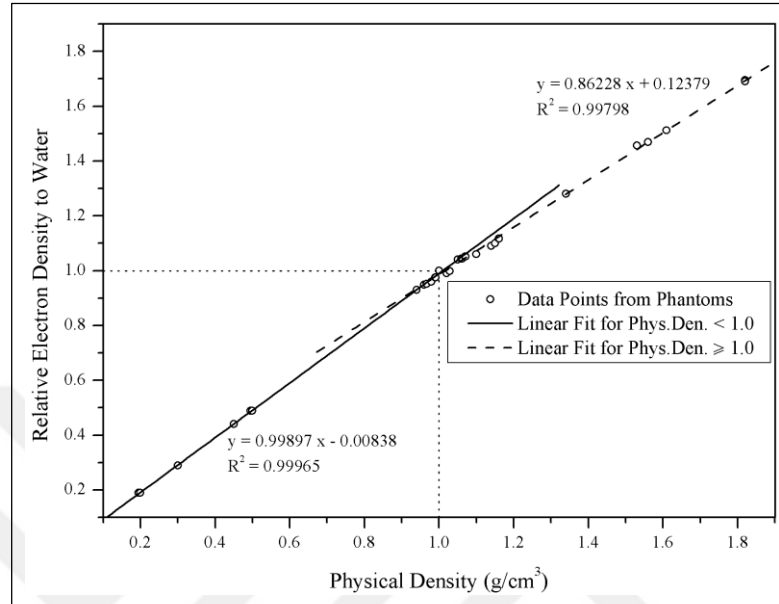


Figure 3.22. Bi-linear transformation used to convert relative electron density to physical density

The linear equation set obtained from this transformation is given in Equation (3.19) and Figure 3.23.

$$Physical\ Density\ (g/cm^3) = \begin{cases} 1.65 \times 10^{-3} \cdot HU - 0.0611, & HU \leq 224 \\ 1.12 \times 10^{-3} \cdot HU + 0.0580, & 224 < HU \leq 590 \\ 7.66 \times 10^{-4} \cdot HU + 0.2664, & 590 < HU \leq 1024 \\ 5.65 \times 10^{-4} \cdot HU + 0.4714, & 1024 < HU \leq 1950 \\ 9.28 \times 10^{-4} \cdot HU - 0.2364, & 1950 < HU \leq 2400 \\ 1.36 \times 10^{-3} \cdot HU - 1.2703, & HU > 2400 \end{cases} \quad (3.19)$$



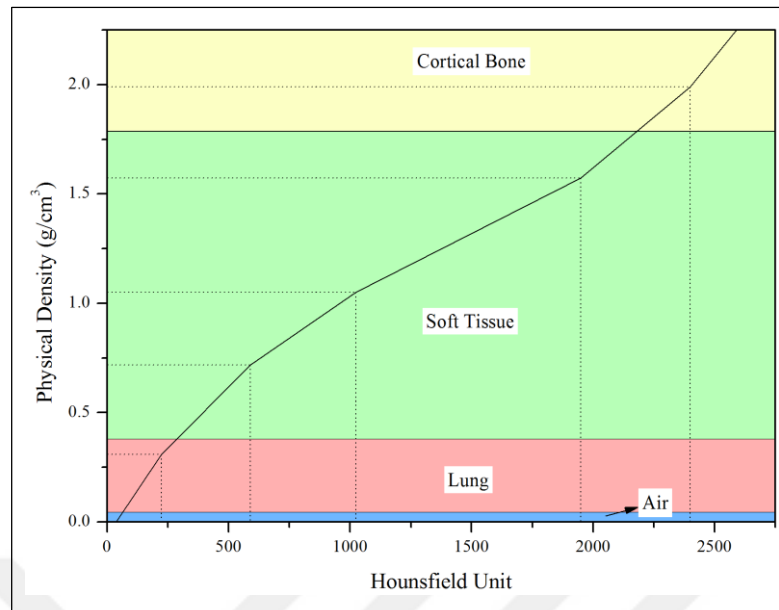


Figure 3.23. HU to physical density conversion used for TPS<sub>CCC</sub> and Monte Carlo

Table 3.1. Density ranges and atomic compositions of the material or tissues used in MC simulation

		MATERIAL OR TISSUE			
		Air	Lung	Soft Tissue	Cortical Bone
DENSITY RANGE (g/cm <sup>3</sup> ) [58]		0.001-0.044	0.044-0.302	0.302-1.101	1.101-2.088
ATOMIC COMPOSITIONS [40] (Fraction by Weight)	H	–	1.03E-01	1.01E-01	4.72E-02
	C	1.24E-04	1.05E-01	1.11E-01	1.44E-01
	N	7.55E-01	3.10E-02	2.60E-02	4.20E-02
	O	2.32E-01	7.49E-01	7.62E-01	4.46E-01
	Na	–	2.00E-03	–	–
	Mg	–	–	–	2.20E-03
	P	–	2.00E-03	–	1.05E-01
	S	–	3.00E-03	–	3.15E-03
	Cl	–	3.00E-03	–	–
	Ar	1.28E-02	–	–	–
	K	–	2.00E-03	–	–
	Ca	–	–	–	2.10E-01
Zn	–	–	–	1.00E-04	

The TPSs assume that the medium that the dose distribution calculations are performed is made up of water. The effects of tissue inhomogeneities are mainly handled by using different algorithms. In Monte Carlo calculations, the properties of medium that is subject to radiation transport is introduced initially then the calculations are made regarding this data. For this reason, not only the conversion of HU values of each pixel in CT images to physical density but also the materials in each pixel should be introduced for MC calculations. For this identification, materials and tissues whose physical density intervals are indicated in DOSXYZnrc user guide [58] are used (Table 3.1).

### 3.2.3. Construction of Slab Phantoms

To compare dose distribution calculations between MC and TPSs, three virtual slab phantom were prepared. The phantoms constructed on a patient's CT images. Initially CT images are transferred to MATLAB as a 3D matrix using CERR software. After that, 3D voxel values (HU values) are arranged by using standard loop functions of MATLAB.

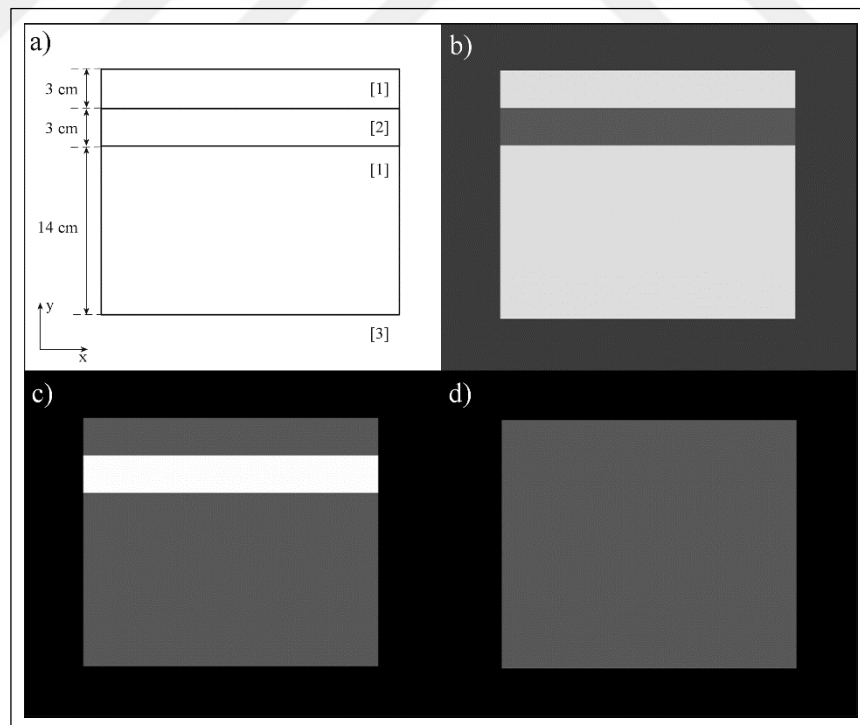


Figure 3.24. Virtual slab phantoms: (a) Geometry, (b) Lung Phantom, (c) Bone Phantom, (d) Water Phantom

In Figure 3.24.a, regions labelled “[1]” were filled with water equivalent material with HU=1000, regions labelled “[3]” were filled with air equivalent material with HU=0 for all phantoms. All the phantoms were constructed by the same slice thickness of 2.5 mm in z direction (in or out of the paper).

In Figure 3.24.b, the region labelled “[2]” was filled with lung equivalent material with HU=175. This value was obtained from the mean HU values of five healthy patients’ lung region. In the figure, phantom is seen in lung window (level:-600, width:1700).

In Figure 3.24.c, the region labelled “[2]” was filled with cortical bone equivalent material with HU=2250. The phantom in Figure 3.24.d was totally formed from water. Both phantoms are seen in mediastinal window (level:50, width:400).

#### **3.2.4. Open Field Plans and Dose Distributions**

All phantoms were planned in TPS<sub>PB</sub> for beams directed to -y direction with open field sizes of 3×3, 10×10 and 20×20 cm<sup>2</sup> and SSD=100 cm. Dose distribution was calculated using dose grid of 0.2×0.2×0.2 cm<sup>3</sup>. Plan details such as, isocenter coordinates, field sizes, MUs etc. were exported from TPS<sub>PB</sub> via DICOM-RT (**D**igital **I**maging and **C**ommunication in **M**edicine - **R**adiation **T**herapy) format. The plans were then imported to TPS<sub>CCC</sub> and dose distribution was calculated using CCC algorithm for each field size.

Dose distributions from TPSs were then imported to CERR. PDD curves and dose profiles were drawn using MATLAB.

#### **3.2.5. Dose Distribution Calculations with MC**

Three BEAMnrc input file was created for open field sizes of 3×3, 10×10 and 20×20 cm<sup>2</sup> with SSD=100 cm. Using  $2 \times 10^8$  to  $10^9$  initial electrons, PhSp files at 70 cm from the target were obtained with BEAMnrc simulations. All the MC parameters in all simulations were chosen to be the same as those determined in the first part of the thesis.

Using the created PhSp files, further simulations were performed with DOSXYZnrc to transport radiation on the phantoms. Instead of creating the phantoms directly in DOSXYZnrc, CT images of the phantoms were converted to DOSXYZnrc phantom files using CTCREATE tool [58] with two different ramps. The first one was based on the transform given in Equation 3.4 and Figure 3.23, i.e., based on the transform with six ramps and four materials. The dose distributions obtained using this transform were called  $MC_{DM}$ , with DM stands for Dose to Medium. The second phantom was based on the same six ramp but composed of only water. The dose distributions obtained using this transform were called  $MC_{H_2O}$ . It was proposed that the dose distribution obtained using this transform was comparable with those from TPSs. Both phantoms had the voxel size of  $0.2 \times 0.2 \times 0.2 \text{ cm}^3$ .

The CTCREATE tool can use a material for only one ramp. To convert ramps with the same material, the same material was copied with different name in the same PEGS4 file. For example, to create second phantom six water materials with the same properties but different names were included in the same PEGS4 file.

DOSXYZnrc simulations were performed using  $10^8$  initial particles included in the PhSp files. The statistical uncertainty for each simulation was under 0.5 percent. Dose output files of DOSXYZnrc in 3-dimensional matrix were read with the DICOM-RT toolbox in MATLAB. PDD curves and dose profiles were also drawn using MATLAB.

Another method suggested by AAPM Task Group No. 105 [28] for converting absorbed dose in medium to absorbed dose in water was also employed. According to this method, MC dose values in each tissue converted by multiplication doses with a constant depending on the type of the tissue. The constants are 1.117, 0.999, 1.01 and 1.116 for air, lung, soft tissue and bone, respectively. To perform this, a small function in Matlab was written (Appendix C). The dose distribution obtained by this method was named  $MC_{DW}$  with DW stands for Dose to Water.

### **3.2.6. Comparisons**

For all phantoms and field sizes, PDD curves thorough the central axis from TPSs and MC calculations were compared.

Dose profiles at 4.5 cm depth (in the middle of the inhomogeneity insert) were also compared. Additionally, penumbra width between 80 and 20 per cent of dose at central axis were calculated. To achieve this, ascending side of each profile's penumbra region fitted to a Boltzmann function (Figure 3.25). Difference between x values of 80 and 20 per cent of dose at central axis gives the penumbra width.

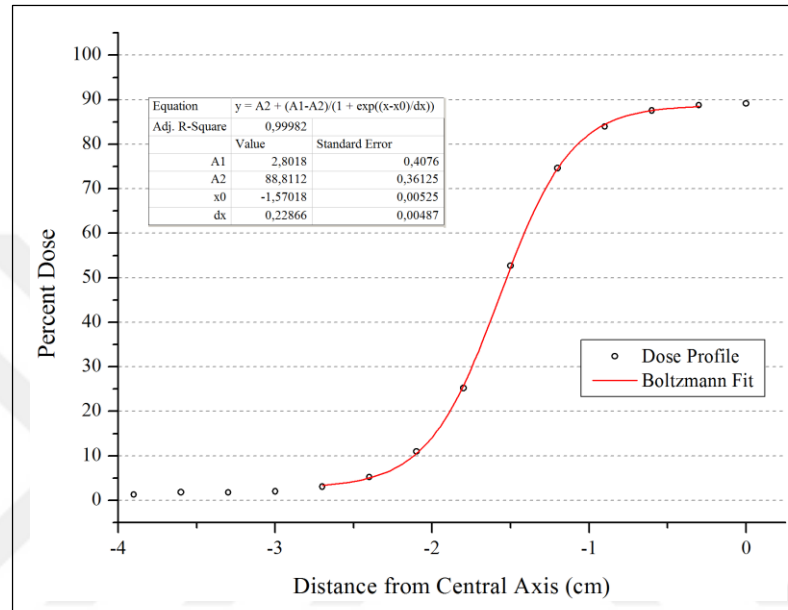


Figure 3.25. An example of Boltzmann fit to ascending side of a dose profile

### 3.3. COMPARISON OF TREATMENT PLANNING SYSTEMS WITH MONTE CARLO SIMULATION IN IMRT OF NON-SMALL CELL LUNG CANCER

#### 3.3.1. Patients

Fifteen Non-Small Cell Lung Cancer (NSCLC) patients with various tumor locations were randomly selected for this thesis. All the patients applied to the Gülhane Military Medical Academy, Department of Radiation Oncology for radiotherapy treatment. The patients were treated with 3-D conformal radiotherapy, as a clinical routine. Patients' CT images, organ and tumor structures were used for intensity-modulated radiotherapy (IMRT) planning. IMRT plans were not used for patient treatment, used for this thesis instead.

### 3.3.2. Target and OAR Delineation and Volumes

The gross tumor volume (GTV) determined by a radiation oncologist was expanded by a 5 mm margin in 3-D to yield the clinical target volume (CTV). A 5-mm-wide isotropic expansion was used to create the Planning Target Volume (PTV). All the volume delineations were done on PrecisePLAN v2.10 (Elekta Oncology Systems, Crawley, UK) treatment planning system (TPS). Target volumes for each patient were given in Table 3.2.

Table 3.2. Target volumes for each patient

<b>Patients</b>	<b>GTV (cm<sup>3</sup>)</b>	<b>CTV (cm<sup>3</sup>)</b>	<b>PTV (cm<sup>3</sup>)</b>
Patient 1	158.2	291.3	439.2
Patient 2	62.2	123.3	197.3
Patient 3	70.9	124.7	198.2
Patient 4	160.1	255.2	368.8
Patient 5	63.8	126.2	200.5
Patient 6	43.4	106.7	146.6
Patient 7	221.8	340.5	483.6
Patient 8	17.3	48.2	93.2
Patient 9	51.8	112.1	186.3
Patient 10	131.0	217.0	326.4
Patient 11	213.2	332.3	473.9
Patient 12	107.1	164.2	225.9
Patient 13	31.0	69.6	123.0
Patient 14	213.9	348.6	503.5
Patient 15	208.9	334.2	481.4

The lungs, heart, esophagus, and spinal cord were delineated as organs at risk (OARs). The lungs include both the ipsilateral and contralateral lung, but they exclude the GTV. To obtain the respective planning organ at risk volumes (PRVs), the esophagus was expanded by a 3-mm-wide isotropic margin, while the spinal cord was expanded by a 5-mm-wide isotropic margin. Expansion was not applied to the lungs and heart.

### 3.3.3. Treatment Plans and Planning Objectives

For each patient, a total dose of 70.0 Gy in 35 fractions of 2.0 Gy was prescribed to the PTV [79]. Six-MV photon beams were used for field in field forward IMRT of lung cancer. A class solution of nine non-coplanar conformal beams (consist of four segments) with a single isocenter was applied. Forward IMRT planning was performed on PrecisePLAN v2.10 (Elekta Oncology Systems, Crawley, UK) TPS where every beam was adjusted for each individual patient to meet the set dose–volume constraints for OARs. These adjustments generally resulted in a change in the number of beams/segments beam/segment shape.

The planning objectives according to Radiation Therapy Oncology Group (RTOG) Protocol no: 0117 [80] were as follows:

- The isodose curve representing 93 percent of the prescription dose must encompass the entire PTV.
- The percentage of total lung volume exceeding 20 Gy ( $V_{20}$ ) and 30 Gy ( $V_{30}$ ) shall be lower than 30 percent and 20 percent respectively. Mean lung dose ( $D_{\text{mean}}$ ) shall be lower than 27 Gy.
- The percentage of this esophageal volume exceeding 55 Gy ( $V_{55}$ ) shall be lower than 30 percent and the mean esophageal dose shall be lower than 34 Gy.
- The maximum spinal cord (point) dose ( $D_{\text{max}}$ ) should not exceed 45 Gy.
- Whole heart dose should not exceed 40 Gy.

### 3.3.4. Dose Distribution Calculations in TPSs

Dose distributions were calculated for each by  $\text{TPS}_{\text{PB}}$  with  $0.4 \times 0.4 \times 0.4 \text{ cm}^3$  voxel sized grid on CT images of the patients. Treatment plans were then exported to a CD or DVD via DICOM-RT format. The exported plans include CT images of the patients, treatment and OAR volumes, plan details such as, isocenter coordinates, positions of MLCs and Jaws for each beam and segment, and monitor units for each segment, and dose distributions.

Exactly the same plans were used to calculate dose distribution in the patients with the  $\text{TPS}_{\text{CC}}$ . To achieve this on  $\text{TPS}_{\text{CC}}$ , plans for each patient were directly imported to TPS

excluding the stored dose distribution. Using the same CT images, structures and plan data, dose distribution for each patient were obtained in TPS<sub>CCC</sub>. To compare these distributions with the others, plans were also exported from the TPS<sub>CCC</sub>.

### 3.3.5. Dose Distribution Calculations in MC

To calculate dose distribution with MC simulation, the exported plans from TPS<sub>PB</sub> were imported to the CERR. All the plan details were then read in CERR.

Using the positions of MLCs and Jaws, for each segment in each beam a BEAMnrc input file was created for each patient. Approximately 30 BEAMnrc input files for each patient were created. Using  $5 \times 10^7$  to  $2 \times 10^8$  initial electrons depending on the size of the segments, PhSp files at 70 cm from the target were obtained with BEAMnrc simulations. Statistical uncertainty for each simulation was under 0.5 percent. All the MC parameters in all simulations were the same as those determined in the first part of the thesis.

To transport radiation in the patients, CT images of each patient were converted to DOSXYZnrc phantom files using CTCREATE tool [58]. The CTCREATE tool can convert HU values to physical densities (in units of  $\text{g}/\text{cm}^3$ ) and can assign a material for each voxel depending on the density of the voxel. The tool can also alter the voxel size.

Two different DOSXYZnrc phantom files with  $0.4 \times 0.4 \times 0.4 \text{ cm}^3$  voxel size were created for each patient using two different HU to physical density transforms as stated above. The dose distributions obtained using these transforms were again called as MC<sub>DM</sub> and MC<sub>H<sub>2</sub>O</sub>. It was proposed that MC<sub>H<sub>2</sub>O</sub> was comparable with dose distributions from TPSs.

Using previously created PhSp files and information about isocenter coordinates and beam directions, DOSXYZnrc simulations were performed for each segment. The number of initial particles used in the simulations was depended on the particles included in the PhSp files. The statistical uncertainty for each simulation was under 0.5 percent.

Dose output files of DOSXYZnrc in 3-dimensional matrix were read with the DICOM-RT toolbox [74] in MATLAB. Each element was multiplied by the calibration factor defined in



Equation 3.2 to obtain dose per MU. The dose distributions of each segment then multiplied by the segments' MU that decided by forward IMRT planning in TPS<sub>PB</sub>. Following this procedure, all segments dose distributions were summed to obtain dose distribution calculated by MC simulation.

The method suggested by AAPM Task Group No. 105 [28] for converting absorbed dose in medium to absorbed dose in water was also employed to produce MC<sub>DW</sub> as stated above.

### 3.3.6. Comparison of Dose Distributions

To compare dose distributions, all the dose distributions (TPS<sub>PB</sub>, TPS<sub>CCC</sub>, MC<sub>DM</sub>, MC<sub>H2O</sub>, MC<sub>DW</sub>) were imported to CERR for each patient. Dose Volume Histograms (DVH) for target volumes (GTV, CTV and PTV) and OARs (heart, esophagus, spinal cord and lungs) were then created.

Dose distributions were compared in terms of DVH parameters. Maximum, minimum, mean doses and dose of 93 percent volume ( $D_{\min}$ ,  $D_{\max}$ ,  $D_{\text{mean}}$  and  $D_{93\%}$ ) were evaluated for the GTV, CTV and PTV. Homogeneity Index (HI) and Conformity Index (CI) in percent were also calculated.  $D_{\max}$ ,  $D_{33\%}$  and  $D_{67\%}$  were evaluated for heart, esophagus and spinal cord, while organ volume of 20 Gy ( $V_{20\text{Gy}}$ ),  $V_{30\text{Gy}}$  and  $D_{\text{mean}}$  for lungs. For each OAR equivalent uniform dose (EUD) and normal tissue complication probability (NTCP) according to Lyman–Kutcher–Burman (LKB) model [81] were calculated. Model parameters used in the calculations for EUD and NTCP are given in Table 3.3.

Table 3.3. Model parameters for NTCP and EUD

Organ at Risk	$n$	$m$	$TD_{50}$
Heart [81]	0.35	0.1	48
Esophagus [82]	0.69	0.36	47
Spinal Cord [81]	0.05	0.175	66.5
Lungs [83]	0.99	0.37	30.8

Statistical analyses were performed using paired samples T-Test for pair-wise comparison of the parameters from different dose distributions. p values lower than 0.05 was considered as statistically significant.



## 4. RESULTS AND DISCUSSION

### 4.1. MONTE CARLO MODELLING OF ELEKTA SYNERGY MLCi TREATMENT HEAD

#### 4.1.1. Monte Carlo Modelling

The simulated linac head was given in Figure 4.1. In the figure, wedge filter, mirror and Y jaws were rotated 90 degrees for a clearer vision. An example input script for MC simulation of Elekta Synergy MLCi treatment head is given in Appendix D.

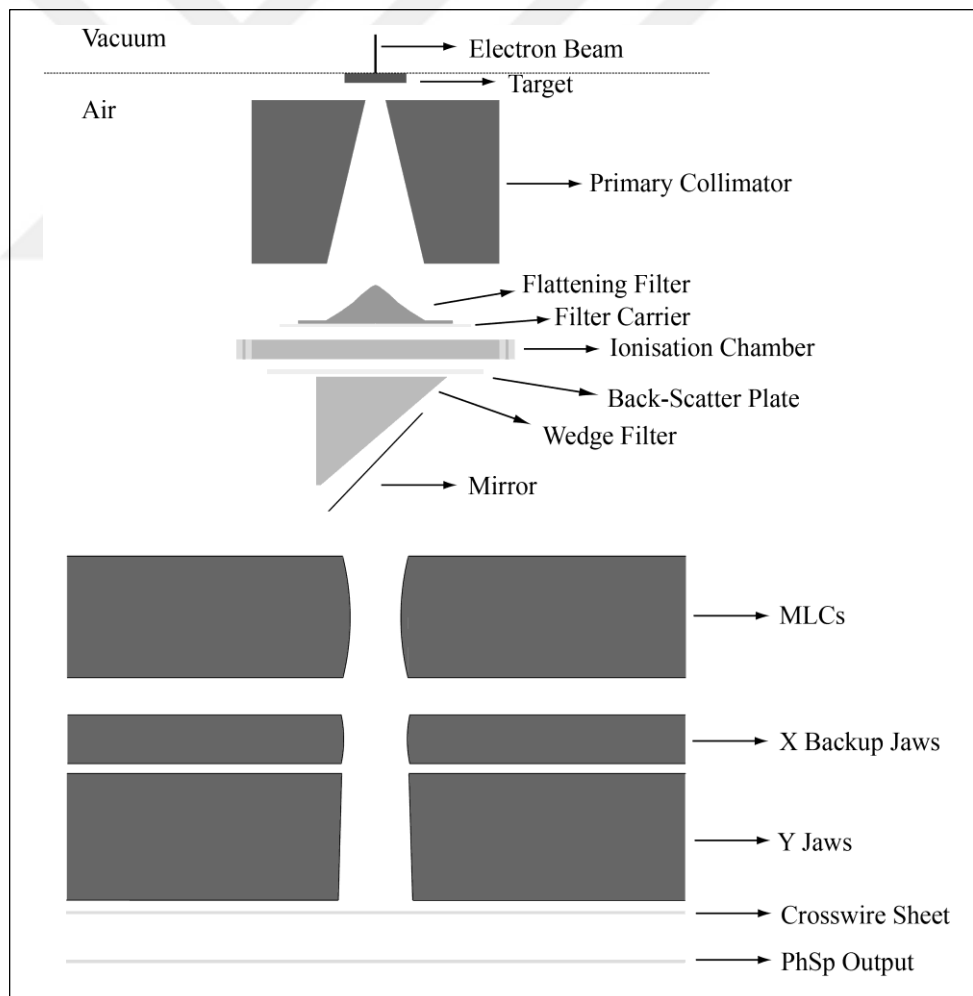


Figure 4.1. Monte Carlo model of Elekta Synergy MLCi treatment head using EGSnrc/BEAMnrc code system

#### 4.1.2. Monte Carlo Radiation Transport Parameters

Effect of inclusion some physical processes on percent depth dose (PDD) curves were given in Figure 4.2. Statistical error of each calculation point is not shown on the graphics to be expressed clearly. Error of difference for each point was calculated using the rule of propagation of errors.

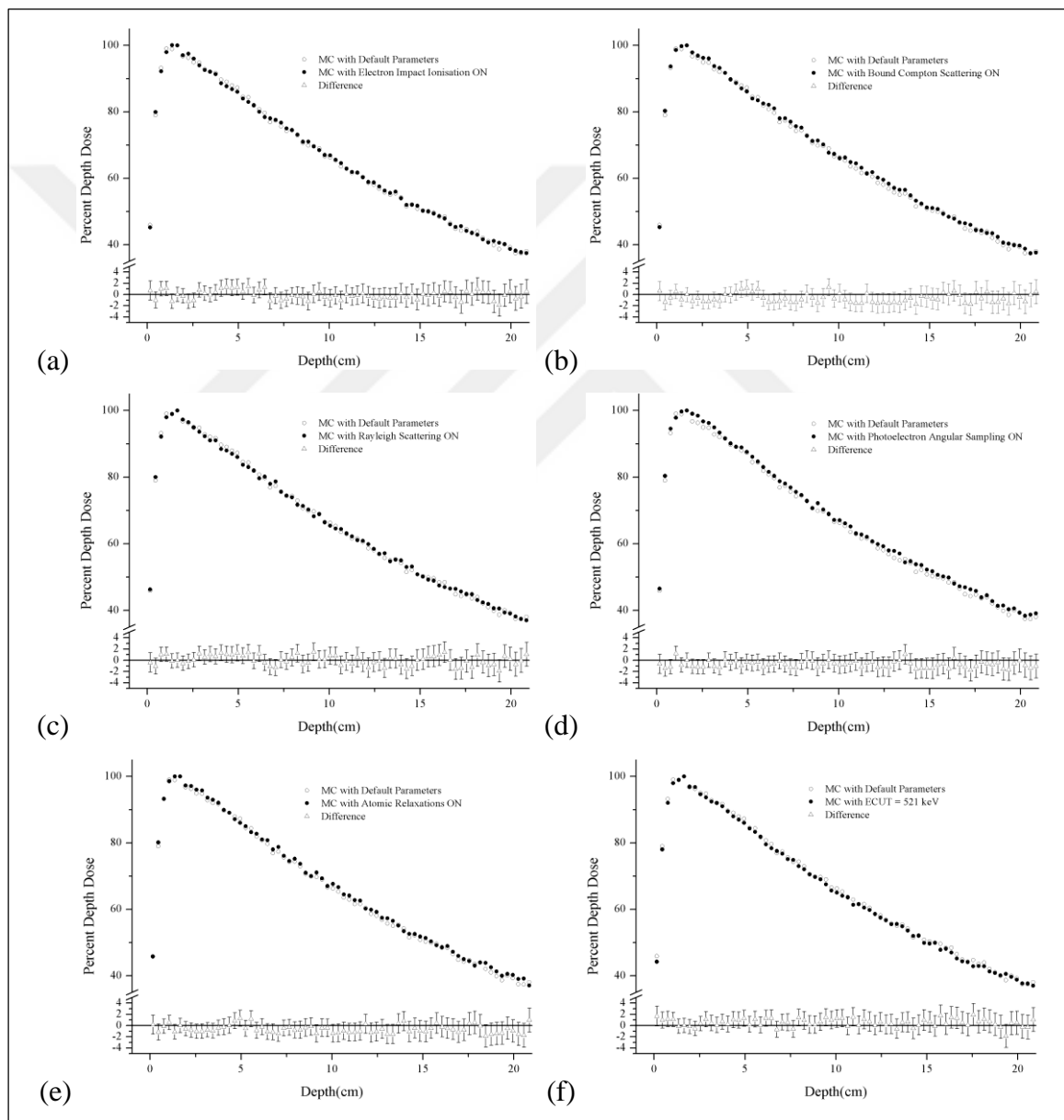


Figure 4.2. Percent depth dose curves of MC simulation with default transport parameters versus MC simulation with (a) electron impact ionisation ON, (b) bound Compton scattering ON, (c) photoelectron angular sampling ON, (d) Rayleigh scattering ON, (e) atomic relaxations ON and (f) ECUT=521 keV

None of the parameters investigated here was significant effect on the PDD curves as seen in Figure 4.2. Using this information, the physical processes investigated were kept OFF; ECUT was chosen as 700 keV; and DBS was used for all simulations.

Effect of these processes on CPU time can be seen on Figure 4.3. Physical processes of electron impact ionisation, Rayleigh scattering, photoelectron angular sampling and atomic relaxations increase CPU time not more than 10 per cent. Bound Compton scattering and selection of ECUT 521 keV increase CPU time almost two-fold.

The figure also includes effect of Directional Bremsstrahlung Splitting (DBS). Use of DBS decrease CPU time about 85 times keeping statistical error at the same level.

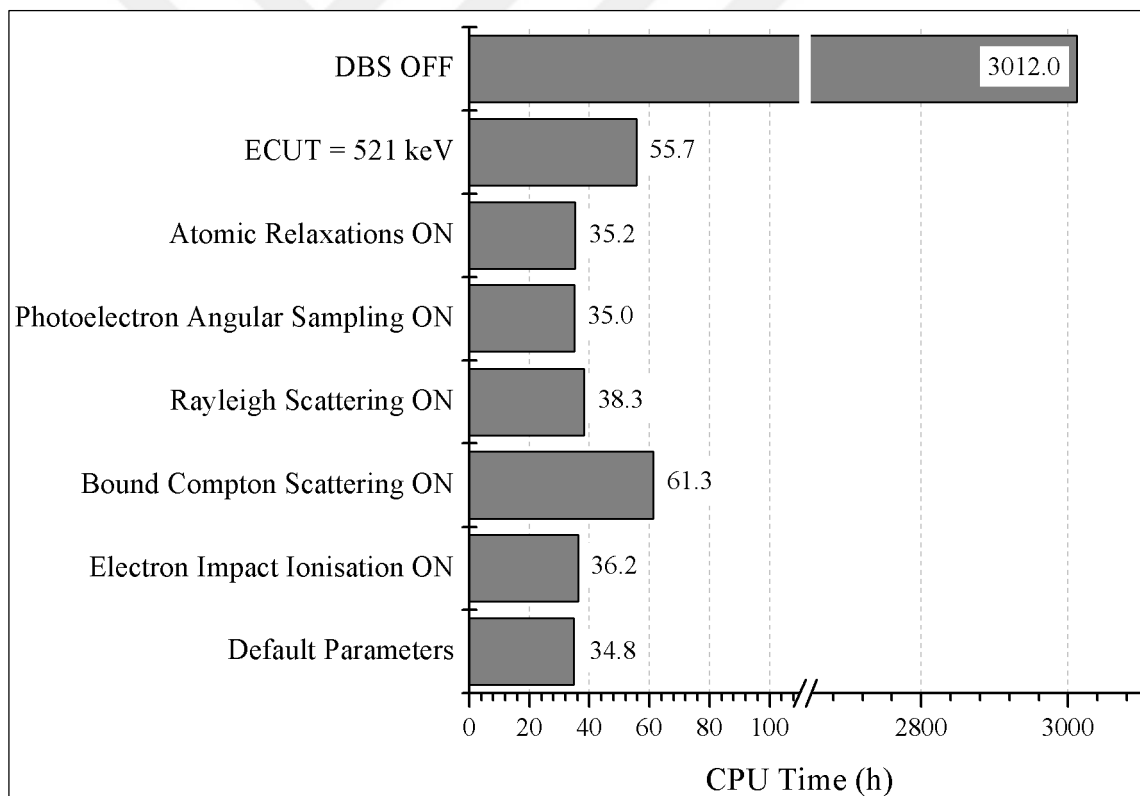


Figure 4.3. Effect of MC transport parameters on CPU time

Effect of global electron cut-off energy for range rejection (ESAVE\_GLOBAL) on PDD curves are given in Figure 4.4. Either value of ESAVE\_GLOBAL was significant effect on the PDD curves as seen in the figure. CPU time increase with ESAVE\_GLOBAL=3.0 MeV

or CPU time decrease with  $\text{ESAVE\_GLOBAL}=1.0$  MeV were not more than 1.7 per cent. Since not significant differences were observed,  $\text{ESAVE\_GLOBAL}$  value was left the default value of 2.0 MeV.

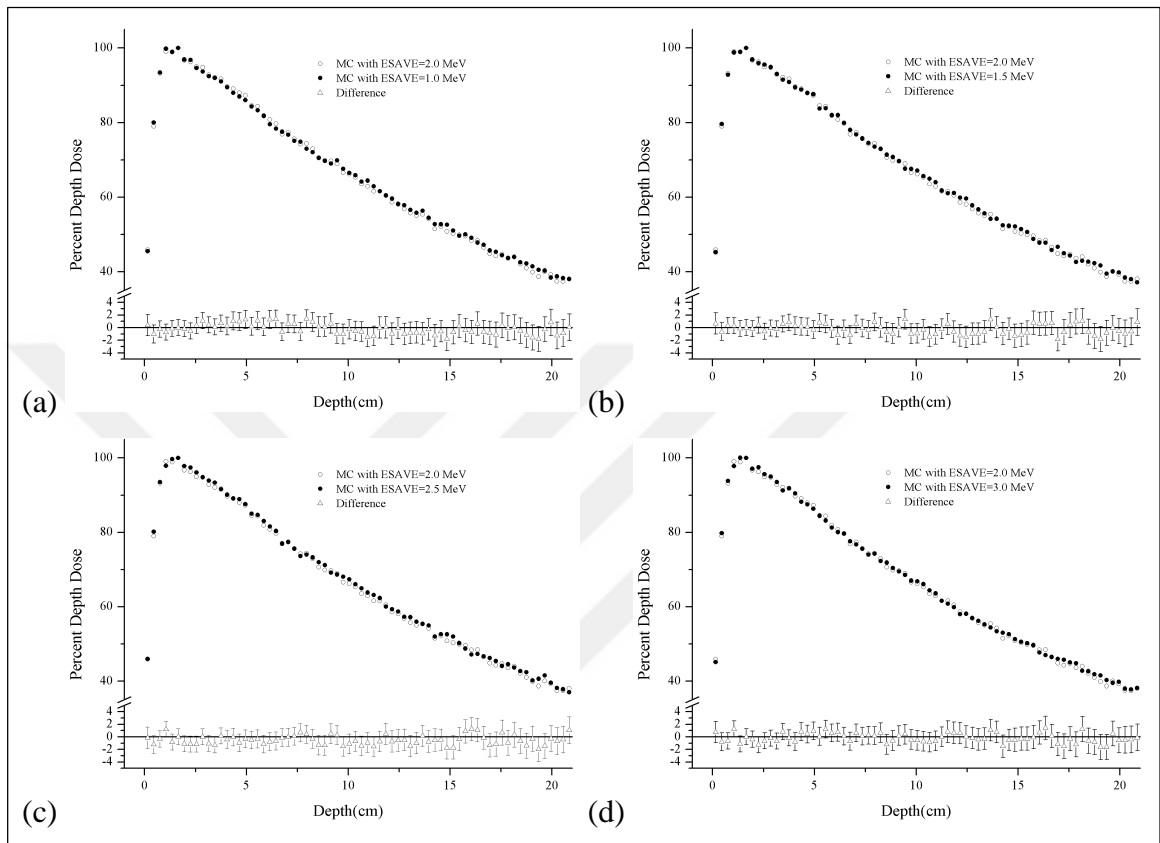


Figure 4.4. Percent depth dose curves of MC simulation with  $\text{ESAVE\_GLOBAL}$  is equals to 2.0 MeV in comparison with MC simulation with  $\text{ESAVE\_GLOBAL}$  is equals to (a) 1.0 MeV, (b) 1.5 MeV, (c) 2.5 MeV, (d) 3.0 MeV

Effect of different cross sections on PDD curves are given in Figure 4.5. None of the cross sections was significant effect on the PDD curves as seen in the figure. Effects of the cross sections on CPU time are also not significant. Not more than 2.5 per cent increase was observed. For this reason, the default cross sections were also not changed.

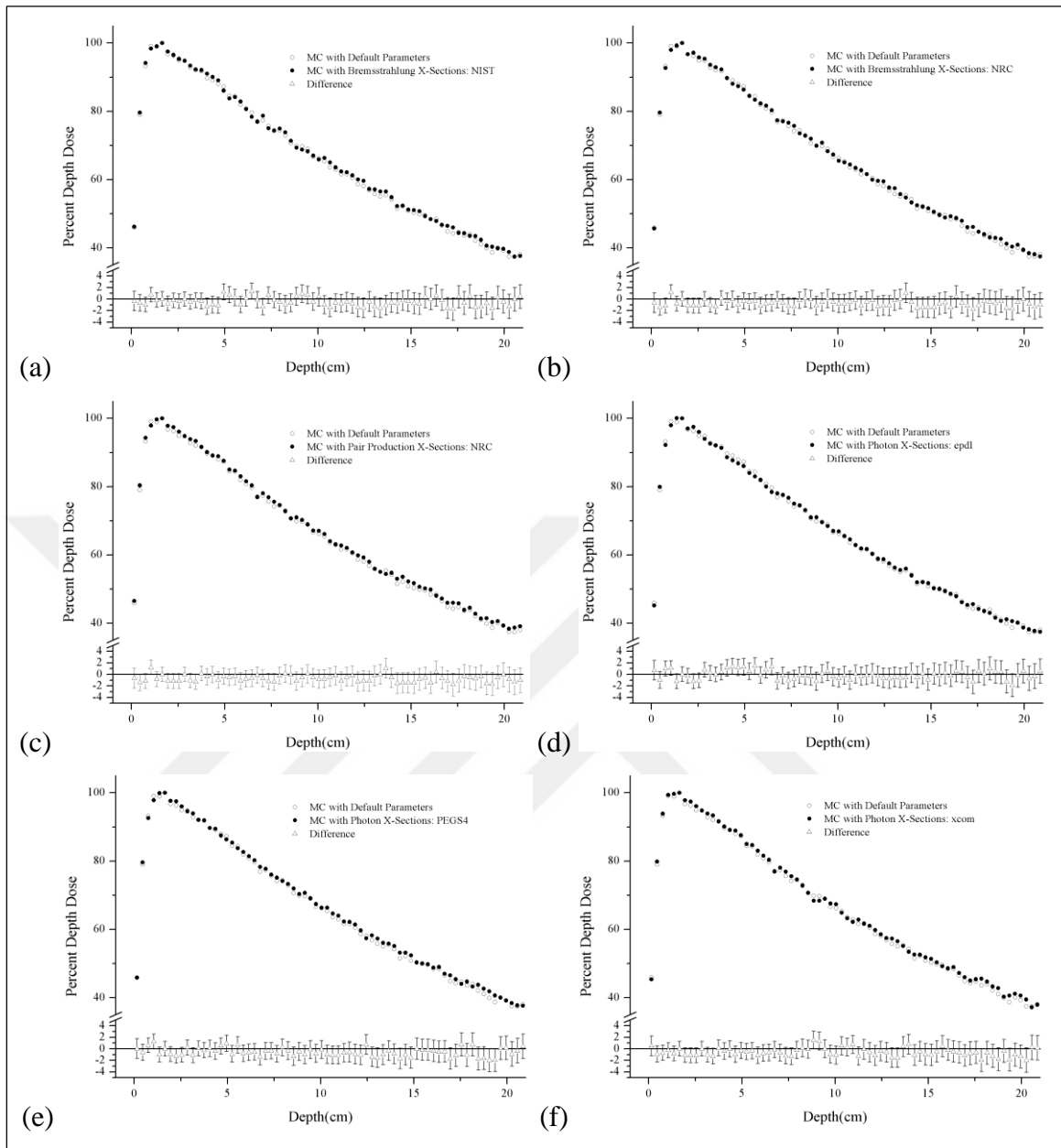


Figure 4.5. Effect of different cross sections on PDD curves

### 4.1.3. Initial Electron Beam Energy Selection

PDD curves obtained with different initial electron energies in comparison with ionisation chamber measurements are given in Figure 4.6. Only three energies are given in the graphics for clarity.

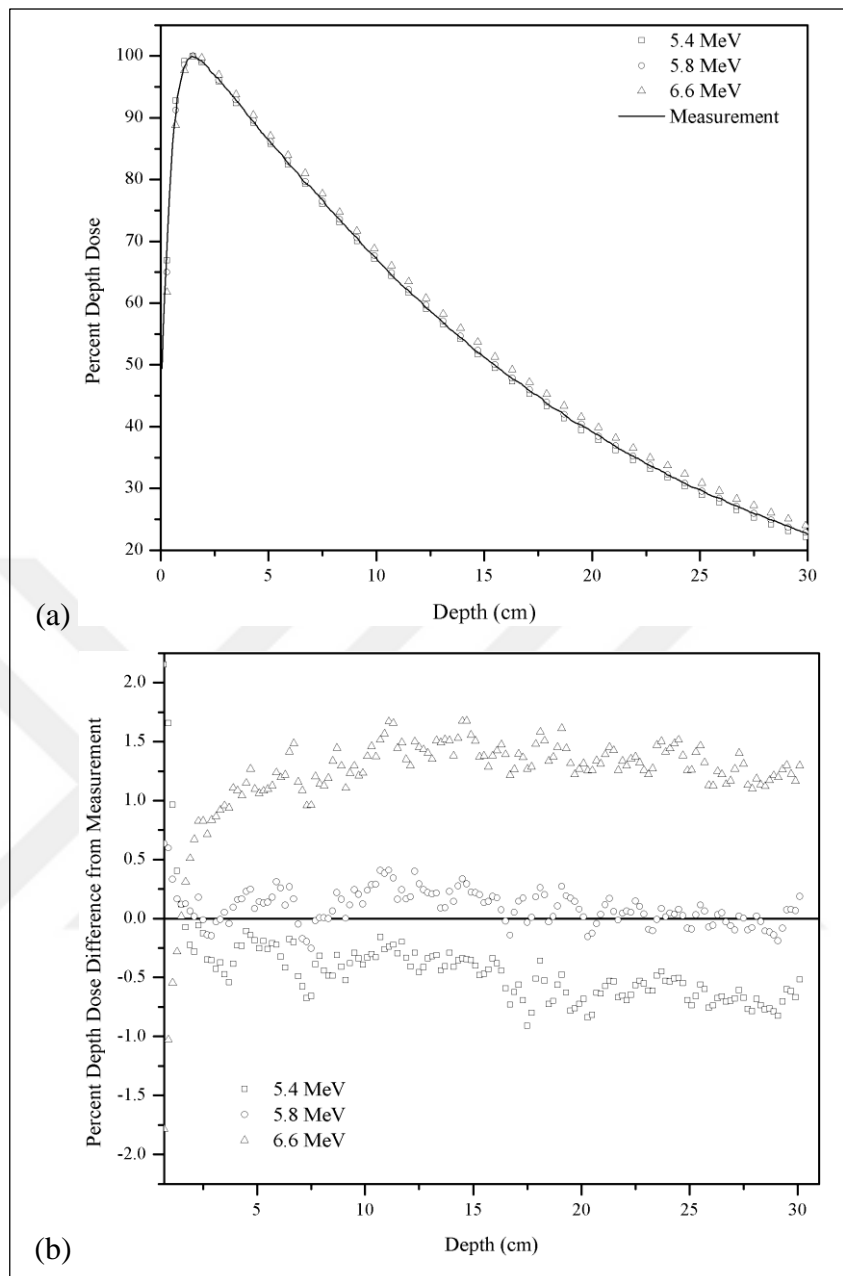


Figure 4.6. (a) PDD curves obtained with different initial electron energies in comparison with ionisation chamber measurements, (b) differences of curves from measurement ( $10 \times 10 \text{ cm}^2$  open field and  $\text{SSD}=100 \text{ cm}$ )

Relatively large differences up to 8.0 per cent were observed in the first 3 mm of the water phantom (not shown in the figure). This differences comes mainly from the size of the ionisation chamber used. The IBA CC13 ionisation chamber has a sensitive volume with the length of 5.8 mm and radius of 3.0 mm. While measuring depth doses near the surface of the



water, some parts of the chamber's sensitive volume lies above the water. This causes measurement errors.

In Figure 4.7, dose profiles at 10 cm depth obtained with different initial electron energies in comparison with ionisation chamber measurements are given.

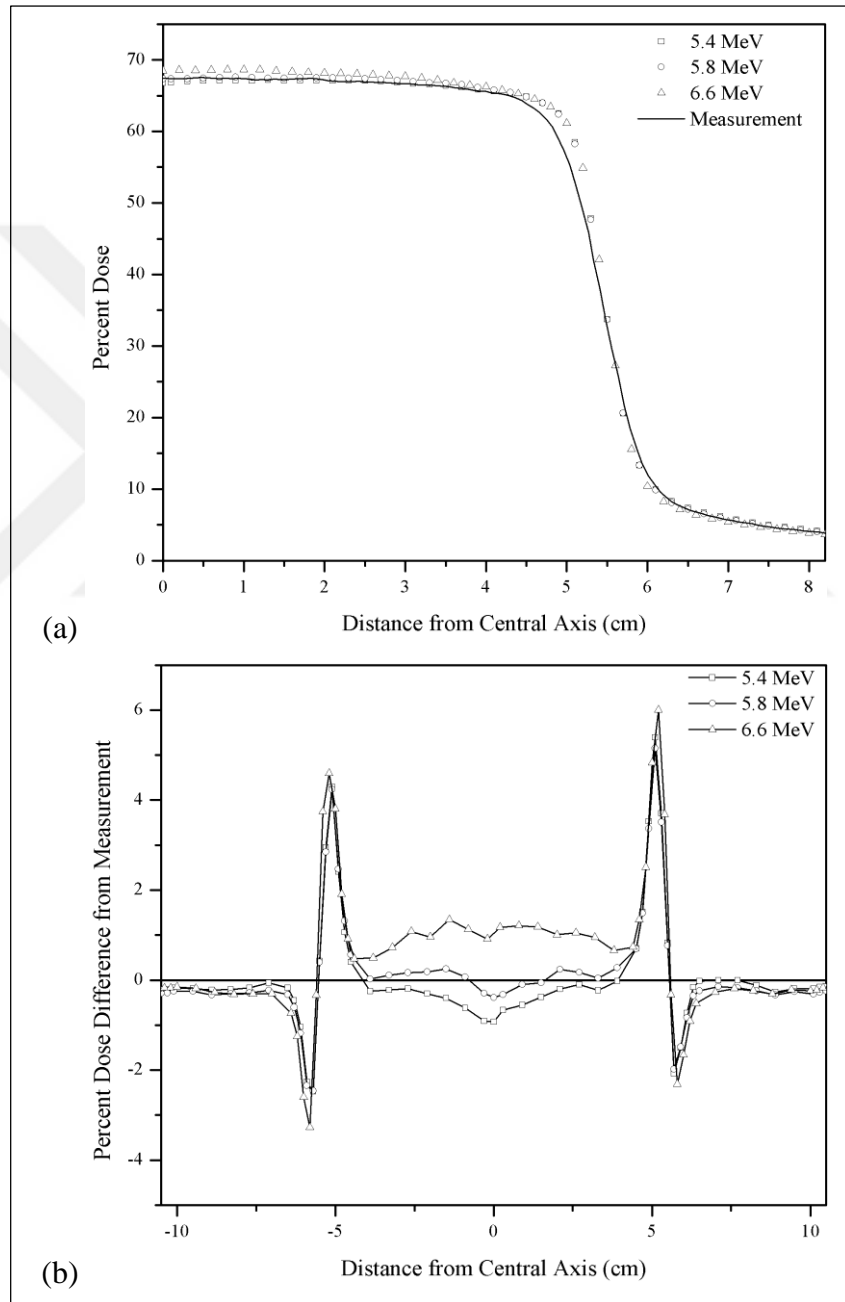


Figure 4.7. (a) Dose profiles at 10 cm depth obtained with different initial electron energies in comparison with ionisation chamber measurements, (b) differences of curves from measurement ( $10 \times 10 \text{ cm}^2$  open field and SSD=100 cm)

Large dose differences up to 6.0 per cent between Monte Carlo and ionisation chamber measurements were observed on the penumbra regions of the profiles. This difference is also caused by the size of the ionisation chamber. Haryanto et al. [84] was also addressed this to the size of the ionisation chamber. They made profile measurements with different type of radiation detectors and compare them with Monte Carlo simulation as shown in Figure 4.8. In their study, they found good agreement within two per cent between Monte Carlo calculated and measured profiles with the diamond and the diode detector. On the other hand, the largest deviations between the calculated and measured profiles using the ionization chamber were found in the penumbra region. They conclude this results that this is mainly due to the larger size of the sensitive volume of the ionization chamber. Other investigators were also found similar results [85,86]. Neither diamond nor diode detectors were available in the department that measurements were made. For this reason, no further comparisons were made.

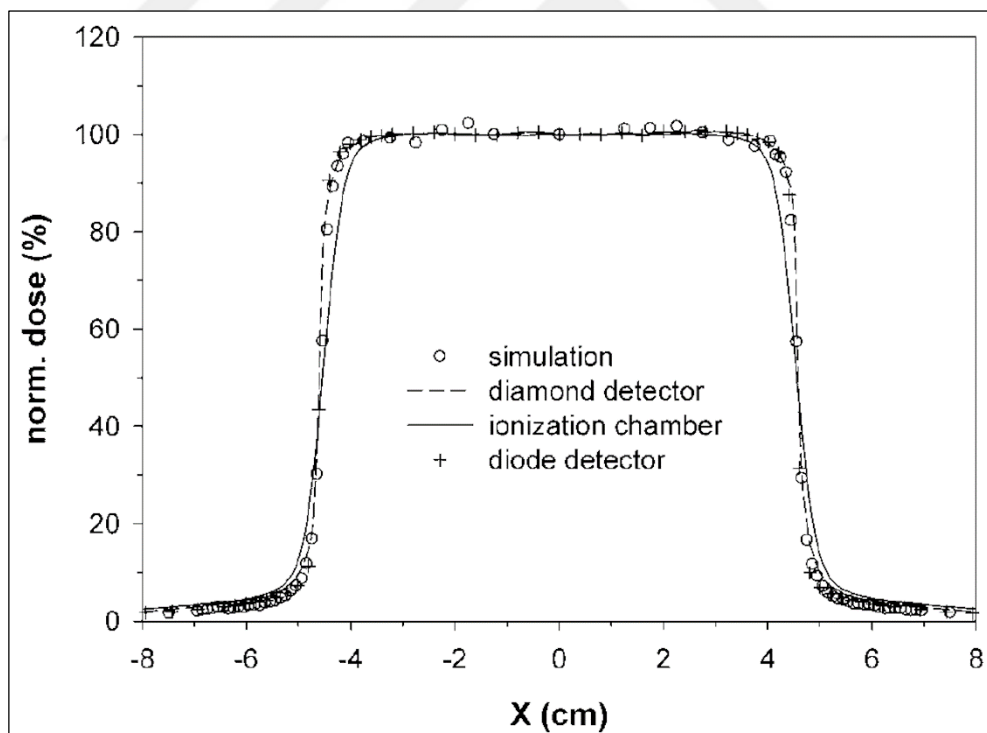


Figure 4.8. Dose profile measurements made by Haryanto et al. [84]

To determine initial electron beam energy objectively,  $\chi^2$  values were calculated. In PDD comparison,  $\chi^2$  values were calculated for depths between 0.5 and 30 cm. In dose profile

comparisons, calculations were made between off-axis distances of -4.5 and 4.5 cm for 10 cm depth, and between -5 and 5 cm for 20 cm depth.  $\chi^2$  results are given in Table 4.1. Following the table, electron beam energy of 5.8 MeV that minimizes the  $\chi^2$  was selected as initial electron beam energy.

Table 4.1.  $\chi^2$  results against initial electron beam energy

Initial Electron Beam Energy (MeV)	$\chi^2$ values		
	PDD curve	Dose Profile @ 10 cm depth	Dose Profile @ 20 cm depth
5.4	0.348	0.208	0.282
5.6	0.117	0.184	0.160
<b>5.8</b>	<b>0.033</b>	<b>0.079</b>	<b>0.049</b>
6.0	0.206	0.100	0.158
6.2	0.574	0.151	0.347
6.4	1.146	0.483	0.835
6.6	1.784	0.595	1.195

At this energy, an excellent correlation was observed between measured and calculated  $\text{TPR}_{20,10}$  values an identifier for beam quality (0.678 vs. 0.679). The rest of the simulations were performed at this initial electron energy.

#### 4.1.4. Validation of the Simulation

Percent depth dose comparison of MC simulation and ionisation chamber measurement for  $10 \times 10 \text{ cm}^2$  open field is given in Figure 4.9. Statistical error level was lower than 0.5 per cent for high-dose regions in MC simulation. As shown in the figure dose difference between MC simulation and ionisation chamber measurement less than 0.5 per cent.

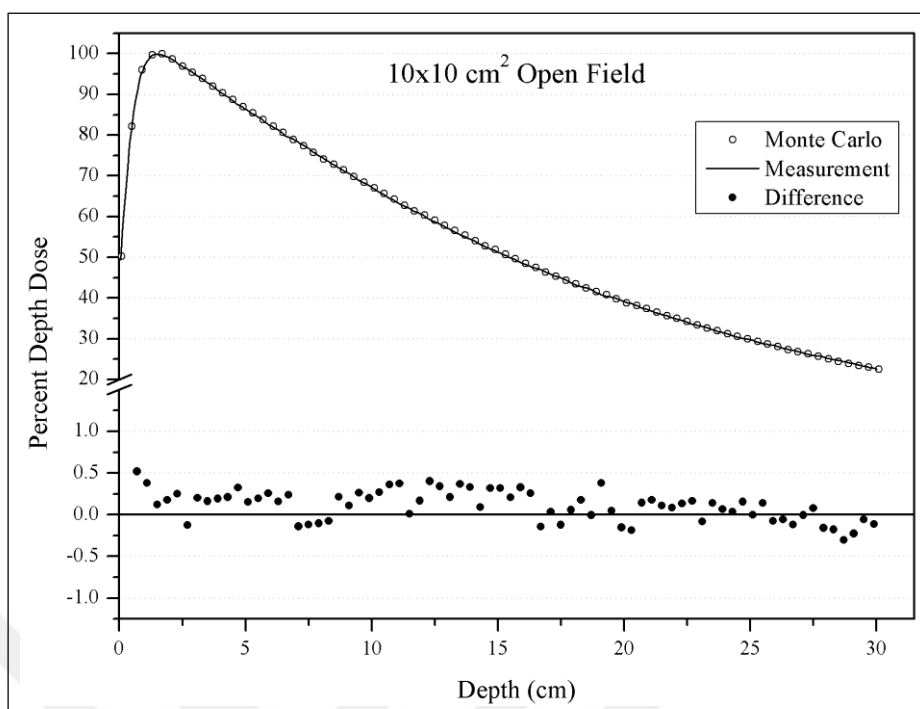


Figure 4.9. Percent depth dose comparison of MC simulation and ionisation chamber measurement for  $10 \times 10 \text{ cm}^2$  open field and  $\text{SSD}=100 \text{ cm}$

In Figure 4.10, some selected PDD curve comparisons are given. Less than 0.5 per cent differences were obtained in PDD comparisons between MC simulation and ionization chamber measurements for field sizes of  $20 \times 20 \text{ cm}^2$  and smaller. Differences between MC simulations and measurements were within 1.0 per cent for larger areas. The increase in the differences observed for larger fields is mainly due to the number of initial electrons. Although the statistical error in MC simulation was less than 0.5 per cent for high dose areas, errors in calculated doses were increase with the increasing depth in the water due to decrease in doses.

For wedged fields, less than 1.5 per cent differences were achieved in PDD comparisons. The raise in the differences is considered to be caused by the approximations used for modelling the wedge filter. The complete set of comparisons are given in Appendix E.

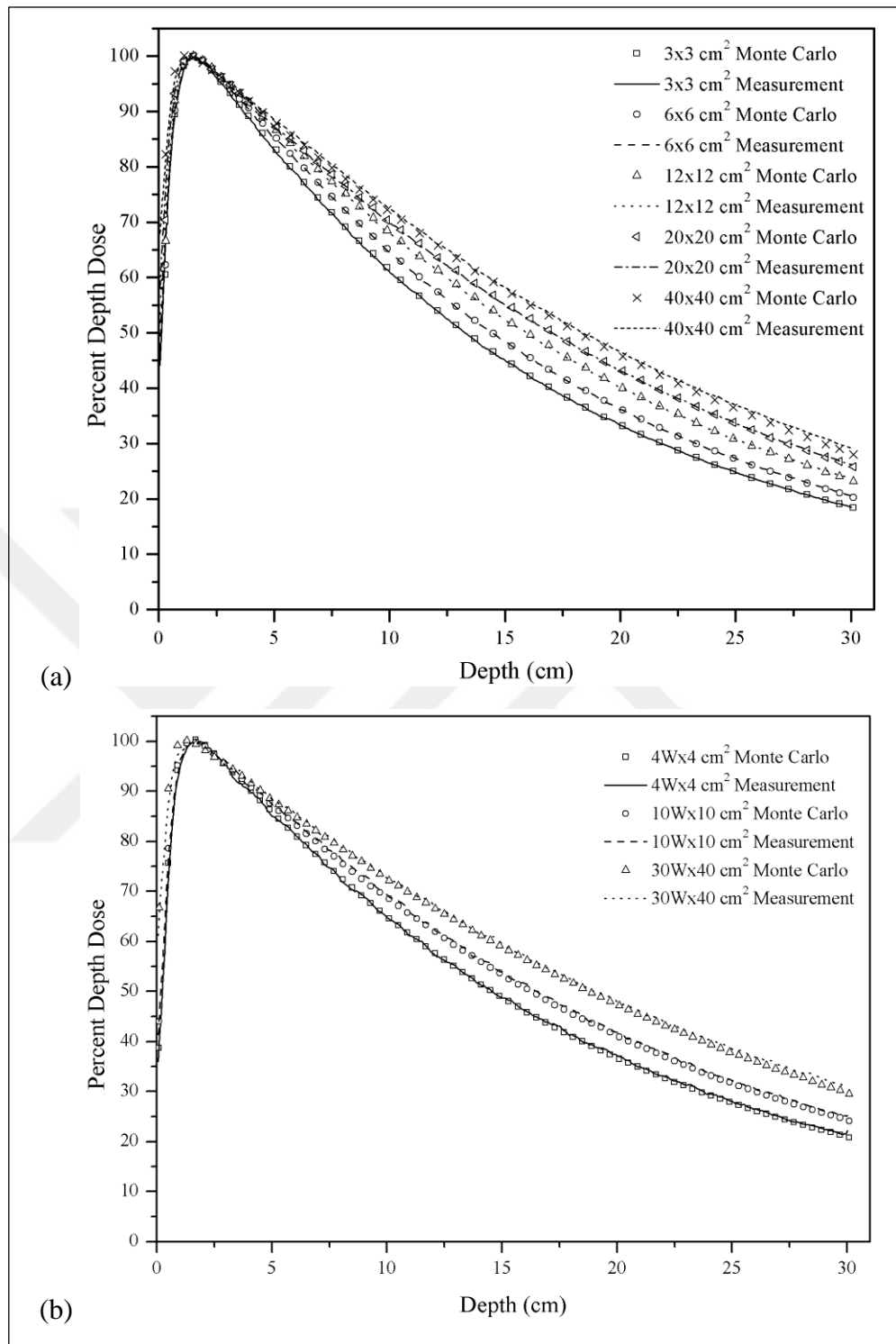


Figure 4.10. Some selected PDD curve comparisons for (a) open fields (b) wedged fields (SSD=100 cm)

Dose profile comparisons for some open fields at 10 cm depth and for 30Wx40 cm<sup>2</sup> wedged field at different depths are given in Figure 4.11. Differences between MC simulations and measurements were within 1.0 per cent except for the penumbra regions. In these regions

differences rose up to 8.0 per cent due to size of the ionisation chamber used in the measurements.

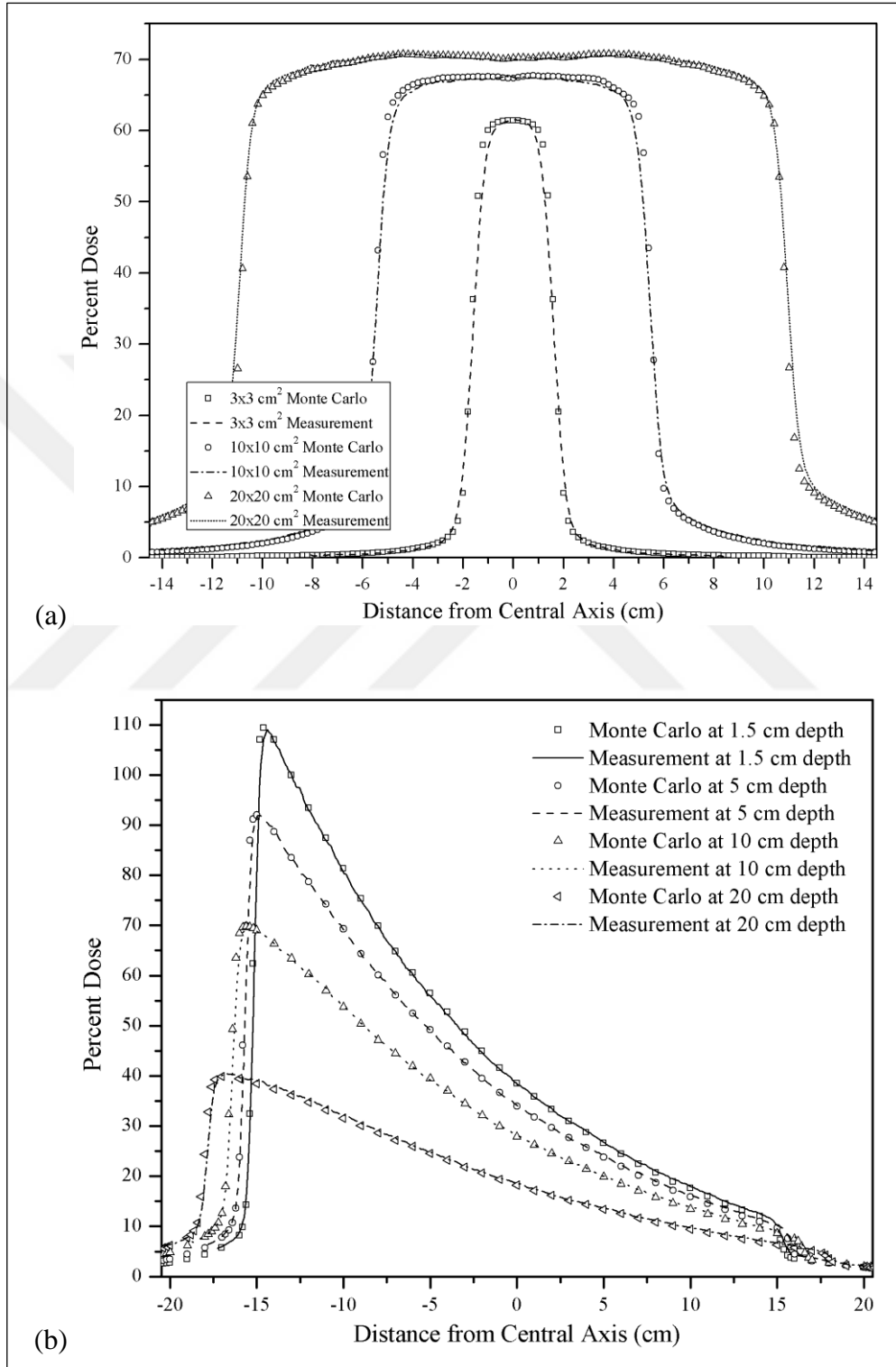


Figure 4.11. Dose profile comparisons for (a) open fields at 10 cm depth (b) 30Wx40 cm<sup>2</sup> wedged field at different depths (SSD=100 cm)

MLC transmission and interleaf leakage comparison between film dosimetry and MC are given in Figure 4.12. In MC simulation average MLC transmission was 9.0 cGy per 1000 MU while average interleaf leakage was 21.4 cGy per 1000 MU. In film measurements, average MLC transmission was 10.5 cGy per 1000 MU and average interleaf leakage was 16.3 cGy per 1000 MU. Maximum leakage values were measured as 22.4 and 21.3 cGy for MC and film measurement, respectively. In film measurements measured interleaf leakage was not equal for adjacent leaves. This distribution cannot be modelled in MC simulation, since the gap between leaves is set as group, not individually.

In their study, Huq et al. [87] was also measured with film dosimetry up to 27 cGy per 1000 MU interleaf leakage for an Elekta linac. The leakage pattern illustrated in the study was similar to the one given in Figure 4.12.

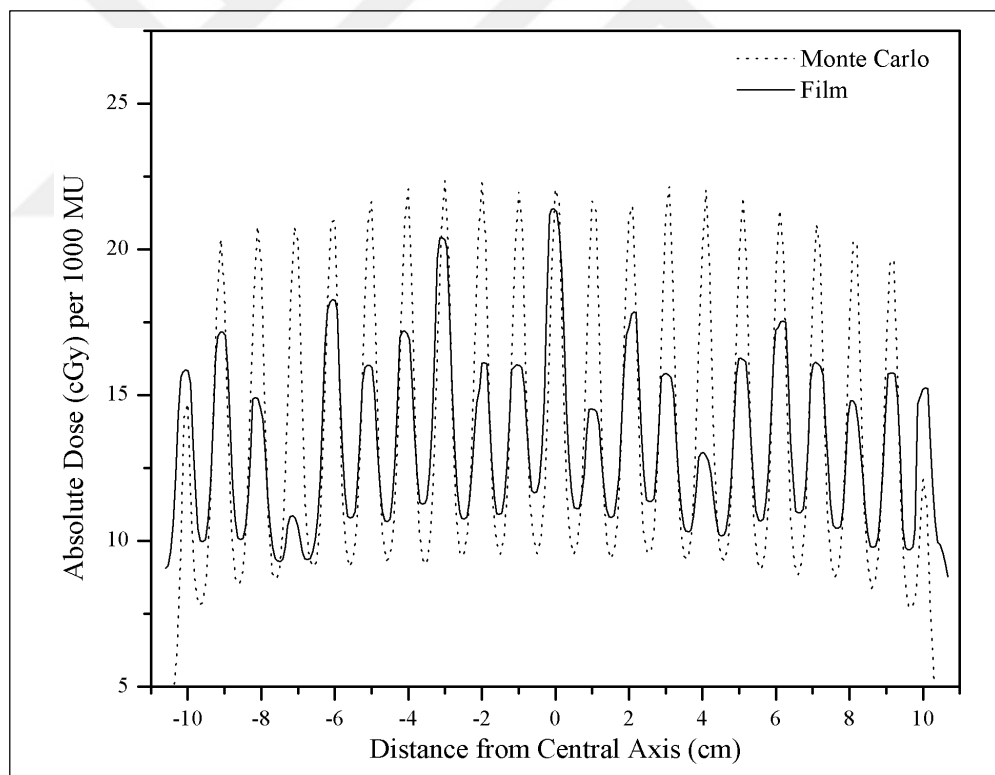


Figure 4.12. MLC transmission and interleaf leakage comparison (SSD=100 cm)

The agreement between the calculated output factors and those measured with the ionization chamber for all open fields was found better than 1.0 per cent (Figure 4.13).

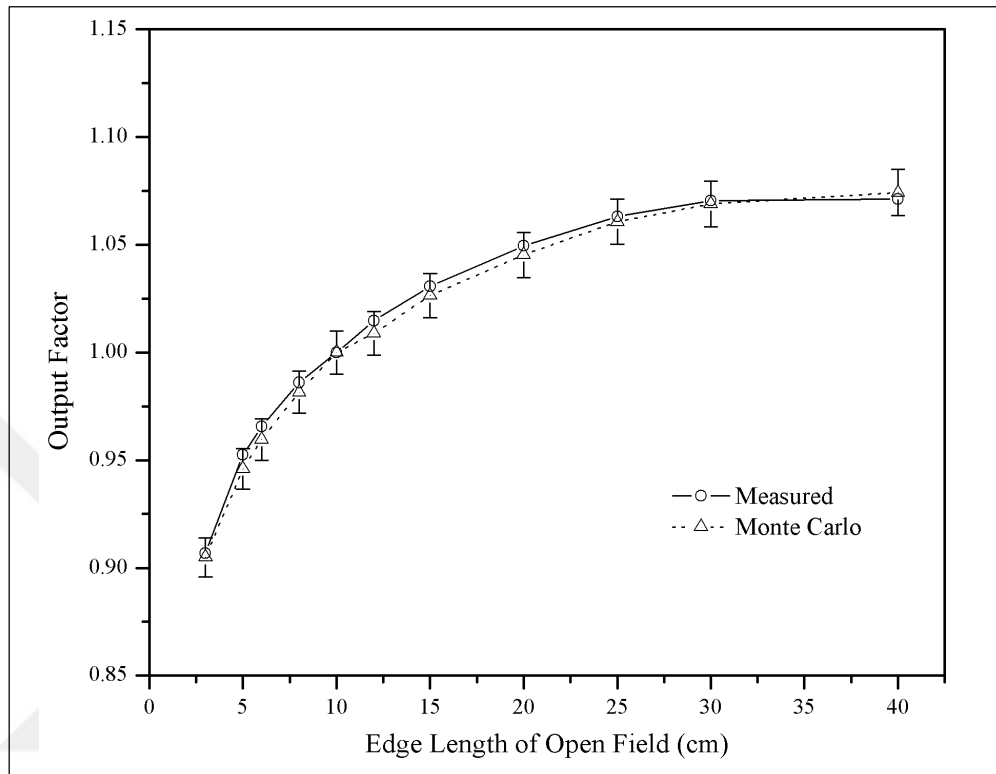


Figure 4.13. Comparison of output factors (SSD=100 cm)

Calibration factor for absolute dose calculations,  $F_Q$ , was calculated as  $1.388 \times 10^{14}$  particles/MU.

#### 4.1.5. Concluding Remarks

In this part of the study, MC simulation and commissioning process were presented. Except for MLC transmission and interleaf leakage, very good agreement with the ionization chamber measurements had been achieved. Because of the limitations of the MC code, it is not possible to define amount of leakage for each interleaf gap individually.



## 4.2. COMPARISON OF TREATMENT PLANNING SYSTEMS WITH MONTE CARLO SIMULATION UNDER CONDITIONS OF TISSUE INHOMOGENITIES

### 4.2.1. Lung Phantom

PDD curves in Lung Phantom are given in Figure 4.14. For  $3 \times 3 \text{ cm}^2$  open field, a rapid dose drop was observed for all calculation methods except for  $\text{TPS}_{\text{PB}}$ . This is mainly due to lateral electronic disequilibrium [9,11,88]. This effect was not observed for larger field sizes where lateral electronic equilibrium has fulfilled. Eight per cent dose difference was observed between  $\text{TPS}_{\text{PB}}$  and  $\text{MC}_{\text{H}_2\text{O}}$  at 4.5 cm depth for  $3 \times 3 \text{ cm}^2$  open field. This value is 2.5 per cent for  $10 \times 10 \text{ cm}^2$  and  $20 \times 20 \text{ cm}^2$  open fields. The difference increase as depth is increases up to 10 per cent for  $3 \times 3 \text{ cm}^2$  and 3.5 per cent for  $10 \times 10 \text{ cm}^2$  and  $20 \times 20 \text{ cm}^2$  open fields.

The difference between  $\text{TPS}_{\text{CCC}}$  and  $\text{MC}_{\text{H}_2\text{O}}$  was 1.0 per cent at 4.5 cm depth for  $3 \times 3 \text{ cm}^2$  open field. Again, the difference increase as depth increases up to 4.5 per cent. The differences were 0.6 and 0.8 per cent for  $10 \times 10 \text{ cm}^2$  and  $20 \times 20 \text{ cm}^2$  open fields, respectively. Measured differences between  $\text{MC}_{\text{H}_2\text{O}}$  and  $\text{MC}_{\text{DW}}$  was not more than 0.5 per cent in Lung region. Up to 1.3 per cent difference was observed between  $\text{MC}_{\text{H}_2\text{O}}$  and  $\text{MC}_{\text{DM}}$ .

In their study, Carrasco et al. [89] had very similar results with other treatment planning systems that uses pencil beam (PB) and collapse cone convolution (CCC) calculation algorithms in comparison with Monte Carlo calculations using PENELOPE MC code. They have found that the CCC calculation algorithm showed good correlation with the MC calculation. The PDD curve that they obtained with the PB algorithm is similar to those that was found in this study. They were also correlated their MC calculations with ionization chamber measurements in lung equivalent material. This could not be performed in this thesis study due to absence of the lung equivalent material.

Dose profiles at 4.5 cm depth (in the middle of lung region) are given in Figure 4.15. Percent dose difference was seen for  $\text{TPS}_{\text{PB}}$  for all field sizes especially in  $3 \times 3 \text{ cm}^2$  field size. Besides, steepness of the dose profiles of  $\text{TPS}_{\text{PB}}$  at the field edges were visually higher in comparison with MC calculations. On the contrary, steepness of the dose profiles of  $\text{TPS}_{\text{CCC}}$  at the field edges were visually lower than MC calculations.

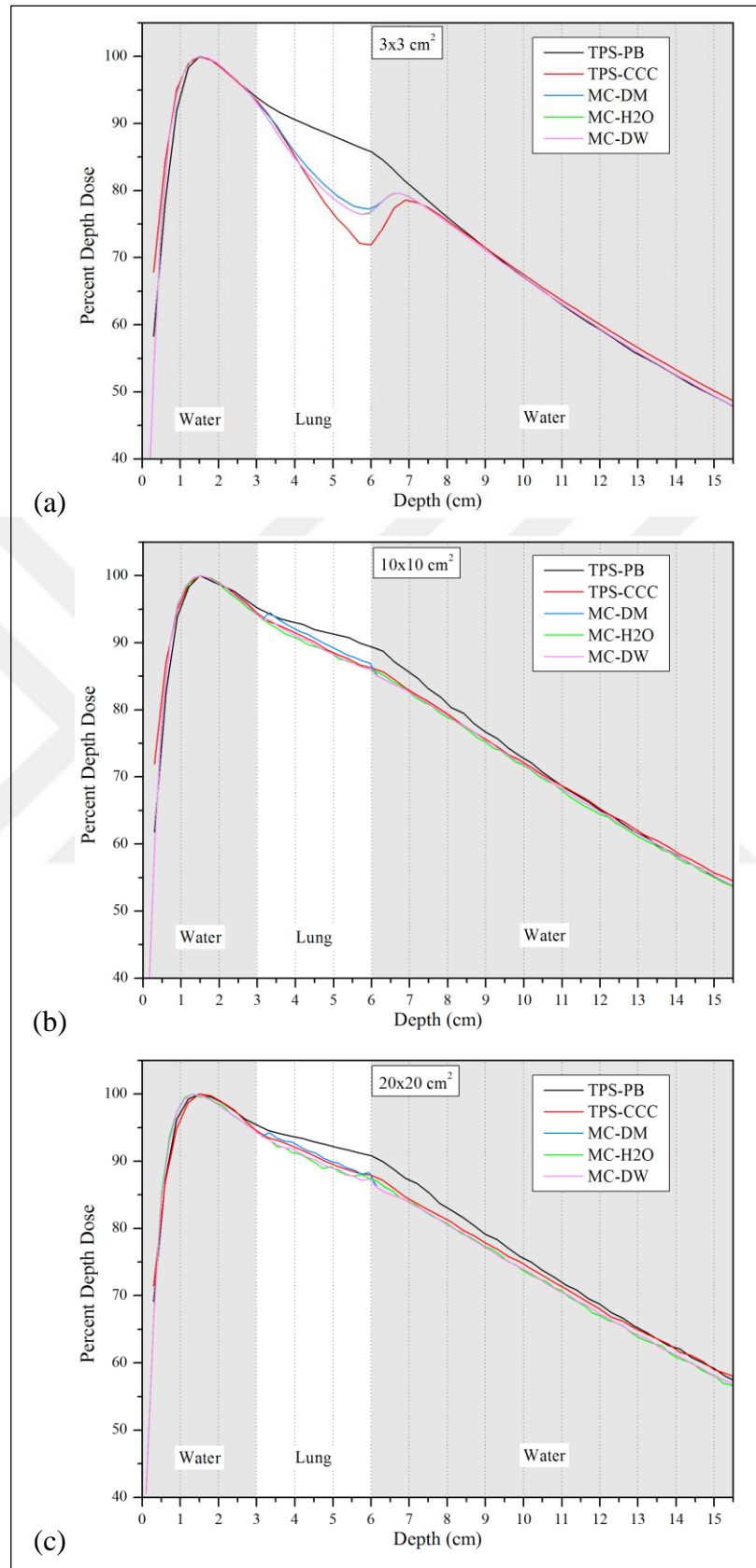


Figure 4.14. PDD curves in Lung Phantom for field sizes of (a)  $3 \times 3 \text{ cm}^2$ , (b)  $10 \times 10 \text{ cm}^2$ , (c)  $20 \times 20 \text{ cm}^2$  (SSD=100 cm)

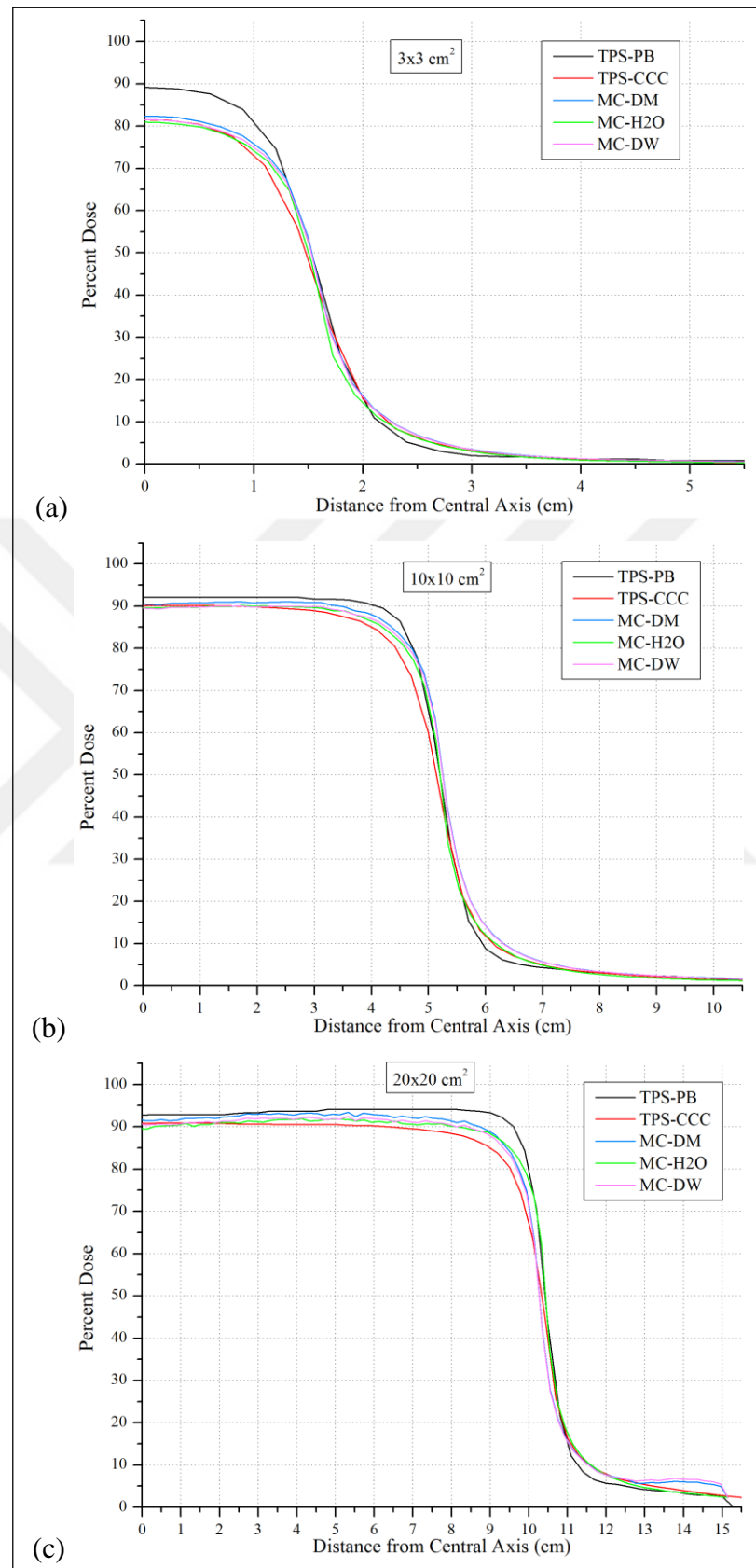


Figure 4.15. Dose profiles at 4.5 cm depth (in the middle of lung region) for field sizes of (a)  $3 \times 3 \text{ cm}^2$ , (b)  $10 \times 10 \text{ cm}^2$ , (c)  $20 \times 20 \text{ cm}^2$  (SSD=100 cm)

Penumbra widths (80%-20%) for Lung Phantom are given in Figure 4.16. As seen from the illustration, the penumbra widths are increasing with increasing field size except for the  $\text{TPS}_{\text{PB}}$ . A small drop was seen for the field size of  $20 \times 20 \text{ cm}^2$  field size. This unexpected behaviour was attributed to commissioning process.

Higher penumbra widths were measured from  $\text{TPS}_{\text{CCC}}$  calculations in comparison with MC calculations. This pattern shows that  $\text{TPS}_{\text{CCC}}$  overestimates lateral electron scattering in lung region according to MC results.

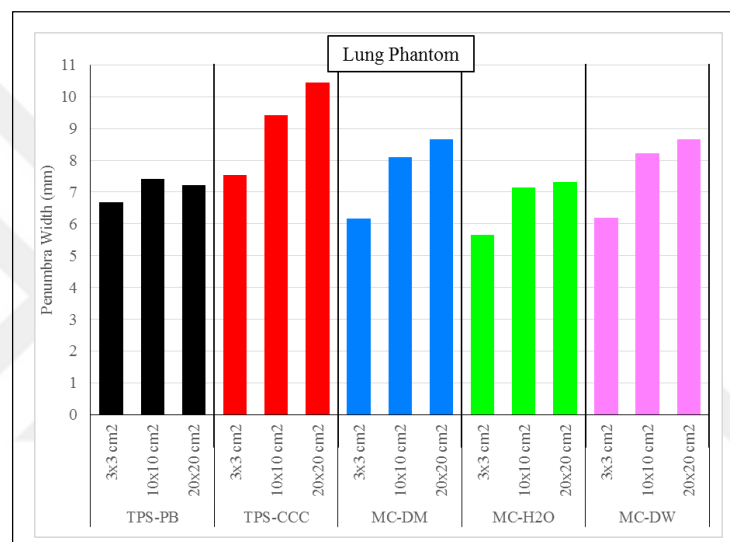


Figure 4.16. Penumbra widths (80%-20%) for Lung Phantom

#### 4.2.2. Bone Phantom

PDD curves in Bone Phantom are given in Figure 4.17. The dose differences between  $\text{MC}_{\text{H}_2\text{O}}$  and TPSs were lower than 2.0 per cent, while the difference between TPSs was lower than 1.0 per cent in bone area.

The dose difference between  $\text{MC}_{\text{H}_2\text{O}}$  and  $\text{MC}_{\text{DM}}$  was about 3.0 per cent. The main difference between these two calculation methods is the cross sections in bone region. In  $\text{MC}_{\text{H}_2\text{O}}$  calculation, all the atoms were composed of hydrogen and oxygen atoms. On the other hand, in  $\text{MC}_{\text{DM}}$  calculation, the bone region is composed of hydrogen, carbon, nitrogen, oxygen, magnesium, phosphor, sulphur, calcium, and zinc atoms. This difference produces distinction in cross section values.

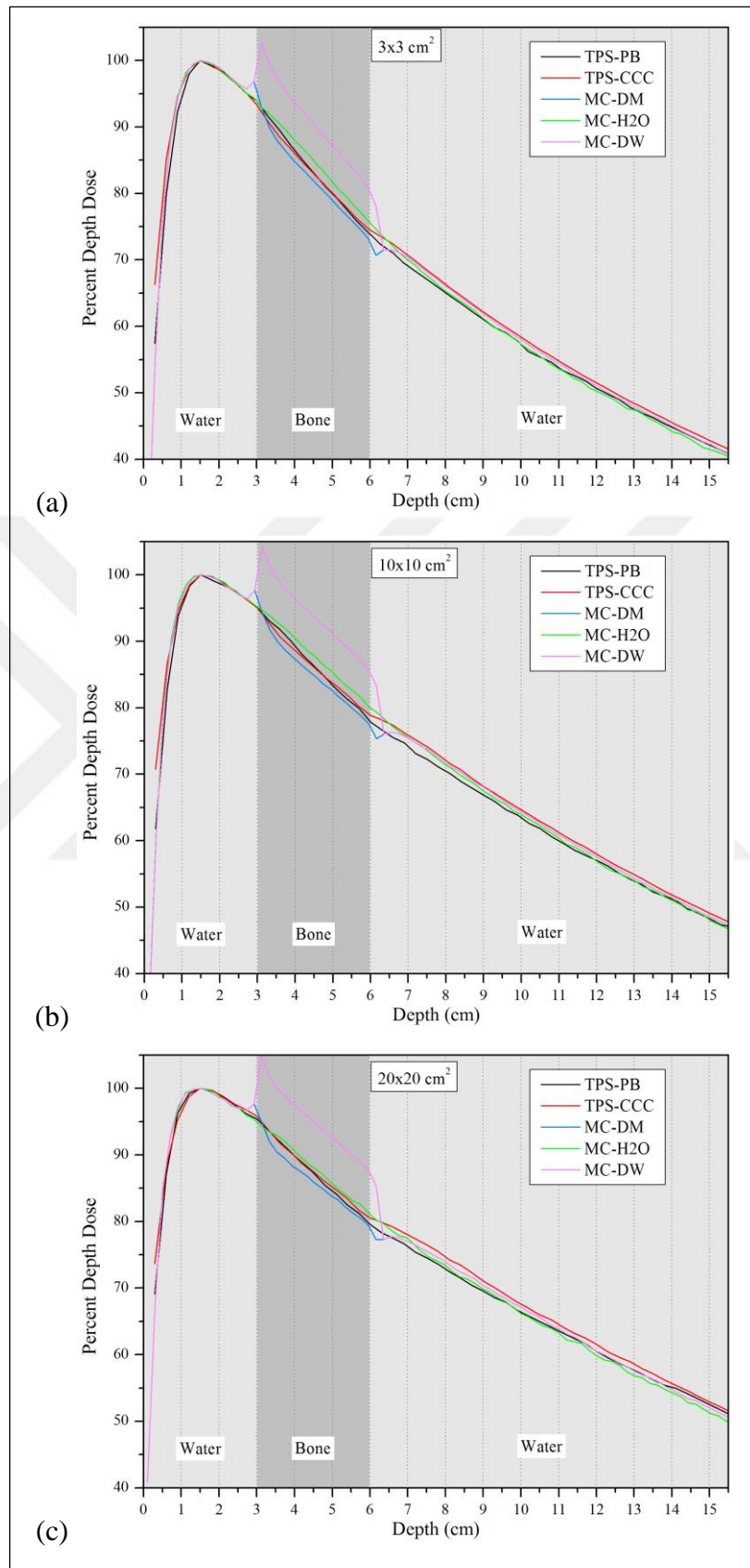


Figure 4.17. PDD curves in Bone Phantom for field sizes of (a)  $3 \times 3 \text{ cm}^2$ , (b)  $10 \times 10 \text{ cm}^2$ , (c)  $20 \times 20 \text{ cm}^2$  (SSD=100 cm)

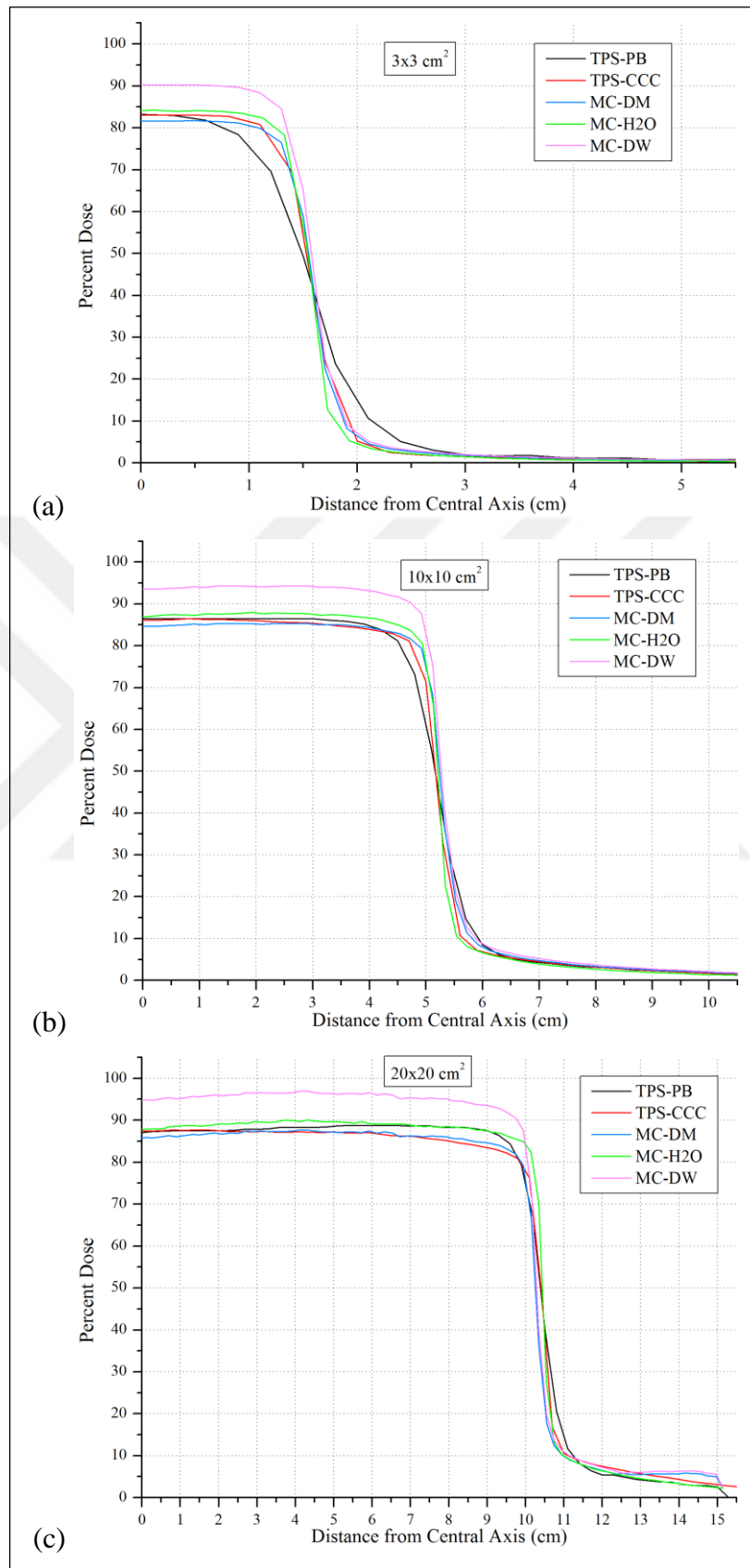


Figure 4.18. Dose profiles at 4.5 cm depth (in the middle of bone region) for field sizes of (a)  $3 \times 3 \text{ cm}^2$ , (b)  $10 \times 10 \text{ cm}^2$ , (c)  $20 \times 20 \text{ cm}^2$  (SSD=100 cm)

The difference between  $MC_{H_2O}$  and  $MC_{DW}$  was up to 8.0 per cent. This was because of the method suggested by AAPM Task Group No. 105 [28] for converting dose to medium to dose to water. According to this method 11.1 per cent increase was applied to MC dose to medium calculation in bone areas.

Ma et al. [90] was found very similar results with a similar bone phantom. In their study they suggested use of heavy density water for bone areas instead of AAPM Task Group's suggestion.

Dose profiles at 4.5 cm depth (in the middle of bone region) are given in Figure 4.18. Percent doses were higher for  $MC_{DW}$  for all field sizes. The steepness of dose profile of  $TPS_{PB}$  was distinctively lower than other calculation methods for  $3 \times 3 \text{ cm}^2$  field size.

Penumbra widths (80%-20%) for Bone Phantom are given in Figure 4.19. Calculated widths were significantly lower in comparison with Lung Phantom results for all calculation methods except for  $TPS_{PB}$ . This decrease was expected, because in high density regions like bone, lateral electron scatter at the field edges is limited due to high electron density of the medium. It was realized that  $TPS_{PB}$ 's algorithm is not sufficient to take into account such density effect.

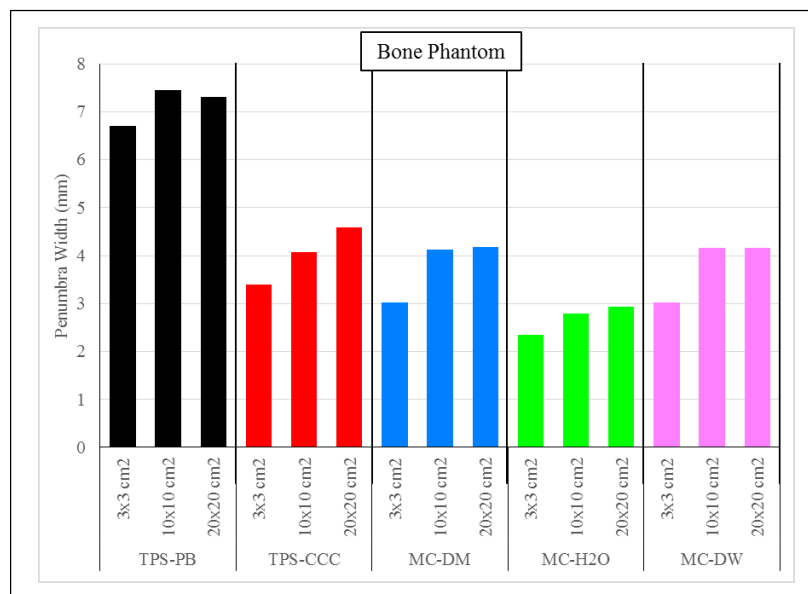


Figure 4.19. Penumbra widths (80%-20%) for Bone Phantom

### 4.2.3. Water Phantom

PDD curves in Water Phantom are given in Figure 4.20. There was no major difference observed between whole calculation methods for three field sizes.

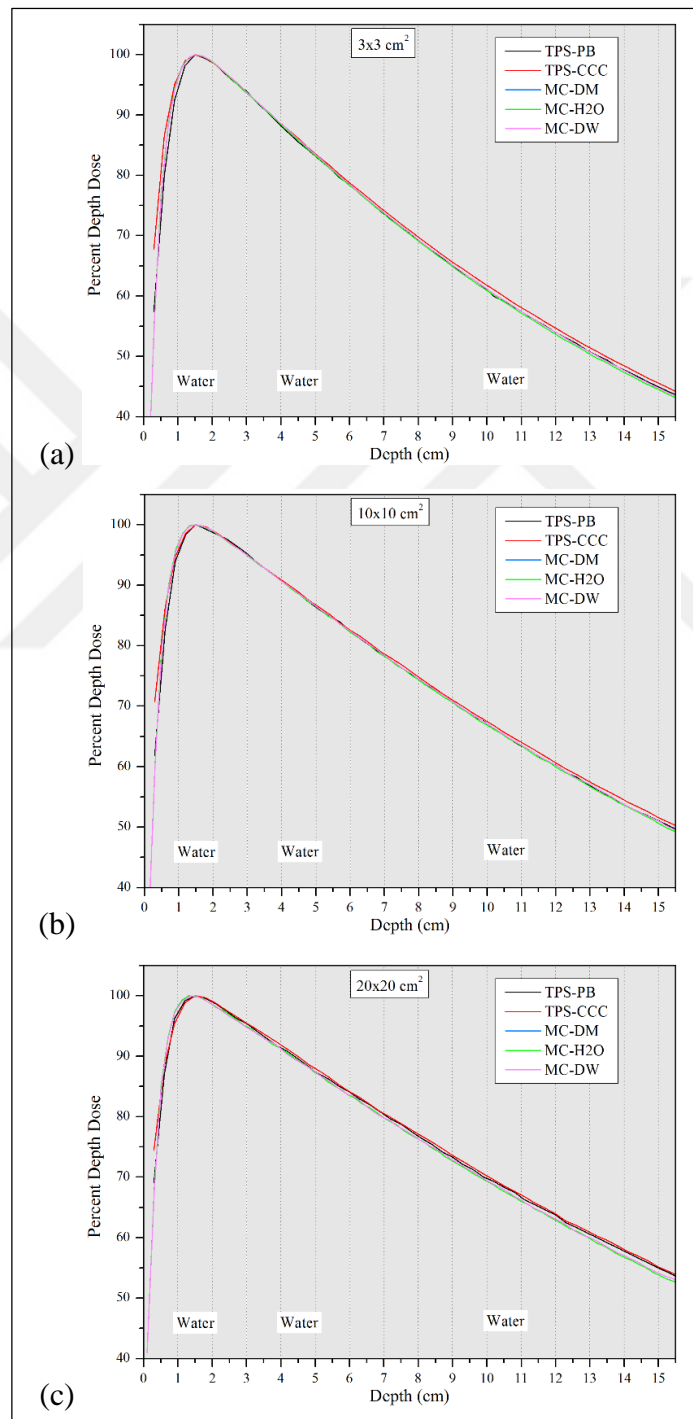


Figure 4.20. PDD curves in Water Phantom for field sizes of (a)  $3 \times 3 \text{ cm}^2$ , (b)  $10 \times 10 \text{ cm}^2$ , (c)  $20 \times 20 \text{ cm}^2$  (SSD=100 cm)



Dose profiles at 4.5 cm depth are given in Figure 4.21.

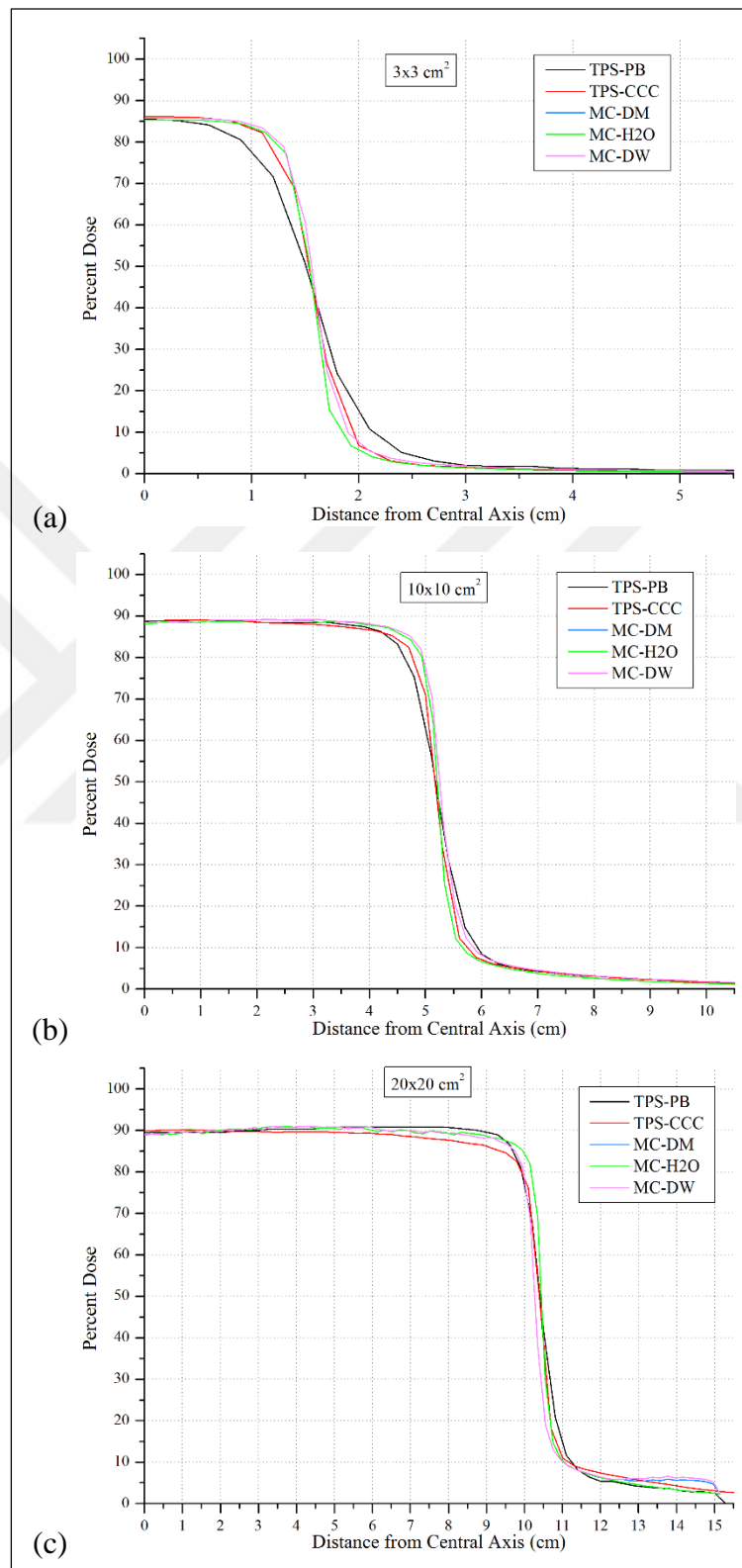


Figure 4.21. Dose profiles at 4.5 cm depth for field sizes of (a)  $3 \times 3 \text{ cm}^2$ , (b)  $10 \times 10 \text{ cm}^2$ , (c)  $20 \times 20 \text{ cm}^2$  (SSD=100 cm)

Penumbra widths (80%-20%) for Water Phantom are given in Figure 4.22. Calculated widths were significantly higher for  $TPS_{PB}$ , which is similar to the situation in Bone Phantom.

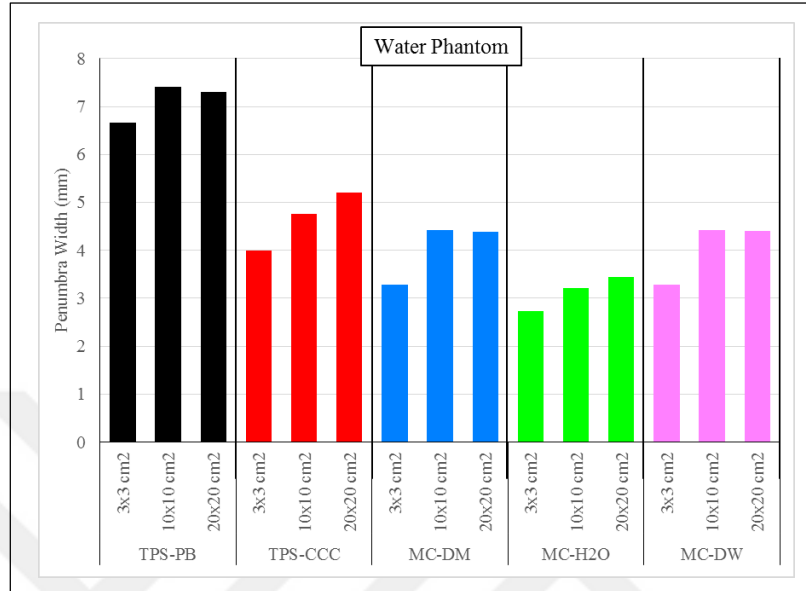


Figure 4.22. Penumbra widths (80%-20%) for Water Phantom

#### 4.2.4. Concluding Remarks

In general,  $TPS_{PB}$  makes huge calculation errors in lung material especially in small fields where electronic disequilibrium exist. Relatively better results were obtained for bone and water phantoms. On the other hand, lateral electron scatter modelling with  $TPS_{PB}$  is not sufficient.

$TPS_{CCC}$  overestimates lateral electron scattering for Lung region. Except for this,  $TPS_{CCC}$  gives similar dose distribution to  $MC_{H_2O}$ .

Similar results was obtained for Lung and Water phantom in MC calculation comparisons. The only difference was observed in bone calculations. Relatively low difference (3.0 per cent) was presence between  $MC_{H_2O}$  and  $MC_{DM}$  calculations, while up to 8.0 per cent difference between  $MC_{H_2O}$  and  $MC_{DM}$  calculations due to AAPM Task Group's suggestions.

### 4.3. COMPARISON OF TREATMENT PLANNING SYSTEMS WITH MONTE CARLO SIMULATION IN IMRT OF NON-SMALL CELL LUNG CANCER

#### 4.3.1. IMRT Dose Distributions

IMRT dose distribution obtained from  $TPS_{PB}$  in transverse, coronal and sagittal planes for one of the patients is given in Figure 4.23. The complete set of dose distributions obtained from  $TPS_{PB}$  for all patients are given in Appendix F.

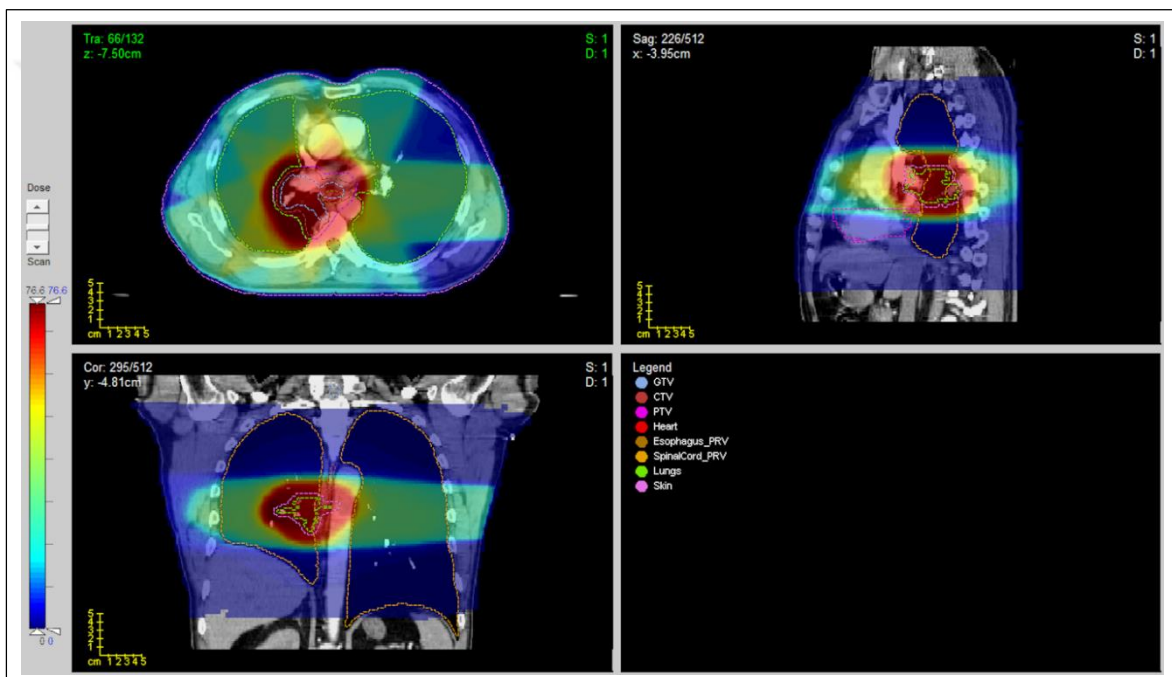


Figure 4.23. Dose distribution of the Patient-9 from  $TPS_{PB}$

Dose Volume Histograms (DVHs) from  $TPS_{PB}$  for the targets and organs at risk (OARs) of the same patient are given in Figure 4.24.

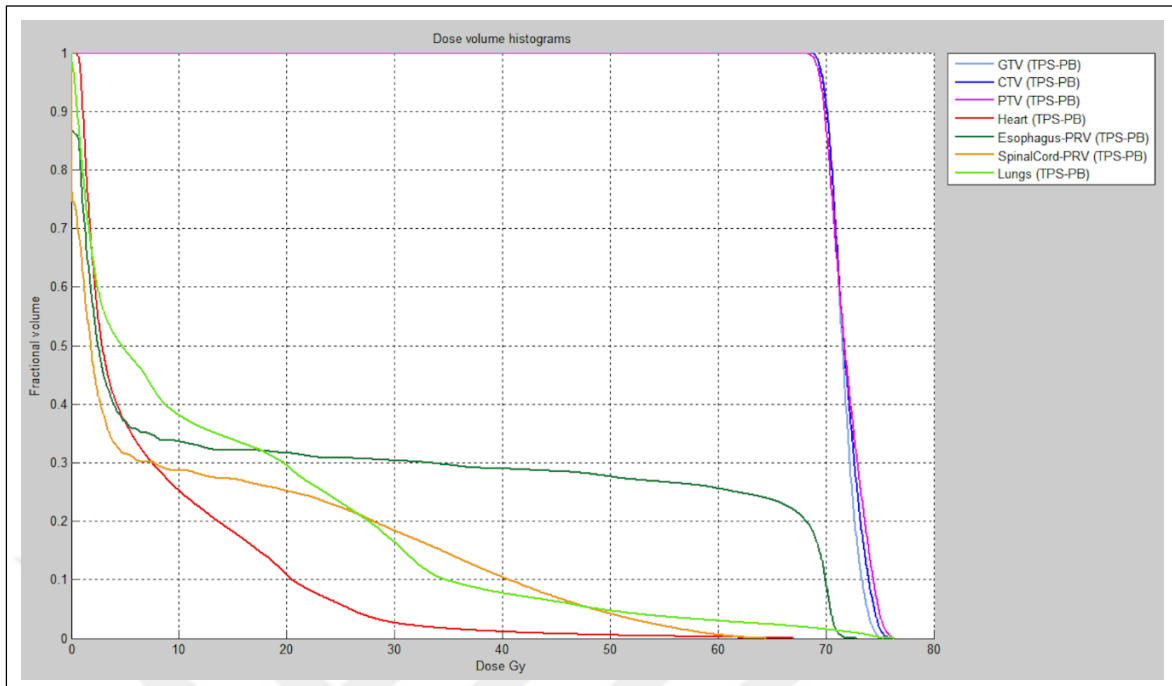


Figure 4.24. DVHs from  $TPS_{PB}$  for targets and OARs of the Patient-9

Dose distributions of the same patient from different calculation methods are given in Figure 4.25. DVHs from different dose distributions for PTV and spinal cord can be seen in Figure 4.26.

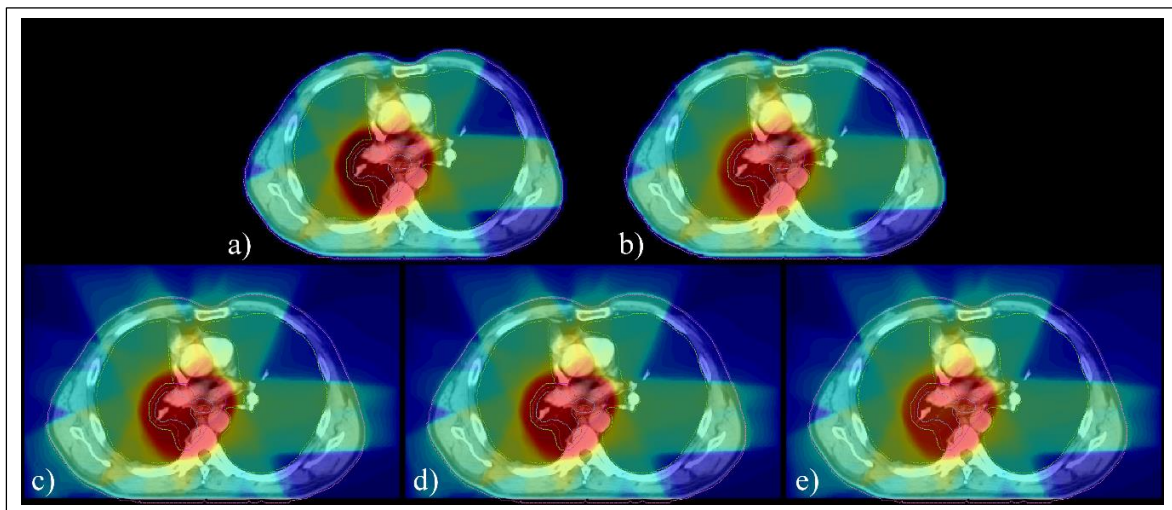


Figure 4.25. Dose distributions of the same patient from different calculation methods:

(a)  $TPS_{PB}$ , (b)  $TPS_{CCC}$ , (c)  $MC_{DM}$ , (d)  $MC_{H2O}$ , (e)  $MC_{DW}$

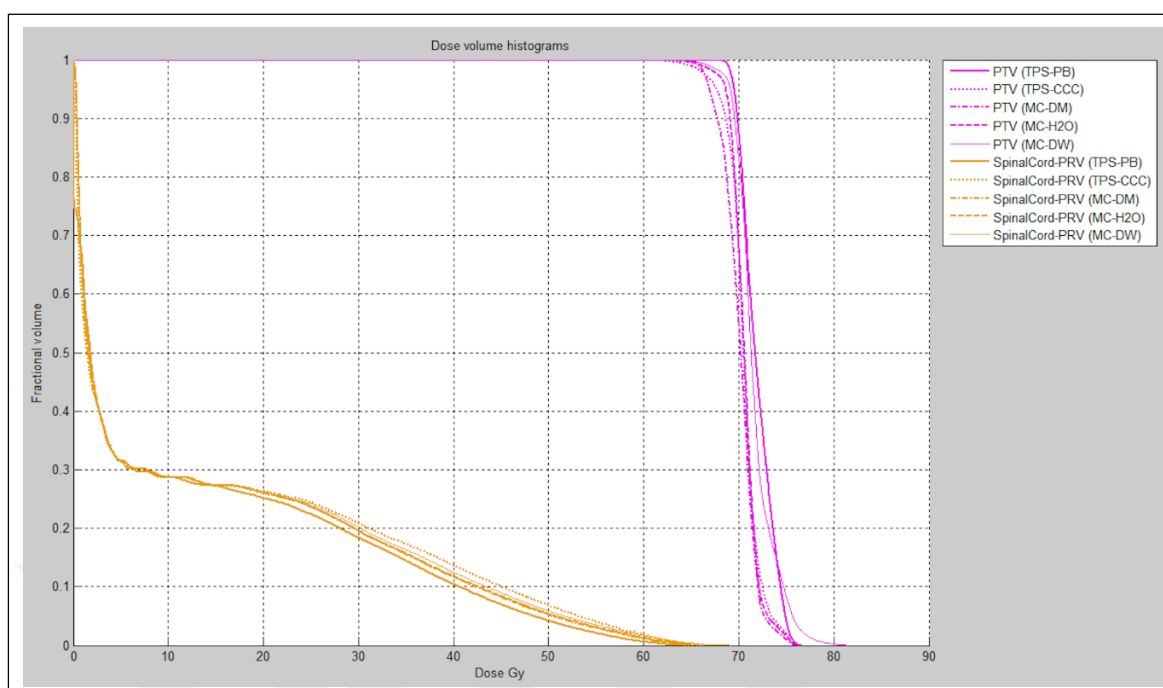


Figure 4.26. DVHs from different dose distributions for PTV and spinal cord

The DVH parameters of target volumes and OARs for all patients were tabulated and given in Appendix G.

#### 4.3.2. Comparison of $MC_{H_2O}$ with TPSs

Graphical comparisons of the DVH parameters for PTV are given in Figure 4.27. Illustrations for GTV and CTV are given in Figure F.1 and Figure F.2 in Appendix H, respectively. It can be seen from the figures that  $TPS_{PB}$  generally overestimates dose parameters in comparison with  $MC_{H_2O}$  for all target volumes. The reason for this is that  $TPS_{PB}$  is not efficient when modelling lateral electron scattering in low density regions as found on Section 4.2. As the PTVs are generally surrounded by the lung tissue for the patient included in this study, doses calculated by  $TPS_{PB}$  are generally higher comparing with  $MC_{H_2O}$ . There was no significant difference observed in HI and CI results.

$TPS_{CCC}$  underestimates  $D_{min}$  and  $D_{93\%}$  values, while other parameters were compatible with  $MC_{H_2O}$  results.

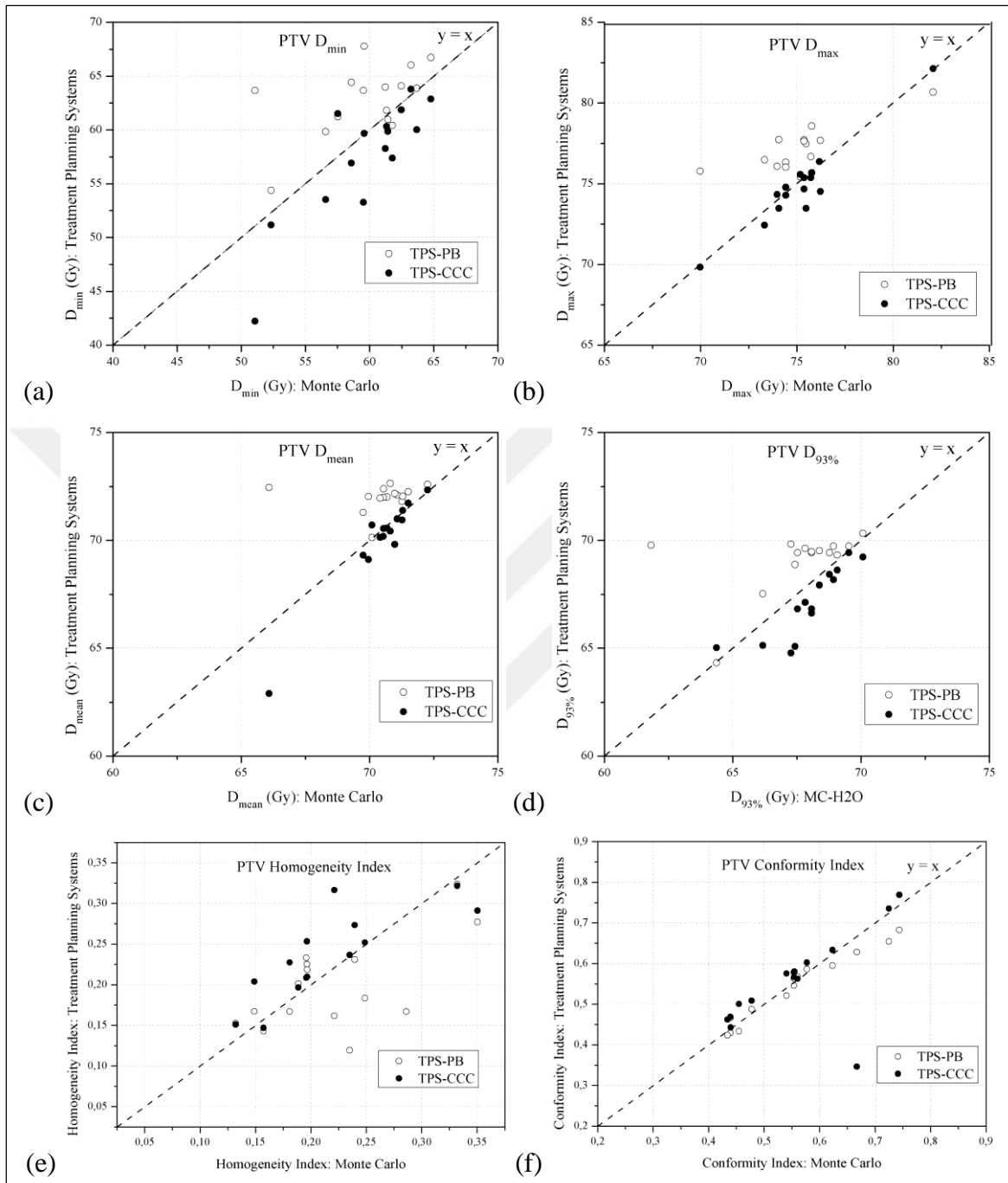


Figure 4.27. Graphical comparisons of the DVH parameters for PTV

Paired-samples T-Test comparison results between  $MC_{H2O}$  and TPSs for target volumes are given in Table 4.2. Statistically significant results are given in bold letters. As seen from the table mean differences between  $MC_{H2O}$  and  $TPS_{PB}$  for all dose parameters are negative that manifests overestimation in  $TPS_{PB}$  calculations. All of these differences were found

statistically significant. Any statistically significant results was observed in HI and CI parameters.

On the other, there was no statistically significant difference between  $MC_{H2O}$  and  $TPS_{CCC}$  except for  $D_{min}$  and  $D_{93\%}$  parameters for PTV. Statistically significant differences were observed between  $TPS_{PB}$  and  $TPS_{CCC}$  as expected.

Table 4.2. Paired-samples T-Test comparison results between  $MC_{H2O}$  and TPSs for target volumes

Parameter	Target	$MC_{H2O} - TPS_{PB}$		$MC_{H2O} - TPS_{CCC}$		$TPS_{PB} - TPS_{CCC}$	
		Mean Difference	P	Mean Difference	P	Mean Difference	P
$D_{min}$	GTV	-1.193	<b>0.007</b>	0.930	0.055	2.123	<b>0.018</b>
	CTV	-2.213	<b>0.018</b>	1.320	0.056	3.533	<b>0.016</b>
	PTV	-3.187	<b>0.004</b>	2.157	<b>0.015</b>	5.343	<b>0.002</b>
$D_{max}$	GTV	-1.550	<b>0.001</b>	0.037	0.818	1.587	<b>0.005</b>
	CTV	-1.807	<b>0.001</b>	0.240	0.221	2.047	<b>0.001</b>
	PTV	-1.937	<b>&lt;0.001</b>	0.353	0.079	2.290	<b>&lt;0.001</b>
$D_{mean}$	GTV	-1.086	<b>&lt;0.001</b>	-0.228	0.143	0.859	<b>0.026</b>
	CTV	-1.344	<b>0.001</b>	0.123	0.568	1.467	<b>0.014</b>
	PTV	-1.510	<b>0.001</b>	0.409	0.094	1.919	<b>0.006</b>
$D_{93\%}$	GTV	-0.967	<b>0.001</b>	0.027	0.902	0.993	<b>0.032</b>
	CTV	-1.290	<b>0.006</b>	0.670	0.077	1.960	<b>0.018</b>
	PTV	-1.533	<b>0.008</b>	1.190	<b>0.007</b>	2.723	<b>0.007</b>
HI	GTV	-0.003	0.460	-0.012	0.072	-0.009	0.365
	CTV	0.009	0.425	-0.016	0.132	-0.025	0.185
	PTV	0.022	0.116	-0.028	0.047	-0.050	<b>0.027</b>
CI	PTV	0.013	0.101	0.0002	0.993	-0.123	0.591

Graphical comparisons of maximum doses for the serial OARs of heart, esophagus and spinal cord are given in Figure 4.28. Other illustrations for these OARs are given in Appendix H. Any major difference was observed between  $MC_{H_2O}$  and TPSs.

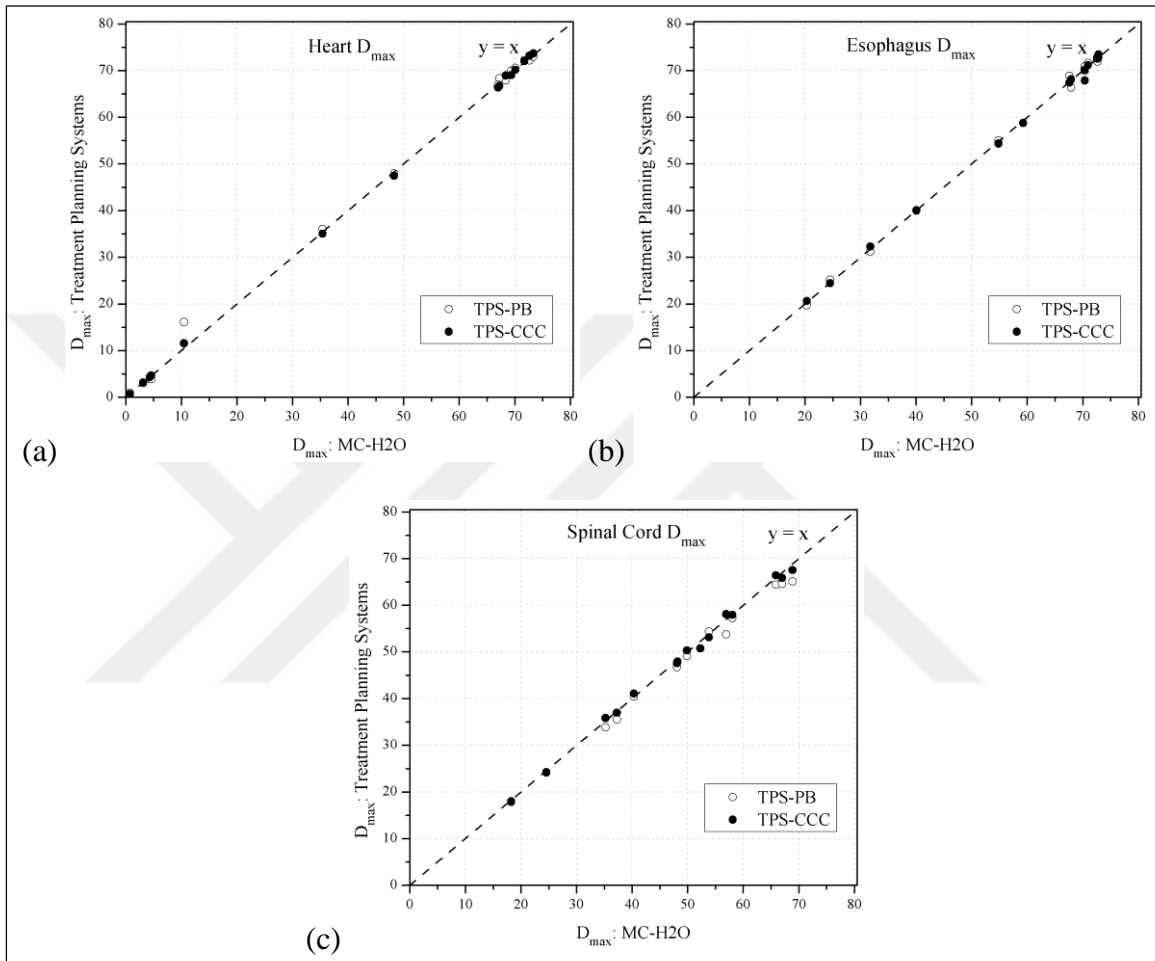


Figure 4.28. Maximum doses for heart, esophagus and spinal cord

Graphical comparisons of DVH parameters for the parallel organ of Lungs are given in Figure 4.29. Any difference was visually observed between  $MC_{H_2O}$  and TPSs.



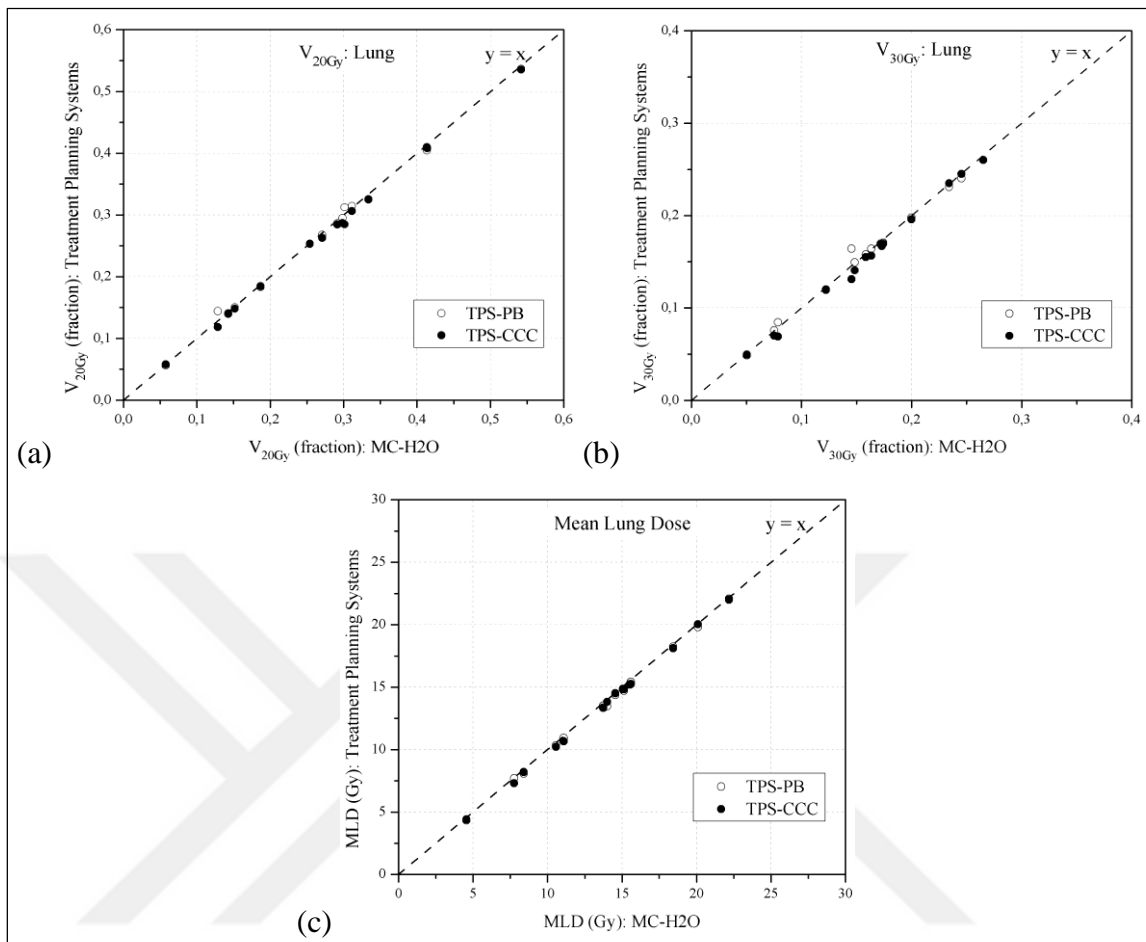


Figure 4.29. Comparisons between MC<sub>H2O</sub> and TPSs for Lungs: (a)  $V_{20Gy}$ , (b)  $V_{30Gy}$ , (c) MLD

Graphical comparisons of the EUDs for OARs are given in Figure 4.30. Underestimation was observed in EUD values of heart, esophagus and spinal cord by TPS<sub>PB</sub> in comparison with MC<sub>H2O</sub>. The difference is larger in spinal cord values. Similar results are observed for NTCP graphs.

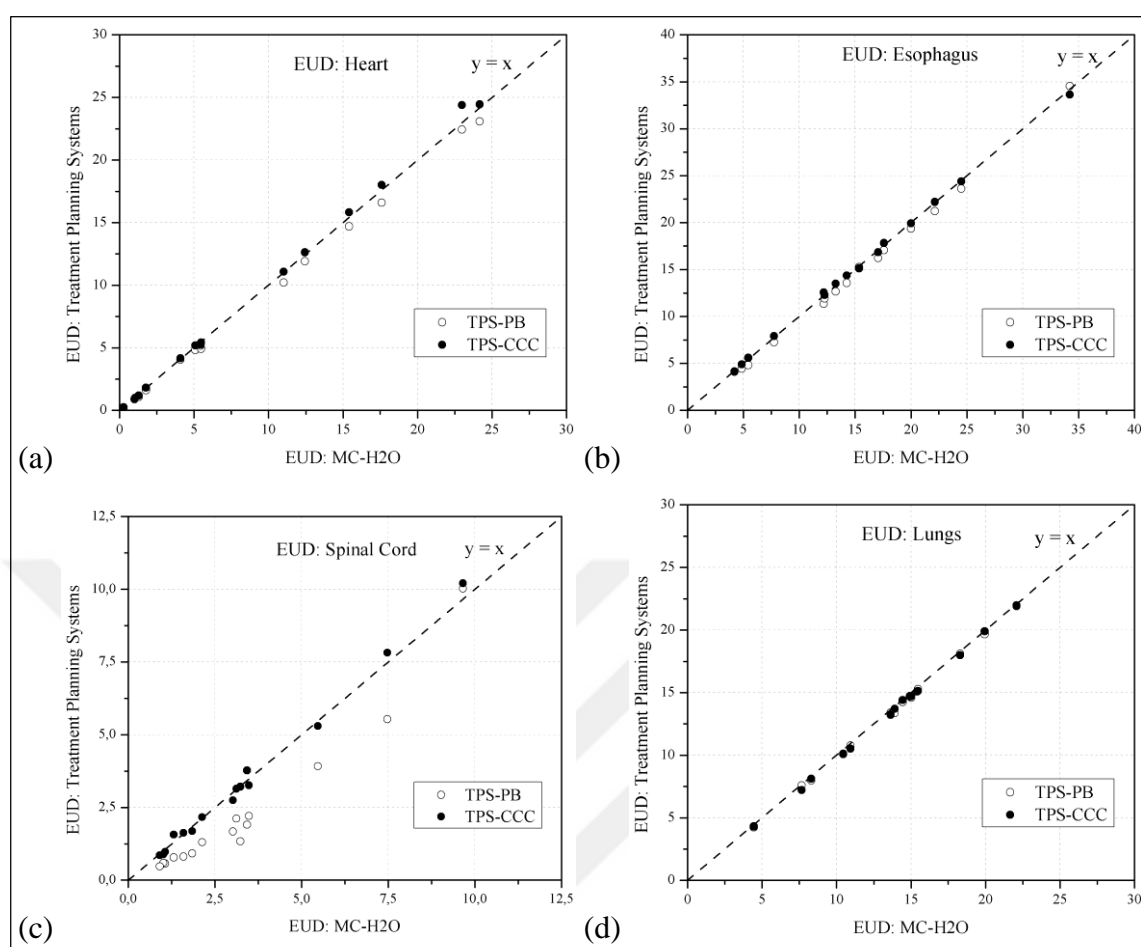


Figure 4.30. Comparisons between MC<sub>H<sub>2</sub>O</sub> and TPSs for EUD (a) Heart, (b) Esophagus, (c) Spinal Cord, (d) Lungs

Paired-samples T-Test comparison results between MC<sub>H<sub>2</sub>O</sub> and TPSs for OARs are given in Table 4.3. Statistically significant results are given in bold letters. As seen from the table mean differences between MC<sub>H<sub>2</sub>O</sub> and TPS<sub>PB</sub> for all dose parameters are mostly positive that exhibits underestimation in TPS<sub>PB</sub> calculations. This behaviour is counter to that observed in target structures. In other words, TPS<sub>PB</sub> calculates higher doses in target organs and lower doses in OARs. Statistically significant differences were obtained for all DVH parameters of spinal cord and most of the parameters of heart. Only the MLD parameter showed statistically significant difference for lungs while no DVH parameter was significant for esophagus. Differences in EUD were statistically significant for all OARs, similarly NTCP values were significantly different except for heart. These differences mainly due to inadequacy in lateral electron scattering modelling of the TPS<sub>PB</sub>.

Table 4.3. Paired-samples T-Test comparison results between MC<sub>H2O</sub> and TPSs for OARs

Parameter	OAR	MC <sub>H2O</sub> – TPS <sub>PB</sub>		MC <sub>H2O</sub> – TPS <sub>CCC</sub>		TPS <sub>PB</sub> – TPS <sub>CCC</sub>	
		Mean Difference	P	Mean Difference	P	Mean Difference	P
D <sub>max</sub>	Heart	-0.413	0.315	-0.010	0.942	0.403	0.280
	Esophagus	0.087	0.644	0.107	0.587	0.020	0.939
	Spinal Cord	1.237	<b>0.001</b>	0.207	0.327	-1.030	<b>0.010</b>
D <sub>33%</sub>	Heart	0.513	<b>0.003</b>	-0.250	0.196	-0.763	<b>0.008</b>
	Esophagus	0.883	0.062	-0.470	<b>0.015</b>	-1.353	<b>0.020</b>
	Spinal Cord	0.570	<b>0.024</b>	-0.260	0.055	-0.830	<b>0.007</b>
D <sub>67%</sub>	Heart	0.280	<b>0.004</b>	-0.083	0.157	-0.363	<b>0.007</b>
	Esophagus	-0.007	0.950	0.000	1.000	0.007	0.955
	Spinal Cord	0.157	<b>0.019</b>	0.057	0.122	-0.100	0.207
V <sub>20Gy</sub>	Lungs	0.002	0.421	0.006	<b>&lt;0.001</b>	0.005	0.085
V <sub>30Gy</sub>	Lungs	0.0002	0.885	0.005	<b>&lt;0.001</b>	0.005	0.078
D <sub>mean</sub>	Lungs	0.243	<b>&lt;0.001</b>	0.264	<b>&lt;0.001</b>	0.022	0.678
EUD	Heart	0.435	<b>&lt;0.001</b>	-0.161	0.133	-0.596	<b>0.002</b>
	Esophagus	0.509	<b>&lt;0.001</b>	-0.008	0.900	-0.516	<b>0.002</b>
	Spinal Cord	0.972	<b>&lt;0.001</b>	-0.033	0.603	-1.004	<b>&lt;0.001</b>
	Lungs	0.255	<b>&lt;0.001</b>	0.262	<b>&lt;0.001</b>	0.007	0.887
NTCP	Heart	0.001	0.311	-0.0003	0.145	-0.001	0.258
	Esophagus	0.005	<b>0.014</b>	0.0003	0.817	-0.005	0.110
	Spinal Cord	0.008	<b>0.032</b>	0.0005	0.745	-0.008	<b>0.040</b>
	Lungs	0.002	<b>&lt;0.001</b>	0.003	<b>&lt;0.001</b>	0.0002	0.794

The main difference between MC<sub>H2O</sub> and TPS<sub>CCC</sub> was seen in lungs. The differences were positive that means that TPS<sub>CCC</sub> underestimates lungs doses. Differences found to be statistically significant. Any statistically significant difference was observed in DVH parameters of the other OARs except for D<sub>33%</sub> of esophagus.

### 4.3.3. Comparison of $MC_{H_2O}$ with the Other MC calculations

As the dose to medium calculation is a different quantity from the dose to water calculation, direct comparison of these two MC calculations is not accurate. Although the comparison results are given in this part of the thesis, it is only for information. The main comparisons was performed between  $MC_{H_2O}$  and  $MC_{DW}$ . Graphical comparisons of the DVH parameters between  $MC_{H_2O}$  and the other MC calculations are given from Figure F.7 to Figure F.15 in Appendix H.

Paired-samples T-Test comparison results between MC calculations for target volumes are given in Table 4.4. Statistically significant results are given in bold letters.

Table 4.4. Paired-samples T-Test comparison results between  $MC_{H_2O}$  and the other MC calculations for target volumes

Parameter	Target	$MC_{H_2O} - MC_{DW}$		$MC_{DM} - MC_{H_2O}$		$MC_{DM} - MC_{DW}$	
		Mean Difference	P	Mean Difference	P	Mean Difference	P
$D_{min}$	GTV	-0.400	<b>0.013</b>	-1.757	<b>&lt;0.001</b>	-2.157	<b>&lt;0.001</b>
	CTV	-0.743	<b>0.022</b>	-0.793	<b>0.024</b>	-1.537	<b>&lt;0.001</b>
	PTV	-0.917	<b>0.022</b>	-0.277	0.397	-1.193	<b>0.001</b>
$D_{max}$	GTV	-1.370	<b>0.001</b>	-0.202	<b>0.049</b>	-1.572	<b>&lt;0.001</b>
	CTV	-1.930	<b>&lt;0.001</b>	0.053	0.605	-1.877	<b>&lt;0.001</b>
	PTV	-2.240	<b>&lt;0.001</b>	0.163	0.095	-2.077	<b>&lt;0.001</b>
$D_{mean}$	GTV	-0.449	<b>&lt;0.001</b>	-0.515	<b>&lt;0.001</b>	-0.964	<b>&lt;0.001</b>
	CTV	-0.485	<b>&lt;0.001</b>	-0.507	<b>&lt;0.001</b>	-0.992	<b>&lt;0.001</b>
	PTV	-0.549	<b>&lt;0.001</b>	-0.501	<b>&lt;0.001</b>	-1.049	<b>&lt;0.001</b>
$D_{93\%}$	GTV	-0.330	<b>&lt;0.001</b>	-0.773	<b>&lt;0.001</b>	-1.103	<b>&lt;0.001</b>
	CTV	-0.367	<b>&lt;0.001</b>	-0.863	<b>&lt;0.001</b>	-1.230	<b>&lt;0.001</b>
	PTV	-0.427	<b>0.001</b>	-0.810	<b>&lt;0.001</b>	-1.237	<b>&lt;0.001</b>
HI	GTV	-0.013	<b>0.010</b>	0.023	<b>0.001</b>	0.010	0.051
	CTV	-0.016	<b>0.012</b>	0.013	<b>0.019</b>	-0.002	0.677
	PTV	-0.017	<b>0.043</b>	0.008	0.165	-0.009	0.123
CI	PTV	0.016	<b>&lt;0.001</b>	0.011	<b>0.002</b>	0.027	<b>&lt;0.001</b>

As seen from the Table 4.4, statistically significant differences were observed between  $MC_{H_2O}$  and  $MC_{DW}$  for all the DVH parameters from target structures. Almost all differences were negative that suggests that  $MC_{DW}$  overestimates the target structure dose values.

Statistically significant differences were observed between  $MC_{DM}$  and the other two dose to water MC calculations as expected.

Paired-samples T-Test comparison results between MC calculations for OARs are given in Table 4.5. Statistically significant results are given in bold letters. Again significant differences were observed between  $MC_{H_2O}$  and  $MC_{DW}$  for the most of the DVH parameters for OARs other than lungs. Relatively compatible results were obtained for lungs.

Differences were statistically significant when comparing  $MC_{DM}$  with the other two dose to water MC calculations.

#### **4.3.4. Concluding Remarks**

In general,  $TPS_{PB}$  overestimates the DVH parameters of target structures, underestimates the DVH parameters of OARs in comparison with  $MC_{H_2O}$ . Almost the same results were obtained with  $TPS_{CCC}$  in comparison with  $MC_{H_2O}$ .

Statistically significant differences were observed between  $MC_{H_2O}$  and  $MC_{DW}$  for all the DVH parameters of both target structures and OARs.

Table 4.5. Paired-samples T-Test comparison results between  $MC_{H_2O}$  and the other MC calculations for OARs

Parameter	OAR	$MC_{H_2O} - MC_{DW}$		$MC_{DM} - MC_{H_2O}$		$MC_{DM} - MC_{DW}$	
		Mean Difference	p	Mean Difference	p	Mean Difference	p
$D_{max}$	Heart	-1.327	<b>0.007</b>	-0.117	0.146	-1.443	<b>0.003</b>
	Esophagus	-0.923	<b>0.002</b>	-0.107	0.128	-1.030	<b>0.001</b>
	Spinal Cord	-2.427	<b>&lt;0.001</b>	-0.640	<b>0.009</b>	-3.067	<b>&lt;0.001</b>
$D_{33\%}$	Heart	-0.407	<b>0.010</b>	-0.193	<b>0.032</b>	-0.600	<b>0.013</b>
	Esophagus	-0.207	<b>0.001</b>	-0.207	<b>0.001</b>	-0.413	<b>&lt;0.001</b>
	Spinal Cord	-0.230	<b>0.017</b>	-0.083	<b>0.006</b>	-0.313	<b>0.010</b>
$D_{67\%}$	Heart	-0.163	<b>0.036</b>	-0.080	<b>0.030</b>	-0.243	<b>0.030</b>
	Esophagus	0.003	0.670	-0.023	<b>0.014</b>	-0.020	0.082
	Spinal Cord	-0.023	<b>0.014</b>	-0.017	<b>0.019</b>	-0.040	<b>0.003</b>
$V_{20Gy}$	Lungs	0.0003	<b>0.045</b>	-0.001	<b>0.003</b>	-0.0004	<b>&lt;0.001</b>
$V_{30Gy}$	Lungs	0.0001	0.429	-0.0004	<b>0.002</b>	-0.0003	<b>0.001</b>
$D_{mean}$	Lungs	0.006	0.099	-0.033	<b>&lt;0.001</b>	-0.027	<b>&lt;0.001</b>
EUD	Heart	-0.278	<b>0.018</b>	-0.137	<b>0.013</b>	-0.415	<b>0.015</b>
	Esophagus	-0.125	<b>&lt;0.001</b>	-0.117	<b>&lt;0.001</b>	-0.242	<b>&lt;0.001</b>
	Spinal Cord	-0.064	<b>0.001</b>	-0.036	<b>&lt;0.001</b>	-0.100	<b>&lt;0.001</b>
	Lungs	0.006	0.085	-0.033	<b>&lt;0.001</b>	-0.027	<b>&lt;0.001</b>
NTCP	Heart	-0.003	0.307	-0.001	0.316	-0.005	0.309
	Esophagus	-0.003	<b>0.002</b>	-0.002	<b>0.003</b>	-0.005	<b>0.002</b>
	Spinal Cord	-0.009	<b>0.018</b>	-0.002	<b>0.008</b>	-0.012	<b>0.014</b>
	Lungs	0.00004	0.647	-0.001	<b>0.019</b>	0.000	<b>0.005</b>

## 5. CONCLUSION

The treatment planning systems are widely used in the radiation oncology departments. The systems calculate dose distributions in patient using variety of calculation algorithms. These algorithms may fail especially in the conditions of lateral electronic disequilibrium. The MC method is generally considered to be the gold standard for determining dose distributions. For this reason, it has been used by many authors to benchmark the accuracy of different dose calculation techniques [10-16].

In this study, the 6-MV photon beam of Elekta Synergy MLCi treatment head (Elekta Oncology Systems, Crawley, UK) installed at Gülhane Military Medical Academy, Department of Radiation Oncology was modelled using EGSnrc/BEAMnrc (version 2010) Monte Carlo code system. Incident electron beam characteristics were optimized using ionization chamber measurement in water phantom for  $10 \times 10 \text{ cm}^2$  open field and SSD=100 cm. using these characteristics, simulation validation was performed using ionization chamber measurements for field sizes other than  $10 \times 10 \text{ cm}^2$ . The other dosimetric parameters, such as, interleaf leakage, MLC transmission and output factor, were also validated. A good agreement was obtained between ionization chamber measurements and MC calculations. The differences were less than two per cent for all field sizes.

As a second step, dose distributions obtained from two different TPSs and MC simulation in virtual slab phantoms that include tissue inhomogeneity were compared. TPS with PB calculation algorithm made huge calculation errors up to 10 per cent in lung phantom, while relatively better results were obtained for bone and water phantoms. TPS with CCC calculation algorithm produced similar dose distribution with MC calculations except for lung phantom where the TPS overestimates the lateral electron scattering. The findings were in accordance with data from the literature. Differences were observed between MC calculations as expected.

In the final part of the thesis, dose distributions obtained from TPSs and MC simulations were compared in real patient situation of IMRT of lung cancer. Exactly the same IMRT plans were used in all the calculations. Dose distributions were compared in terms of the

DVH parameters. Statistically significant differences in almost all parameters were observed when comparing  $\text{TPS}_{\text{PB}}$  with MC. Observed differences were not significant in comparisons between  $\text{TPS}_{\text{CCC}}$  and MC. It can be concluded from this part of the thesis that  $\text{TPS}_{\text{PB}}$  is not suitable for IMRT planning of lung cancer patients.

According to our best knowledge, it was the first attempt to MC simulate a real clinical linac in our country. The MC model produced in this thesis gives the ability of MC plan verification to the clinic. The model can also be used for dose calculations in the situations of small fields and tissue inhomogeneities where  $\text{TPS}_{\text{PB}}$  fails.





## REFERENCES

1. N. Reynaert, S. C. Van der Marck, D. R. Schaart, W. Van der Zee, C. Van Vliet-Vroegindeweij, M. Tomsej, J. Jansen, B. Heijmen, M. Coghe, and De Wagter C., Monte Carlo Treatment Planning for Photon and Electron Beams, *Radiation Physics and Chemistry*, 76:643-686, 2007.
2. J. W. Wong and J. A. Purdy, On Methods of Inhomogeneity Corrections for Photon Transport, *Medical Physics*, 17:807-814, 1990.
3. K. J. Cassell, P. A. Hobday, and R. P. Parker, The Implementation of a Generalised Batho Inhomogeneity Correction for Radiotherapy Planning with Direct Use of CT Numbers, *Physics in Medicine and Biology*, 26:825-833, 1981.
4. M. R. Sontag and J. R. Cunningham, The Equivalent Tissue-Air Ratio Method for Making Absorbed Dose Calculations in Heterogeneous Medium, *Radiology*, 129:787-794, 1978.
5. N. Papanikolaou, T. R. Mackie, C. Meger-Wells, M. Gehring, and P. Reckwerdt, Investigation of the Convolution Method for Polyenergetic Spectra, *Medical Physics*, 20:1327-1336, 1993.
6. A. Ahnesjö, P. Andreo, and A. Brahme, Calculation and Application of Point Spread Functions for Treatment Planning with High Energy Photon Beams, *Acta Oncologica*, 26:46-56, 1987.
7. L. Tillikainen, H. Helminen, T. Torsti, S. Siljamäki, J. Alakuijala, J. Pyry, and W. Ulmer, A 3D Pencil-Beam-Based Superposition Algorithm for Photon Dose Calculation in Heterogeneous Media, *Physics in Medicine and Biology*, 53:3821-3839, 2008.

8. P. Andreo, Monte Carlo Techniques in Medical Radiation Physics, *Physics in Medicine and Biology*, 36:861-920, 1991.
9. B. Disher, G. Hajdok, S. Gaede, and Battista J. J., An In-Depth Monte Carlo Study of Lateral Electron Disequilibrium for Small Fields in Ultra-Low Density Lung: Implications for Modern Radiation Therapy, *Physics in Medicine and Biology*, 57:1543-1559, 2012.
10. L. R. Aarup, A. E. Nahum, C. Zacharatou, T. Juhler-Nøttrup, T. Knöös, H. Nyström, L. Specht, E. Wieslander, and S. S. Korreman, The Effect of Different Lung Densities on the Accuracy of Various Radiotherapy Dose Calculation Methods: Implications for Tumour Coverage, *Radiotherapy and Oncology*, 91:405-414, 2009.
11. A. Fogliata, E. Vanetti, D. Albers, C. Brink, A. Clivio, T. Knöös, G. Nicolini, and L. Cozzi, On the Dosimetric Behaviour of Photon Dose Calculation Algorithms in the Presence of Simple Geometric Heterogeneities: Comparison with Monte Carlo Calculations, *Physics in Medicine and Biology*, 52:1363-1385, 2007.
12. F. Hasenbalg, H. Neuenschwander, R. Mini, and E. J. Born, Collapsed Cone Convolution and Analytical Anisotropic Algorithm Dose Calculations Compared to VMC++ Monte Carlo Simulations in Clinical Cases, *Physics in Medicine and Biology*, 52:3679-3691, 2007.
13. V. Panettieri, B. Wennberg, G. Gagliardi, M. A. Duch, M. Ginjaume, and I. Lax, SBRT of Lung Tumours: Monte Carlo Simulation with PENELOPE of Dose Distributions Including Respiratory Motion and Comparison with Different Treatment Planning Systems, *Physics in Medicine and Biology*, 52:4265-4281, 2007.
14. J. C. Chow, M. K. Leung, and J. Van Dyk, Variations of Lung Density and Geometry on Inhomogeneity Correction Algorithms: a Monte Carlo Dosimetric Evaluation, *Medical Physics*, 36:3619-3630, 2009.

15. A. O. Jones and I. J. Das, Comparison of Inhomogeneity Correction Algorithms in Small Photon Fields, *Medical Physics*, 32:766-776, 2005.
16. P. Carrasco, N. Jornet, M. A. Duch, L. Weber, M. Ginjaume, T. Eudaldo, D. Jurado, A. Ruiz, and M. Ribas, Comparison of Dose Calculation Algorithms in Phantoms with Lung Equivalent Heterogeneities Under Conditions of Lateral Electronic Disequilibrium, *Medical Physics*, 31:2899-2911, 2004.
17. T. R. Mackie, E. el-Khatib, J. Battista, J. Scrimger, J. Van Dyk, and J. R. Cunningham, Lung Dose Corrections for 6- and 15-MV X Rays, *Medical Physics*, 12:327-332, 1985.
18. M. Engelsman, E. M. Damen, P. W. Koken, A. A. Van 't Veld, K. M. Van Ingen, and B. J. Mijnheer, Impact of Simple Tissue Inhomogeneity Correction Algorithms on Conformal Radiotherapy of Lung Tumours, *Radiotherapy and Oncology*, 60:299-309, 2001.
19. T. Knöös, E. Wieslander, L. Cozzi, C. Brink, A. Fogliata, D. Albers, H. Nyström, and S. Lassen, Comparison of Dose Calculation Algorithms for Treatment Planning in External Photon Beam Therapy for Clinical Situations, *Physics in Medicine and Biology*, 51:5785-5807, 2006.
20. U. Haedinger, T. Krieger, M. Flentje, and J. Wulf, Influence of Calculation Model on Dose Distribution in Stereotactic Radiotherapy for Pulmonary Targets, *International Journal of Radiation Oncology, Biology, Physics*, 61:239-249, 2005.
21. C. L. Hartmann Siantar, R. S. Walling, T. P. Daly, B. Faddegon, N. Albright, P. Bergstrom, A. F. Bielajew, C. Chuang, D. Garrett, R. K. House, D. Knapp, D. J. Wiczorek, and L. J. Verhey, Description and Dosimetric Verification of the PEREGRINE Monte Carlo Dose Calculation System for Photon Beams Incident on a Water Phantom, *Medical Physics*, 28:1322-1337, 2001.

22. J. J. DeMarco, T. D. Solberg, and J. B. Smathers, A CT-Based Monte Carlo Simulation Tool for Dosimetry Planning and Analysis, *Medical Physics*, 25:1-11, 1998.
23. D. W. O. Rogers and A. F. Bielajew, Monte Carlo Techniques of Electron and Photon Transport for Radiation Dosimetry, *Dosimetry of Ionization Radiation*, 3:427-539, 1990.
24. K. Aljarrah, G. C. Sharp, T. Neicu, and S. B. Jiang, Determination of the Initial Beam Parameters in Monte Carlo Linac Simulation, *Medical Physics*, 33:850-858, 2006.
25. A. Tzedakis, J. E. Damilakis, M. Mazonakis, J. Stratakis, H. Varveris, and N. Gourtsoyiannis, Influence of Initial Electron Beam Parameters on Monte Carlo Calculated Absorbed Dose Distributions for Radiotherapy Photon Beams, *Medical Physics*, 31:907-913, 2004.
26. C.-M. Ma and J. Li, Dose Specification for Radiation Therapy: Dose to Water Or Dose to Medium?, *Physics in Medicine and Biology*, 56:3073–3089, 2011.
27. J. V. Siebers, P. J. Keall, A. E. Nahum, and R. Mohan, Converting Absorbed Dose to Medium to Absorbed Dose to Water for Monte Carlo Based Photon Beam Dose Calculations, *Physics in Medicine and Biology*, 45:983-995, 2000.
28. I. J. Chetty, B. Curran, J. E. Cygler, J. J. DeMarco, G. Ezzell, B. A. Faddegon, I. Kawrakow, P. J. Keall, H. Liu, C. M. Ma, D. W. O. Rogers, J. Seuntjens, D. Sheikh-Bagheri, and J. V. Siebers, Report of the AAPM Task Group No. 105: Issues Associated with Clinical Implementation of Monte Carlo-Based Photon and Electron External Beam Treatment Planning, *Medical Physics*, 34:4818-4853, 2007.
29. C. M. Ma and S. B. Jiang, Monte Carlo Modelling of Electron Beams From Medical Accelerators, *Physics in Medicine and Biology*, 44:R157-R189, 1999.

30. C. M. Ma, E. Mok, A. Kapur, T. Pawlicki, D. Findley, S. Brain, K. Forster, and A. L. Boyer, Clinical Implementation of a Monte Carlo Treatment Planning System, *Medical Physics*, 26:2133-2143, 1999.
31. P. Francescon, C. Cavedon, S. Reccanello, and S. Cora, Photon Dose Calculation of a Three-Dimensional Treatment Planning System Compared to the Monte Carlo Code BEAM, *Medical Physics*, 27:1579-1587, 2000.
32. MC. Lee, S. B. Jiang, and C. M. Ma, Monte Carlo and Experimental Investigations of Multileaf Collimated Electron Beams for Modulated Electron Radiation Therapy, *Medical Physics*, 27:2708-2718, 2000.
33. C. M. Ma, T. Pawlicki, S. B. Jiang, J. S. Li, J. Deng, E. Mok, A. Kapur, L. Xing, L. Ma, and A. L. Boyer, Monte Carlo Verification of IMRT Dose Distributions From a Commercial Treatment Planning Optimization System, *Physics in Medicine and Biology*, 45:2483-2495, 2000.
34. A. Bielajew, The Monte Carlo Simulation of Radiation Transport, In: P. Mayles, A. Nahum, and J. C. Rosenwald, editors, *Handbook of Radiotherapy Physics: Theory and Practice*, pages 75-87. CRC Press, Boca Raton, FL, 2007.
35. M. J. Berger, Monte Carlo Calculation of the Penetration and Diffusion of Fast Charged Particles, *Methods in Computational Physics*, 1:135-215, 1963.
36. H. A. Bethe, Theory of Passage of Swift Corpuscular Rays Through Matter, *Annalen der Physik*, 5:325, 1930.
37. H. A. Bethe, Scattering of Electrons, *Zeitschrift für Physik*, 76:293, 1932.
38. F. Bloch, Stopping Power of Atoms with Several Electrons, *Zeitschrift für Physik*, 81:363, 1933.

39. International Commission on Radiation Units and Measurements, Radiation Dosimetry; Electron Beams with Energies Between 1 and 50 MeV, ICRU Report No. 35, ICRU, Bethesda, MD, 1984.
40. International Commission on Radiation Units and Measurements, Stopping Powers for Electrons and Positrons, ICRU Report No. 37, ICRU, Bethesda, MD, 1984.
41. L. Landau, On the Energy Loss of Fast Particles by Ionisation, *Journal of Physics - U.S.S.R.*, 8:201, 1944.
42. P. V. Vavilov, Ionisation Losses of High-Energy Heavy Particles, *Soviet Physics - JETP*, 5:749, 1957.
43. G. Z. Moliere, Theorie der Streuung schneller geladener Teilchen. I. Einzelstreuung am abgeschirmten Coulomb-Feld, *Zeitschrift für Naturforschung*, 2a:133-145, 1947.
44. G. Z. Moliere, Theorie der Streuung schneller geladener Teilchen.II. Mehrfach- und Vielfachstreuung, *Zeitschrift für Naturforschung*, 3a:78-97, 1948.
45. L. Eyles, Multiple Scattering with Energy Loss, *Physical Review*, 74:1534, 1948.
46. H. A. Bethe, Moliere's Theory of Multiple Scattering, *Physical Review*, 89:1256-1266, 1953.
47. S. A. Goudsmit and J. L. Saunderson, Multiple Scattering of Electrons, *Physical Review*, 57:24-29, 1940.
48. S. A. Goudsmit and J. L. Saunderson, Multiple Scattering of Electrons II, *Physical Review*, 58:36-42, 1940.

49. R. Mayol and F. Salvat, Total and Transport Cross Sections for Elastic Scattering of Electrons by Atoms, *Atomic Data and Nuclear Data Tables*, 65:55-154, 1997.
50. E. W. Larsen, A Theoretical Derivation of the Condensed History Algorithm, *Annals of Nuclear Energy*, 19:701-714, 1992.
51. A. F. Bielajew and D. W. O. Rogers, PRESTA: The Parameter Reduced Electron-Step Transport Algorithm for Electron Monte Carlo Transport, *Nuclear Instruments and Methods*, B18:165-181, 1987.
52. S. M. Seltzer, Electron-Photon Monte Carlo Calculations: The ETRAN Code, *The International Journal of Applied Radiation and Isotopes*, 42:917-941, 1991.
53. J. M. Fernandez-Varea, R. Mayol, J. Baro, and F. Salvat, On the Theory and Simulation of Multiple Elastic Scattering of Electrons, *Nuclear Instruments and Methods*, B73:447-473, 1993.
54. I. Kawrakow and A. F. Bielajew, On the Condensed History Technique for Electron Transport, *Nuclear Instruments and Methods*, B142:253-280, 1998.
55. A. E. Nahum, Condensed-History Monte-Carlo Simulation for Charged Particles: What Can It Do for Us?, *Radiation and Environmental Biophysics*, 38:163-173, 1999.
56. I. Kawrakow and D.W.O. Rogers, The EGSnrc Code System: Monte Carlo Simulation of Electron and Photon Transport, NRCC Report PIRS-701, National Research Council of Canada, Ottawa, 2006.
57. D. W. Rogers, B. A. Faddegon, G. X. Ding, C. M. Ma, J. We, and T. R. Mackie, BEAM: a Monte Carlo Code to Simulate Radiotherapy Treatment Units, *Medical Physics*, 22:503-524, 1995.

58. B. R. B. Walters, I. Kawrakow, and D. W. O. Rogers, DOSXYZnrc User's Manual, Report PIRS-794 RevB, National Research Council of Canada, Ottawa, 2009.
59. A. Nahum, Linear Accelerators, In: P. Mayles, A. Nahum, and J. C. Rosenwald, editors, *Handbook of Radiotherapy Physics: Theory and Practice*, pages 197-239. CRC Press, Boca Raton, FL, 2007.
60. F. M. Khan and J. P. Gibbons, *Khan's The Physics of Radiation Therapy*, 5th ed., Lippincott Williams & Wilkins, Philadelphia, PA, 2014.
61. International Commission on Radiation Units and Measurements, Prescribing, Recording, and Reporting Photon Beam Therapy, ICRU Report 50, ICRU, Bethesda, MD, 1993.
62. International Commission on Radiation Units and Measurements, Prescribing, Recording, and Reporting Photon Beam Therapy (Supplement to ICRU Report 50), ICRU Report 62, ICRU, Bethesda, MD, 1999.
63. M. Bidmead and J. C. Rosenwald, Dose Evaluation of Treatment Plans, In: P. Mayles, A. Nahum, and J. C. Rosenwald, editors, *Handbook of Radiotherapy Physics: Theory and Practice*, pages 719-729. CRC Press, Boca Raton, FL, 2007.
64. J. T. Lyman, Complication Probability as Assessed From Dose-Volume Histograms, *Radiation Research*, 104:S13-S19, 1985.
65. G. J. Kutcher and C. Burman, Calculation of Complication Probability Factors for Non Uniform Normal Tissue Irradiation: the Effective Volume Method, *International Journal of Radiation Oncology Biology Physics*, 16:1623-1630, 1989.
66. Elekta Oncology Systems, MLCi Radiation Head Technical Data, In: *Clinical Mode User Manual for Desktop Pro R6.0x, R6.1x, and R6.2x*. Elekta Oncology Systems, Crawley, UK, 2006.



67. D. W. O. Rogers, B. A. Faddegon, G. X. Ding, C.-M. Ma, J. We, and T. R. Mackie, BEAM: a Monte Carlo Code to Simulate Radiotherapy Treatment Units, *Medical Physics*, 22:503-524, 1995.
68. I. Kawrakow, Accurate Condensed History Monte Carlo Simulation of Electron Transport: I. EGSnrc, the New EGS4 Version, *Medical Physics*, 27:485-498, 2000.
69. D. W. O. Rogers, B. R. B. Walters, and I. Kawrakow, BEAMnrc User's Manual, Report PIRS-509(A) revL, National Research Council of Canada, Ottawa, 2009.
70. I. Kawrakow, D. W. O. Rogers, and B. R. B. Walters, Large Efficiency Improvements in BEAMnrc Using Directional Bremsstrahlung Splitting, *Medical Physics*, 31:2883-2898, 2004.
71. D. Sheikh-Bagheri and D. W. O. Rogers, Sensitivity of Megavoltage Photon Beam Monte Carlo Simulations to Electron Beam and Other Parameters, *Medical Physics*, 29:379-390, 2002.
72. C.-M. Ma and D. W. O. Rogers, BEAMDP as a General-Purpose Utility, Report PIRS-0509(E) revA, National Research Council of Canada, Ottawa, 2006.
73. I. Kawrakow and B. R. B. Walters, Efficient Photon Beam Dose Calculations using DOSXYZnrc with BEAMnrc, *Medical Physics*, 33:3046-3056, 2006.
74. E. Spezi, D. G. Lewis, and C. W. Smith, A DICOM-RT-Based Toolbox for the Evaluation and Verification of Radiotherapy Plans, *Physics in Medicine and Biology*, 47:4223-4232, 2002.
75. J. O. Deasy, A. I. Blanco, and V. H. Clark, CERR: A Computational Environment for Radiotherapy Research, *Medical Physics*, 30:979-985, 2003.

76. K. Aljarrah, G. C. Sharp, T. Neicu, and S. B. Jiang, Determination of the Initial Beam Parameters in Monte Carlo Linac Simulation, *Medical Physics*, 33:850-858, 2006.
77. A. Nahum, Monte-Carlo Based Patient Dose Calculation, In: P. Mayles, A. Nahum, and J. C. Rosenwald, editors, *Handbook of Radiotherapy Physics: Theory and Practice*, pages 603-631. CRC Press, Boca Raton, FL, 2007.
78. Van Dyk J., R. B. Barnett, J. E. Cygler, and P. C. Shragge, Commissioning and Quality Assurance of Treatment Planning Computers, *International Journal of Radiation Oncology Biology Physics*, 26:261-273, 1993.
79. B. Vanderstraeten, N. Reynaert, L. Paelinck, I. Madani, C. De Wagter, W. De Gersem, W. De Neve, and H. Thierens, Accuracy of Patient Dose Calculation for Lung IMRT: a Comparison of Monte Carlo, Convolution/Superposition, and Pencil Beam Computations, *Medical Physics*, 33:3149-3158, 2006.
80. Radiation Oncology Therapy Group RTOG. RTOG 0117 Protocol Information, <https://www.rtog.org/ClinicalTrials/ProtocolTable/StudyDetails.aspx?action=openFile&FileID=10603> [retrieved 05 January 2012]
81. C. Burman, G. J. Kutcher, B. Emami, and M. Goitein, Fitting of Normal Tissue Tolerance Data to an Analytic Function, *International Journal of Radiation Oncology, Biology and Physics*, 21:123-135, 1991.
82. J. Belderbos, W. Heemsbergen, M. Hoogeman, K. Pengel, M. Rossi, and J. Lebesque, Acute Esophageal Toxicity in Non-Small Cell Lung Cancer Patients After High Dose Conformal Radiotherapy, *Radiotherapy and Oncology*, 75:157-164, 2005.
83. Y. Seppenwoolde, J. V. Lebesque, K. de Jaeger, J. S. A. Belderbos, L. J. Boersma, C. Schilstra, G. T. Henning, and J. A. Hayman, Comparing Different NTCP Models that Predict the Incidence of Radiation, *International Journal of Radiation Oncology, Biology and Physics*, 55:724-735, 2003.

84. F. Haryanto, M. Fippel, W. Laub, O. Dohm, and F. Nüsslin, Investigation of Photon Beam Output Factors for Conformal Radiation Therapy—Monte Carlo Simulations and Measurements, *Physics in Medicine and Biology*, 47:N133-N143, 2002.
85. A. J. Scott, A. E. Nahum, and J. D. Fenwick, Using a Monte Carlo Model to Predict Dosimetric Properties of Small Radiotherapy Photon Fields, *Medical Physics*, 35:4671-4684, 2008.
86. M. Heydarian, P. W. Hobany, and A. H. Beddoe, A Comparison of Dosimetry Techniques in Stereotactic Radiosurgery, *Physics in Medicine and Biology*, 41:93-110, 1996.
87. M. S. Huq, I. J. Das, T. Steinberg, and J. M. Galvin, A Dosimetric Comparison of Various Multileaf Collimators, *Physics in Medicine and Biology*, 47:N159-N170, 2002.
88. N. Reynaert, S. C. Van der Marck, D.R. Schaart, W. Van der Zee, C. Van Vliet-Vroegindewij, M. Tomsej, J. Jansen, B. Heijmen, M. Coghe, and C. De Wagter, Monte Carlo Treatment Planning for Photon and Electron Beams, *Radiation Physics and Chemistry*, 76:643-686, 2007.
89. P. Carrasco, N. Jornet, M. A. Duch, L. Weber, M. Ginjaume, T. Eudaldo, D. Jurado, A. Ruiz, and M. Ribas, Comparison of Dose Calculation Algorithms in Phantoms with Lung Equivalent Heterogeneities Under Conditions of Lateral Electronic Disequilibrium, *Medical Physics*, 31:2899-2911, 2004.
90. C. M. Ma and J. Li, Dose Specification for Radiation Therapy: Dose to Water Or Dose to Medium?, *Physics in Medicine and Biology*, 56:3073-3089, 2011.
91. A. Nahum, Interactions of Charged Particles with Matter, In: P. Mayles, A. Nahum, and J. C. Resenwald, editors, *Handbook of Radiotherapy Physics: Theory and Practice*, pages 35-55. CRC Press, Boca Raton, FL, 2007.

92. R. D. Evans, *The Atomic Nucleus*, McGraw Hill, New York, NY, 1955.
93. International Commission on Radiation Units and Measurements, Linear Energy Transfer, ICRU Report No. 16, ICRU, Bethesda, MD, 1970.
94. A. Nahum, The Interactions of Electrons with Matter, Vol. I. Energy Losses, Stopping Power and Range, In: A. Nahum, editor, *The Computation of Dose Distributions in Electron Beam Radiotherapy*, pages 27-55. Medical Physics Publishing, Madison, WI, 1985.
95. M. J. Berger and S. M. Selter, Tables of Energy Losses and Ranges of Electrons and Positrons, NASA SP-3012, NASA (National Aeronautics and Space Administration), Washington, DC, 1964.
96. E. Fermi, The Ionisation Loss of Energy in Gases and in Condensed Materials, *Physical Review*, 57(6):485-493, 1940.
97. R. M. Sternheimer, Interactions of Radiation in Matter, In: L. C. L. Yuan and C. S. Wu, editors, *Methods of Experimental Physics*, pages 1-89. Academic Press, New York, NY, 1961.
98. F. H. Attix, *Introduction to Radiological Physics and Radiation Dosimetry*, Wiley, New York, NY, 1986.
99. M. J. Berger and R. Wang, Multiple-Scattering Angular Deflections and Energy-Loss Straggling, In: T. M. Jenkins, W. R. Nelson, A. Rindi, A. E. Nahum, and D. W. O. Rogers, editors, *Monte Carlo Transport of Electrons and Photons*, pages 21-56. Plenum, New York, NY, 1988.
100. A. E. Nahum and A. Brahme, Electron Depth-Dose Distributions in Uniform and Nonuniform Media, In: A. E. Nahum, editor, *The Computation of Dose Distributions*

- in Electron Beam Radiotherapy*, pages 98-127. Medical Physics Publishing, Madison, WI, 1985.
101. S. M. Seltzer, J. H. Hubbel, and M. J. Berger, National and International Standardization of Radiation Dosimetry, Vol. 2, IAEA-SN-222/05, IAEA (International Atomic Energy Agency), Vienna, 1978.
  102. D. Dance and G. A. Carlsson, Interactions of Photons with Matter, In: P. Mayles, A. Nahum, and J. C. Rosenwald, editors, *Handbook of Radiotherapy Physics: Theory and Practice*, pages 57-74. CRC Press, Boca Raton, FL, 2007.
  103. M. J. Berger and J. H. Hubbell, XCOM: Photon Cross Sections on a Personal Computer, NBSIR 87-3597, National Bureau of Standards, Washington, DC, 1987.
  104. O Klein and Y. Nishina, U"ber die Streuung von Strahlung durch freie Elektronen nach der neuen relativistischen Quantendynamik von Dirac, *Zeitschrift f"ur Physik*, 52:853-868, 1929.
  105. W. Greiner and J. Reinhardt, *Quantum Electrodynamics*, 3rd ed., Springer, Berlin, 2003.
  106. A. Nahum, Principles and Basic Concepts in Radiation Dosimetry, In: P. Mayles, A. Nahum, and J. C. Rosenwald, editors, *Handbook of Radiotherapy Physics: Theory and Practice*, pages 89-115. CRC Press, Boca Raton, FL, 2007.
  107. International Commission on Radiation Units and Measurements, Radiation Quantities and Units, ICRU Report No. 33, ICRU, Bethesda, MD, 1980.
  108. International Commission on Radiation Units and Measurements, Fundamental Quantities and Units for Ionising Radiation, ICRU Report No. 60, ICRU, Bethesda, MD, 1998.

109. J. R. Greening, *Fundamentals of Radiation Dosimetry*, Adam Hilger, Bristol, 1981.
110. F. H. Attix, The Partition of Kerma to Account for Bremsstrahlung, *Health Physics*, 36:347-354, 1979.
111. H. E. Johns and J. R. Cunningham, *The Physics of Radiology*, 4th ed., Charles C. Thomas Pub, Springfield, IL, 1983.
112. A. M. Kellerer, K. Hahn, and H. H. Rossi, Intermediate Dosimetric Quantities, *Radiation Research*, 130(1):15-25, 1992.
113. A. Nahum, Principles and Basic Concepts in Radiation Dosimetry, In: P. Mayles, A. Nahum, and J. C. Rosenwald, editors, *Handbook of Radiotherapy Physics: Theory and Practice*, pages 89-115. CRC Press, 2007.
114. A. E. Nahum, Water/Air Mass Stopping-Power Ratios for Megavoltage Photon and Electron Beams, *Physics in Medicine and Biology*, 23:24-38, 1978.
115. W. H. Bragg, *Studies in Radioactivity*, Macmillan, New York, NY, 1912.
116. L. H. Gray, The Absorption of Penetrating Radiation, *Proceedings of the Royal Society A*, 112:647-668, 1929.
117. L. H. Gray, An Ionisation Method for the Absolute Measurement of Gamma-Ray Energy, *Proceedings of the Royal Society A*, 156:578-596, 1936.
118. J. E. Burns, Conversion of Percentage Depth Dose for Photon Beams From One SSD to Another and Calculation of TAR, TMR and TPR, *British Journal of Radiology*, Suppl. 17:115-119, 1983.

119. P. Mayles and P. Williams, Megavoltage Photon Beams, In: P. Mayles, A. Nahum, and J. C. Rosenwald, editors, *Handbook of Radiotherapy Physics: Theory and Practice*, pages 451-481. CRC Press, Boca Raton, FL, 2007.
120. J. Kalef-Ezra, M. Bazioglou, K. Theodorou, and C. Kappas, A Phantom for Dosimetric Characterization of Small Radiation Fields: Design and Use, *Medical Dosimetry*, 25:9-15, 2000.
121. J. C. Rosenwald, I. Rosenberg, and G. Shentall, Patient Dose Computation for Photon Beams, In: P. Mayles, A. Nahum, and J. C. Rosenwald, editors, *Handbook of Radiotherapy Physics: Theory and Practice*, pages 559-585. CRC Press, Boca Raton, FL, 2007.
122. H. F. Batho, Lung Corrections in Cobalt-60 Beam Therapy, *Journal of the Canadian Association of Radiologists*, 15:79-83, 1964.
123. E. El-Khatib and J. J. Battista, Improved Lung Dose Calculation Using Tissue-Maximum Ratios in the Batho Correction, *Medical Physics*, 11:279-286, 1984.
124. M. R. Sontag and J. R. Cunningham, Corrections to Absorbed Dose Calculations for Tissue Inhomogeneities, *Medical Physics*, 4:431-436, 1977.
125. R. P. Parker, L. Contier de Freitas, M. Cassell, S. Webb, and P. Hobday, A Method of Implementing Inhomogeneity Corrections in Radiotherapy Treatment Planning, *Journal of European Radiotherapy*, 1:93-100, 1980.

## APPENDIX A: INTERACTIONS OF RADIATION WITH MATTER

### A.1. INTERACTIONS OF CHARGED PARTICLES WITH MATTER

For medical applications of radiation, charged particles are vital. For even a photon beam, the biological effect (e.g. cell killing or other changes that might cause cancer) caused by charged particles, which are known as secondary particles in this situation. In fact, charged particles are often termed ionising radiation, and photons (and neutrons) termed indirectly ionising.

The generation of x-rays, i.e. bremsstrahlung, is a charged-particle interaction. Radiotherapy is sometimes delivered by primary charged particle beams, usually megavoltage electrons, where electron interactions with matter are obviously crucial [91].

#### A.1.1. Collision Losses

The electrons that are bound in the atoms may interact with charged particles such as electrons or protons by the way of Coulomb interactions. The particles create a trail of ionisations and excitations along its path and lose energy in the material during such processes in radiotherapy. In some cases, the energy transferred to the atomic electron is enough to create a delta ray (or  $\delta$ -ray) which is a (secondary) electron with a peculiar appreciable range. This process is shown in Figure A.1 [92,93].

The physical model for the Coulomb force between the incident charged particle and an electron in the medium is seen in Figure A.2. The electron is supposed to be free and its binding energy to be negligible compared with the energy it gets. The incoming electron is moving at a speed of  $V$  in the  $-x$  direction. The primary particle imparts a net impulse to the bound electron in a direction perpendicular to its path [94].



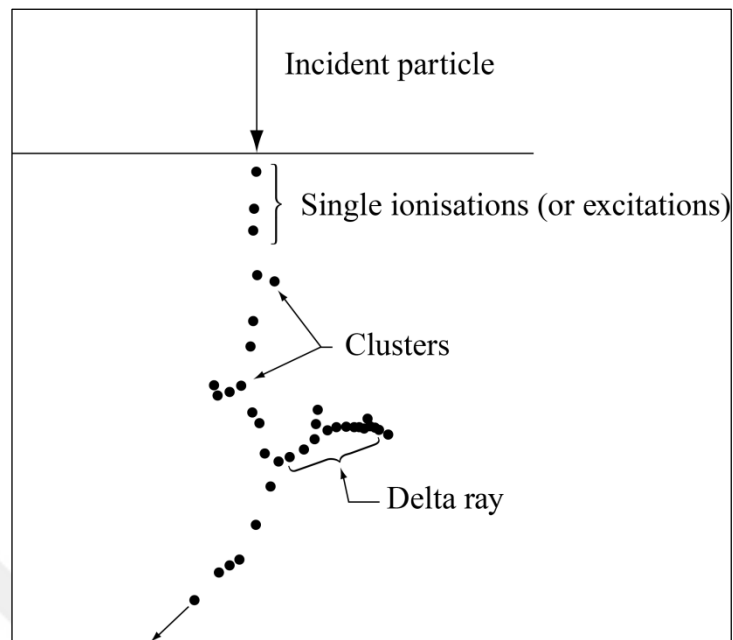


Figure A.1. Diagrammatic representation of the track followed by a charged particle in matter

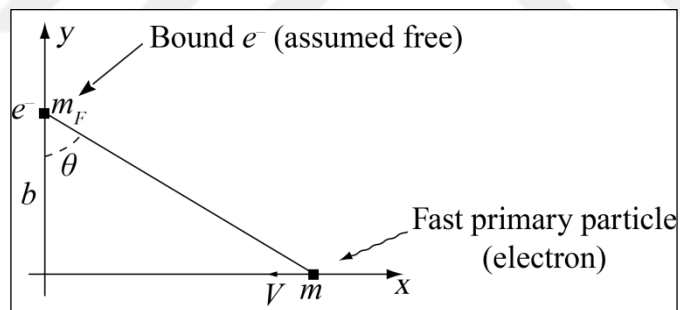


Figure A.2. Interaction between a fast primary charged particle and a bound electron

Using the classical, nonrelativistic collision theory, it is understood from Newton's second law, (i.e. the change in momentum is equal to the impulse [the time integral of the force]) and from Coulomb's law for the force between charged particles that the energy transfer  $Q$  is given by:

$$Q = \frac{2k^2 z^2 e^4}{m_e b^2 V^2} \quad (\text{A.1})$$

where  $b$ , the distance of closest approach, is known as the impact parameter;  $m_e$  is the mass of the electron;  $z$  is the charge on the primary particle;  $v$  is the velocity of the primary particle and the constant  $k$  is  $1/4\pi\epsilon_0$  that appears in the Coulomb-force expression (equals to  $8.9875 \times 10^9 \text{ Nm}^2\text{C}^{-2}$ ). It should be noted that the mass of the primary particle does not enter into Equation (A.1), which can also be applied to electrons, protons (both having  $z=1$ ), and other heavier charged particles. Equation (A.1) leads to the following classical expression for the cross-section per electron, differential in the energy transfer  $Q$ :

$$\frac{d\sigma}{dQ} = \frac{2\pi z^2 e^4 k^2}{m_e V^2} \frac{1}{Q^2} \quad (\text{A.2})$$

#### A.1.1.1. Collision Stopping Power

The collision stopping power is defined as the average energy loss,  $dE$ , per unit distance,  $ds$ . This is usually expressed as the mass collision stopping power, written  $(1/\rho)(dE/ds)_{col}$  or  $S_{col}/\rho$ :

$$\frac{S_{col}}{\rho} = \frac{1}{\rho} \left( \frac{dE}{ds} \right)_{col} = N_A \left\langle \frac{Z}{A} \right\rangle \int_{Q_{min}}^{Q_{max}} Q \frac{d\sigma}{dQ} dQ \quad (\text{A.3})$$

where  $N_A$ ,  $Z$  and  $A$  are Avogadro's number, atomic and mass number, respectively. Although  $Q_{max} = E_0 / 2$  where  $E_0$  is electron's kinetic energy, minimum energy transfer  $Q_{min}$  is difficult to obtain.

The full quantum-mechanical expression for the electron mass collision stopping power [39,40,95] is given by

$$\frac{1}{\rho} \left( \frac{dE}{ds} \right)_{col} = \frac{2\pi r_e^2 m_e c^2 N_A}{\beta^2} \left\langle \frac{Z}{A} \right\rangle \left\{ \ln \left[ \frac{\tau^2(\tau+2)}{2(L/m_e c^2)^2} \right] + F(\tau) - \delta \right\} \quad (\text{A.4})$$

where

$$F(\tau) = 1 - \beta^2 + \left[ \tau^2 / 8 - (2\tau + 1) \ln 2 \right] / (\tau + 1)^2$$

$m_e c^2$ , rest mass energy of the electron

$$\beta = v/c$$

$r_e$ , electron radius ( $=e^2/m_e c^2 = 2.818 \times 10^{-15}$  m)

$L$ , mean excitation energy

$\delta$ , density-effect correction

The mean excitation energy or potential,  $L$ , is an average of the transition energies  $E_i$  weighted by their oscillator strengths  $f_i$ . In general,  $L$  can only be derived theoretically in the simplest cases such as monatomic gases. It must rather be derived from measurements of stopping power or the range. The most recent values of  $L$ , obtained largely by experiments, are given in the report of International Commission on Radiation Units and Measurements (ICRU) [39] (Table A.1).

Table A.1. Mean excitation energies,  $L$ , and other quantities relevant to the collision stopping power of selected tissues and other materials

Material	$L$ (eV)	$\langle Z/A \rangle$	Density (g cm <sup>-3</sup> )
Adipose tissue (ICRP)	63.2	0.558468	0.920
Air (dry)	85.7	0.499190	$1.205 \times 10^{-3}$
Bone, compact (ICRU)	91.9	0.530103	1.850
Bone, cortical (ICRP)	106.4	0.521299	1.850
Ferrous-sulphate dosimeter solution	76.3	0.553282	1.024
Lithium fluoride	94.0	0.462617	2.635
Muscle, skeletal (ICRP)	75.3	0.549378	1.040
Muscle, striated (ICRU)	74.7	0.550051	1.040
Photographic emulsion	331.0	0.454532	3.815
PMMA (lucite, perspex)	74.0	0.539369	1.190
Polystyrene	68.7	0.537680	1.060
Water (liquid)	75.0	0.555087	1.000

ICRP: International Commission on Radiological Protection, ICRU: International Commission on Radiation Units and Measurements

The important features of the mass collision stopping power are shown in the following expression:

$$\frac{S_{col}}{\rho} \propto \left\langle \frac{Z}{A} \right\rangle \frac{1}{V^2} [F(\tau) - 2 \ln L - \delta] \quad (\text{A.5})$$

Comparing this expression with Equation (A.4), the increase at decreasing subrelativistic energies due to the  $(1/V^2)$  factor can be identified. This can simply be explained by the fact that slow electrons spend more time in the vicinity of an atom while fast ones leave the region in a shorter time and consequently the impulse is greater and thus more energy is lost. At relativistic energies, there is a more gradual increase in the stopping power that is known as the relativistic rise (Figure A.3) [94].

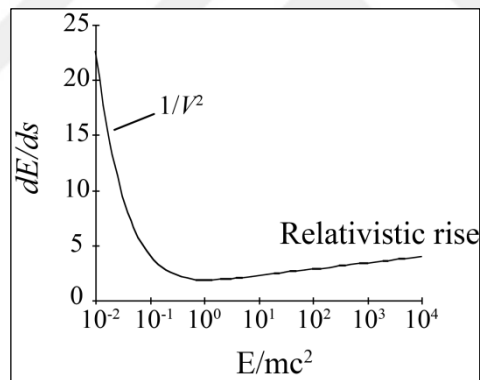


Figure A.3. Collision energy loss as a function of electron kinetic energy

#### ***A.1.1.2. Density Effect***

The density or polarization effect [40,96,97] reduces the value of  $S_{col}$  at relativistic energies in condensed media by the way of the term  $\delta$  in Equation (A.4) and Equation (A.5). It is related to the relativistic rise in the stopping power. In case that the density of the stopping medium is high, (i.e. condensed media as opposed to gases) then the electric field seen by the atoms distant from the fast particle track is reduced due to the polarization of the intervening atoms (as illustrated in Figure A.4 [94]). Consequently, the contribution of these

distant collisions to the stopping power will be reduced, which an effect in collision stopping power is known as the polarization or the density effect.

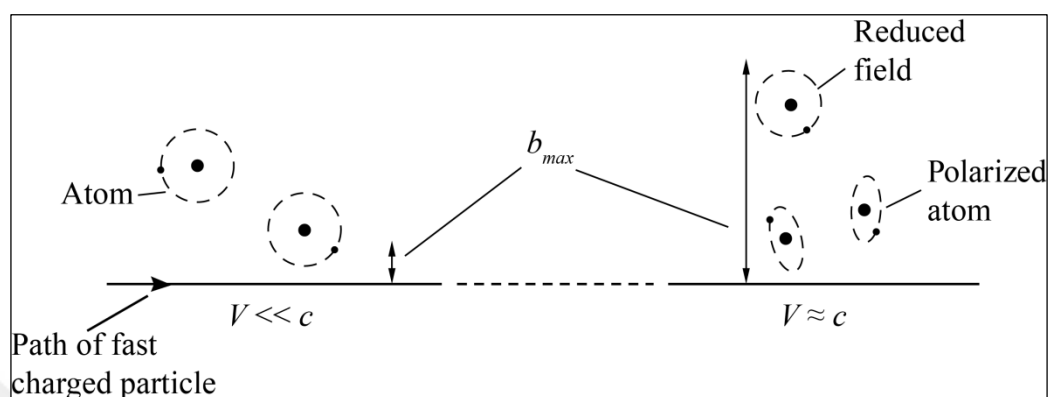


Figure A.4. Schematic explanation of the mechanism of the density effect

### A.1.1.3. Electron Stopping-Power Data for Substances of Medical Interest

The parameters for various human tissues and some other substances of dosimetric interest obtained from ICRU [40] are tabulated in Table A.1, as well as for water to make a comparison. It is seen that the  $L$ -values, which are in fact approximately proportional to the mean atomic number, vary between 73 eV and 75 eV but the adipose tissue having a high hydrogen content and the bone with a high calcium content are exceptions. Given the similarity of the values of  $L$ ,  $\langle Z/A \rangle$ , and the (mass) density, which is involved in the density-effect correction  $\delta$  in the table, the values of  $(S_{col}/\rho)$  must also be very similar. This is very convenient, as it means that the electron energy loss over a given distance in the body can be derived from that in water by simply multiplying by the density, assuming that radiation losses are also very similar.

The values of the (mass) stopping-power ratio,  $S_{med,air}$ , for various substances of interest in medical dosimetry, as a function of electron kinetic energy in the megavoltage region are given in Figure A.5. The ratio does not depend on the energy except for that of air; this is very convenient for dosimeter response evaluation and treatment planning purposes. These medium-to-water stopping-power ratios can be used directly in the applications for which a

conversion of Monte-Carlo-derived dose distributions in patients to water-equivalent doses is required [27].

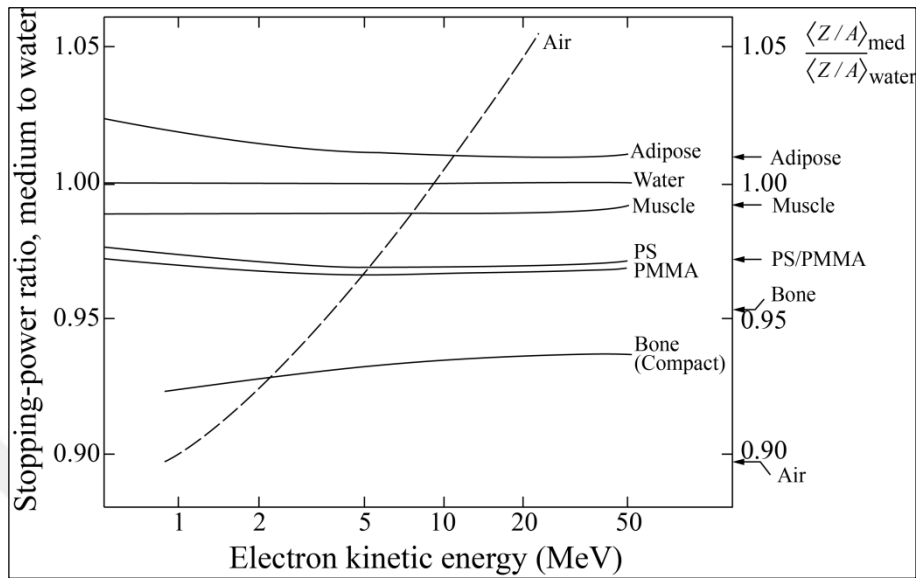


Figure A.5. Ratios of mass collision stopping powers, medium to water, for various substances of medical and dosimetric interest

PS: Polystyrene, PMMA: Polymethyl methacrylate (perspex).

#### A.1.1.4. Restricted Stopping Power

In restricted stopping power, only energy transfers under a certain value  $\Delta$  are included and are calculated by setting  $Q_{max}$  equal to  $\Delta$  in Equation (A.3). The full expression is again given by Equation (A.4) and Equation (A.5), but with the new  $F(\tau)$  term:

$$F(\tau, \Delta) = -1 - \beta^2 + \ln\{4\Delta(\tau - \Delta)\tau^{-2}\} + \tau / (\tau - \Delta) + \{\Delta^2 / 2 + (2\tau + 1) \ln(1 - \Delta / \tau)\}(\tau + 1)^{-2} \quad (\text{A.6})$$

The expression for the restricted stopping power still includes  $\delta$ , the density-effect correction factor.

### A.1.2. Radiative Losses (Bremsstrahlung)

As the electrons are accelerated in the strong electric field of a nucleus, a phenomenon called “bremsstrahlung” occurs. The acceleration is proportional to the number of protons  $Z$  in the nucleus, divided by the mass,  $m$ , of the moving electron. The intensity of radiation produced is then proportional to  $(Z/m)^2$ . For a low- $Z$  substance the energy loss mechanism is relatively insignificant below about 10 MeV and it is completely negligible for heavy charged particles. The cross-section,  $\sigma_{rad}$ , for this completely non-classical process is extremely complicated. One significant feature is that, very approximately:

$$\frac{d\sigma_{rad}}{dh\nu} \propto \frac{1}{h\nu} \quad (\text{A.7})$$

Hence, the losses will be appreciably larger than those for collisions on the average will. This means that considerable energy-loss straggling due to radiation losses can be expected.

#### A.1.2.1. Radiation Stopping Power

In an exactly analogous fashion to that for collision losses in the previous section, a radiative stopping power,  $(dE/ds)_{rad}$  or  $S_{rad}$ , and also a mass radiation stopping power ( $S_{rad}/\rho$ ) can be defined. The general form of the mass radiative stopping power for high energies (complete screening:  $\tau \gg 1/\alpha Z^{1/3}$ ) is given by:

$$\frac{S_{rad}}{\rho} = \frac{4r_e^2\alpha}{\beta^2} N_A \frac{Z(Z+1)}{M_A} (\tau+1)m_e c^2 \ln(183Z^{-1/3} + 1/18) \quad (\text{A.8})$$

where  $\alpha$  is the fine structure constant ( $\alpha \cong 1/137$ ). It is understood from Equation (A.8) that the radiative stopping power increases almost linearly with the kinetic energy in the MeV region, unlike the weak logarithmic energy dependence of the collision stopping power (Figure A.6) [98].

### A.1.2.2. Radiation Yield

A useful quantity is the fraction of the initial electron energy  $E_0$ , that is lost to bremsstrahlung in slowing down to rest which is known as the *Radiation Yield*,  $\Upsilon(E_0)$ , and is given by [91]:

$$\Upsilon(E_0) = \frac{1}{E_0} \int_0^{E_0} \frac{S_{rad}(E)}{S_{col}(E) + S_{rad}(E)} dE \quad (\text{A.9})$$

The dependence of  $\Upsilon(E_0)$  on  $E_0$  and on  $Z$  is approximately linear, which closely corresponds to the relation between  $S_{rad}/\rho$ ,  $E$  and  $Z$ .

The radiation yield is involved in calculating the dosimetric quantity,  $g$ , which is the fraction of energy transferred (by photons) to a medium in the form of electron kinetic energy that is subsequently re-radiated as bremsstrahlung.

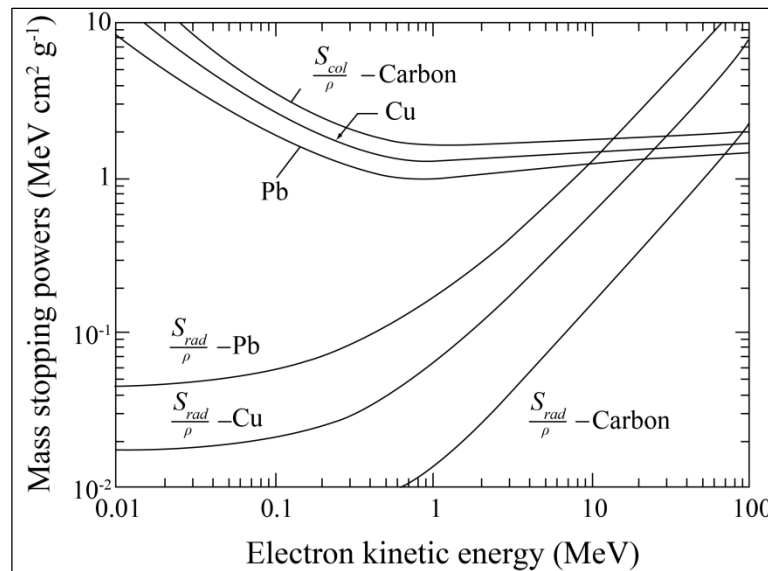


Figure A.6. A comparison of the mass radiative and mass collision stopping powers,  $S_{rad}/\rho$  and  $S_{col}/\rho$  respectively, for carbon, copper, and lead



### A.1.2.3. Angular Distribution of Bremsstrahlung Photons

The angular distribution of the emitted photons is very strongly forward-peaked at relativistic electron energies, the average value being  $\theta \cong mc^2 / E$  where  $E$  is the total energy of the electrons. This forward peaking is the reason for the flattening filter in a linear accelerator treatment head.

## A.1.3. Total Energy Losses

### A.1.3.1. Total Stopping Power

In order to find the total stopping power that can be written as  $(dE/ds)_{tot}$  or  $S_{tot}$  we should add the collision and radiative stopping powers:

$$\left(\frac{dE}{ds}\right)_{tot} = \left(\frac{dE}{ds}\right)_{col} + \left(\frac{dE}{ds}\right)_{rad} \quad (\text{A.10})$$

Figure A.7 shows the total mass stopping power (labelled “Total Loss”), mass collision stopping power, and several restricted mass collision stopping powers ( $\Delta = 10$  keV, 1 keV and 100 eV) for water against electron kinetic energy  $E$  for values between  $10^{-5}$  MeV and  $10^4$  MeV. It is observed that  $S_{tot}/\rho$  varies slowly with  $E$  over the energy range (from  $1.937$  MeV  $\text{cm}^2 \text{g}^{-1}$  at 4 MeV to only  $2.459$  MeV  $\text{cm}^2 \text{g}^{-1}$  at 25 MeV) that is important as far as radiotherapy is concerned.

Several features should be noted [91,93]:

- Radiation losses may be significant above around 10 MeV in water,
- The collision losses increase relativistically, but not much due to the density effect,
- Limited collision losses (such as  $\Delta < 10$  keV) are observed in cases where there is mild reduction in stopping power compared to the unrestricted  $S_{col}$  that emphasizes the predominance of very small losses,
- The approximate comparable value for the electronic stopping power in water is around  $2 \text{ MeV cm}^{-1}$ ; the value in tissue being of the same order of magnitude

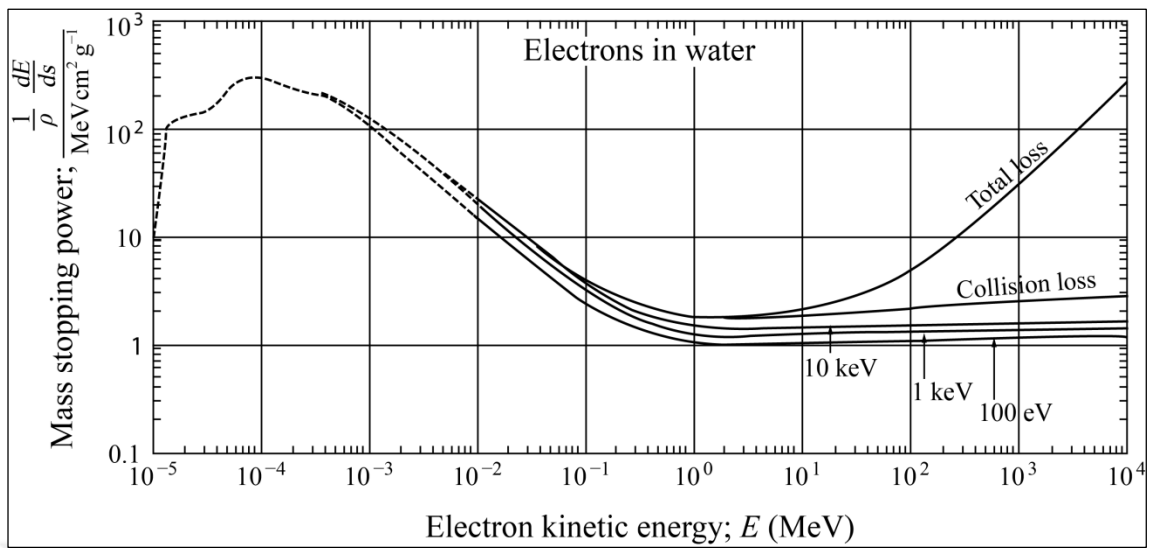


Figure A.7. Mass stopping power in water for electrons

#### A.1.3.2. Energy-Loss Straggling

The stopping power is a mean value for the energy loss per unit distance. In real cases some fluctuations will occur about this average that may create the so called “energy-loss straggling” (Figure A.8) [99].

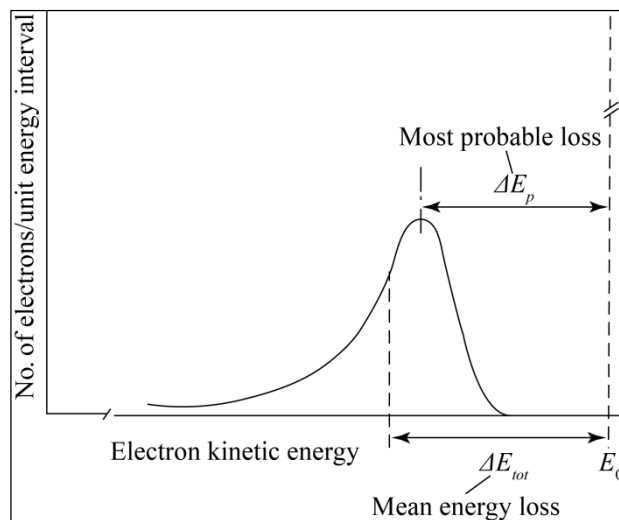


Figure A.8. Energy broadening because of energy-loss straggling after the passage of a monoenergetic electron beam (energy  $E_0$ ) through a thin absorber

### A.1.3.3. Continuous-Slowing-Down-Approximation (CSDA) Range

Charged particles lose energy in a quasi-continuous way along their tracks in matter and finally they stop. Therefore, charged particles have a finite, reasonably well defined range unlike photons. Mathematically it has been found convenient to define the so-called continuous-slowing-down-approximation (CSDA) range,  $r_0$  in the following fashion:

$$r_0 = \int_0^{E_0} \frac{1}{S_{tot}(E)} dE \quad (\text{A.11})$$

The average path length covered by a charged particle of kinetic energy,  $E_0$  until it stops is given by this expression. For the electrons, it is considerably larger than the average penetration depth because of the significant angular deflections that electrons suffer in slowing down. The CSDA range  $r_0$  is approximately proportional to  $E_0$  in the therapeutic energy range because of the relatively slow variation of  $S_{tot}$  [93].

### A.1.4. Elastic Nuclear Scattering

When a charged particle passes by an atomic nucleus, at a distance much smaller than the atomic radius, the Coulomb interaction will now be between the fast particle and the nuclear charge instead of just one of the bound electrons. In the case of electrons, this changes the direction several times, but does not change the energy (except the bremsstrahlung process). The scattering is primarily elastic and the energy lost is negligible (to satisfy momentum conservation between the very light electron and the positively charged nucleus).

This interaction process is essentially Rutherford scattering with differential cross-section [99]:

$$\frac{d\sigma}{d\theta} = \frac{\pi e^4 Z^2 (1-\beta)}{2m^2 V^4} \frac{\sin\theta}{\sin^4(\theta/2)} \quad (\text{A.12})$$

### A.1.5. Application to an Electron Depth–Dose Curve

Figure A.9 shows the electronic interactions physically as they apply to electron beams used in radiotherapy with three different depth–dose curves obtained through Monte-Carlo simulation, corresponding to different approximations about electron transport physics for a 30 MeV broad, monoenergetic and parallel electron beam in water [100,101].

The curve labelled “CSDA straight ahead” corresponds to straight tracks and shows the Bragg Peak, normally associated with heavy charged particles; this extremely simple approximation illustrates very clearly the behaviour of the total stopping power  $S_{tot}$  as the electron energy drops with depth gradually. This drop in dose with depth denotes the decrease in total stopping power with falling electron energy. But at an energy close to that of the electron rest mass (0.511 MeV), the collision stopping power goes through a minimum and then rises rapidly (principally because of the  $1/\beta^2$  term in Equation (A.4)).

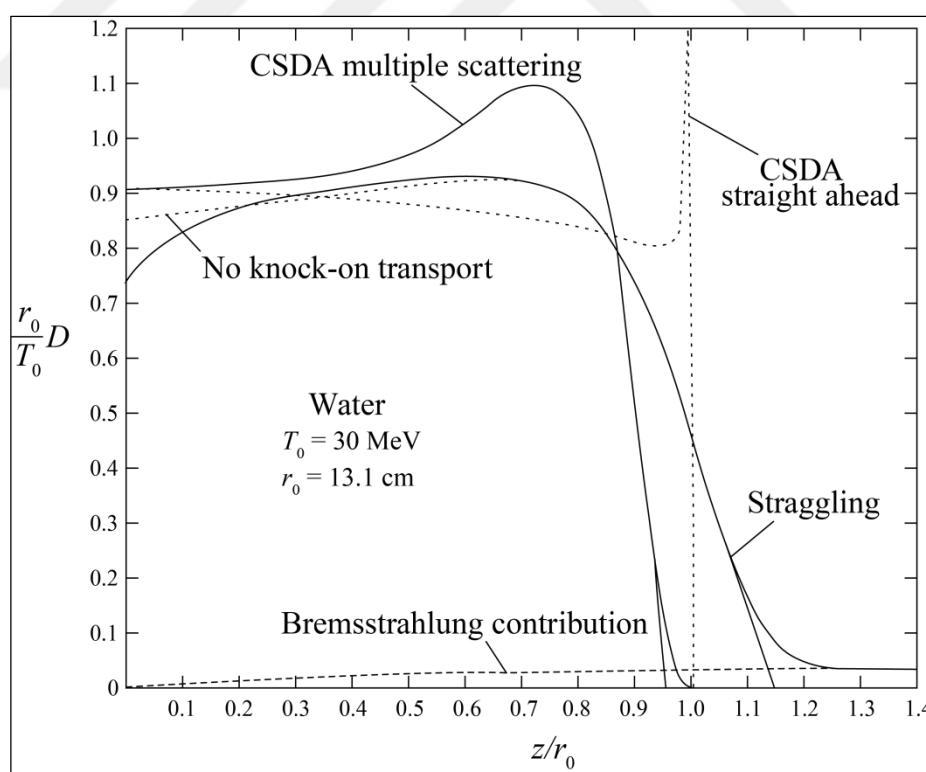


Figure A.9. The effect of various approximations on the electron depth-dose curve for a broad, 30 MeV electron beam in water (CSDA range  $r_0 = 13.1$ cm)

The “CSDA multiple scattering” curve is related with directional changes by multiple scattering (Equation (A.12)), but not with any secondary particle transport or any simulation of energy-loss straggling. The increase in dose away from the surface is entirely due to the increasing average obliquity of the electron tracks with depth and the fact that the beam is broad (i.e. there is lateral scattering equilibrium); this is sometimes known as scatter build-up). At around  $z/r_0=0.7$ , the planar fluence starts to decrease as electron tracks begin to reach their end. The maximum occurs as a result of a competition between the scatter build-up and the decrease in the planar fluence because of electrons reaching the end of their range.

The generation and transport of knock-on electrons or delta-rays are not given in the “No knock-on transport” curve, while the radiative losses (i.e. bremsstrahlung) appear beyond the practical range. Furthermore, the slope of the dose fall-off is much less, because the energy-loss straggling is included.

Consequently, the unlabelled full curve corresponds to a simulation having the full electron transport physics (most significant in this energy range). The effect of simulating  $\delta$ -ray transport is clearly seen in the build-up close to the surface; it is similar to the highly pronounced one in megavolt range photon beams where the ranges of the mainly Compton electrons are significantly greater than those of the predominantly low-energy  $\delta$ -rays.

## **A.2. INTERACTIONS OF PHOTONS WITH MATTER**

Photon interactions are stochastic (i.e. random) by nature. Unlike electrons, they may undergo a few, one, or no interactions as they pass through matter. In each interaction, secondary ionising particles are created. These may be charged particles (usually electrons) or uncharged particles (usually photons). The charged particles deposit their energies close to the interaction site and contribute to the local energy deposition, whereas, secondary photons may be transported some distance before interacting.

Secondary photons are important because they contribute to the photon fluence inside and around an irradiated body and to dose when they interact and produce secondary electrons. The relative importance of secondary photons depends on the energies of the primary

photons. In external beam therapy using megavoltage beams, the dominant contribution to the absorbed doses within the patient is due to primary photons [102].

### A.2.1. Photon Interaction Cross-Sections

Photons interact with various target entities such as atomic electrons, nuclei, atoms or molecules. The probability of interaction with a target entity is usually expressed in terms of the cross-section  $\sigma$ . The type of target for the interaction is marked, when necessary, by adding an index to  $\sigma$ . Therefore,  ${}_e\sigma$  and  ${}_a\sigma$  designate the cross-section per electron and per atom, respectively. The relation between them is given by  ${}_a\sigma = Z \times {}_e\sigma$  where  $Z$  is the atomic number of the atom.

Photon interactions can be characterized as absorption or scattering processes. In a full absorption process, the incoming photon loses all its energy and the energy is transferred to the target entity. Secondary particles are emitted during or subsequently to the interaction. In a full scattering process, an incoming photon interacts with a target entity and its direction of motion, energy and momentum may be changed because of this interaction. The photon, however, is not absorbed, and changes of energy and momentum are governed by the laws of relativistic kinematics. The main absorption processes are photoelectric (pe) absorption, pair (pair), and triplet (trip) production. The main scattering processes are coherent (coh) and incoherent (incoh) scattering. Nuclear photo-effect (phn) is an absorption process that is mostly neglected but needs to be considered in some cases. The total interaction cross-section, independent of which process occurs, is the sum of the cross-sections for the individual processes:

$$\sigma = \sigma_{pe} + \sigma_{coh} + \sigma_{incoh} + \sigma_{pair} + \sigma_{trip} + \sigma_{phn} \quad (\text{A.13})$$

The unit of cross-section is  $\text{m}^2$ . Although it does not belong to the International System of Units, the barn ( $1 \text{ barn} = 10^{-24} \text{ cm}^2 = 10^{-28} \text{ m}^2$ ) is still frequently used.

In a scattering process, the distribution of scattered photons may not be isotropic, but may instead be anisotropic in some fashion related to the direction of the incoming photon and its polarisation. In order to quantify such effects, the cross-section is regarded as a function

of the solid angle  $\Omega$  in the direction of the scattered photon and the concept of the differential cross-section  $d\sigma/d\Omega$  is introduced. The differential cross-section is defined in a way analogous to the total cross-section with  $(d\sigma/d\Omega)d\Omega$  related to the probability that the photon scatters into solid angle  $d\Omega$ . It follows that:

$$\sigma = \int_{4\pi} \frac{d\sigma(\theta, \phi)}{d\Omega} d\Omega \quad (\text{A.14})$$

where  $\theta$  is the scattering (polar) angle, and  $\phi$  is an azimuthal angle. In many situations, the scattering will, on average, have no azimuthal dependence, and the equation can then be written

$$\sigma = \int_0^\pi \frac{d\sigma(\theta)}{d\Omega} 2\pi \sin\theta d\theta \quad (\text{A.15})$$

Equation (A.15) may also be written

$$\sigma = \int_0^\pi \frac{d\sigma(\theta)}{d\theta} d\theta \quad (\text{A.16})$$

where

$$\frac{d\sigma(\theta)}{d\theta} = 2\pi \sin\theta \frac{d\sigma(\theta)}{d\Omega} \quad (\text{A.17})$$

The quantity  $d\sigma/d\theta$  is also referred to as a differential cross-section [102].

### A.2.2. Photoelectric Absorption

Photoelectric absorption is illustrated in Figure A.10. In this process, an incoming photon interacts with an atom and is absorbed. An atomic electron is ejected with kinetic energy  $T$  from one of the atomic shells. Its kinetic energy is given by:

$$T = h\nu - E_B \quad (\text{A.18})$$

Here,  $h\nu$  is the energy of the interacting photon, and  $E_B$  is the binding energy of the atomic electron. The process cannot occur with a free electron. The atom is needed in order to conserve momentum. Because of the heavy mass of the nucleus, the energy transferred to the atom is negligible [102].

In general, the cross-section  $\sigma_{pe}$  for photoelectric absorption increases strongly with decreasing photon energy. Figure A.11 shows this cross-section for lead. The cross-section displays a series of discontinuities at energies corresponding to the binding energies of the electrons in the atomic shells. These discontinuities are known as absorption edges. Below the absorption edge, the photon does not have sufficient energy to liberate an electron from the shell. At energies just above the edge, the photon has sufficient energy to liberate the electron. Therefore, the cross-section abruptly increases because the number of electrons that can take part in the absorption process increases. The absorption edge is most pronounced at the K shell in a high atomic number material. The L-shell has three sub-shells and, correspondingly, three absorption edges are seen in Figure A.11 at the energies 13.04 keV, 15.20 keV, and 15.86 keV of the L sub-shells in lead. At energies above the K absorption edge, about 80% of the interactions take place in the K shell [103].

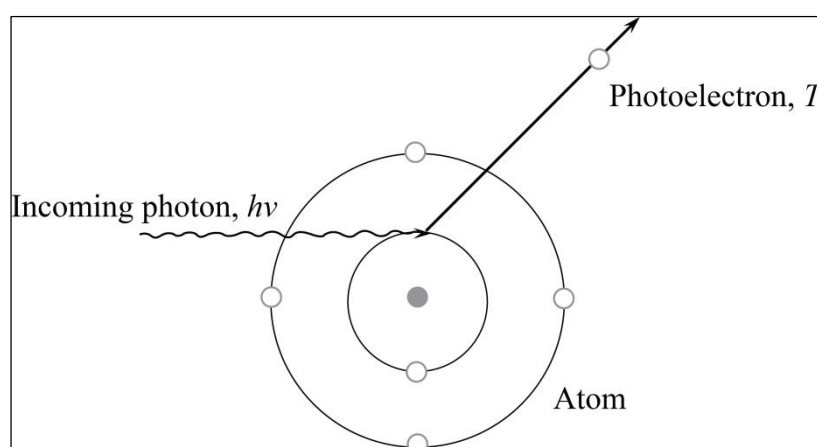


Figure A.10. Photoelectric absorption



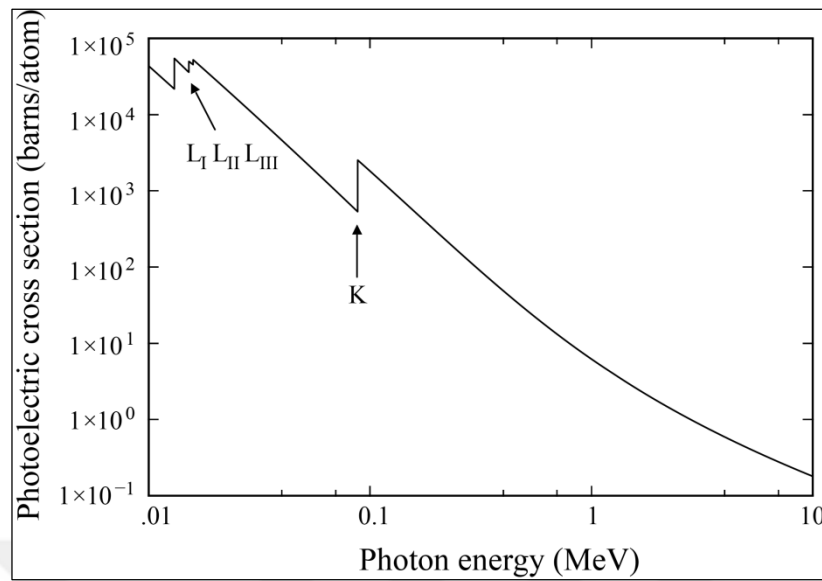


Figure A.11. The total photoelectric absorption cross-section for lead as a function of photon energy

The cross-section for photoelectric absorption depends strongly on atomic number. Above the K absorption edge, the cross-section per atom as a function of photon energy and atomic number is approximately given by

$${}_a\sigma_{pe} \cong \frac{kZ^4}{(h\nu)^3} \quad (\text{A.19})$$

The cross-section increases as the fourth power of the atomic number and is inversely proportional to the third power of photon energy. This points to the strong impact of this process at low photon energies, particularly, at high atomic numbers.

The angular distribution of the photoelectrons is peaked at angles of  $\pi/2$  to the forward direction at low photon energies, but it becomes forward directed increasingly as the photon energy increases.

After photoelectric absorption, a vacancy is left in the atomic shell. This vacancy is subsequently filled with an electron from an outer shell. The energy released is equal to the difference in the binding energies of an electron in the two shells (e.g.  $E_K - E_L$  in a transition

from the L to the K shell). The energy released is carried away either by the emission of a photon or an electron. The photon is known as a characteristic x-ray because of its fixed energy determined by the atomic number of the atom and the shells involved. Characteristic x-rays are isotropically emitted. At energies immediately above an absorption edge, they may carry a substantial fraction of the incident photon energy. Electrons emitted after electronic rearrangement are known as Auger electrons. They are also isotropically emitted. The kinetic energy of an Auger electron is equal to the energy released in the transition minus its binding energy [102].

### **A.2.3. Compton Interaction and Scattering Processes**

In a scattering process, the photon changes its direction of motion. If its energy is reduced, the scattering is called incoherent. The scattering may also occur without energy loss and is then referred to as coherent scattering. The terms elastic or Rayleigh scattering have also been used for this process.

For photon energies that considerably exceed the binding energies of the atomic electrons, the kinematics of the scattering process is usually described by considering the target electron to be free and at rest at the moment of collision. In this case, the scattering is incoherent because the photon will lose energy upon being scattered. At lower photon energies, the binding energies of the atomic electrons cannot be neglected. The photon can then scatter from individual bound electrons (incoherent scattering) or from all the bound electrons together, scattering in phase (coherent scattering). In the latter case, the whole atom takes part in the scattering process to conserve momentum.

#### ***A.2.3.1. Incoherent Scattering***

In incoherent scattering, the photon transfers part of its energy to an atomic electron that is ejected from the atomic shell. The process was first described by Compton who assumed the electron to be free and at rest at the moment of collision. In this approximation, the process is also known as Compton scattering. The kinematics of Compton scattering is illustrated in Figure A.12.

$$h\nu' = \frac{h\nu}{1 + \kappa(1 - \cos\theta)} \quad (\text{A.20})$$

where  $\kappa = h\nu/(m_0c^2)$  and  $m_0$  is the rest mass of the electron.

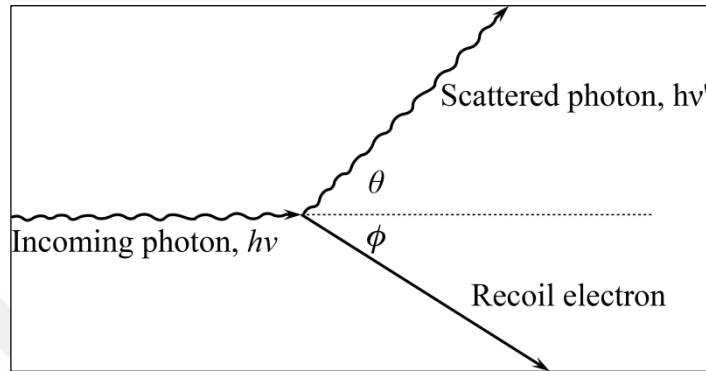


Figure A.12. Scattering angles and energies for Compton scatter

The cross-section for Compton scattering is named after Klein and Nishina who first derived an expression for its value. The differential Klein–Nishina cross-section per electron is given by [104]:

$$\frac{d_e \sigma_{KN}(\theta)}{d\Omega} = \frac{r_e}{2} \left( \frac{h\nu'}{h\nu} \right)^2 \left[ \frac{h\nu'}{h\nu} + \frac{h\nu}{h\nu'} - \sin^2\theta \right] \quad (\text{A.21})$$

At low energies ( $h\nu \rightarrow 0$ ), this reduces to

$$\frac{d_e \sigma_{Th}(\theta)}{d\theta} = \frac{r_e}{2} (1 + \cos^2\theta) \quad (\text{A.22})$$

This cross-section is known as the classical Thomson differential cross-section. The total Klein–Nishina cross-section per electron may be obtained by integrating Equation (A.21), substituting for  $h\nu'$  using Equation (A.20). The result is [105]:

$${}_e \sigma_{KN} = 2\pi r_e^2 \left( \frac{1 + \kappa}{\kappa^2} \left[ \frac{2(1 + \kappa)}{1 + 2\kappa} - \frac{\ln(1 + 2\kappa)}{\kappa} \right] + \frac{\ln(1 + 2\kappa)}{2\kappa} - \frac{1 + 3\kappa}{(1 + 2\kappa)^2} \right) \quad (\text{A.23})$$

The differential Klein–Nishina cross-section is shown in Figure A.13.

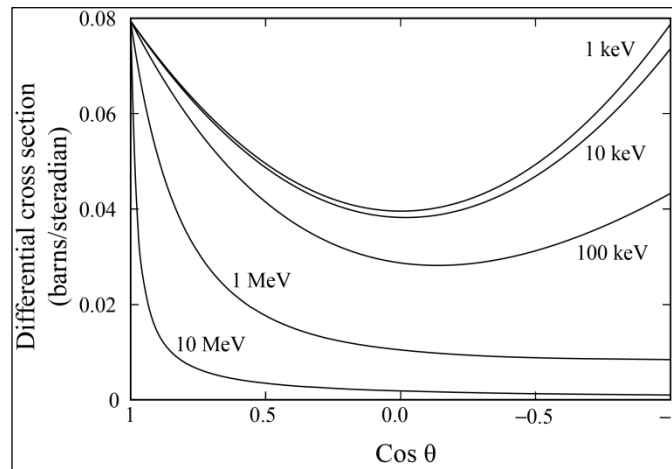


Figure A.13. Cross-sections for Compton scattering from free electrons

The influence of electron binding on the incoherent scattering cross-section is usually quantified by the incoherent scattering function  $S(x, Z)$ . The differential scattering cross-section for incoherent scattering per atom is then given by

$$\frac{d_a \sigma_{incoh}(\theta)}{d\Omega} = \frac{d_e \sigma_{KN}(\theta)}{d\Omega} S(x, Z) \quad (\text{A.24})$$

The incoherent scattering function is generally assumed to be a function of the momentum transfer and the atomic number,  $Z$ . It is tabulated in terms of the momentum transfer related quantity  $x$  given by

$$x = \frac{\text{Sin}(\theta/2)}{\lambda} \quad (\text{A.25})$$

where  $\lambda$  is the wavelength of the primary photon.

### A.2.3.2. Coherent Scattering

In coherent scattering, the photon is collectively scattered by the atomic electrons. Essentially, no energy is lost by the photon as it transfers momentum  $x$  to the atom while being scattered through the angle  $\theta$ . The scattering from the different electrons is in phase, and the resultant angular deflection is determined by an interference pattern characteristic of the atomic number of the atom. The differential cross-section for coherent scattering is obtained as the product of the differential Thomson scattering cross-section and the atomic form factor  $F$  squared

$$\frac{d_e \sigma_{coh}(\theta)}{d\Omega} = \frac{d_e \sigma_{Th}(\theta)}{d\Omega} F^2(x, Z) \quad (\text{A.26})$$

The atomic form factor is, like the incoherent scattering function, a universal function of  $x$ . It takes its maximum value in the forward direction ( $\theta=0$ ) where  $F(0,Z)=Z$ . It decreases to zero as  $x$  increases; with increasing momentum transfer  $x$ , it gets increasingly difficult for all electrons to scatter in phase without absorbing energy.

### A.2.4. Pair and Triplet Production

Pair production is illustrated in Figure A.14. In pair production, the photon is absorbed in the electric field of the nucleus. An electron (negatron)-positron pair is created and emitted with the sum of their kinetic energies,  $T^-+T^+$ , being determined by the requirement for conservation of energy

$$T^- + T^+ = h\nu - 2m_0c^2 \quad (\text{A.27})$$

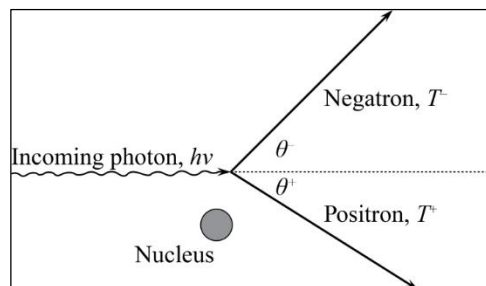


Figure A.14. Pair production

From the above Equation (A.27), it is clear that the process has a threshold value of  $2m_0c^2$  (1.02 MeV), the minimum energy required to create two electrons. On average, the electron–positron pair about equally shares the kinetic energy available.

The process of pair production may also occur in the electric field of an atomic electron. The atomic electron will recoil with sufficient energy to be ejected from the atomic shell. Three electrons appear as a result of the interaction and, accordingly, the process is called triplet production. Triplet production has an energy threshold at  $4m_0c^2$  (2.04 MeV).

The cross-section for pair production in the nuclear field is zero below threshold. It then rapidly increases with increasing energy and, well above threshold, varies approximately as the square of the nuclear charge  $Z$ . The cross-section for triplet production, at energies above threshold, approximately varies as  $Z$ .

#### **A.2.5. Nuclear Photoeffect**

When the photon energy exceeds that of the binding energy of a nucleon, it can be absorbed in a nuclear reaction. As a result of the reaction, one or more nucleons (neutrons and/or protons) are ejected. The cross-section for the nuclear photoeffect depends on both the atomic number,  $Z$ , and the atomic mass,  $A$ , and thus on the isotopic abundance in a sample of a given element. The cross-section has an energy threshold, and it is shaped as a giant resonance peak. The peak occurs between 5 and 40 MeV, depending on the element, and it can contribute between 2% (high- $Z$  element) and 6% (low- $Z$  element) to the total cross-section [102].

#### **A.2.6. The Total Atomic Cross-Section**

The total atomic cross-section and its partial cross-sections are given in Figure A.15 for the elements carbon ( $Z=6$ ) and lead ( $Z=82$ ) [103].

### A.2.7. Macroscopic Behaviour

Photons incident on an absorber will either interact in it (producing secondary electrons and/or scattered photons) or else pass through it without interacting. The number of photons transmitted undisturbed through an absorber of thickness  $t$  of a given element and density can be derived in the following way for mono-energetic photons (Figure A.16). The number of primary photons,  $d\Phi$ , interacting in a thin layer  $dx$  at depth  $x$  is proportional to the thickness of the layer and the number of photons incident on the layer so that

$$d\Phi = -\mu dx\Phi(x) \quad (\text{A.28})$$

The linear attenuation coefficient  $\mu$  is a property of the material and depends on photon energy. The minus sign indicates that photons are removed from the beam. Integrating the equation from  $x=0$  to  $x=t$  gives the number,  $\Phi(t)$ , of primary photons that are transmitted through the absorber. This number decreases exponentially with increasing thickness  $t$  according to

$$\Phi(t) = \Phi_0 e^{-\mu t} \quad (\text{A.29})$$

with  $\Phi_0 = \Phi(0)$  the number of incident photons.

The linear attenuation coefficient is the probability per unit length for interaction and is related to the total atomic cross-section,  $\sigma_{tot}$ , through the relation

$$\mu = N\sigma_{tot} \quad (\text{A.30})$$

where  $N$  is the number of target entities per unit volume. It is given by  $N = (N_A/A)\rho$ .

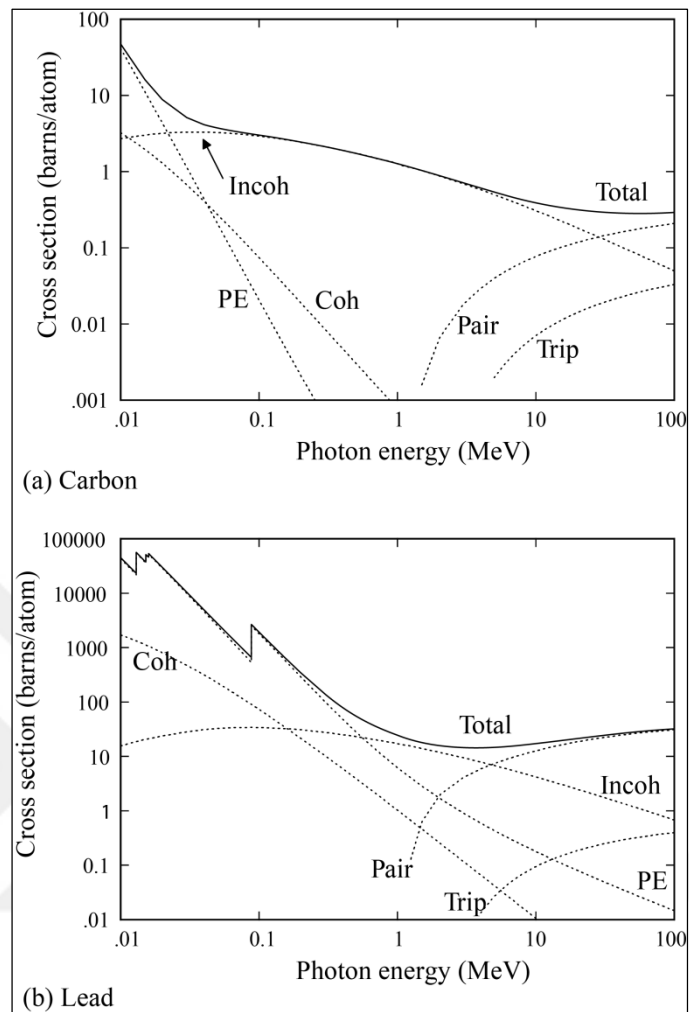


Figure A.15. The total and partial cross-sections for (a) carbon and (b) lead for photon energies from 10 keV to 100 MeV

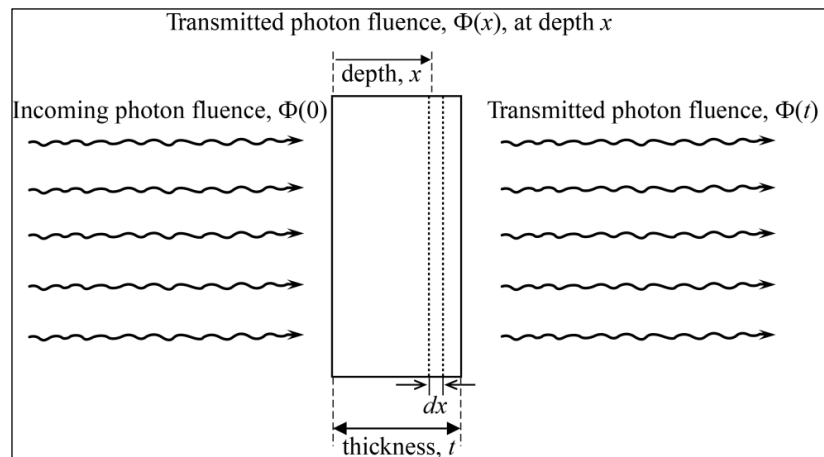


Figure A.16. Calculation of photon transmission through a slab of matter



The mass attenuation coefficient,  $\mu/\rho$ , obtained by dividing  $\mu$  with  $\rho$ , is independent of the actual density of the absorber and makes this quantity attractive for use in compilations.

The penetration power of a photon beam is commonly expressed by means of the mean free path. This is defined as the average distance,  $\bar{x}$ , travelled by the photon before it interacts. For mono-energetic photons it is given by

$$\bar{x} = \int_0^{\infty} x e^{-\mu x} dx = \frac{1}{\mu} \quad (\text{A.31})$$

## APPENDIX B: DOSIMETRIC CONCEPTS IN RADIATION THERAPY

### B.1. PRINCIPLES AND BASIC CONCEPTS IN RADIATION DOSIMETRY

The accurate determination of absorbed dose is crucial to the success of radiotherapy because of the relatively steep sigmoidal dose-response curves for both tumour control and normal-tissue damage. There are many different steps involved in the determination of the absorbed dose distribution in the patient. One of the most important of these involves measurements with a detector (often termed a dosimeter) in a phantom (often water, sometimes water-like plastic) placed in the radiation field [106].

#### B.1.1. Absorbed Dose

ICRU [107,108] defines absorbed dose as the quotient of  $d\bar{\varepsilon}$  by  $dm$ , where  $d\bar{\varepsilon}$  is the mean energy imparted by ionising radiation to matter of mass  $dm$ :

$$D = \frac{d\bar{\varepsilon}}{dm} \quad (\text{B.1})$$

The unit of absorbed dose is the ‘‘Gray (Gy)’’ which is 1 Joule per kilogram ( $\text{J kg}^{-1}$ ); the old unit is the ‘‘rad’’ which is  $10^{-2}$  Gy (sometimes referred as a cGy).

Figure B.1 illustrates the concept of energy imparted [98]. In the left part of the figure that represents a Compton interaction within the volume  $V$ , the energy imparted is given by

$$\varepsilon = h\nu_1 - (h\nu_2 + h\nu_3 + T') \quad (\text{B.2})$$

where  $T'$  is the kinetic energy of the charged particle—of initial kinetic energy  $T$ —upon leaving the volume  $V$ . The photon  $h\nu_4$  does not appear, as this is not emitted within the volume  $V$ .

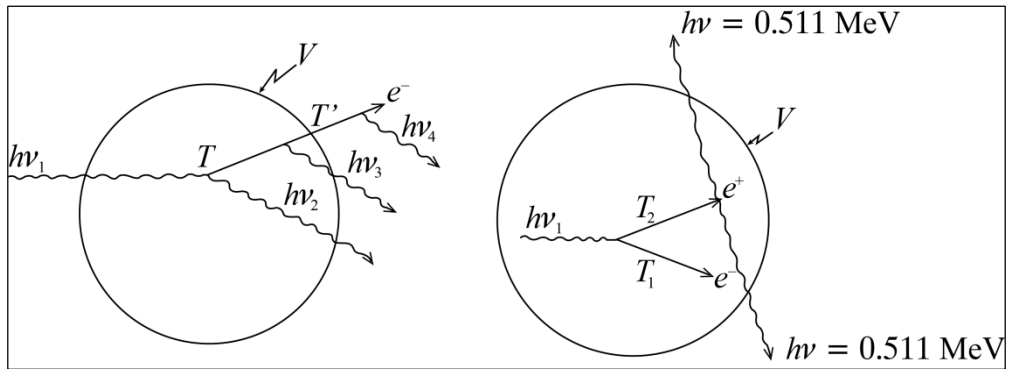


Figure B.1. An illustration of the concept of the energy imparted to an elementary volume by radiation

The volume on the right in the figure involves  $\gamma$ -ray emission ( $h\nu_1$ ) from a radioactive atom, pair production (kinetic energies  $T_1$  and  $T_2$ ), and annihilation radiation as the positron comes to rest. The energy imparted in this case is given by

$$\varepsilon = 0 - 1.022 \text{ MeV} \quad (\text{B.3})$$

### B.1.2. Kerma and Exposure

The quantity kerma, can be thought of as a step towards absorbed dose. It is conceptually very close to exposure, the first radiation quantity to be formally defined [109]. The formal definition follows [107,108]:

The kerma,  $K$ , is the quotient  $dE_{tr}$  by  $dm$ , where  $dE_{tr}$  is the sum of the initial kinetic energies of all the charged ionising particles liberated by uncharged ionising particles in a material of mass  $dm$ :

$$K = \frac{dE_{tr}}{dm} \quad (\text{B.4})$$

The units of kerma are the same as for absorbed dose, i.e.  $\text{J kg}^{-1}$  or Gray (Gy). Kerma applies only to indirectly ionising particles, which usually mean photons.

Exposure, usually denoted by  $X$ , is the quotient of  $dQ$  by  $dm$  where  $dQ$  is the absolute value of the total charge of the ions of one sign produced in air when all the electrons liberated by photons in air of mass  $dm$  are completely stopped in air.

Figure B.2 illustrates the concept of kerma (and exposure). It is the initial kinetic energies that are involved; the eventual fate of the charged particles (i.e. if they do or do not leave the elementary volume), does not affect kerma. In the volume in the figure, the initial kinetic energies of the two electrons labelled  $e_1$  contribute to the kerma, as both were generated in the volume. The fact that one of these electrons leaves the volume with a residual kinetic energy  $T$  is irrelevant. None of the kinetic energy of the electron entering the volume with kinetic energy  $T$  contributes to kerma as this electron was generated outside the volume [98].

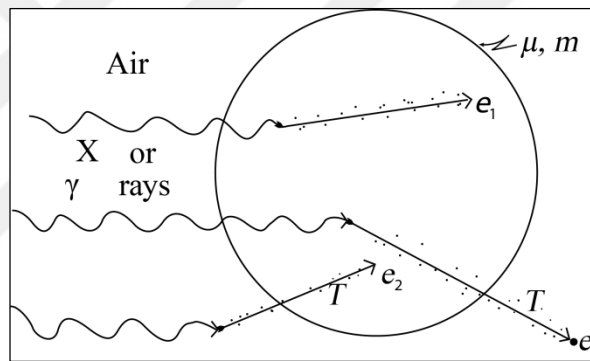


Figure B.2. Illustration of the concepts of kerma and exposure

It is important to realise that kerma includes the energy that the charged particles will eventually re-radiate in the form of bremsstrahlung photons. Kerma can be partitioned as follows [110]:

$$K = K_c + K_r \quad (\text{B.5})$$

where  $c$  refers to collision losses and  $r$  to radiation losses. The collision kerma  $K_c$  is related to the (total) kerma by

$$K_c = K(1 - g) \quad (\text{B.6})$$

The quantity  $g$  is the fraction of the initial kinetic energy of the electrons that is reradiated as bremsstrahlung.

Exposure and air kerma can be related to each other as follows. Multiplying the charge  $dQ$  by the mean energy required to produce one ion pair, divided by the electron charge, i.e.  $W/e$ , yields the collision part of the energy transferred, i.e.  $dE_{tr}(1-g)$  and therefore

$$X(W/e) = K_{air}(1-g) \quad (\text{B.7})$$

### B.1.3. Relation between Kerma and Absorbed Dose

The absorbed dose  $D_{med}$  in medium  $med$  concerns the (mean) value of energy imparted to an elementary volume, whereas kerma concerns energy transferred as the charged particles can leave the elementary volume, taking a fraction of the initial kinetic energy with them. This is illustrated in Figure B.3 [106]. The quantity denoted in the figure by  $E_{tr}^n$  is the net energy transferred and excludes that part of the initial kinetic energy converted into bremsstrahlung photons. It is equal to  $dE_{tr}(1-g)$ . The (net) kinetic energy leaving the layer denoted by  $E_{out}^n$  and the (net) kinetic energy entering the layer on charged particles denoted by  $E_{in}^n$ . Then, the energy imparted to the layer,  $\varepsilon$ , is:

$$\varepsilon = E_{tr}^n - E_{out}^n + E_{in}^n \quad (\text{B.8})$$

If the electron track that leaves the layer is replaced by an identical track that enters the layer ( $E_{in}^n = E_{out}^n$ ), it then follows that:

$$\varepsilon = E_{tr}^n \quad (\text{B.9})$$

The equality between energy leaving and energy entering on charged particles is known as charged particle equilibrium (CPE). This can be realised under certain circumstances.

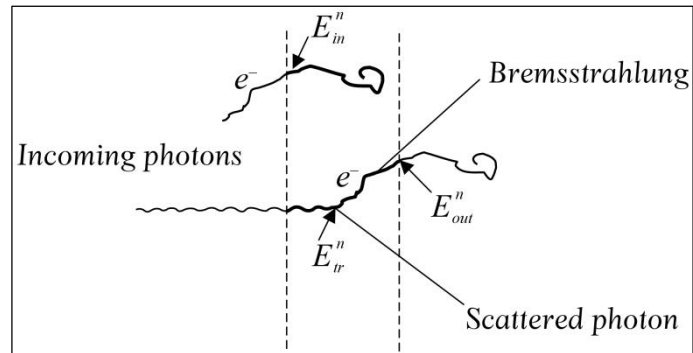


Figure B.3. Schematic illustration of how secondary electrons created by photons can transfer energy  $E_{in}^n$  to a thin layer, leave that layer, and enter the layer from outside

Dividing both sides of Equation (B.9) by the mass of the layer or volume element and changing from stochastic to average quantities it can be written:

$$D_{med}^{CPE} = (K_c)_{med} \quad (B.10)$$

which is a very important result states that under the special condition of charged particle equilibrium, the absorbed dose is equal to the collision kerma.

#### B.1.4. Charged Particle Equilibrium

Charged particle equilibrium (CPE), also known as electronic equilibrium, is said to exist in a volume  $V$  in an irradiated medium if each charged particle of a given type and energy leaving  $V$  is replaced by an identical particle of the same energy entering  $V$ .

Figure B.4 illustrates schematically how charged particle equilibrium can actually be achieved in a photon beam. In each voxel (labelled A to G in the figure), one electron is generated and therefore, the kerma will be constant as it is assumed here that there is no photon attenuation. Only a fraction of the electron track deposits energy in voxel A; therefore, the dose is low. In voxel B a new electron starts but here there is also part of the electron track which started in voxel A. Hence, the dose is higher than in voxel A; in voxel C the dose is higher still. However, in voxel D, where the electron started in voxel A comes

to rest, all the sections of an electron track are present. This means that the sum of the kinetic energies leaving this volume must be exactly balanced by the sum of the kinetic energies entering and remaining in the volume. Subsequent voxels will contain patterns of electron tracks identical to those in D and, therefore, CPE must also apply in these volumes. At the depth of voxel D, the absorbed dose is now equal to collision kerma and this will also be the case in the subsequent voxels E, F, G, in the absence of photon attenuation [111].

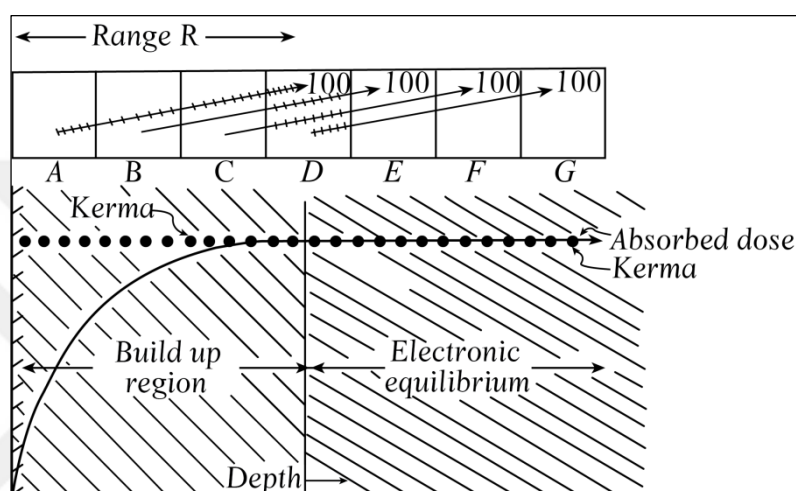


Figure B.4. Diagram showing the build up to charged particle equilibrium for the idealised case of no attenuation of the photon beam and one straight electron track generated in each slab labelled A to G

In the situation of a photon beam, true CPE is strictly impossible to achieve in practice. Attenuation means that the photon fluence does not remain constant and, therefore, the number of secondary particles (electrons) starting at different depths also cannot be constant. Table B.1 illustrates the degree of photon attenuation in water thicknesses ensuring transient electronic equilibrium for photon beams of different energies [109]. The degree of CPE failure increases as the photon energy increases. Consequently, experimental determination of exposure (now air kerma) is not attempted at maximum photon energies above approximately 3 MeV. Even below this energy, small corrections have to be made for the effect of photon attenuation.

Table B.1. Approximate thickness of water required to establish transient charged particle equilibrium. For bremsstrahlung beams of different maximum energies

Maximum Energy of Photons (MeV)	Approximate Thickness of Water for Equilibrium (mm)	Approximate Photon Attenuation (%)
0.3	0.1	0.03
0.6	0.4	0.1
1	0.8	0.3
2	2.5	0.8
3	8	2
6	15	4
8	25	6
10	30	7
15	50	9
20	60	11
30	80	13

Even though strict CPE may not exist, in many situations it is very well approximated, such as at depths beyond the dose maximum in media irradiated by photons below around 1 MeV in energy. At higher energies, the equals sign in Equation (B.10) can be replaced by a proportionality sign. This is then termed transient charged particle equilibrium (TCPE):

$$D \stackrel{TCPE}{\propto} K_c \quad (\text{B.11})$$

The quantities  $K$ ,  $K_c$  and dose  $D$  are plotted as a function of depth in Figure B.5 [98]. The build-up region and the region of TCPE, where the  $D$  and  $K_c$  curves become parallel to each other are illustrated.



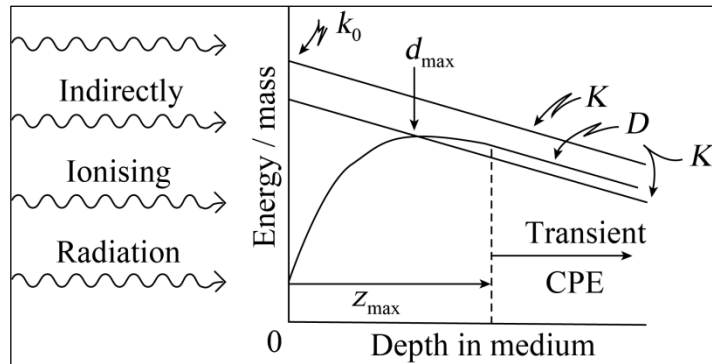


Figure B.5. Variation of kerma,  $K$ , collision kerma,  $K_c$ , and dose,  $D$ , with depth in a beam of indirectly ionising radiation such as a photon beam

### B.1.5. Stopping Power and Cema

$N$  electron tracks incident perpendicularly on the thin layer of medium  $med$  and thickness  $dl$  can be considered. Instead of the mass energy-transfer coefficient for photons, for charged particles the quantity of relevance is stopping power, the energy lost per unit track length and this energy denoted by  $dE_l$ . The main interest here is the locally deposited energy in the thin layer so it is clearly appropriate to employ the collision stopping power,  $S_{col}$ , rather than the total stopping power. Thus, it can be written as [106]:

$$dE_l = S_{col} dlN \quad (\text{B.12})$$

Dividing both sides by the mass of the layer  $dm$  and expressing this as  $\rho \times dV$  on the right hand side,

$$\frac{dE_l}{dm} = \frac{S_{col} N dl}{\rho dV} \quad (\text{B.13})$$

which can be rearranged to give:

$$\frac{dE_l}{dm} = \frac{S_{col}}{\rho} \left[ \frac{N dl}{dV} \right] \quad (\text{B.14})$$

where, as in the case of indirectly ionising radiation, the quantity in the square brackets is the fluence  $\Phi$  and therefore:

$$\frac{dE_l}{dm} = \frac{S_{col}}{\rho} \Phi \quad (\text{B.15})$$

Until recently, there was no equivalent of kerma for the case of charged particles. However, the quantity cema, converted energy per unit mass, was proposed by Kellerer et al. [112]. ICRU [108] defines cema as the energy lost by charged particles, excluding secondary electrons, in electronic collisions in a mass  $dm$  of a material. ‘Secondary electrons’ refer to the delta rays generated by the incident primary electrons, and their kinetic energies have already been included in  $dE_l$ . Therefore, cema is equal to  $dE_l/dm$  and, consequently, to the product of electron fluence and mass collision stopping power.

Cema is not necessarily equal to absorbed dose, as some of the delta rays can leave the thin layer. To involve absorbed dose, it must follow that any charged particle kinetic energy leaving the thin layer or elementary volume is replaced by an exactly equal amount entering the layer and being deposited in it or imparted to it. Consequently, it must be assumed that there is delta-ray equilibrium in order to be able to equate cema with absorbed dose. Therefore, for a medium  $m$ , it can be written:

$$D_m^{\delta\text{-eqm}} = \Phi \left( \frac{S_{col}}{\rho} \right)_m \quad (\text{B.16})$$

or, in the case of polyenergetic electron radiation:

$$D_m^{\delta\text{-eqm}} = \int_0^{E_{\max}} \Phi_E \left( \frac{S_{col}(E)}{\rho} \right)_m dE \quad (\text{B.17})$$

where  $\Phi_E$  is the fluence, differential in energy.

### B.1.6. Delta-Ray Equilibrium

Naturally, delta-ray equilibrium must always exist if charged particle equilibrium exists. However, where the primary radiation consists of charged particles CPE can never be achieved except in the rather special case of uniformly distributed  $\beta$  sources in a large medium. For the beams of high-energy electrons used in radiotherapy, the energy of the primary electrons decreases continuously with depth and hence there cannot be equilibrium. However, the ranges of the delta rays are predominantly extremely short and almost all the energy transferred through collision losses, i.e. the cema, is deposited locally. Thus, delta-ray equilibrium is generally fulfilled to a high degree in media irradiated by electron beams [106].

One situation where delta-ray equilibrium is definitely not a good approximation, however, is very close to the phantom surface in an electron beam. The appreciable range in the forward direction of the most energetic delta-rays result in a small but discernible delta-ray build-up.

### B.1.7. Cavity Theory

When a measurement is made with a detector, the detector material will, in general, differ from that of the medium into which it is introduced. The signal from a radiation detector will generally be proportional to the energy absorbed in its sensitive material and thus to the absorbed dose in this material,  $D_{det}$ .

The detector can be thought of as a cavity introduced into the uniform medium of interest; this name stems from the fact that gas-filled ionisation chambers dominated the development of the subject [109] and the associated theory, which relates  $D_{det}$  to  $D_{med}$ , is known as cavity theory. In its most general form, the aim of cavity theory is to determine the factor  $f_Q$  given by

$$f_Q = \left( \frac{D_{med}}{D_{det}} \right)_Q \quad (\text{B.18})$$

for an arbitrary detector ‘*det*’, in an arbitrary medium ‘*med*’, and in an arbitrary radiation quality *Q* (photons or electrons). Figure B.6 illustrates the situation schematically.

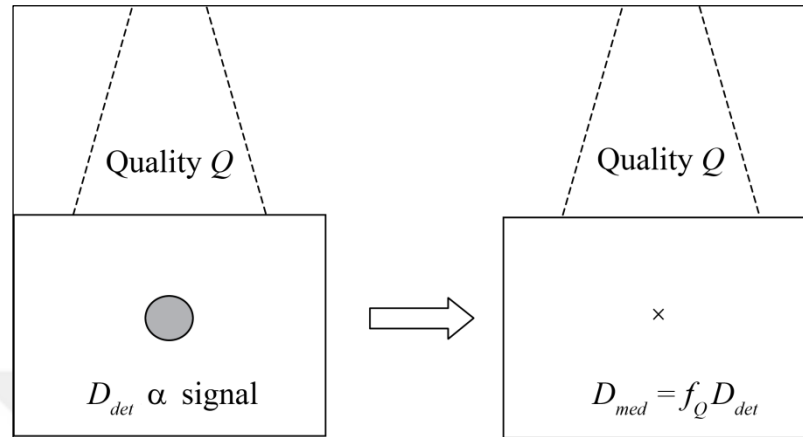


Figure B.6. The general situation of a detector introduced into a medium (left), yielding  $D_{det}$  for a given exposure to radiation of quality  $Q$  and then being converted into the dose  $D_{med}$  at  $\times$  in the absence of the detector by multiplying by the cavity theory factor  $f_Q$

#### **B.1.7.1. Cavity Theory for Large Photon Detectors**

The radiation beam in Figure B.6 consisting for simplicity of monoenergetic photons is incident on a phantom of material, *med*, and has energy fluence  $\psi$  at the depth of interest  $z$ . Provided that this depth is sufficient for CPE to be established, the dose in the medium at depth  $z$  can be written as [113]:

$$D_{med,z} = \psi_{med,z}^{CPE} \left( \frac{\mu_{en}}{\rho} \right)_{med} \quad (\text{B.19})$$

A detector is placed with its centre at depth  $z$  and that the sensitive material of the detector, denoted by ‘*det*’, is large enough for there to be charged particle equilibrium in this material, i.e. that its extent is greater than the maximum range of the secondary electrons generated in this material. Figure B.7 illustrates the situation schematically.

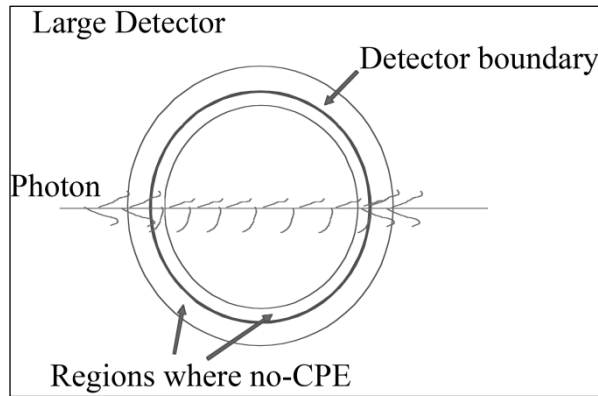


Figure B.7. The deposition of energy by photons in a large detector

The photons interact with the detector material and produce secondary electrons tracks. Within a narrow rind region on either side of the detector wall (labelled ‘boundary’) there is no CPE, as electrons there are generated partly in the surrounding medium, partly in the material of the detector wall and partly in the detector itself. In the detector material away from the boundary CPE will be re-established. The absorbed dose in the detector, with the bar indicating that this is an average over the detector volume, will be given by [113]:

$$\bar{D}_{det,z}^{CPE} = \psi_{det,z} \left( \frac{\mu_{en}}{\rho} \right)_{det} \quad (B.20)$$

where the energy fluence is that in the detector material (an average over the detector volume) and the mass–energy absorption coefficient applies to the detector material ‘det’. The large detector condition is fulfilled when the volume of the no-CPE rind is only a small fraction of the total volume of the sensitive material of the detector.

Combining Equation (B.19) and Equation (B.20),

$$\frac{D_{med}}{\bar{D}_{det}} = \frac{\psi_{med,z} (\mu_{en} / \rho)_{med}}{\psi_{det,z} (\mu_{en} / \rho)_{det}} \quad (B.21)$$

Assuming further that the detector does not disturb the photon (energy) fluence existing in the medium, i.e.  $\psi_{det,z} = \psi_{med,z}$  then the ratio of the absorbed doses, or the cavity theory factor  $f_Q$ , is given by

$$f_Q = \frac{D_{med,z}}{\bar{D}_{det}} = \frac{(\mu_{en} / \rho)_{med}}{(\mu_{en} / \rho)_{det}} \quad (\text{B.22})$$

In all practical situations, there will be a spectrum of photon energies. This will be true even for a monoenergetic photon source as scattered photons of lower energy will be present at a depth in the medium. The dose ratio is then given by:

$$\frac{D_{med,z}}{\bar{D}_{det}} = \frac{\int_0^{E_{max}} E \frac{d\Phi_{med,z}}{dE} \left( \frac{\mu_{en}(E)}{\rho} \right)_{med} dE}{\int_0^{E_{max}} E \frac{d\Phi_{med,z}}{dE} \left( \frac{\mu_{en}(E)}{\rho} \right)_{det} dE} \quad (\text{B.23})$$

This ratio, often written in shorthand form as

$$\frac{D_{med,z}}{\bar{D}_{det}} = (\bar{\mu}_{en} / \rho)_{med,det} \quad (\text{B.24})$$

is the well-known mass–energy absorption coefficient ratio.

In general, the photon fluence spectrum at a depth in the medium can only be obtained by using Monte-Carlo simulation.

### ***B.1.7.2. Bragg–Gray Cavity Theory***

In Figure B.8 a very different class of detector, one that is small compared to the ranges of the secondary electrons, is shown. Photons irradiate the uniform medium on the left and the tracks of several secondary electrons are shown. On the right a detector has been introduced which is small enough so as not to disturb the electron tracks.

In this case, the extent of the detector in any direction represents only a tiny fraction of the build-up depth required for the establishment of charged particle equilibrium. Therefore, the absorbed dose cannot be derived in this small detector from the product of photon energy fluence and  $(\mu_{en}/\rho)_{det}$ . Instead, it is much more logical to use the relationship between electron fluence and absorbed dose.

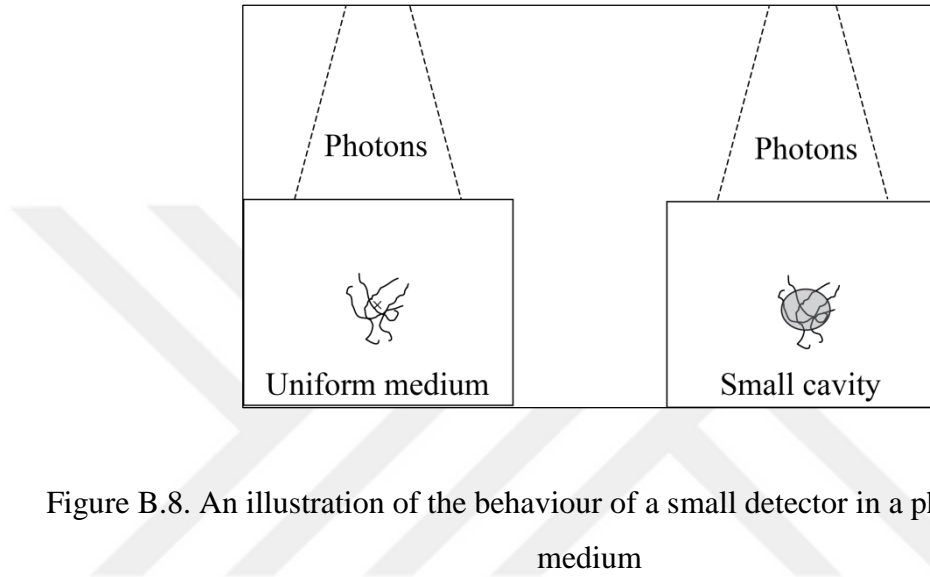


Figure B.8. An illustration of the behaviour of a small detector in a photon-irradiated medium

It therefore follows from Equation (B.16) that at the depth  $z$  in the medium:

$$\frac{D_{med,z}}{\bar{D}_{det}} = \frac{\Phi_{med,z} (S_{col} / \rho)_{med}}{\Phi_{det} (S_{col} / \rho)_{det}} \quad (\text{B.25})$$

If we assume that the introduction of the detector does not disturb the electron fluence existing in the undisturbed medium, i.e.  $\Phi_{det} = \Phi_{med,z}$ , then

$$\frac{D_{med}}{\bar{D}_{det}} = \frac{(S_{col} / \rho)_{med}}{(S_{col} / \rho)_{det}} \quad (\text{B.26})$$

The above expression is known as the (mass) stopping-power ratio, often written simply as  $S_{med,det}$ .

In all practical cases, there will be a spectrum of electron energies and the stopping-power ratio must be evaluated from

$$\frac{D_{med}}{D_{det}} = S_{med,det}^{BG} = \frac{\int_0^{E_{max}} (\Phi_E)_{med,z} (S_{col}(E) / \rho)_{med} dE}{\int_0^{E_{max}} (\Phi_E)_{med,z} (S_{col}(E) / \rho)_{det} dE} \quad (B.27)$$

where the energy dependence of the collision stopping power has been made explicit and it is understood that  $(\Phi_E)_{med,z}$  refers to the medium in the absence of the detector in both the numerator and the denominator. It must be remembered that this is the fluence of primary electrons only; no delta-rays are involved. For reasons, it is convenient to denote the stopping-power ratio evaluated according to Equation (B.27) by  $S_{med,det}^{BG}$  [39,114].

Detectors that behave in the above fashion in photon-irradiated media, i.e. that respond to, but do not disturb, the electron fluence that exists in the absence of any detector, are known as Bragg–Gray cavities after the pioneering work of Bragg [115] and Gray [116,117]. Bragg presented qualitative arguments and Gray reasoned in a more quantitative way that a small gas-filled cavity ought to negligibly modify the number, energy, and direction of electrons present in a photon-irradiated medium. Gray showed that the ratio of energy lost per unit mass in the medium to that in the gas was equal to the ratio of mass stopping powers  $S_{med,gas}$  and then assumed further that ratio of energy absorbed in the respective media was also equal to  $S_{med,gas}$ .

In order for a detector to be treated as a Bragg–Gray (BG) cavity there is really only one condition that must be fulfilled:

*“The cavity must not disturb the charged particle fluence (including its distribution in energy) existing in the absence of the cavity.”*

In practice, this means that the cavity must be small compared to the electron ranges, and in the case of photon beams, only gas-filled cavities, i.e. ionisation chambers fulfil this.



Generally, a second condition is added:

*“The absorbed dose in the cavity is deposited entirely by the charged particles crossing it.”*

This means that any contribution to the dose due to photon interactions in the cavity must be negligible. In many ways, it is a corollary to the first condition. If the cavity is small enough to fulfil the first condition then the build-up of dose due to interactions in the cavity material itself has to be negligible; if this is not the case then the charged particle fluence will differ from that in the undisturbed medium for this very reason.

A third condition is sometimes added:

*“Charged particle equilibrium must exist in the absence of the cavity.”*

In fact, provided that the stopping-power ratio is evaluated over the charged particle spectrum at the position of the detector, then CPE is not required. Nor in the electron beams used in radiotherapy is there ever CPE as has already mentioned. Gray and other early workers required this condition as they did not have the theoretical tools to evaluate  $\Phi_E$  in Equation (B.27), except in the CPE situation, as Attix points out [98].

The air-filled ionisation chamber of the dimensions used in radiotherapy irradiated by a megavoltage photon beam is a clear case of a Bragg–Gray cavity. The same is true for electron beams.

## **B.2. DOSIMETRIC CHARACTERISTICS OF MEGAVOLTAGE PHOTON BEAMS**

### **B.2.1. Percent Depth Dose (PDD)**

Percent depth dose (PDD) is one of the basic measured quantities from which many of the other parameters are derived [118]. PDD defined as (Figure B.9):

$$PDD(d, A_s, SSD) = 100 \times \frac{D(d, A_s, SSD)}{D(d_{\max}, A_s, SSD)} \quad (\text{B.28})$$

where  $D$  is the dose measured at the depth  $d$ ,  $A_s$  is the field size at surface of the phantom,  $d_{\max}$  is reference depth of maximum dose.

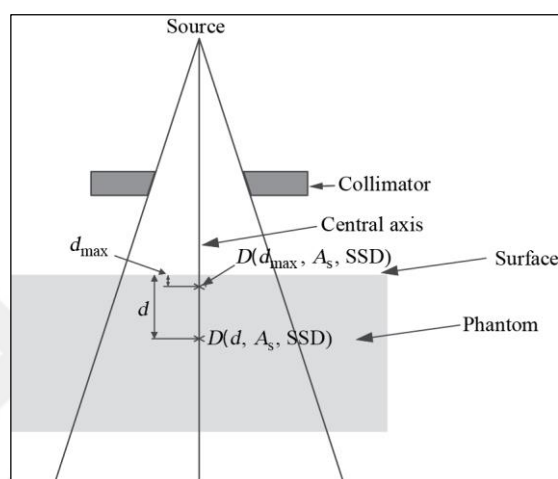


Figure B.9. Diagram for measuring PDD

### B.2.2. Dose Build-up

The depth dose curve for cobalt-60 and all megavoltage photon beams exhibits the phenomenon called build-up. The dose is higher a short distance below the skin compared to the dose at the surface (Figure B.10). This is the result of the lack of electronic equilibrium at shallow depth. Absorbed dose is delivered not directly by the photons but by the secondary electrons generated by their interactions with tissues. At these higher energies, the secondary electrons are principally Compton electrons directed in the forward direction and give up their energy further away from the point of interaction than is the case with low energy x-rays. The number of electrons passing through each layer of the phantom will progressively increase until the point at which equilibrium is reached. Since electrons lose energy almost uniformly along their path, the dose deposited will progressively increase until electron equilibrium is attained at a depth approximating to the range of the electrons. This depth is about 5 mm for a cobalt-60 beam. For a megavoltage beam, the depth expressed in cm is approximately 1/4 of the maximum energy expressed in MeV [119].

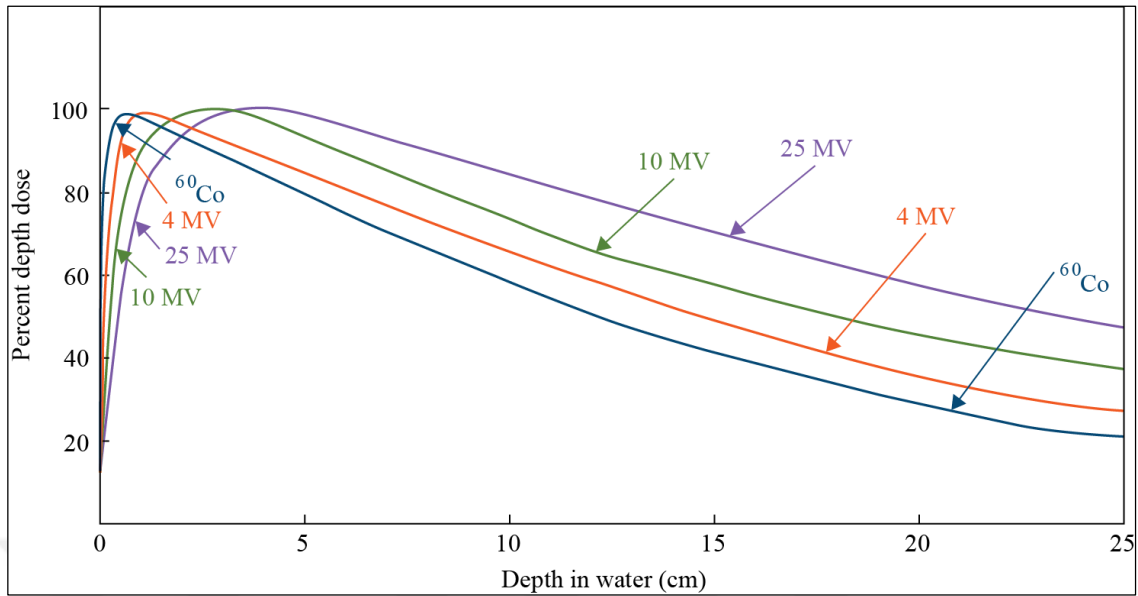


Figure B.10. Percent depth dose curves from different beam energies

### B.2.3. Off-Axis (Dose) Profiles

The variation of dose with distance from the central axis of beam but at the same depth, known as off-axis (dose) profiles or off-axis ratios, is also a fundamental parameter required to characterise a megavoltage photon beam.

### B.2.4. Tissue Air Ratio (TAR)

Tissue Air Ratio (TAR) is defined as the ratio of dose in water measured at depth on the beam central axis in a large phantom, to the dose to water measured in air at the same point (i.e. at same distance from the source) (Figure B.11):

$$TAR(d, A_d) = \frac{D(d, A_d, SSD)}{D(\text{air}, A_d, SAD)} \quad (\text{B.29})$$

where in this case,  $SSD = SAD - d$  ( $SAD$ , source to axis (isocenter) distance), to emphasise that the doses refer to the same point in space. In contrast to PDD, the field size parameter  $A_d$  always refers to the value at the point of measurement or calculation.

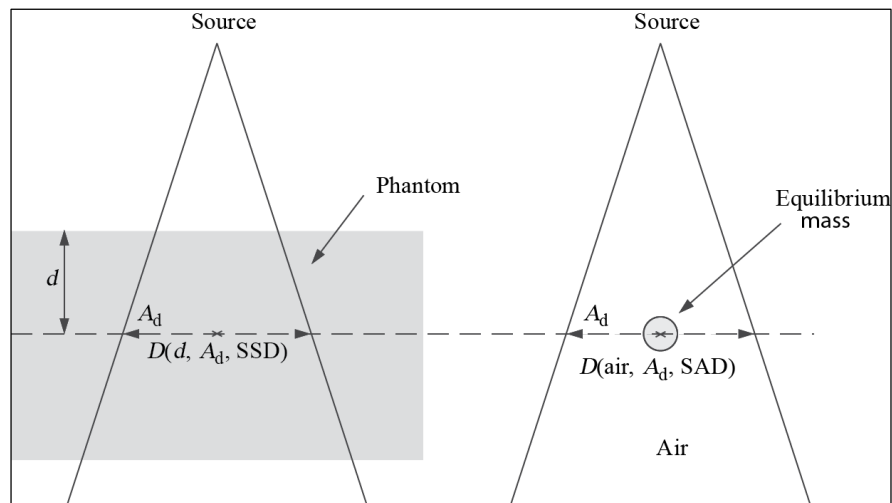


Figure B.11. Illustration for the Tissue Air Ratio measurement

### B.2.5. Tissue Phantom Ratio (TPR) and Tissue Maximum Ratio (TMR)

Tissue Phantom Ratio (TPR), is defined as the ratio of the dose at a given point on the beam central axis in phantom to the dose at the same point at a fixed reference depth  $d_{ref}$ , all other machine parameters being constant (Figure B.12):

$$TPR(d, A_d) = \frac{D(d, A_d, SSD)}{D(d_{ref}, A_d, SSD + d - d_{ref})} \quad (\text{B.30})$$

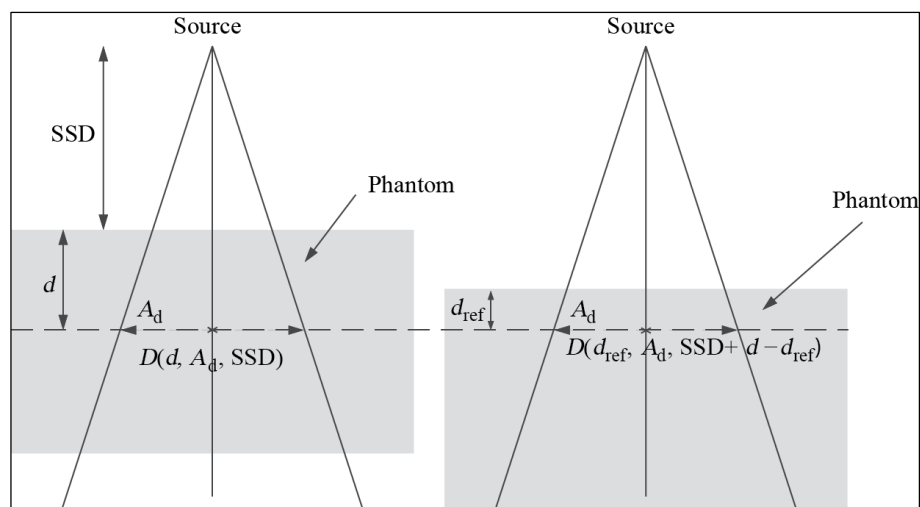


Figure B.12. Illustration for the Tissue Phantom Ratio measurement

When  $d_{ref}$  is chosen as  $d_{max}$ , the TPR becomes the Tissue Maximum Ratio (TMR). These quantities are measured in water or water-substitute solid phantoms by keeping the detector at a constant distance from the source and varying the overlying depth of material. As TPR is a ratio of two doses at the same point for the same field size, it is practically independent of the distance of the point in question from the source. Note that, by definition, both  $TPR(d_{ref}, A_d)$  and  $TMR(d_{max}, A_d)$  are equal to one [119].

### **B.2.6. Beam Quality Specification**

For megavoltage photon beams, instead of specifying the beam quality in terms of nominal energy (in MV), it is clearly recognized that it is much better to use the beam attenuation in water. This attenuation is generally expressed by the quantity  $TPR_{20,10}$  defined as the ratio of absorbed dose to water on the beam axis at the depths of 20 cm and 10 cm in a water phantom, obtained with a constant source-detector distance and a 10 cm × 10 cm field size at the position of the detector.

### **B.2.7. Monitor Unit Calibration**

A monitor unit (MU) is a measure of machine output from a linac. Linear accelerators are generally calibrated to give 1 cGy absorbed dose per MU to the dose maximum point for the reference field size of 10 cm × 10 cm and SSD=100 cm.

### **B.2.8. Output Factors**

Measurements of the dose rate (or dose per MU) in phantom as a function of field size is a necessary step in the commissioning process. A large number of measurements are required because the dose per MU to a fixed point in a phantom depends on the size of the beam at that point, generally increasing monotonically with field size.

Measurements of output factors should be performed with an ionization chamber in a water (or water substitute) phantom. The measurements should be at the depth and distance from the source, corresponding to the reference conditions used for calibration. Measurements

should never be made at the depth of dose maximum, but instead should be made at a larger depth such as 5 cm or 10 cm where the influence of electrons scattered from the collimator is negligible. The measured dose rates could then be converted to values at the depth of maximum dose by applying a PDD correction.

### B.3. DOSE CALCULATION ALGORITHMS IN TPS

#### B.3.1. Empirical methods

Empirical methods are limited in accuracy and often fail to model generalized beam set-ups. They use measurements and functions to represent dose in a homogeneous medium, algorithms for reconstituting the treatment beam and correcting it for the clinical situation, beam modifier corrections, contour corrections, and inhomogeneity corrections [120]. When using an empirical method, the total dose in a point P of coordinates  $(x_p, y_p, z_p)$  is calculated as the sum of the contribution of the primary and scattered components.

The empirical methods of dose calculation are using the patient data in the forms described above and dosimetric data measured in water-like medium. The information provided to the TPS is used to calculate the dose inside the patient by first “looking” at the patient as water-like medium and then by applying correction factors for any inhomogeneity that is present. The general rule of this method is:

$$D_{Heterogeneity} = D_{HomogeneousMedium} \times CorrectionFactor \quad (B.31)$$

There are several correction factors that are used in the TPSs:

*Equivalent Path Length Method:* The simplest method to correct for an inhomogeneity is the equivalent path length method. The effective depth to a calculation point P is the thickness of water-equivalent tissue that would attenuate the radiation by the same amount as the actual tissue along a fan line between the surface and point P. It is a one dimensional correction that ignores changes in scatter. If the radiation passes through  $n$  different tissues, each of thickness  $t_i$  and density  $\rho_i$  to reach the calculation point then the effective depth  $d_{eff}$  is:

$$d_{eff} = \sum_{i=1}^n t_i \rho_i \quad (\text{B.32})$$

The dose at a point below the inhomogeneity can be obtained from the uncorrected dose by applying a correction factor,  $C$ , given by [121]:

$$C = \frac{PDD(d_{eff})}{PDD(d)} \times \left( \frac{SSD + d_{eff}}{SSD + d} \right)^2 \quad (\text{B.33})$$

Here  $d$  is actual depth.

*TAR Ratio (or TPR Ratio) Method:* The TAR ratio method is a slightly more precise implementation of the equivalent path length approach. The correction factor is calculated as a ratio of TARs or TPRs. The correction factor to be applied to the uncorrected dose is [121]:

$$C = \frac{T(d_{eff}, A_d)}{T(d, A_d)} \quad (\text{B.34})$$

where  $T$  is the TAR or TPR and  $A_d$  is the field size at depth  $d$ .

*Power-Law Correction (Batho Correction):* The power-law correction is again a ratio of two TARs (or TPRs) but in this instance they are raised to a power that depends on the density of the surrounding material [122]. For a point located in a slab of density  $\rho_1$  overlaid by a slab of density  $\rho_2$ , the correction factor is:

$$C = \frac{TAR(l_2, A_d)^{(\rho_2 - \rho_1)}}{TAR(l_1, A_d)^{(1 - \rho_1)}} \quad (\text{B.35})$$

where  $l_1$  and  $l_2$  are the distances from the point to the upper (i.e. closest to the source) boundaries of inhomogeneities 1 and 2, respectively (Figure B.13).

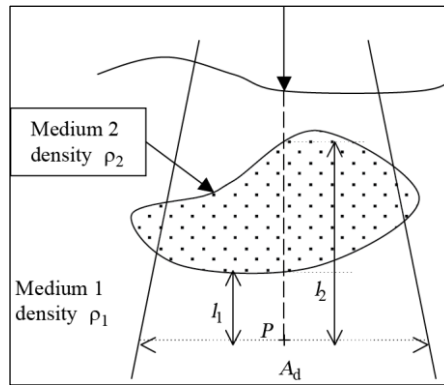


Figure B.13. Illustration of the power law correction method applied at point  $P$

Batho's original suggestion to use TAR has been shown to exaggerate the correction for a point lying in a low density inhomogeneity since it ignores the backscatter from underlying material; the accuracy was improved by using Tissue Maximum Ratio (TMR) or TPR instead [123]. For a series of superimposed inhomogeneous slabs a more general form for this correction can be written as [124,125]:

$$C = \prod_{i=1}^n TPR(l_i, A_d)^{(\rho_i - \rho_{i-1})} \quad (\text{B.36})$$

*Equivalent Tissue Air Ratio Method:* The use of water-equivalent depth in TAR method appropriately corrects for the primary component of dose. However, the change in scattered dose is not correctly predicted because the effect of scattering structures depends on their geometric arrangement with respect to point  $P$ . Sontag and Cunningham [4] accounted for these geometric factors through the scaling of the field size parameter. Their method using "equivalent" tissue air ratios (ETARs) is given by:

$$C = \frac{T(d_{eff}, A'_d)}{T(d, A_d)} \quad (\text{B.37})$$

where  $A_d$  in the numerator has been replaced by  $A'_d$  obtained by scaling  $A_d$  according to the density of the surrounding inhomogeneities. In practice, Sontag and Cunningham scaled the field size using an effective density,  $\tilde{\rho}$  different from the one used for scaling the depth  $d_{eff}$ . The quantity  $\tilde{\rho}$  is calculated as:



$$\tilde{\rho} = \frac{\sum_i \sum_j \sum_k \rho_{ijk} W_{ijk}}{\sum_i \sum_j \sum_k W_{ijk}} \quad (\text{B.38})$$

using the densities  $\rho_{ijk}$  for each voxel  $ijk$  of a series of CT images, where the  $W_{ijk}$  are weighting factors describing the relative contribution of each voxel to the effective density at the calculation point. These weighting factors are different for each calculation point.

### B.3.2. Convolution/Superposition methods

A convolution-superposition method involves a convolution equation that separately considers the transport of primary photons and that of the scatter photon and electron emerging from the primary photon interaction. The dose  $D(\vec{r})$  at a point  $\vec{r}$  is given by (Figure B.14) [60]:

$$\begin{aligned} D(\vec{r}) &= \int \frac{\mu}{\rho} \Psi_p(\vec{r}') A(\vec{r} - \vec{r}') d^3 \vec{r}' \\ &= \int T_p(\vec{r}') A(\vec{r} - \vec{r}') d^3 \vec{r}' \end{aligned} \quad (\text{B.39})$$

where  $\mu/\rho$  is the mass attenuation coefficient,  $\Psi_p(\vec{r}')$  is the primary photon energy fluence, and  $A(\vec{r} - \vec{r}')$  is the convolution kernel (a matrix of dose distribution deposited by scattered photons and electrons set in motion at the primary photon interaction site). The product of mass attenuation coefficient and the primary energy fluence is called terma,  $T_p(\vec{r}')$ , which stands for total energy released per unit mass. Terma is analogous to kerma, which represents the kinetic energy released per unit mass in the form of electrons set in motion by photons. Kernel is the dose matrix generated per unit terma at the interaction site. The product of terma and the dose kernel when integrated (convolved) over a volume gives the dose  $D(\vec{r})$ .

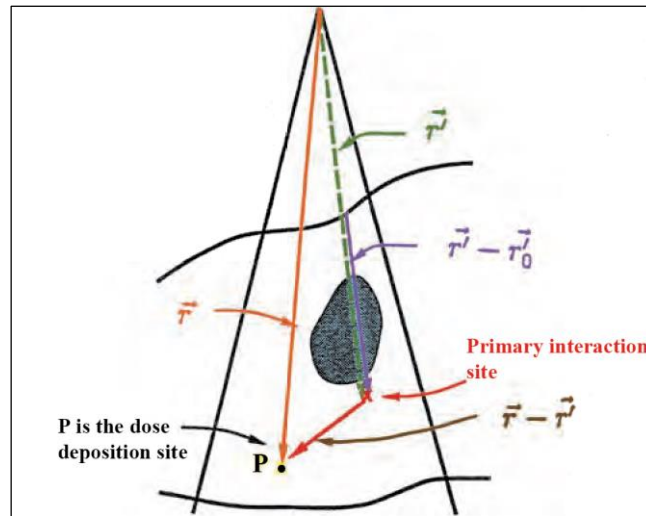


Figure B.14. Geometry of photon interaction and radiation transport from the site of interaction.

The convolution kernel,  $A(\vec{r} - \vec{r}')$ , can be represented by a dose spread array obtained by calculation or by direct measurement. The most commonly used method is the Monte Carlo, which simulates interactions of a large number of primary photons and determines dose deposited in all directions by electrons and scattered photons originating at the primary photon interaction site.

A convolution equation when modified for radiologic path length (distance corrected for electron density relative to water) is called the convolution-superposition equation:

$$D(\vec{r}) = \int T_p(\rho_{\vec{r}} \cdot \vec{r}') A(\rho_{\vec{r}-\vec{r}'} \cdot (\vec{r} - \vec{r}')) d^3\vec{r}' \quad (\text{B.40})$$

where  $\rho_{\vec{r}} \cdot \vec{r}'$  is the radiologic path length from the source to the primary photon interaction site and  $\rho_{\vec{r}-\vec{r}'} \cdot (\vec{r} - \vec{r}')$  is the radiologic path length from the site of primary photon interaction to the site of dose deposition. The dose kernel  $A(\rho_{\vec{r}-\vec{r}'} \cdot (\vec{r} - \vec{r}'))$  can be calculated by using range scaling by electron density of the Monte Carlo-generated kernel in water.

### **B.3.3. Monte Carlo Methods**

The Monte Carlo technique consists of a computer program (MC code) that simulates the transport of millions of photons and particles through matter. It uses fundamental laws of physics to determine probability distributions of individual interactions of photons and particles. The larger the number of simulated particles (histories), the greater the accuracy of predicting their distributions. However, as the number of simulated particles is increased, the computational time becomes prohibitively long. So the challenge in writing an MC code is that of being able to use a relatively small sample of randomly selected particles to predict the average behavior of the particles in the beam. The dose distribution is calculated by accumulating (scoring) ionizing events in bins (voxels) that give rise to energy deposition in the medium. It is estimated that the transport of a few hundred million to a billion histories will be required for radiation therapy treatment planning with adequate precision [60].

Notwithstanding inordinate amounts of computational times, Monte Carlo is the most accurate method of calculating dose distribution in a patient. Sample plans done with Monte Carlo simulation have shown improvements in dose calculation accuracy, especially at interfaces of heterogeneous tissues and in lung where particle disequilibrium can occur under certain conditions. With the continuing advancement in computer technology and computation algorithms, it now seems probable that the Monte Carlo methodology will be implemented for routine treatment planning in the not too distant future.

**APPENDIX C: MATLAB FUNCTION WRITTEN TO CONVERT MONTE CARLO DOSE DISTRIBUTION TO DOSE TO WATER ACCORDING TO RECOMMENDATIONS OF AAPM TASK GROUP NO. 105**

```

function [media,density,medname,dose,err,dwdose] =
doseToWater (MU, filename, dfilename)

%READ phantom file
filename=[filename, '.egsphant'];
fid=fopen(filename);
nummedia = fscanf(fid, '%i');
medname=cell(nummedia,1);

for i=1:nummedia
    medname{i,1}=fgetl(fid);
end

for i=1:nummedia
    estepe(i,:) = fscanf(fid, '%f',1);
end

global xnum;
global ynum;
global znum;

xnum = fscanf(fid, '%i',1);
ynum = fscanf(fid, '%i',1);
znum = fscanf(fid, '%i',1);

xbound = fscanf(fid, '%f',xnum+1);
ybound = fscanf(fid, '%f',ynum+1);
zbound = fscanf(fid, '%f',znum+1);

xbound = dicomrt_mmdigit(xbound,7,10,'fix');
ybound = dicomrt_mmdigit(ybound,7,10,'fix');
zbound = dicomrt_mmdigit(zbound,7,10,'fix');

%LOAD the material matrix
media=[];
for k=1:znum
    media_temp = fscanf(fid, '%li', [xnum, ynum]);
    media(:, :, k) = media_temp';
    line = fgets(fid);
end
%LOAD the density matrix
for k = 1:znum
    density_temp = fscanf(fid, '%f', [xnum, ynum]);
    density(:, :, k) = density_temp';
end
fclose(fid);

```

```

%READ 3ddose file
dfid = fopen(dfilename,'r');

dxnum = fscanf(dfid,'%i',1);
dynam = fscanf(dfid,'%i',1);
dznum = fscanf(dfid,'%i',1);

dxbound = fscanf(dfid,'%f',dxnum+1);
dybound = fscanf(dfid,'%f',dynam+1);
dzbound = fscanf(dfid,'%f',dznum+1);

dxbound = dicomrt_mmdigit(dxbound,7);
dybound = dicomrt_mmdigit(dybound,7);
dzbound = dicomrt_mmdigit(dzbound,7);

%LOAD the dose matrix
for j = 1:dznum
    dose_temp = fscanf(dfid,'%e',[dxnum, dynam]);
    dose(:, :, j) = MU*1.388149E+14*dose_temp';
end
%LOAD the error matrix
for j = 1:dznum
    error_temp = fscanf(dfid,'%e',[dxnum, dynam]);
    err(:, :, j) = error_temp';
end
fclose(dfid);

%Dose to water calculation
media_temp = media;

media_temp(media_temp == 1) = 1.117; %For Air
media_temp(media_temp == 2) = 0.999; %For Lung
media_temp(media_temp == 3) = 0.999; %For Lung
media_temp(media_temp == 4) = 1.01; %For Tissue
media_temp(media_temp == 5) = 1.01; %For Tissue
media_temp(media_temp == 6) = 1.01; %For Tissue
media_temp(media_temp == 7) = 1.116; %For Bone
media_temp(media_temp == 8) = 1.116; %For Bone

```

## APPENDIX D: AN EXAMPLE INPUT SCRIPT FOR MC SIMULATION OF ELEKTA SYNERGY MLC<sub>i</sub> TREATMENT HEAD\*

```

Elekta Synergy - Build on 27.08.2010                                     #!GUI1.0
AIR700ICRU
0, 0, 0, 0, 0, 2, 1,  IWATCH ETC.
100000000, 37, 84, 990, 2, 1000, 0, 0,  NCASE ETC.
15, 100, 3, 4, 1, 0.0, 0.0,  DIRECTIONAL BREM OPTIONS
-1, 19, -0.1, 0, 0, 1, 0, -0.1, 0.0, 0.0,  IQIN, ISOURCE + OPTIONS
1, SPECTRUM
/home/turkay/HEN_HOUSE/spectra/synergy5p8MV1FWHM.spectrum
1
0, 0, 0.7, 0.01, 0, -2, 2.0, 0,  ECUT, PCUT, IREJCT, ESAVE
0, 0, 0, 0, 0,  PHOTON FORCING
1, 12,  SCORING INPUT
10, 0
2, 4, 6, 8, 10, 12, 14, 16, 18, 20,
0,  DOSE COMPONENTS
0.0, Z TO FRONT FACE
***** start of CM SLABS with identifier Target *****
0, RMAX
Tungsten target
1, NSLABS
0, ZMIN
0.0, 0.7, 0.01, 1, 1, 1.0
W700ICRU
***** start of CM CONS3R with identifier PrimCol *****
0, RMAX
Primary collimator
0.0, ZMIN
0.0, ZTHICK
2, NUM_NODE
0.0, 0.0,
0.0, 0.0,
0.7, 0.01, 0, 0, 0,
AIR700ICRU
0.7, 0.01, 2, 2, 0,
WRE_18P0_700
***** start of CM FLATFILT with identifier ScatFilt *****
0, RMAX
Flattening filter with radius of 5 cm
0.0, ZMIN
6, NUMBER OF LAYERS
1, 0.0, # CONES, ZTHICK OF LAYER 1
0.0,
0.0,
1, 0.0, # CONES, ZTHICK OF LAYER 2
0.0,
0.0,
1, 0.0, # CONES, ZTHICK OF LAYER 3
0.0,
0.0,
1, 0.0, # CONES, ZTHICK OF LAYER 4
0.0,
0.0.

```

```

1, Ø.ØØ, # CONES, ZTHICK OF LAYER 5
Ø.ØØ,
Ø.ØØ,
1, Ø.ØØ, # CONES, ZTHICK OF LAYER 6
Ø.ØØ,
Ø.ØØ,
0.7, 0.01, 3, 3,
STEEL700ICRU
0.7, 0.01, 0, 0,
AIR700ICRU
0.7, 0.01, 3, 3,
STEEL700ICRU
0.7, 0.01, 0, 0,
AIR700ICRU
0.7, 0.01, 3, 3,
STEEL700ICRU
0.7, 0.01, 0, 0,
AIR700ICRU
0.7, 0.01, 3, 3,
STEEL700ICRU
0.7, 0.01, 0, 0,
AIR700ICRU
0.7, 0.01, 3, 3,
STEEL700ICRU
0.7, 0.01, 0, 0,
AIR700ICRU
0.7, 0.01, 3, 3,
STEEL700ICRU
0.7, 0.01, 0, 0,
AIR700ICRU
***** start of CM SLABS with identifier Alcarr *****
Ø.Ø, RMAX
2 mm thick Al filter carrier
1, NSLABS
ØØ.ØØ, ZMIN
0.2, 0.7, 0.01, 4, 4, 1.0
AL700ICRU
***** start of CM CHAMBER with identifier Chamber *****
9, RMAX
15 mm thick ionisation chamber
16.44, ZMIN
0, 7, 0, N_TOP, N_CHM, N_BOT
8, 8.4, 8.6, RADII FOR CENTRAL PART
0.009, 0, ZTHICK, FLAG FOR LAYER 1 IN CENTRAL PART
0.7, 0.01, 5, 5,
MYLAR700ICRU
0.001, 0, ZTHICK, FLAG FOR LAYER 2 IN CENTRAL PART
0.7, 0.01, 6, 5,
AL700ICRU
0.6, 0, ZTHICK, FLAG FOR LAYER 3 IN CENTRAL PART
0.7, 0.01, 7, 5,
AIR700ICRU
0.005, 0, ZTHICK, FLAG FOR LAYER 4 IN CENTRAL PART
0.7, 0.01, 6, 5,
AL700ICRU
0.6, 0, ZTHICK, FLAG FOR LAYER 5 IN CENTRAL PART
0.7, 0.01, 7, 5,
AIR700ICRU
0.001, 0, ZTHICK, FLAG FOR LAYER 6 IN CENTRAL PART
0.7, 0.01, 6, 5.

```

```

AL700ICRU
0.009, 0, ZTHICK, FLAG FOR LAYER 7 IN CENTRAL PART
0.7, 0.01, 5, 5,
MYLAR700ICRU
0.7, 0.01, 0, 6, chamber wall
MYLAR700ICRU
0.7, 0.01, 0, 6, gap
AIR700ICRU
0.7, 0.01, 0, 6, container
MYLAR700ICRU
1, MRNGE
***** start of CM SLABS with identifier BackScat *****
7, RMAX
2 mm thick Al plate
1, NSLABS
ØØ.ØØ, ZMIN
0.3, 0.7, 0.01, 8, 7, 1.0
AL700ICRU
***** start of CM MIRROR with identifier Ayna *****
10, RMAX
Mirror
21.0, 6.0, ZMIN, ZTHICK
3.0, -3.0, XFMIN, XBMIN
2, # LAYERS
0.0001, thickness of layer 1
0.0065, thickness of layer 2
0.7, 0.01, 9, 8,
AL700ICRU
0.7, 0.01, 10, 8,
PMMA700ICRU
0.7, 0.01, 0, 0,
AIR700ICRU
0.7, 0.01, 0, 0,
AIR700ICRU
***** start of CM MLCE with identifier MLC *****
30, RMAX
MLC collimator
1, ORIENT
40, NUM_LEAF
ØØ.Ø, ØØ.Ø, ZMIN, ZMAX
ØØ.Ø, ØØ.Ø, ZSTEPL, ZSTEPR
Ø.ØØ, TGW
Ø.ØØ, Ø.ØØ, X3, X4
1, 100, SPACE, SSD
0, LBROT
0, ENDTYPE
ØØ, ØØ.Ø, LEAFRADIUS, CIL
-14.664, 15.336, 10
-14.664, 15.336, 1
-14.664, 15.336, 1
-15.5712, 15.6384, 1
-15.8064, 15.84, 1
-16.3776, 16.1088, 1
-16.5792, 16.4112, 1
-16.9152, 16.8816, 1
-16.9488, 16.9488, 1
-16.9824, 16.9824, 1
-17.016, 16.9488, 1
-16.9488, 16.9488, 1

```



```

-16.8816, 16.8144, 1
-16.7136, 16.4784, 1
-16.5456, 16.5456, 1
-16.2096, 16.5456, 1
-16.1088, 16.512, 1
-15.9408, 16.344, 1
-15.336, 16.1424, 1
-14.664, 15.336, 1
-14.664, 15.336, 1
-14.664, 15.336, 10
0.7, 0.01, 0, 23,
AIR700ICRU
0.7, 0.01, 12, 10,
WRE_18P0_700
***** start of CM MLCQ with identifier Backup *****
30, RMAX
X Backup Jaws
1, IDMLFC
ØØ.Ø, ZMIN
3, ZTHICK
2, 50, # LEAVES, TOTAL WIDTH
0, ZFOCUS(1)
Ø, ØØ.Ø, RØLEAF, ZØLEAF
-9.466, 9.4249, 2
0.7, 0.01, 0, 23,
AIR700ICRU
0.7, 0.01, 0, 23,
WRE_18P0_700
***** start of CM JAWS with identifier YJaws *****
30, RMAX
Y jaws
1, # PAIRED BARS OR JAWS
Y
ØØ.Ø, ØØ.Ø, 3.10320, 3.66480, -3.14630, -3.71570,
0.7, 0.01, 0, 23,
0.7, 0.01, 0, 23,
WRE_18P0_700
***** start of CM SLABS with identifier MylarSht *****
20, RMAX
Mylar crosswire sheet
1, NSLABS
ØØ.Ø, ZMIN
0.2, 0.7, 0.01, 14, 12, 0
MYLAR700ICRU
***** start of CM SLABS with identifier PhSp *****
20, RMAX
0.01 cm thick slab for PhSp at 70 cm
1, NSLABS
69.99, ZMIN
0.01, 0.7, 0.01, 15, 13, 0
AIR700ICRU
*****end of all CMs*****
#####
:Start MC Transport Parameter:

Global ECUT= 0.7
Global PCUT= 0.01
Global SMAX= 5
ESTEPE= 0.25
XIMAX= 0.5

```

```

Boundary crossing algorithm= EXACT
Skin depth for BCA= 0
Electron-step algorithm= PRESTA-II
Spin effects= On
Brems angular sampling= Simple
Brems cross sections= NRC
Bound Compton scattering= Off
Compton cross sections= default
Pair angular sampling= Simple
Pair cross sections= BH
Photoelectron angular sampling= Off
Rayleigh scattering= Off
Atomic relaxations= Off
Electron impact ionization= Off
Photon cross sections= si
Photon cross-sections output= On

```

```

:Stop MC Transport Parameter:
#####
:Start DBS rejection plane:

Use a rejection plane= On
Z(cm) from zero reference plane= 60

:Stop DBS rejection plane:
#####
:Start BCSE:

Use BCSE= On
Media to enhance= W700ICRU
Enhancement constant= 5
Enhancement power= 2
Russian Roulette= on

:Stop BCSE:
#####

```

\* Characters with “Ø” sign represent numbers which were hidden due to “Non-Disclosure Agreement” signed between manufacturer of the linac and the user.

**APPENDIX E: COMPLETE SET OF PDD COMPARISONS BETWEEN MC SIMULATION AND IONISATION CHAMBER MEASUREMENTS**

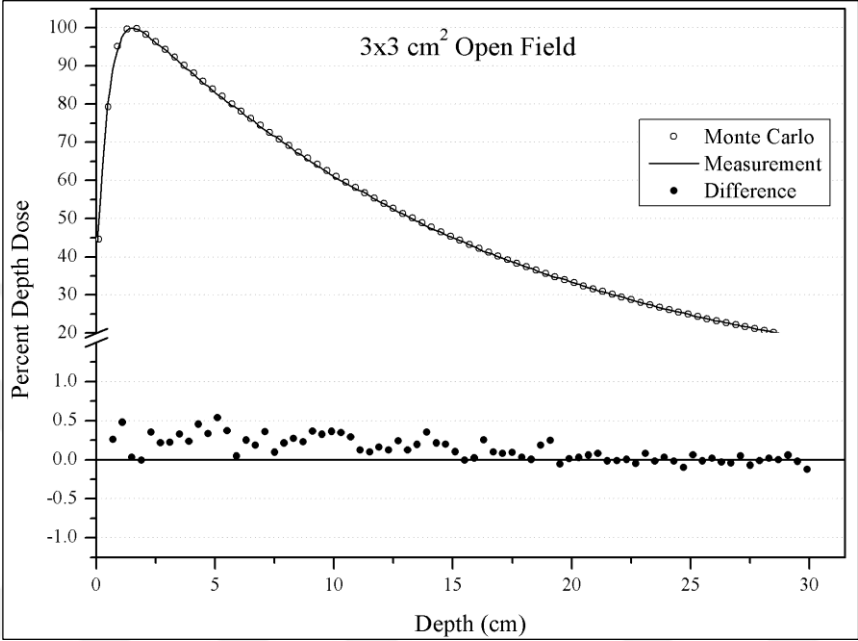


Figure E.1. PDD comparison for 3×3 cm<sup>2</sup> open field, SSD=100 cm

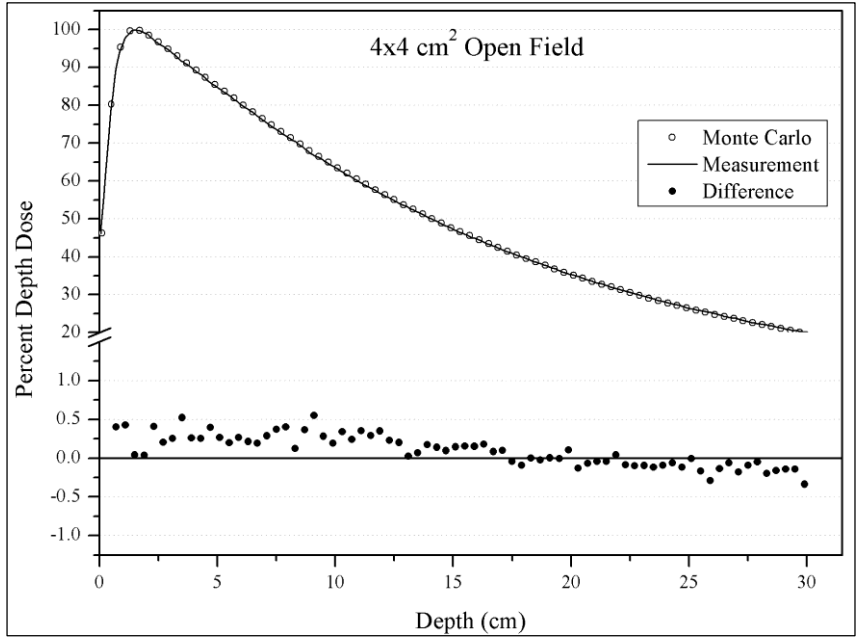


Figure E.2. PDD comparison for 4×4 cm<sup>2</sup> open field, SSD=100 cm

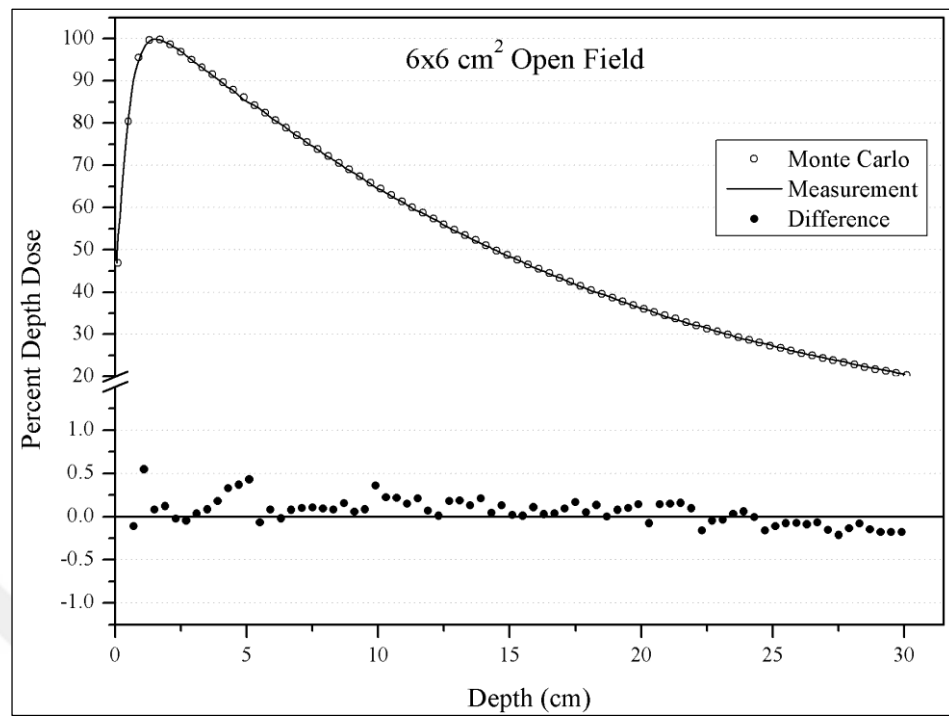


Figure E.3. PDD comparison for 6×6 cm<sup>2</sup> open field, SSD=100 cm

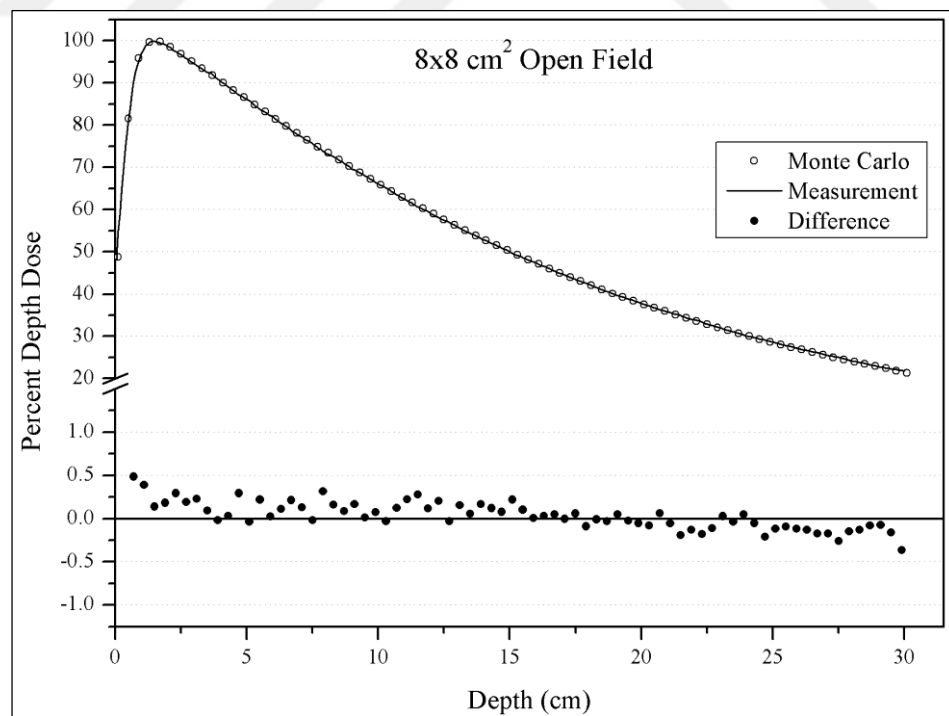


Figure E.4. PDD comparison for 8×8 cm<sup>2</sup> open field, SSD=100 cm

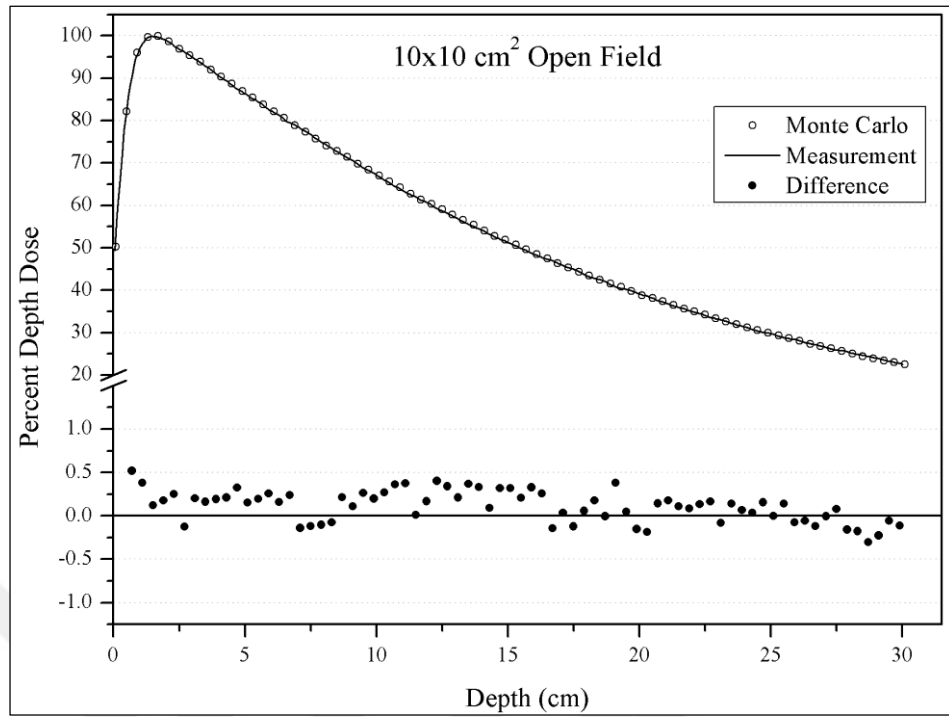


Figure E.5. PDD comparison for 10×10 cm<sup>2</sup> open field, SSD=100 cm

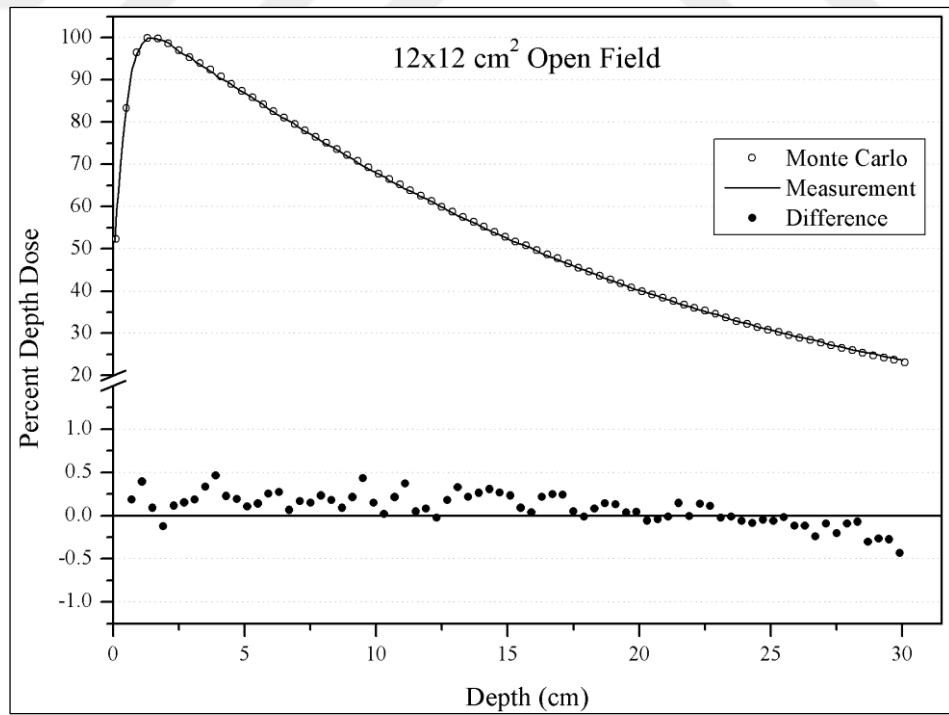


Figure E.6. PDD comparison for 12×12 cm<sup>2</sup> open field, SSD=100 cm

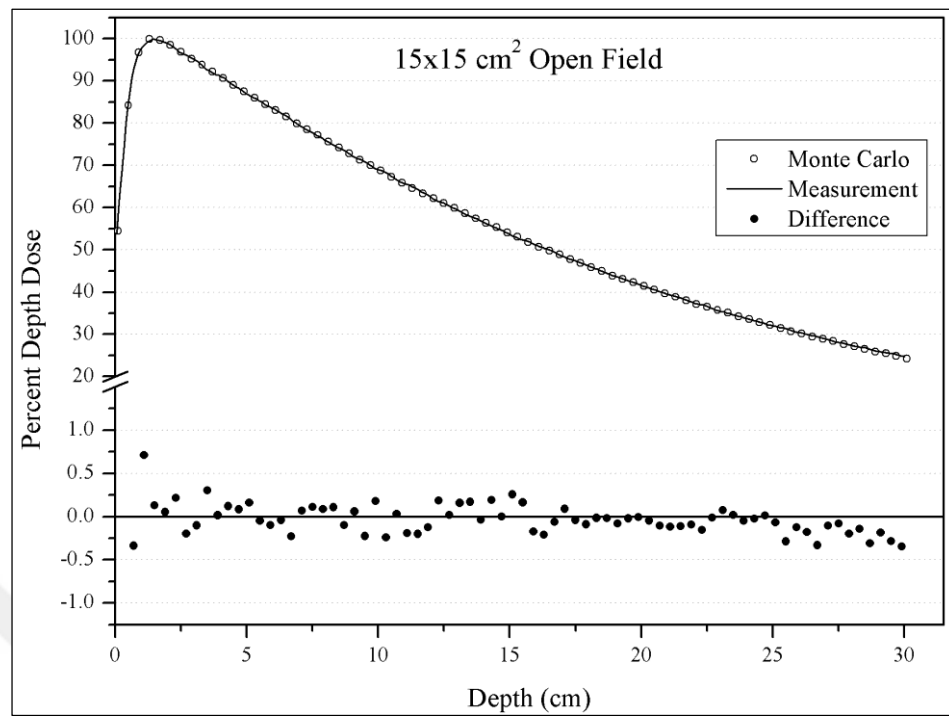


Figure E.7. PDD comparison for 15×15 cm<sup>2</sup> open field, SSD=100 cm

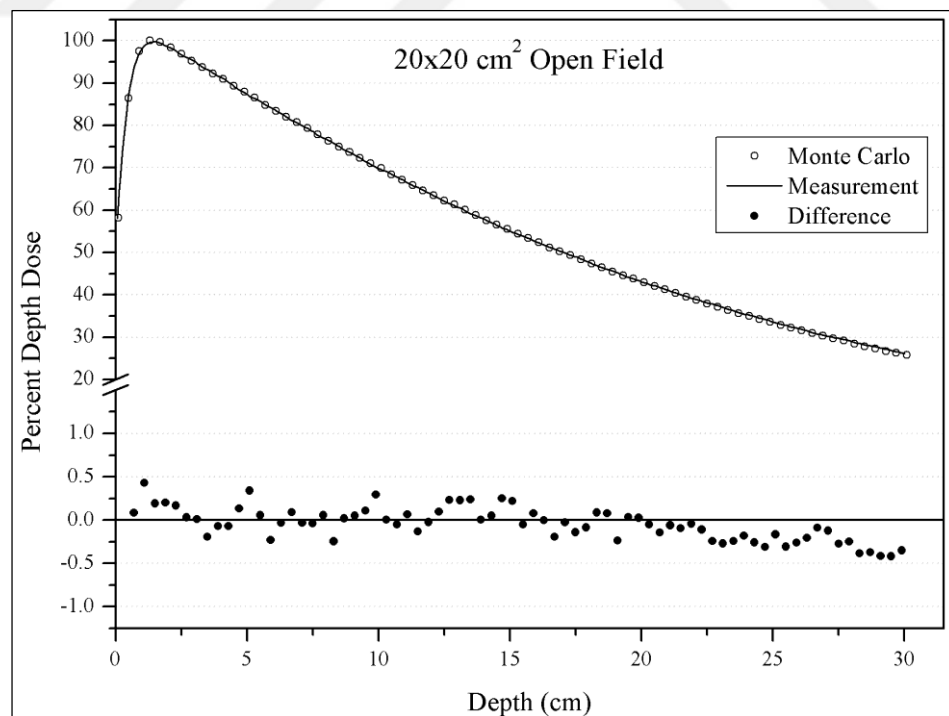


Figure E.8. PDD comparison for 20×20 cm<sup>2</sup> open field, SSD=100 cm

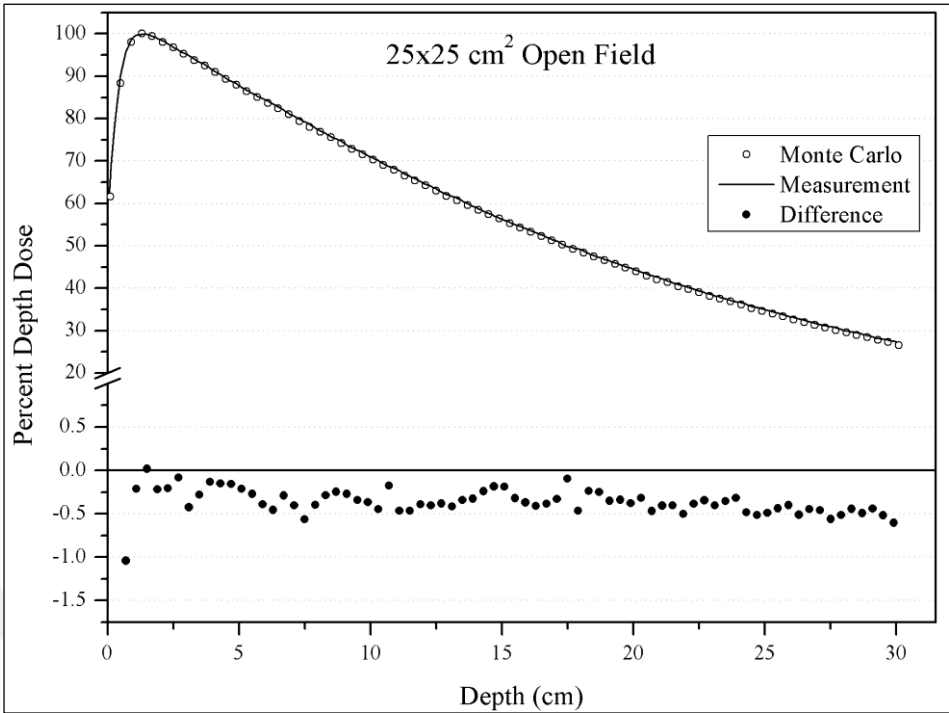


Figure E.9. PDD comparison for 25x25 cm² open field, SSD=100 cm

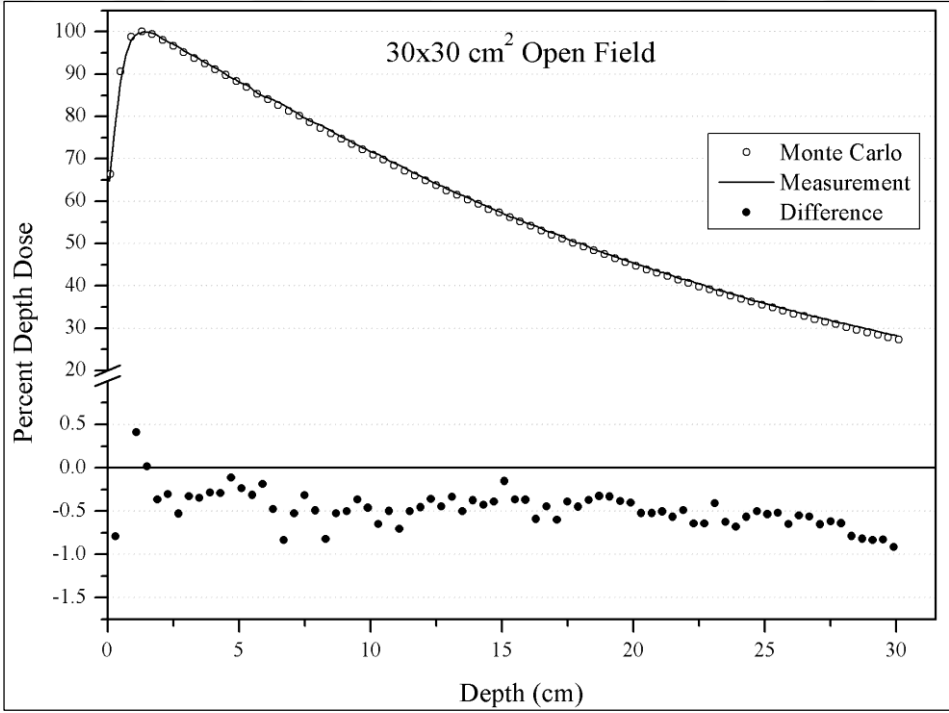


Figure E.10. PDD comparison for 30x30 cm² open field, SSD=100 cm

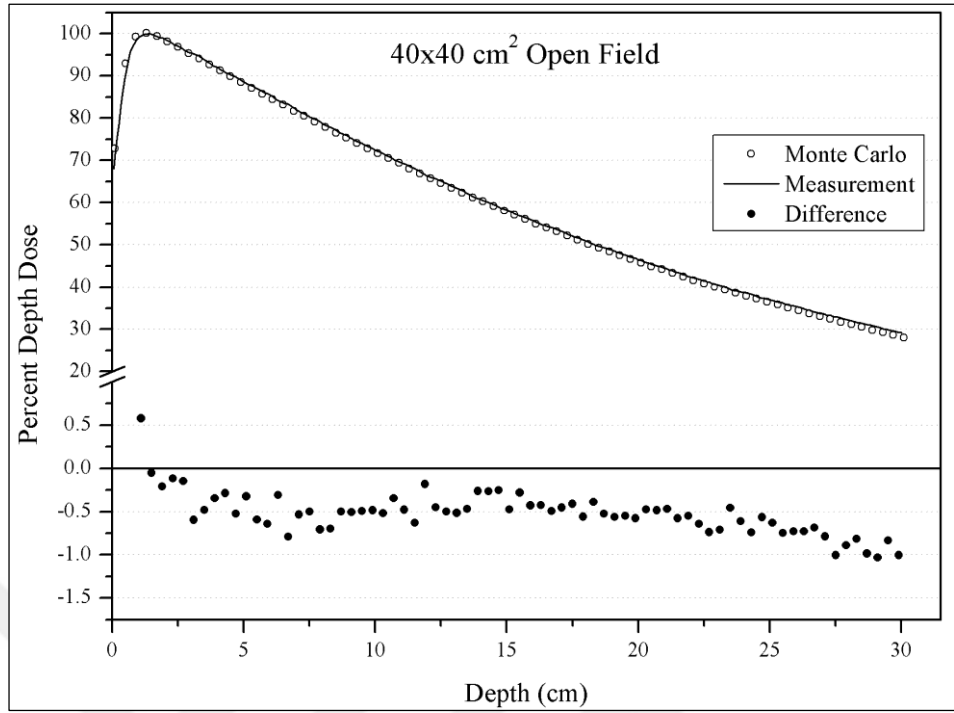


Figure E.11. PDD comparison for 40×40 cm<sup>2</sup> open field, SSD=100 cm

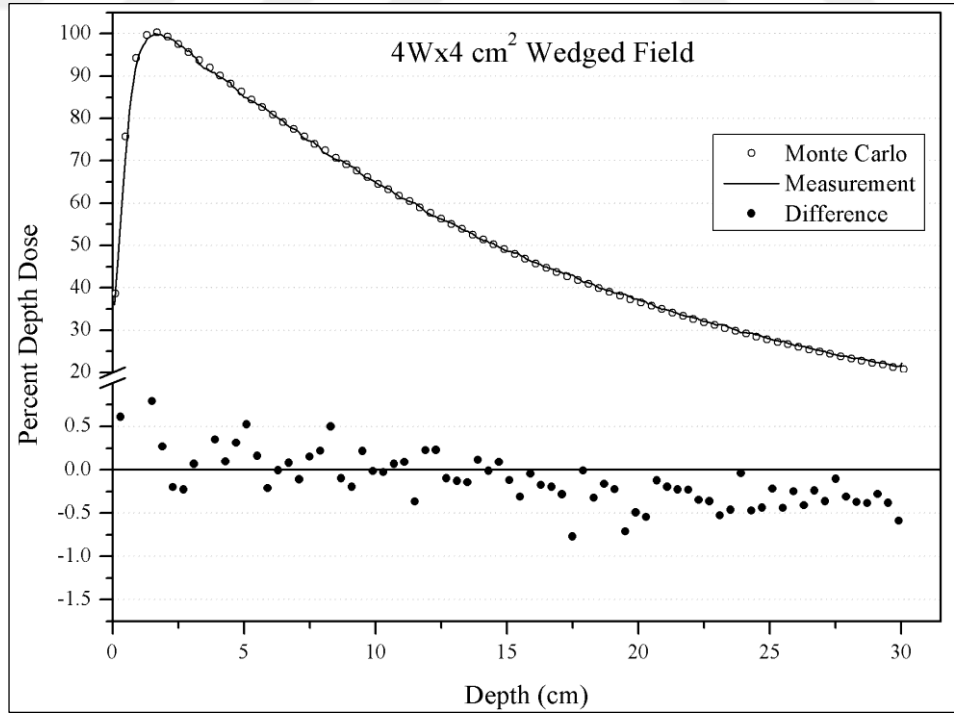


Figure E.12. PDD comparison for 4W×4 cm<sup>2</sup> wedged field, SSD=100 cm



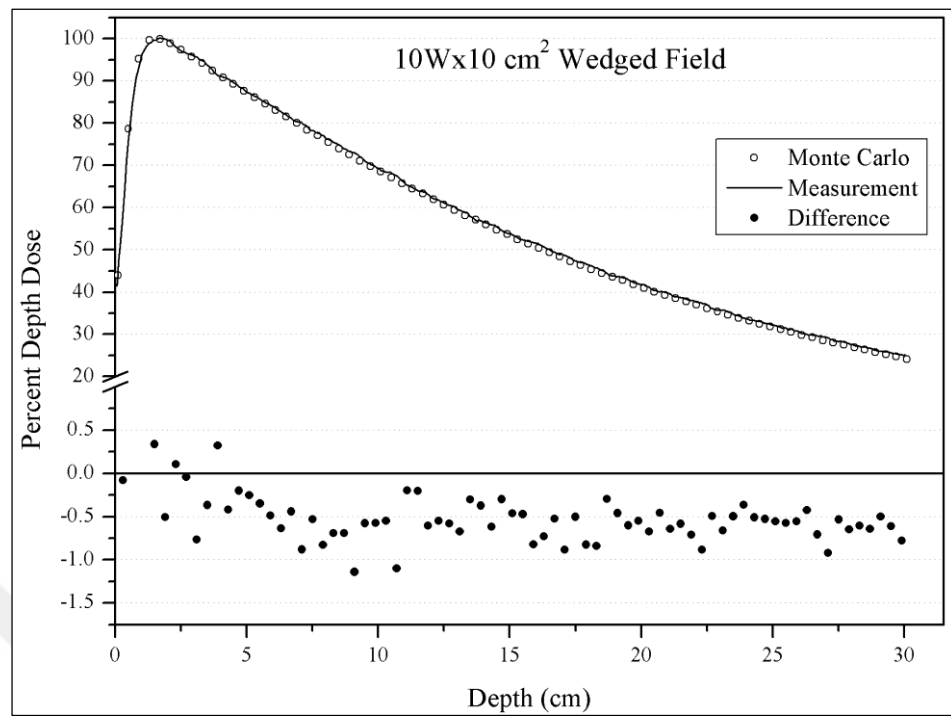


Figure E.13. PDD comparison for 10W×10 cm<sup>2</sup> wedged field, SSD=100 cm

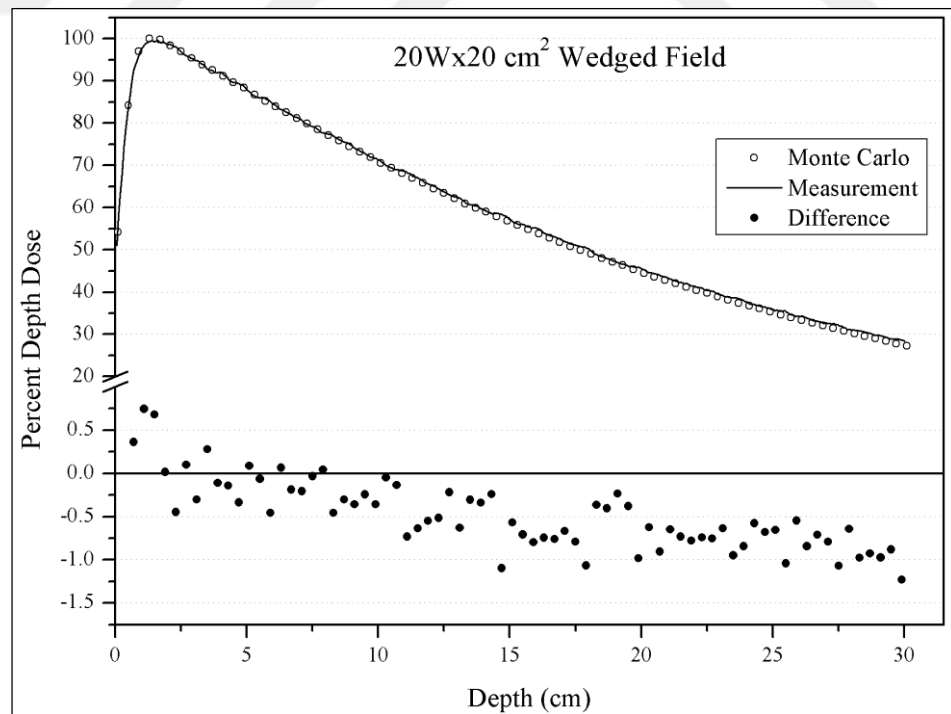


Figure E.14. PDD comparison for 20W×20 cm<sup>2</sup> wedged field, SSD=100 cm

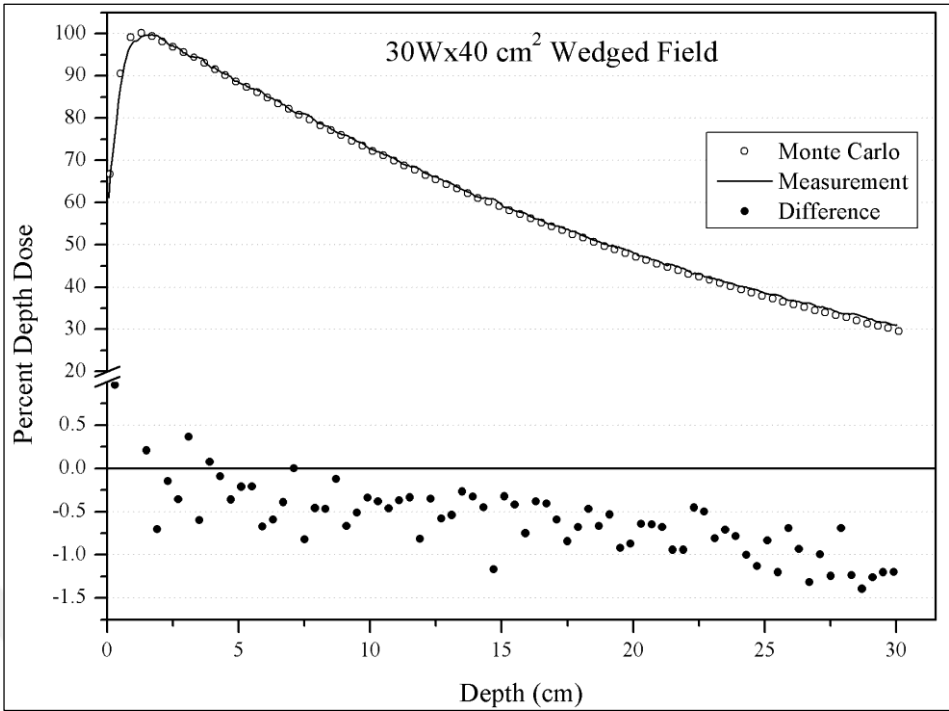


Figure E.15. PDD comparison for 30W×40 cm<sup>2</sup> wedged field, SSD=100 cm

**APPENDIX F: THE COMPLETE SET OF DOSE DISTRIBUTIONS  
OBTAINED FROM TPS<sub>PB</sub>**

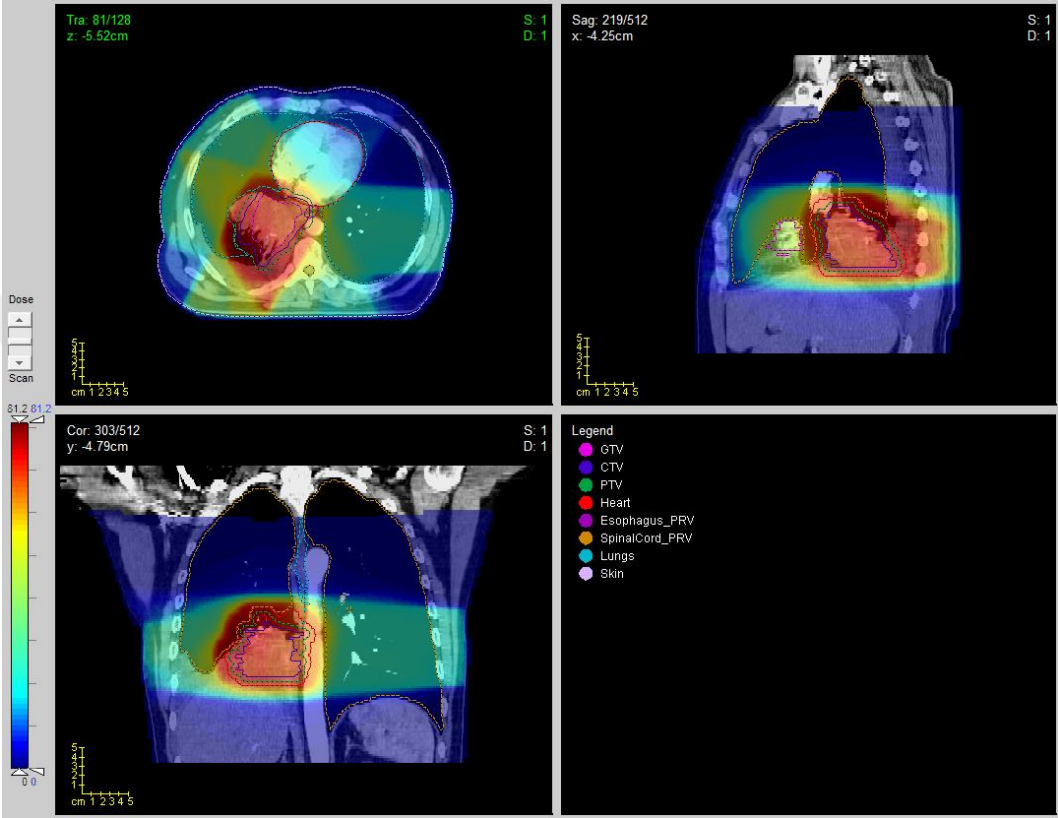


Figure F.1. Dose distribution for Patient-1

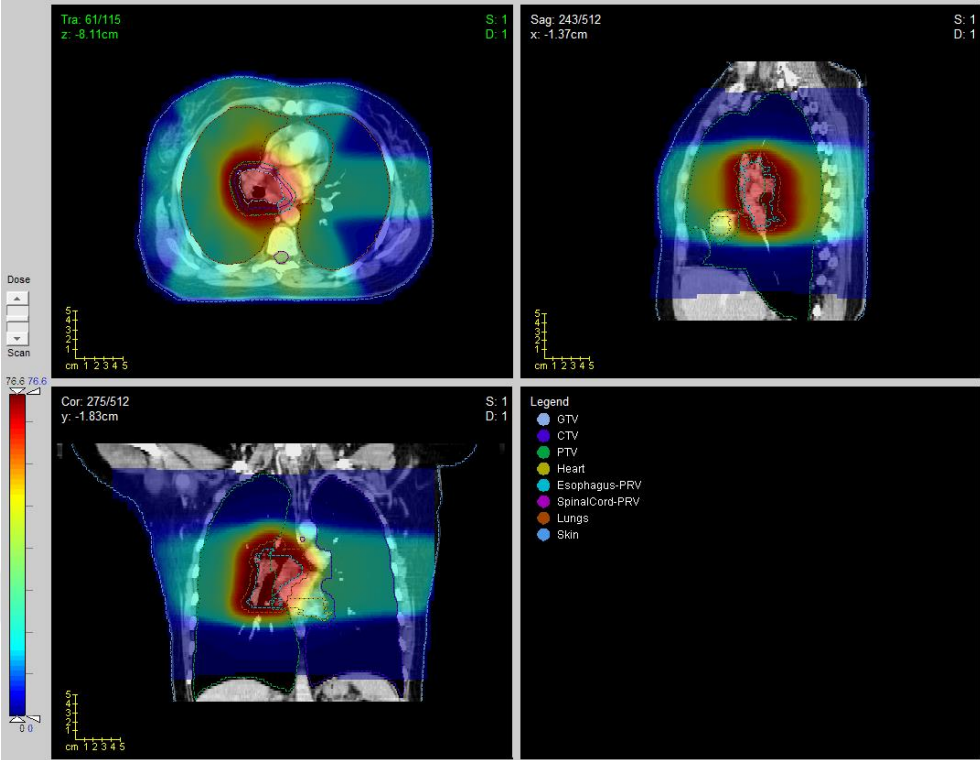


Figure F.2. Dose distribution for Patient-2

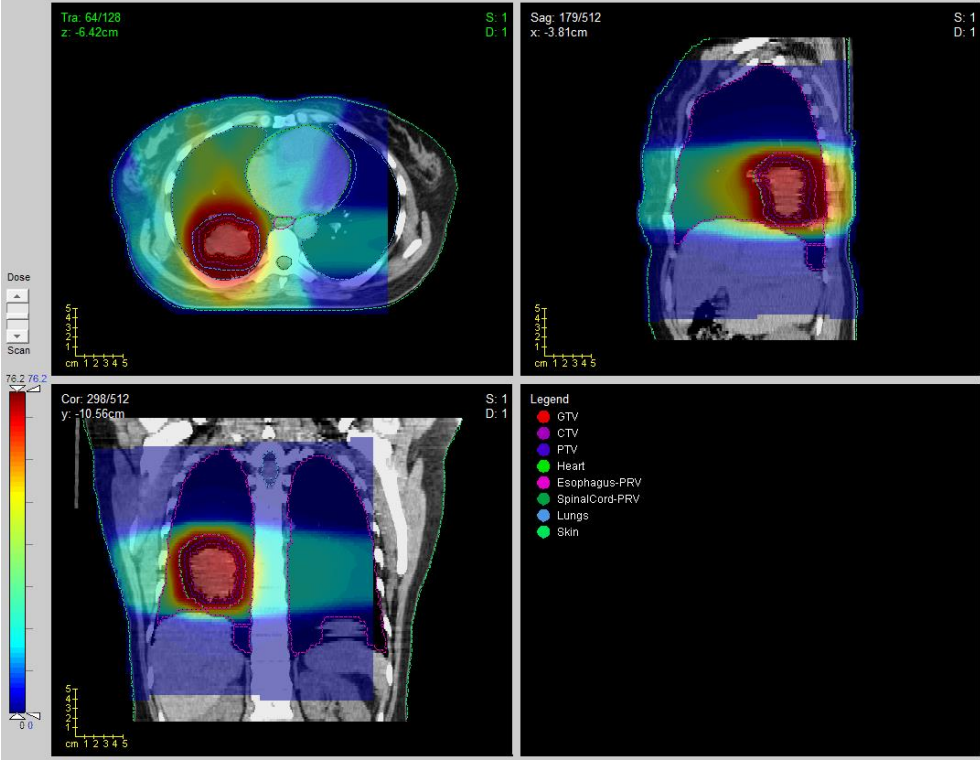


Figure F.3. Dose distribution for Patient-3

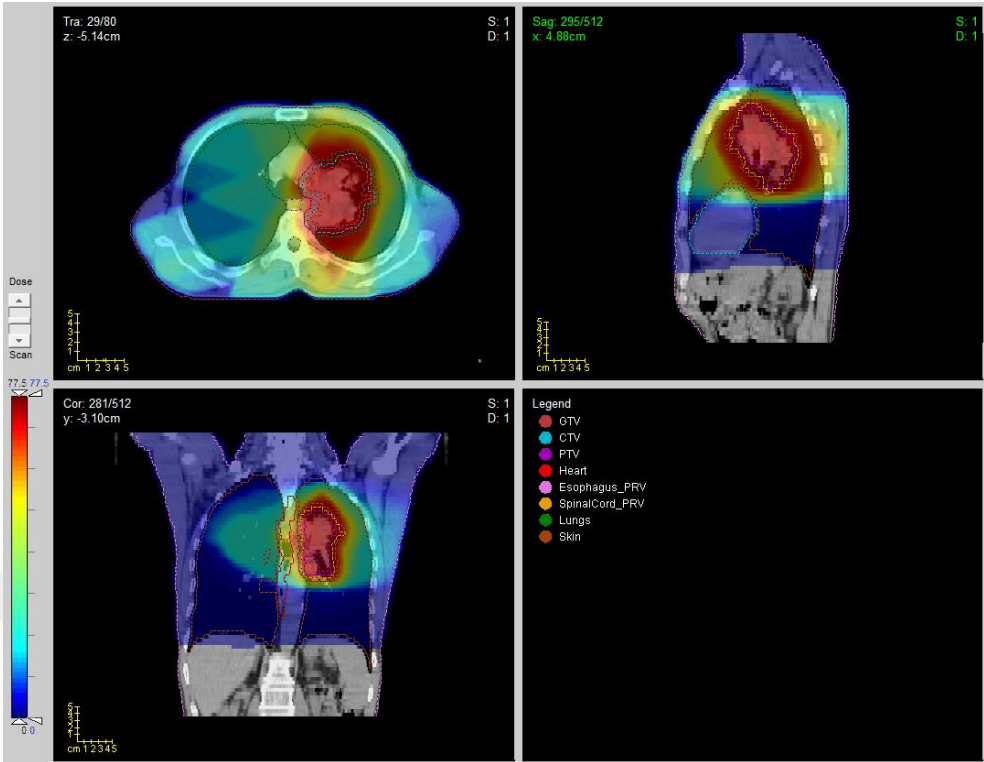


Figure F.4. Dose distribution for Patient-4

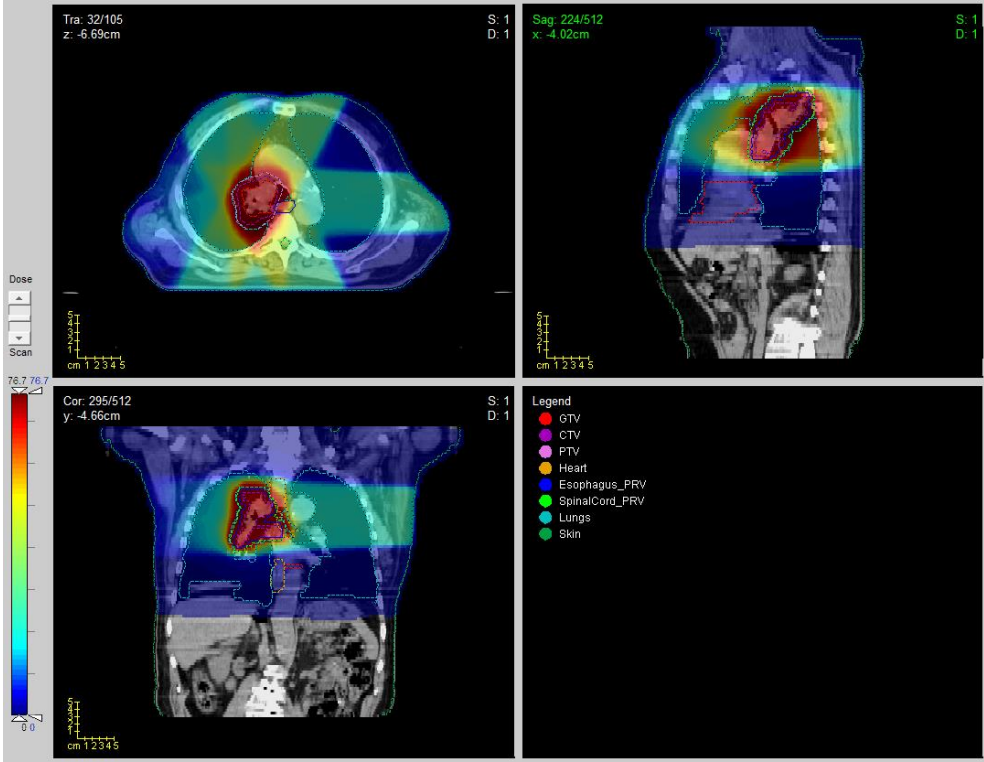


Figure F.5. Dose distribution for Patient-5

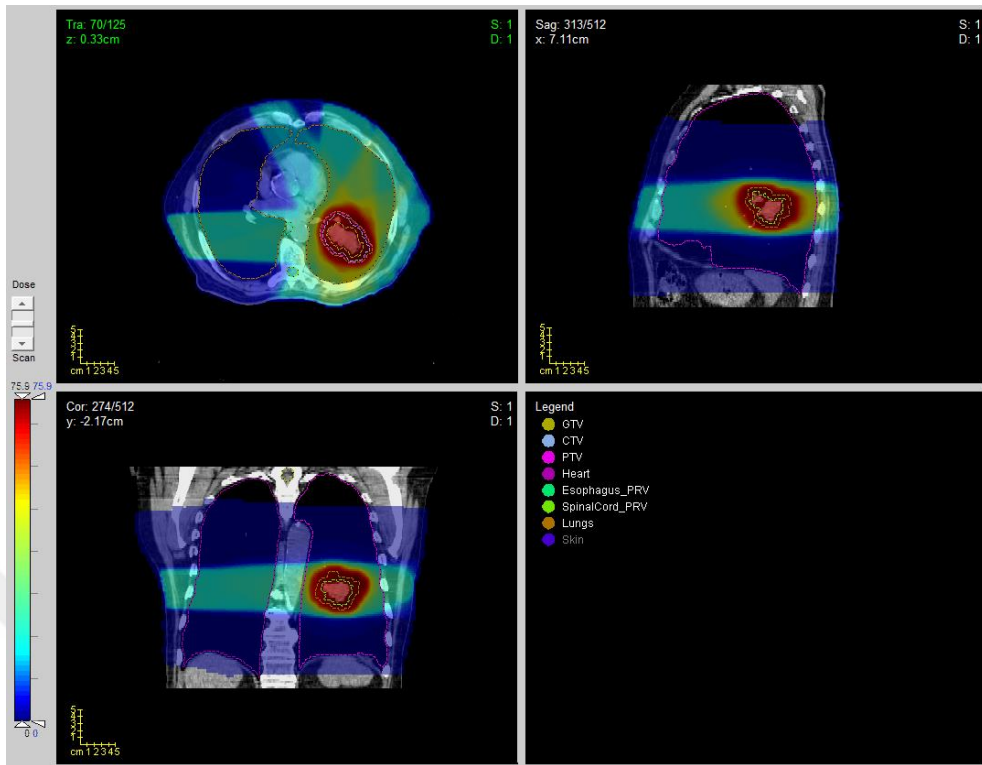


Figure F.6. Dose distribution for Patient-6

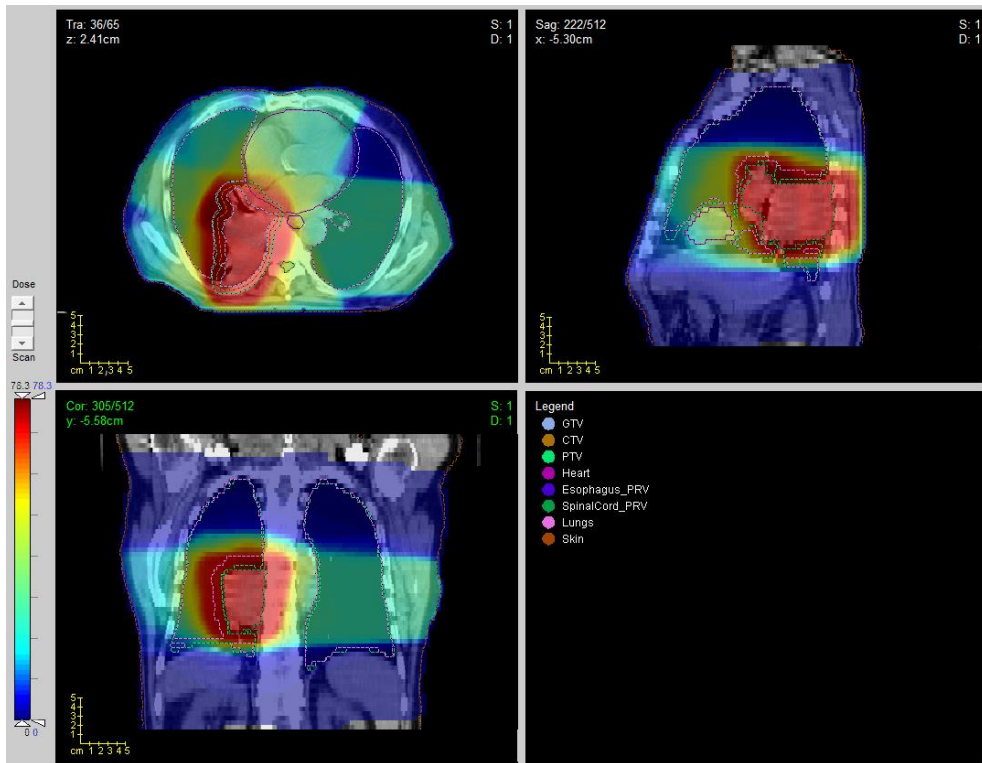


Figure F.7. Dose distribution for Patient-7

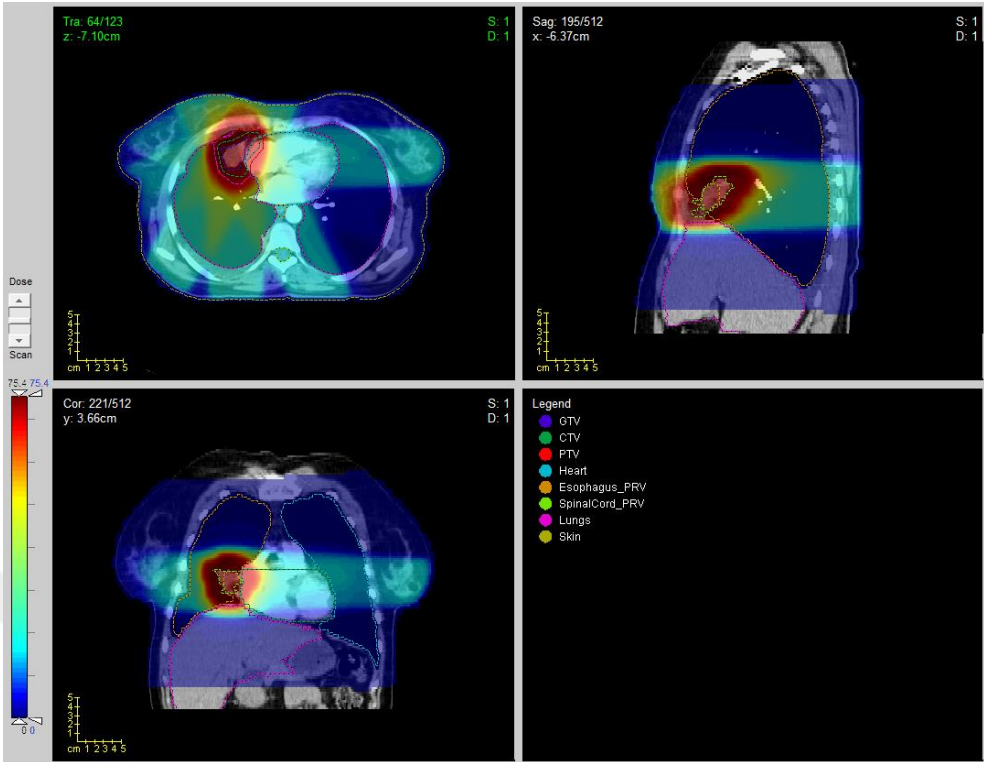


Figure F.8. Dose distribution for Patient-8

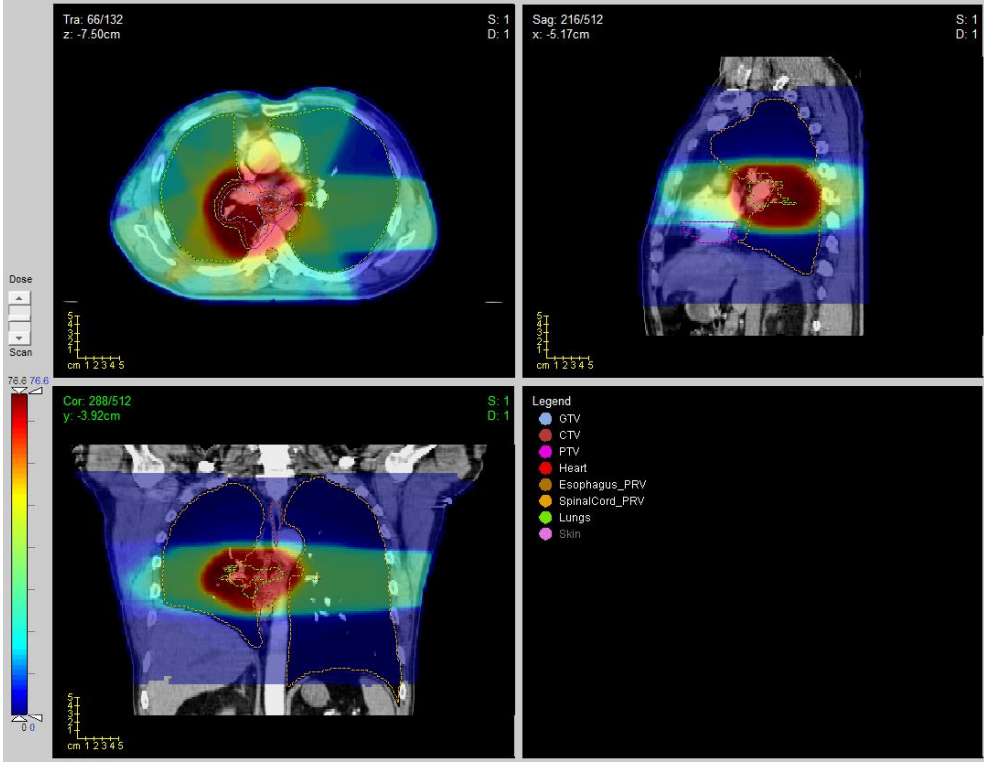


Figure F.9. Dose distribution for Patient-9

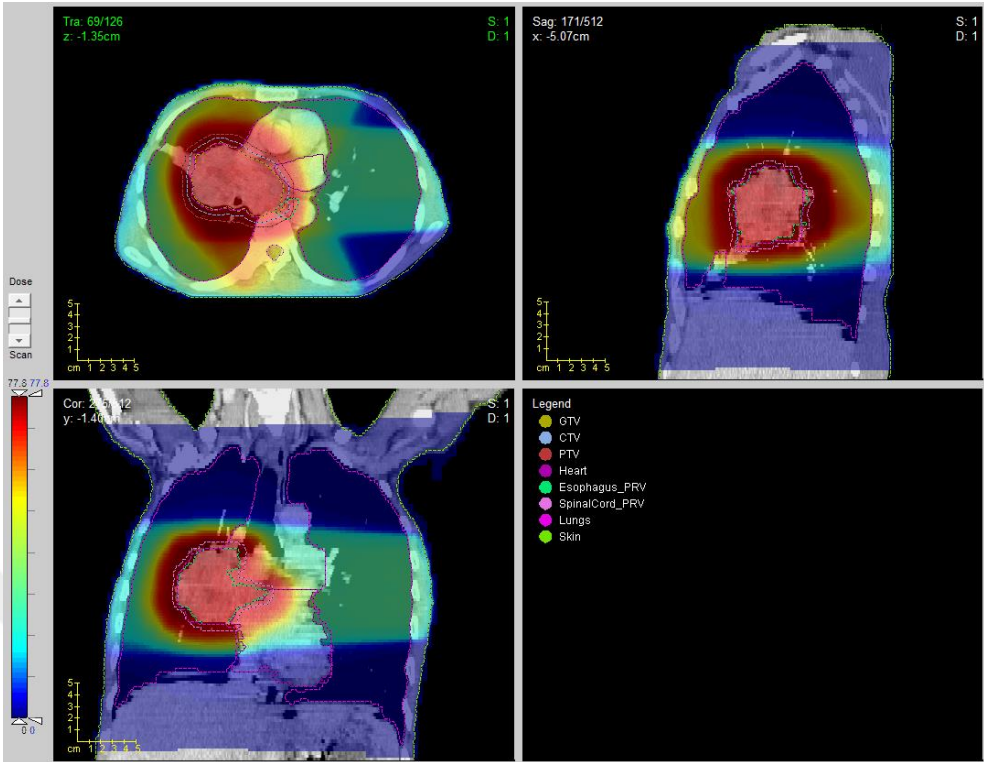


Figure F.10. Dose distribution for Patient-10

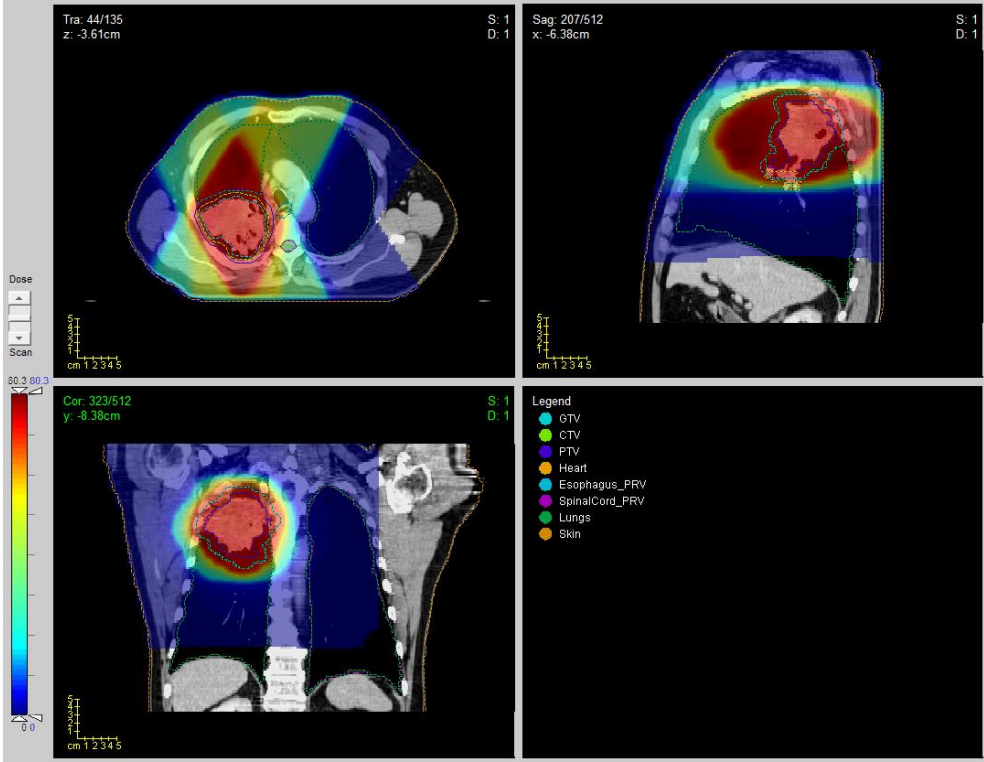


Figure F.11. Dose distribution for Patient-11



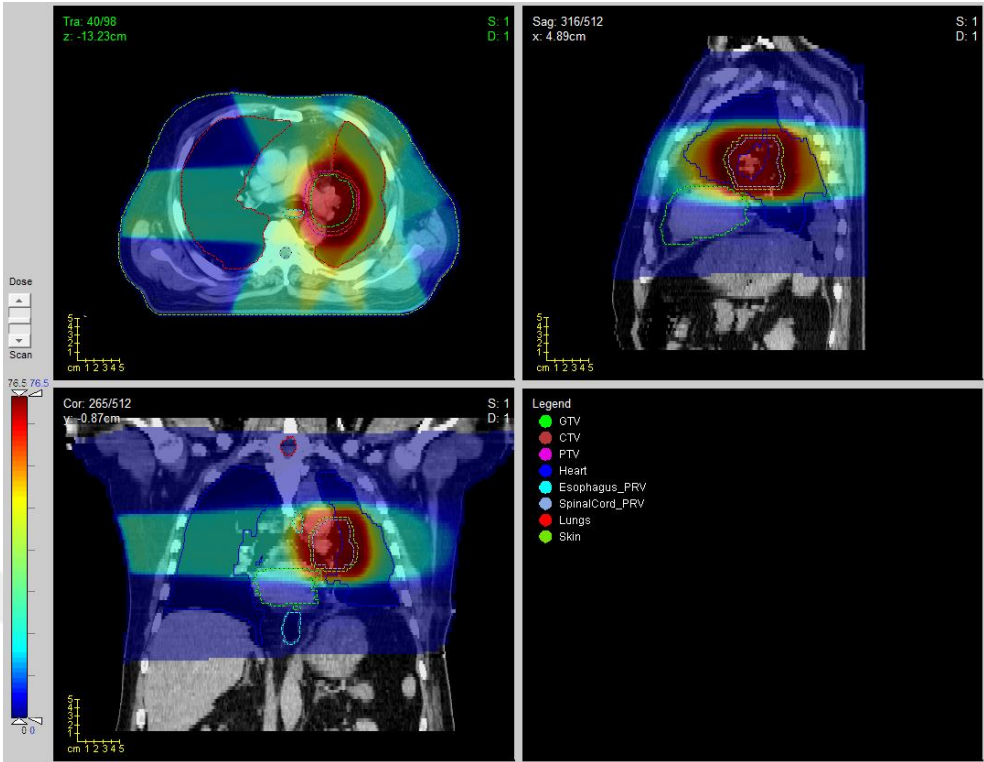


Figure F.12. Dose distribution for Patient-12

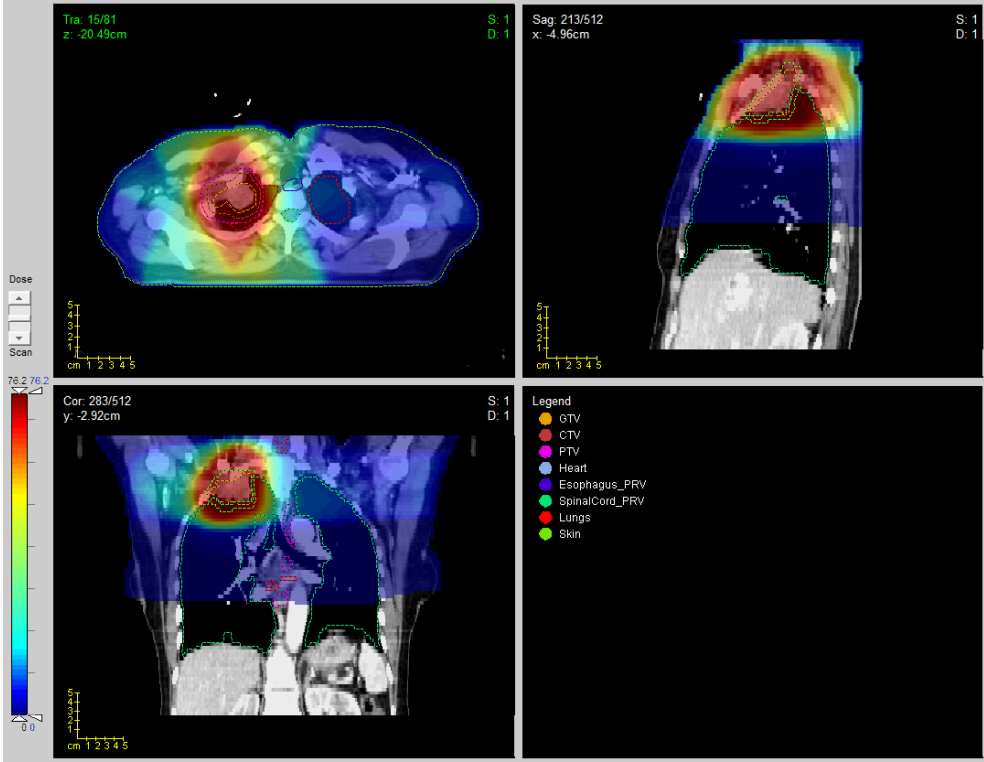


Figure F.13. Dose distribution for Patient-13

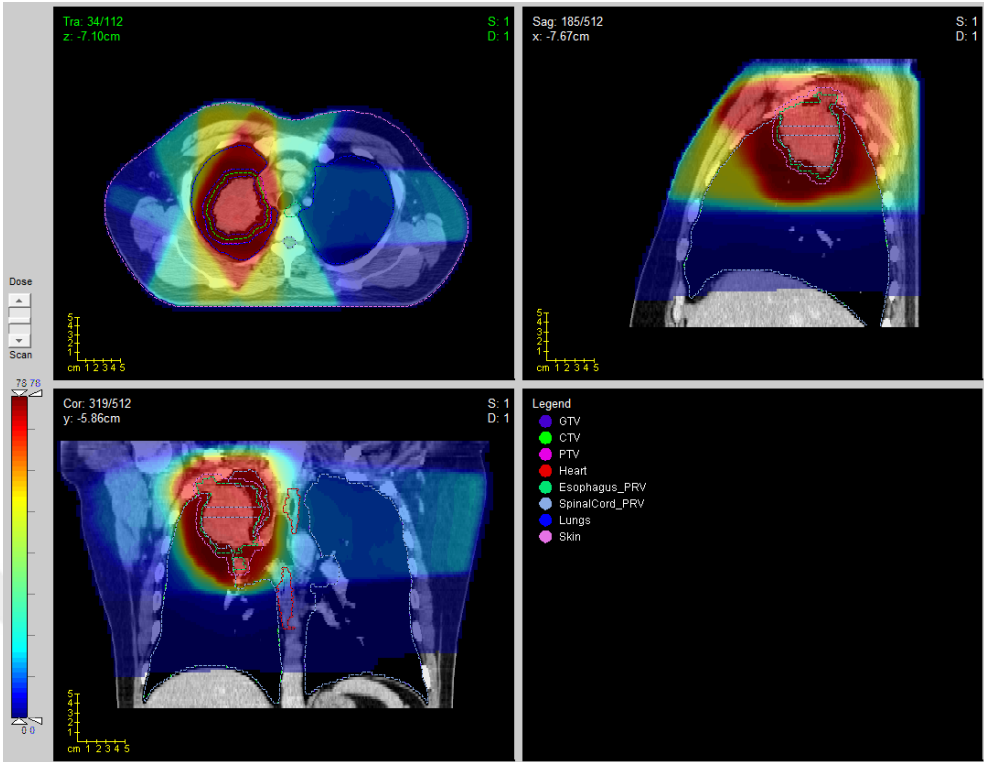


Figure F.14. Dose distribution for Patient-14

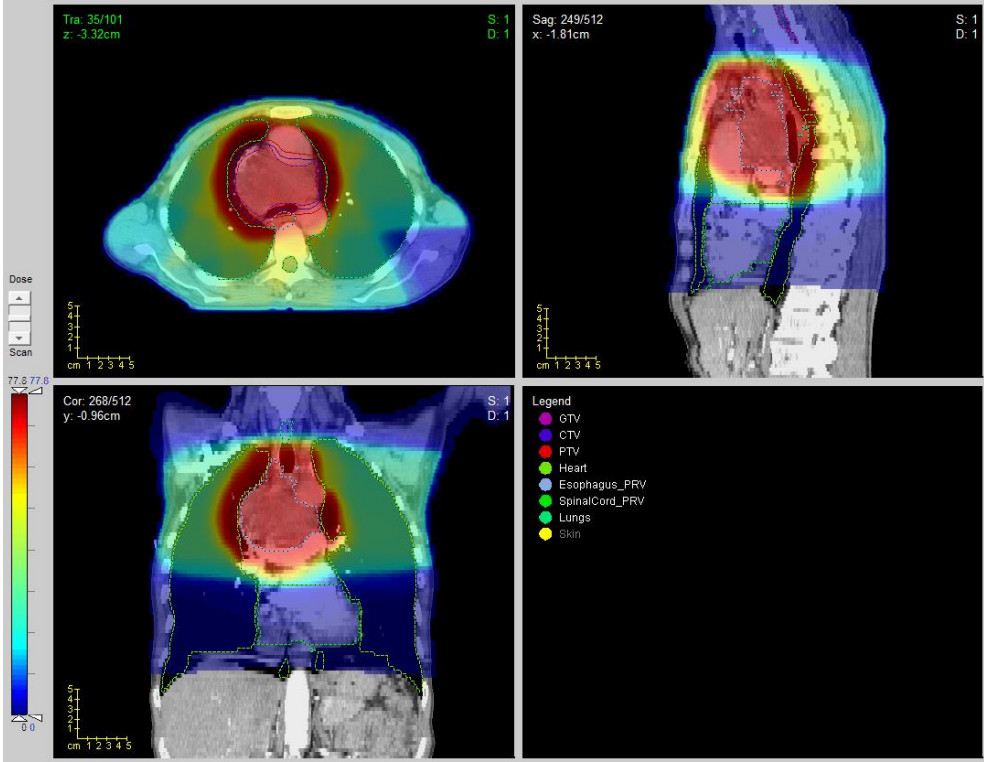


Figure F.15. Dose distribution for Patient-15

## APPENDIX G: THE TABLES FOR THE DVH PARAMETERS

Table G.1. DVH parameters for Patient-1

	Parameter	Volume	TPSPB	TPSCCC	MC <sub>H2O</sub>	MC <sub>DM</sub>	MC <sub>DW</sub>
Targets	D <sub>min</sub>	GTV	62.73	63.18	62.68	61.58	63.08
		CTV	62.23	62.43	61.93	60.13	62.23
		PTV	61.23	61.53	57.53	58.68	61.23
	D <sub>max</sub>	GTV	78.83	80.98	80.23	79.63	80.43
		CTV	79.73	81.93	81.53	80.98	81.83
		PTV	80.68	82.13	82.08	81.63	82.43
	D <sub>mean</sub>	GTV	69.80	70.88	69.98	69.53	70.41
		CTV	70.09	70.95	70.17	69.70	70.69
		PTV	70.13	70.71	70.10	69.60	70.70
	D <sub>93%</sub>	GTV	66.38	67.43	66.58	66.18	67.13
		CTV	65.18	66.03	65.23	64.73	66.38
		PTV	64.33	65.03	64.38	63.63	65.93
	HI	GTV	23%	25%	25%	26%	25%
		CTV	25%	27%	28%	30%	28%
PTV		28%	29%	35%	33%	30%	
CI	PTV	49%	51%	48%	47%	49%	
OARs	D <sub>max</sub>	Heart	67.93	68.93	68.38	68.08	70.73
		Esophagus	66.38	68.13	67.88	67.68	68.33
		Spinal Cord	54.38	53.13	53.83	52.03	57.78
	D <sub>33%</sub>	Heart	24.68	28.28	25.53	25.03	26.98
		Esophagus	48.73	52.28	51.53	51.38	51.78
		Spinal Cord	4.88	4.98	4.73	4.63	4.83
	D <sub>67%</sub>	Heart	15.33	16.43	15.73	15.38	16.73
		Esophagus	2.78	2.68	2.78	2.73	2.78
		Spinal Cord	1.33	0.98	1.18	1.18	1.23
	V <sub>20Gy</sub>	Lungs	0.31	0.31	0.31	0.31	0.31
	V <sub>30Gy</sub>	Lungs	0.16	0.15	0.16	0.16	0.16
	D <sub>mean</sub>	Lungs	14.37	14.51	14.55	14.53	14.55
	EUD	Heart	22.44	24.39	22.98	22.48	24.26
		Esophagus	19.37	19.91	20.00	19.93	20.16
		Spinal Cord	2.21	3.26	3.48	3.44	3.59
		Lungs	14.25	14.40	14.45	14.42	14.44
NTCP	Heart	6.23E-04	2.78E-03	8.60E-04	4.73E-04	2.88E-03	
	Esophagus	1.80E-01	1.88E-01	1.85E-01	1.84E-01	1.90E-01	
	Spinal Cord	2.52E-02	2.56E-02	2.86E-02	2.47E-02	4.28E-02	
	Lungs	7.55E-02	7.72E-02	7.77E-02	7.74E-02	7.76E-02	

Table G.2. DVH parameters for Patient-2

	Parameter	Volume	TPS <sub>PB</sub>	TPS <sub>CCC</sub>	MC <sub>H2O</sub>	MC <sub>DM</sub>	MC <sub>DW</sub>
Targets	D <sub>min</sub>	GTV	69.13	67.08	68.43	64.93	68.93
		CTV	67.18	63.08	63.28	63.38	66.28
		PTV	59.83	53.53	56.58	56.13	56.63
	D <sub>max</sub>	GTV	75.88	72.43	73.33	73.68	75.93
		CTV	76.48	72.43	73.33	73.68	76.18
		PTV	76.48	72.43	73.33	73.68	76.18
	D <sub>mean</sub>	GTV	72.52	70.77	70.76	69.99	71.77
		CTV	72.59	70.17	70.62	69.97	71.45
		PTV	72.03	69.11	69.96	69.39	70.71
	D <sub>93%</sub>	GTV	70.78	69.53	69.78	67.38	70.33
		CTV	70.43	67.88	69.38	67.38	69.83
		PTV	68.88	65.08	67.43	66.38	67.78
	HI	GTV	9%	8%	7%	13%	10%
		CTV	13%	13%	14%	15%	14%
		PTV	23%	27%	24%	25%	28%
CI	PTV	65%	74%	72%	75%	68%	
OARs	D <sub>max</sub>	Heart	69.93	69.03	69.38	69.03	73.83
		Esophagus	71.63	71.18	70.93	70.88	73.38
		Spinal Cord	46.73	47.58	48.08	47.18	50.18
	D <sub>33%</sub>	Heart	16.78	17.68	17.88	17.38	18.78
		Esophagus	28.48	30.58	30.58	30.48	30.93
		Spinal Cord	7.58	8.28	7.98	7.93	8.13
	D <sub>67%</sub>	Heart	4.53	5.13	5.08	4.98	5.33
		Esophagus	1.68	1.58	1.63	1.63	1.63
		Spinal Cord	0.23	0.78	0.88	0.88	0.93
	V <sub>20Gy</sub>	Lungs	0.32	0.33	0.33	0.33	0.33
	V <sub>30Gy</sub>	Lungs	0.17	0.17	0.17	0.17	0.17
	D <sub>mean</sub>	Lungs	14.70	14.82	15.13	15.09	15.11
	EUD	Heart	10.21	11.07	11.02	10.76	11.54
		Esophagus	16.23	16.85	17.06	16.93	17.19
		Spinal Cord	1.33	3.21	3.23	3.19	3.29
		Lungs	14.59	14.71	15.02	14.99	15.00
	NTCP	Heart	2.82E-07	5.26E-07	6.90E-07	3.36E-07	2.27E-06
		Esophagus	1.50E-01	1.54E-01	1.56E-01	1.54E-01	1.60E-01
Spinal Cord		5.20E-03	6.00E-03	6.31E-03	5.88E-03	8.03E-03	
Lungs		7.97E-02	8.11E-02	8.53E-02	8.48E-02	8.51E-02	

Table G.3. DVH parameters for Patient-3

	Parameter	Volume	TPS <sub>PB</sub>	TPS <sub>CCC</sub>	MC <sub>H2O</sub>	MC <sub>DM</sub>	MC <sub>DW</sub>
Targets	D <sub>min</sub>	GTV	69.13	67.73	67.18	66.68	67.33
		CTV	67.93	65.38	66.28	65.73	66.38
		PTV	63.98	58.28	61.23	60.83	61.23
	D <sub>max</sub>	GTV	75.73	74.33	73.68	72.98	73.68
		CTV	76.08	74.33	73.98	73.73	74.08
		PTV	76.08	74.33	73.98	74.03	74.13
	D <sub>mean</sub>	GTV	72.37	71.71	70.85	70.38	71.09
		CTV	72.65	71.45	70.93	70.45	71.11
		PTV	72.39	70.54	70.54	70.12	70.69
	D <sub>93%</sub>	GTV	70.38	69.63	68.83	68.38	69.08
		CTV	70.23	68.83	68.58	68.13	68.78
		PTV	69.43	66.83	67.53	67.18	67.63
HI	GTV	9%	9%	9%	9%	9%	
	CTV	11%	13%	11%	11%	11%	
	PTV	17%	23%	18%	19%	18%	
CI	PTV	60%	63%	62%	64%	61%	
OARs	D <sub>max</sub>	Heart	47.98	47.43	48.28	47.98	48.43
		Esophagus	39.98	40.08	40.08	40.18	40.28
		Spinal Cord	40.48	41.08	40.33	40.83	41.58
	D <sub>33%</sub>	Heart	15.13	15.63	15.33	15.23	15.38
		Esophagus	12.88	14.53	13.93	13.88	13.98
		Spinal Cord	3.03	3.28	3.03	3.03	3.13
	D <sub>67%</sub>	Heart	8.28	9.13	8.88	8.83	8.93
		Esophagus	1.28	1.18	1.28	1.28	1.28
		Spinal Cord	0.58	0.53	0.63	0.63	0.68
	V <sub>20Gy</sub>	Lungs	0.25	0.25	0.25	0.25	0.25
	V <sub>30Gy</sub>	Lungs	0.20	0.20	0.20	0.20	0.20
	D <sub>mean</sub>	Lungs	14.82	14.86	15.06	15.00	15.05
	EUD	Heart	11.92	12.63	12.45	12.37	12.50
		Esophagus	7.27	7.90	7.75	7.69	7.79
		Spinal Cord	1.31	2.17	2.13	2.11	2.17
		Lungs	14.68	14.73	14.93	14.88	14.92
NTCP	Heart	2.02E-10	3.39E-10	2.85E-10	2.42E-10	3.08E-10	
	Esophagus	1.90E-02	2.09E-02	2.02E-02	2.00E-02	2.05E-02	
	Spinal Cord	9.15E-04	1.11E-03	1.04E-03	9.97E-04	1.32E-03	
	Lungs	8.15E-02	8.19E-02	8.47E-02	8.39E-02	8.45E-02	

Table G.4. DVH parameters for Patient-4

	Parameter	Volume	TPS <sub>PB</sub>	TPS <sub>CCC</sub>	MC <sub>H2O</sub>	MC <sub>DM</sub>	MC <sub>DW</sub>
Targets	D <sub>min</sub>	GTV	66.33	64.88	65.53	64.88	65.53
		CTV	62.63	60.93	62.23	61.83	62.48
		PTV	54.38	51.18	52.33	52.08	52.58
	D <sub>max</sub>	GTV	76.68	73.38	74.43	74.03	74.68
		CTV	77.48	73.48	75.48	75.68	75.68
		PTV	77.48	73.48	75.48	75.68	75.68
	D <sub>mean</sub>	GTV	72.27	70.95	70.93	70.47	71.17
		CTV	71.99	70.33	70.53	70.07	70.74
		PTV	71.30	69.31	69.75	69.33	69.96
	D <sub>93%</sub>	GTV	70.33	69.03	69.13	68.63	69.33
		CTV	69.28	67.53	67.98	67.53	68.18
		PTV	67.53	65.13	66.18	65.83	66.28
	HI	GTV	14%	12%	13%	13%	13%
		CTV	21%	18%	19%	20%	19%
		PTV	32%	32%	33%	34%	33%
CI	PTV	68%	77%	74%	74%	73%	
OARs	D <sub>max</sub>	Heart	68.33	66.68	67.23	66.93	67.58
		Esophagus	58.73	58.78	59.28	58.73	59.33
		Spinal Cord	47.83	47.98	48.18	48.83	50.58
	D <sub>33%</sub>	Heart	3.43	3.78	3.58	3.53	3.58
		Esophagus	35.38	37.58	37.23	36.88	37.58
		Spinal Cord	2.03	2.93	2.53	2.48	2.53
	D <sub>67%</sub>	Heart	1.38	1.38	1.33	1.33	1.33
		Esophagus	2.23	3.03	2.63	2.63	2.63
		Spinal Cord	0.03	0.38	0.28	0.28	0.28
	V <sub>20Gy</sub>	Lungs	0.27	0.26	0.27	0.27	0.27
	V <sub>30Gy</sub>	Lungs	0.17	0.17	0.17	0.17	0.17
	D <sub>mean</sub>	Lungs	15.42	15.25	15.59	15.56	15.57
	EUD	Heart	4.04	4.16	4.09	4.05	4.09
		Esophagus	17.06	17.83	17.58	17.41	17.67
		Spinal Cord	0.78	1.56	1.31	1.30	1.32
		Lungs	15.30	15.13	15.47	15.44	15.45
	NTCP	Heart	6.38E-10	9.02E-10	1.12E-09	9.70E-10	1.25E-09
		Esophagus	9.83E-02	1.05E-01	1.04E-01	1.02E-01	1.05E-01
Spinal Cord		4.19E-03	5.16E-03	4.83E-03	4.85E-03	6.31E-03	
Lungs		8.97E-02	8.72E-02	9.21E-02	9.16E-02	9.17E-02	

Table G.5. DVH parameters for Patient-5

	Parameter	Volume	TPSPB	TPSCCC	MC <sub>H2O</sub>	MC <sub>DM</sub>	MC <sub>DW</sub>
Targets	D <sub>min</sub>	GTV	69.23	65.98	67.38	66.88	67.53
		CTV	67.08	64.13	66.43	65.93	66.58
		PTV	60.43	57.38	61.78	61.78	61.68
	D <sub>max</sub>	GTV	75.38	74.83	74.73	74.75	75.33
		CTV	76.33	75.23	75.68	75.68	76.23
		PTV	76.68	75.38	75.73	76.18	78.03
	D <sub>mean</sub>	GTV	72.26	71.86	71.42	71.03	71.74
		CTV	72.36	71.59	71.39	71.01	71.69
		PTV	72.10	71.00	71.07	70.71	71.39
	D <sub>93%</sub>	GTV	70.33	69.28	69.53	69.08	69.78
		CTV	70.23	68.58	69.13	68.68	69.33
		PTV	69.43	66.83	68.08	67.73	68.28
	HI	GTV	9%	12%	10%	11%	11%
		CTV	13%	16%	13%	14%	13%
		PTV	23%	25%	20%	20%	23%
CI	PTV	59%	60%	58%	58%	55%	
OARs	D <sub>max</sub>	Heart	3.93	4.33	4.33	4.28	4.33
		Esophagus	73.18	73.23	72.83	72.93	74.18
		Spinal Cord	53.73	58.08	56.93	55.53	59.68
	D <sub>33%</sub>	Heart	1.38	1.58	1.58	1.53	1.58
		Esophagus	46.08	49.83	48.98	48.38	49.28
		Spinal Cord	3.03	3.58	3.38	3.33	3.38
	D <sub>67%</sub>	Heart	0.78	0.83	0.93	0.93	0.93
		Esophagus	2.48	2.68	2.63	2.63	2.68
		Spinal Cord	0.03	0.33	0.33	0.33	0.33
	V <sub>20Gy</sub>	Lungs	0.29	0.28	0.29	0.29	0.29
	V <sub>30Gy</sub>	Lungs	0.15	0.14	0.15	0.15	0.15
	D <sub>mean</sub>	Lungs	13.48	13.82	14.01	13.98	14.01
	EUD	Heart	1.07	1.18	1.28	1.26	1.28
		Esophagus	21.22	22.20	22.14	21.96	22.30
		Spinal Cord	0.92	1.69	1.84	1.82	1.88
		Lungs	13.37	13.71	13.90	13.87	13.90
	NTCP	Heart	0.00E+00	0.00E+00	0.00E+00	0.00E+00	0.00E+00
		Esophagus	2.06E-01	2.30E-01	2.27E-01	2.22E-01	2.31E-01
Spinal Cord		1.53E-02	2.37E-02	2.24E-02	2.08E-02	3.06E-02	
Lungs		6.50E-02	6.88E-02	7.00E-02	7.06E-02	7.10E-02	

Table G.6. DVH parameters for Patient-6

	Parameter	Volume	TPS <sub>PB</sub>	TPS <sub>CCC</sub>	MC <sub>H2O</sub>	MC <sub>DM</sub>	MC <sub>DW</sub>
Targets	D <sub>min</sub>	GTV	69.58	57.18	63.68	63.68	63.73
		CTV	68.33	48.48	56.53	56.53	56.48
		PTV	63.68	42.23	51.08	51.13	51.08
	D <sub>max</sub>	GTV	75.03	69.83	69.98	69.38	70.03
		CTV	75.63	69.83	69.98	69.78	70.03
		PTV	75.78	69.83	69.98	69.78	70.03
	D <sub>mean</sub>	GTV	72.16	67.36	68.29	67.72	68.34
		CTV	72.62	64.45	67.05	66.68	67.04
		PTV	72.45	62.90	66.09	65.80	66.08
	D <sub>93%</sub>	GTV	70.48	64.53	66.88	66.33	66.88
		CTV	70.33	58.88	63.93	63.83	63.93
		PTV	69.78	56.28	61.83	61.83	61.83
	HI	GTV	8%	19%	9%	8%	9%
CTV		10%	33%	20%	20%	20%	
PTV		17%	44%	29%	28%	29%	
CI	PTV	63%	35%	67%	65%	67%	
OARs	D <sub>max</sub>	Heart	36.03	35.03	35.43	35.83	36.13
		Esophagus	25.18	24.43	24.53	24.43	24.68
		Spinal Cord	24.23	24.13	24.58	24.58	25.83
	D <sub>33%</sub>	Heart	7.93	8.73	8.58	8.78	8.88
		Esophagus	2.28	2.28	2.08	2.03	2.08
		Spinal Cord	1.18	1.33	1.28	1.28	1.33
	D <sub>67%</sub>	Heart	1.83	1.98	1.83	1.83	1.88
		Esophagus	0.73	0.68	0.68	0.68	0.68
		Spinal Cord	0.28	0.28	0.43	0.43	0.43
	V <sub>20Gy</sub>	Lungs	0.14	0.12	0.13	0.13	0.13
	V <sub>30Gy</sub>	Lungs	0.08	0.07	0.08	0.08	0.08
	D <sub>mean</sub>	Lungs	7.70	7.30	7.76	7.76	7.77
	EUD	Heart	4.82	5.20	5.08	5.12	5.17
		Esophagus	4.16	4.11	4.21	4.18	4.22
		Spinal Cord	0.57	0.97	1.06	1.07	1.10
		Lungs	7.59	7.21	7.66	7.66	7.68
	NTCP	Heart	1.76E-14	2.67E-14	2.73E-14	3.12E-14	3.79E-14
Esophagus		1.09E-02	1.05E-02	1.09E-02	1.06E-02	1.08E-02	
Spinal Cord		2.51E-05	2.49E-05	2.87E-05	2.88E-05	3.78E-05	
Lungs		2.16E-02	1.98E-02	2.18E-02	2.18E-02	2.19E-02	



Table G.7. DVH parameters for Patient-7

	Parameter	Volume	TPS <sub>PB</sub>	TPS <sub>CCC</sub>	MC <sub>H2O</sub>	MC <sub>DM</sub>	MC <sub>DW</sub>
Targets	D <sub>min</sub>	GTV	68.38	67.93	67.73	67.13	68.03
		CTV	65.78	65.68	64.63	64.48	65.13
		PTV	60.98	59.88	61.43	60.43	61.73
	D <sub>max</sub>	GTV	75.98	74.68	74.83	74.98	76.13
		CTV	77.23	74.68	75.18	75.28	78.63
		PTV	77.73	74.68	75.38	75.48	79.18
	D <sub>mean</sub>	GTV	72.07	71.72	71.78	71.35	72.11
		CTV	72.00	71.40	71.58	71.05	71.98
		PTV	71.81	70.94	71.27	70.67	71.82
	D <sub>93%</sub>	GTV	70.28	69.78	69.88	69.38	70.18
		CTV	69.98	69.28	69.53	68.73	69.83
		PTV	69.43	68.43	68.78	67.73	69.08
	HI	GTV	11%	9%	10%	11%	11%
		CTV	16%	13%	15%	15%	19%
		PTV	23%	21%	20%	21%	24%
CI	PTV	56%	58%	55%	57%	54%	
OARs	D <sub>max</sub>	Heart	70.58	70.13	70.08	69.73	70.43
		Esophagus	70.88	70.13	70.33	70.23	72.48
		Spinal Cord	65.13	67.53	68.88	67.53	73.68
	D <sub>33%</sub>	Heart	30.53	31.38	31.23	31.08	31.43
		Esophagus	48.83	50.93	50.53	50.13	50.73
		Spinal Cord	24.58	27.43	27.78	27.63	28.93
	D <sub>67%</sub>	Heart	21.63	22.38	22.38	22.23	22.48
		Esophagus	3.78	4.28	4.18	4.13	4.18
		Spinal Cord	1.48	1.28	1.33	1.33	1.38
	V <sub>20Gy</sub>	Lungs	0.54	0.54	0.54	0.54	0.54
	V <sub>30Gy</sub>	Lungs	0.23	0.24	0.23	0.23	0.23
	D <sub>mean</sub>	Lungs	22.08	22.01	22.19	22.12	22.16
	EUD	Heart	23.09	24.45	24.17	24.04	24.29
		Esophagus	23.60	24.40	24.51	24.36	24.67
		Spinal Cord	3.92	5.30	5.47	5.40	5.56
		Lungs	21.98	21.91	22.09	22.02	22.06
	NTCP	Heart	6.37E-04	1.04E-03	9.03E-04	8.07E-04	1.02E-03
		Esophagus	2.22E-01	2.37E-01	2.39E-01	2.36E-01	2.44E-01
Spinal Cord		1.12E-01	1.44E-01	1.57E-01	1.49E-01	2.07E-01	
Lungs		2.24E-01	2.21E-01	2.26E-01	2.24E-01	2.26E-01	

Table G.8. DVH parameters for Patient-8

	Parameter	Volume	TPS <sub>PB</sub>	TPS <sub>CCC</sub>	MC <sub>H2O</sub>	MC <sub>DM</sub>	MC <sub>DW</sub>
Targets	D <sub>min</sub>	GTV	70.03	67.13	68.18	67.78	68.38
		CTV	68.83	61.78	65.98	65.98	65.98
		PTV	63.68	53.28	59.53	59.48	59.43
	D <sub>max</sub>	GTV	75.23	75.38	75.03	74.53	75.28
		CTV	75.43	75.58	75.13	74.58	75.33
		PTV	75.43	75.58	75.18	74.68	76.53
	D <sub>mean</sub>	GTV	72.93	72.65	71.78	71.33	72.06
		CTV	73.06	71.75	71.50	71.08	71.81
		PTV	72.64	70.43	70.81	70.44	71.22
	D <sub>93%</sub>	GTV	71.53	70.33	69.98	69.43	70.13
		CTV	71.13	67.93	68.98	68.43	69.03
		PTV	69.83	64.78	67.28	66.83	67.38
	HI	GTV	7%	11%	10%	9%	10%
		CTV	9%	19%	13%	12%	13%
		PTV	16%	32%	22%	22%	24%
CI	PTV	57%	56%	56%	58%	54%	
OARs	D <sub>max</sub>	Heart	72.18	73.18	72.63	72.38	75.28
		Esophagus	19.73	20.63	20.33	20.33	21.58
		Spinal Cord	17.98	17.88	18.23	18.18	18.73
	D <sub>33%</sub>	Heart	19.38	20.68	20.28	19.68	21.53
		Esophagus	6.08	6.88	6.83	6.78	6.83
		Spinal Cord	1.03	1.18	1.08	1.08	1.13
	D <sub>67%</sub>	Heart	13.13	14.28	14.08	13.68	14.63
		Esophagus	1.03	0.83	0.98	0.93	0.93
		Spinal Cord	0.23	0.23	0.38	0.33	0.38
	V <sub>20Gy</sub>	Lungs	0.15	0.15	0.15	0.15	0.15
	V <sub>30Gy</sub>	Lungs	0.08	0.07	0.08	0.08	0.08
	D <sub>mean</sub>	Lungs	8.08	8.20	8.40	8.40	8.40
	EUD	Heart	16.59	18.02	17.60	17.10	18.54
		Esophagus	4.42	4.90	4.85	4.80	4.89
		Spinal Cord	0.59	0.89	1.01	1.00	1.03
		Lungs	7.98	8.11	8.30	8.30	8.31
	NTCP	Heart	8.77E-05	2.84E-04	2.41E-04	1.07E-04	8.47E-04
		Esophagus	9.51E-03	1.04E-02	1.02E-02	1.01E-02	1.04E-02
Spinal Cord		4.50E-06	5.74E-06	5.50E-06	5.21E-06	6.23E-06	
Lungs		2.34E-02	2.39E-02	2.49E-02	2.49E-02	2.49E-02	

Table G.9. DVH parameters for Patient-9

	Parameter	Volume	TPSPB	TPSCCC	MC <sub>H2O</sub>	MC <sub>DM</sub>	MC <sub>DW</sub>
Targets	D <sub>min</sub>	GTV	68.63	66.98	68.28	64.83	68.43
		CTV	68.58	64.23	62.43	63.98	66.08
		PTV	67.78	59.68	59.58	60.98	63.13
	D <sub>max</sub>	GTV	75.33	76.38	75.83	75.78	76.53
		CTV	76.08	76.38	75.83	76.28	79.68
		PTV	76.38	76.38	76.18	76.53	81.33
	D <sub>mean</sub>	GTV	71.70	71.06	70.68	70.11	71.63
		CTV	71.94	70.94	70.81	70.32	71.75
		PTV	72.01	70.57	70.69	70.16	71.74
	D <sub>93%</sub>	GTV	69.98	69.73	69.08	67.03	69.53
		CTV	69.93	69.43	69.18	67.48	69.63
		PTV	69.73	68.18	68.93	67.33	69.38
	HI	GTV	9%	13%	11%	16%	11%
		CTV	10%	17%	19%	17%	19%
PTV		12%	24%	23%	22%	25%	
CI	PTV	43%	47%	44%	46%	42%	
OARs	D <sub>max</sub>	Heart	66.93	66.33	66.98	66.93	70.38
		Esophagus	72.83	73.48	72.83	73.13	73.58
		Spinal Cord	64.43	66.43	65.88	64.83	69.08
	D <sub>33%</sub>	Heart	6.28	6.93	6.73	6.68	7.03
		Esophagus	11.58	9.18	8.28	8.18	8.38
		Spinal Cord	4.18	4.18	4.23	4.18	4.28
	D <sub>67%</sub>	Heart	1.88	2.23	2.18	2.13	2.28
		Esophagus	1.43	0.93	1.23	1.23	1.23
		Spinal Cord	0.93	0.63	0.83	0.83	0.83
	V <sub>20Gy</sub>	Lungs	0.29	0.29	0.30	0.30	0.30
	V <sub>30Gy</sub>	Lungs	0.16	0.13	0.15	0.15	0.15
	D <sub>mean</sub>	Lungs	13.52	13.32	13.74	13.73	13.74
	EUD	Heart	4.90	5.41	5.48	5.39	5.71
		Esophagus	15.27	15.12	15.36	15.26	15.45
		Spinal Cord	1.67	2.75	3.02	2.98	3.06
		Lungs	13.40	13.22	13.63	13.63	13.64
	NTCP	Heart	5.00E-12	2.38E-11	3.18E-11	1.84E-11	8.59E-11
Esophagus		1.51E-01	1.54E-01	1.52E-01	1.50E-01	1.55E-01	
Spinal Cord		6.97E-02	1.08E-01	9.41E-02	8.79E-02	1.16E-01	
Lungs		6.55E-02	6.32E-02	6.79E-02	6.78E-02	6.79E-02	

Table G.10. DVH parameters for Patient-10

	Parameter	Volume	TPSPB	TPSCCC	MC <sub>H2O</sub>	MC <sub>DM</sub>	MC <sub>DW</sub>
Targets	D <sub>min</sub>	GTV	68.73	68.83	68.88	65.98	69.48
		CTV	67.33	66.98	67.08	64.58	68.53
		PTV	61.83	60.33	61.33	59.73	61.83
	D <sub>max</sub>	GTV	77.23	75.38	75.28	74.78	76.78
		CTV	77.63	75.38	75.38	75.63	77.53
		PTV	77.63	75.38	75.38	75.63	77.53
	D <sub>mean</sub>	GTV	72.28	72.35	71.74	71.22	72.41
		CTV	72.39	72.17	71.73	71.16	72.45
		PTV	72.26	71.73	71.50	70.83	72.33
	D <sub>93%</sub>	GTV	70.38	70.63	70.23	69.48	70.73
		CTV	70.23	70.18	70.03	69.03	70.63
		PTV	69.73	69.43	69.53	67.83	70.28
	HI	GTV	12%	9%	9%	12%	10%
CTV		14%	12%	12%	16%	12%	
PTV		22%	21%	20%	22%	22%	
CI	PTV	55%	57%	55%	58%	53%	
OARs	D <sub>max</sub>	Heart	72.98	73.68	73.33	73.98	77.53
		Esophagus	72.13	72.73	72.58	72.23	75.63
		Spinal Cord	57.23	57.93	58.03	57.28	61.43
	D <sub>33%</sub>	Heart	32.78	34.73	34.78	33.78	36.08
		Esophagus	15.53	18.63	17.38	17.23	17.58
		Spinal Cord	7.53	8.43	8.08	7.98	8.28
	D <sub>67%</sub>	Heart	3.38	3.98	3.68	3.63	3.88
		Esophagus	1.73	1.73	1.63	1.63	1.63
		Spinal Cord	0.78	0.68	0.83	0.78	0.83
	V <sub>20Gy</sub>	Lungs	0.41	0.41	0.41	0.41	0.41
	V <sub>30Gy</sub>	Lungs	0.24	0.24	0.25	0.24	0.25
	D <sub>mean</sub>	Lungs	19.80	20.03	20.09	20.00	20.08
	EUD	Heart	14.69	15.83	15.41	15.01	16.11
		Esophagus	13.57	14.36	14.25	14.02	14.48
		Spinal Cord	2.12	3.14	3.12	3.07	3.18
		Lungs	19.66	19.89	19.95	19.86	19.94
	NTCP	Heart	2.44E-02	4.02E-02	3.82E-02	2.14E-02	8.63E-02
Esophagus		9.60E-02	1.07E-01	1.05E-01	1.01E-01	1.11E-01	
Spinal Cord		5.24E-02	6.29E-02	6.30E-02	5.59E-02	7.87E-02	
Lungs		1.69E-01	1.74E-01	1.76E-01	1.74E-01	1.75E-01	

Table G.11. DVH parameters for Patient-11

	Parameter	Volume	TPS <sub>PB</sub>	TPS <sub>CCC</sub>	MC <sub>H2O</sub>	MC <sub>DM</sub>	MC <sub>DW</sub>
Targets	D <sub>min</sub>	GTV	67.73	66.38	66.58	64.03	68.83
		CTV	66.03	64.53	64.73	64.03	65.08
		PTV	64.08	61.88	62.48	60.38	62.98
	D <sub>max</sub>	GTV	76.83	74.68	74.58	74.73	76.58
		CTV	77.78	75.18	75.03	75.43	79.13
		PTV	78.58	75.68	75.78	76.33	80.13
	D <sub>mean</sub>	GTV	71.81	70.74	70.67	70.22	70.98
		CTV	71.97	70.53	70.67	70.21	71.05
		PTV	72.00	70.18	70.54	70.05	71.07
	D <sub>93%</sub>	GTV	70.38	68.83	68.88	68.43	69.23
		CTV	70.23	68.03	68.48	68.03	68.93
		PTV	69.63	67.13	67.83	67.28	68.43
	HI	GTV	13%	12%	11%	15%	11%
		CTV	16%	15%	15%	16%	20%
		PTV	20%	20%	19%	23%	24%
CI	PTV	43%	50%	45%	46%	44%	
OARs	D <sub>max</sub>	Heart	3.03	3.18	3.13	3.03	3.23
		Esophagus	68.83	67.43	67.58	67.33	68.03
		Spinal Cord	64.58	65.83	66.98	67.08	68.48
	D <sub>33%</sub>	Heart	1.18	1.08	1.23	1.23	1.28
		Esophagus	15.98	20.18	18.33	18.23	18.53
		Spinal Cord	10.33	13.73	11.93	11.88	12.23
	D <sub>67%</sub>	Heart	0.73	0.63	0.73	0.73	0.78
		Esophagus	1.28	1.28	1.38	1.33	1.33
		Spinal Cord	0.78	0.73	0.88	0.83	0.88
	V <sub>20Gy</sub>	Lungs	0.18	0.18	0.19	0.19	0.19
	V <sub>30Gy</sub>	Lungs	0.16	0.16	0.16	0.16	0.16
	D <sub>mean</sub>	Lungs	10.93	10.67	11.08	11.08	11.09
	EUD	Heart	0.90	0.87	1.00	1.00	1.03
		Esophagus	11.34	12.56	12.18	12.09	12.29
		Spinal Cord	1.90	3.77	3.43	3.39	3.47
		Lungs	10.77	10.53	10.93	10.93	10.94
	NTCP	Heart	0.00E+00	0.00E+00	0.00E+00	0.00E+00	0.00E+00
		Esophagus	5.98E-02	6.52E-02	6.22E-02	6.13E-02	6.37E-02
Spinal Cord		4.20E-02	6.40E-02	6.52E-02	5.87E-02	8.36E-02	
Lungs		4.15E-02	3.94E-02	4.26E-02	4.26E-02	4.27E-02	

Table G.12. DVH parameters for Patient-12

	Parameter	Volume	TPS <sub>PB</sub>	TPS <sub>CCC</sub>	MC <sub>H2O</sub>	MC <sub>DM</sub>	MC <sub>DW</sub>
Targets	D <sub>min</sub>	GTV	68.63	68.88	68.63	66.78	69.13
		CTV	67.63	67.28	67.83	66.78	68.28
		PTV	66.03	63.78	63.23	64.58	66.48
	D <sub>max</sub>	GTV	75.48	74.18	74.03	74.43	75.58
		CTV	76.23	74.28	74.38	74.53	75.58
		PTV	76.33	74.28	74.43	74.58	75.58
	D <sub>mean</sub>	GTV	72.22	72.01	71.58	71.23	71.87
		CTV	72.26	71.79	71.54	71.22	71.83
		PTV	72.04	71.39	71.29	71.00	71.59
	D <sub>93%</sub>	GTV	70.43	70.63	70.18	69.78	70.53
		CTV	70.18	69.83	69.93	69.58	70.28
		PTV	69.33	68.63	69.08	68.78	69.38
	HI	GTV	9%	7%	8%	11%	9%
CTV		12%	10%	9%	11%	10%	
PTV		14%	15%	16%	14%	13%	
CI	PTV	56%	58%	55%	56%	55%	
OARs	D <sub>max</sub>	Heart	72.18	72.03	71.73	71.33	72.03
		Esophagus	71.93	72.53	72.68	72.23	73.23
		Spinal Cord	35.53	36.98	37.28	36.08	39.08
	D <sub>33%</sub>	Heart	5.13	5.23	5.33	5.28	5.33
		Esophagus	10.08	9.58	9.13	9.03	9.13
		Spinal Cord	2.33	2.18	2.28	2.23	2.33
	D <sub>67%</sub>	Heart	2.03	2.08	2.13	2.08	2.13
		Esophagus	1.83	1.48	1.63	1.63	1.63
		Spinal Cord	0.03	0.48	0.58	0.58	0.58
	V <sub>20Gy</sub>	Lungs	0.31	0.28	0.30	0.30	0.30
	V <sub>30Gy</sub>	Lungs	0.17	0.17	0.17	0.17	0.17
	D <sub>mean</sub>	Lungs	15.24	15.20	15.53	15.48	15.53
	EUD	Heart	5.17	5.26	5.44	5.39	5.45
		Esophagus	11.92	12.28	12.27	12.20	12.35
		Spinal Cord	0.81	1.63	1.59	1.57	1.62
		Lungs	15.11	15.08	15.40	15.35	15.40
	NTCP	Heart	3.82E-09	1.35E-08	1.37E-08	1.23E-08	1.60E-08
Esophagus		6.60E-02	7.43E-02	7.20E-02	7.12E-02	7.33E-02	
Spinal Cord		3.98E-04	5.40E-04	5.50E-04	5.07E-04	7.20E-04	
Lungs		8.72E-02	8.64E-02	9.11E-02	9.04E-02	9.11E-02	

Table G.13. DVH parameters for Patient-13

	Parameter	Volume	TPS <sub>PB</sub>	TPS <sub>CCC</sub>	MC <sub>H2O</sub>	MC <sub>DM</sub>	MC <sub>DW</sub>
Targets	D <sub>min</sub>	GTV	71.23	69.88	70.43	67.53	70.48
		CTV	68.28	66.48	68.98	67.38	69.08
		PTV	63.88	60.03	63.68	62.88	63.83
	D <sub>max</sub>	GTV	75.93	74.58	74.18	73.88	77.43
		CTV	76.03	74.78	74.33	74.53	78.38
		PTV	76.03	74.78	74.43	74.88	78.43
	D <sub>mean</sub>	GTV	72.83	73.22	72.60	71.70	73.19
		CTV	72.96	72.94	72.62	71.79	73.51
		PTV	72.59	72.33	72.26	71.44	73.24
	D <sub>93%</sub>	GTV	71.93	72.38	71.88	70.83	72.18
		CTV	71.78	71.33	71.73	69.33	71.93
		PTV	70.33	69.23	70.08	68.63	70.48
	HI	GTV	6%	6%	5%	9%	9%
CTV		11%	11%	7%	10%	13%	
PTV		17%	20%	15%	17%	20%	
CI	PTV	47%	44%	44%	46%	42%	
OARs	D <sub>max</sub>	Heart	0.93	0.68	0.78	0.78	0.88
		Esophagus	31.23	32.28	31.78	31.48	31.78
		Spinal Cord	33.88	35.83	35.23	34.53	36.93
	D <sub>33%</sub>	Heart	0.23	0.28	0.33	0.33	0.38
		Esophagus	11.38	12.33	12.03	11.93	12.23
		Spinal Cord	1.98	2.63	2.23	2.23	2.23
	D <sub>67%</sub>	Heart	0.03	0.18	0.23	0.23	0.23
		Esophagus	0.48	0.58	0.58	0.58	0.58
		Spinal Cord	0.03	0.18	0.18	0.18	0.18
	V <sub>20Gy</sub>	Lungs	0.06	0.06	0.06	0.06	0.06
	V <sub>30Gy</sub>	Lungs	0.05	0.05	0.05	0.05	0.05
	D <sub>mean</sub>	Lungs	4.32	4.40	4.55	4.53	4.55
	EUD	Heart	0.11	0.24	0.27	0.28	0.31
		Esophagus	4.82	5.60	5.43	5.38	5.50
		Spinal Cord	0.48	0.86	0.91	0.90	0.93
		Lungs	4.22	4.31	4.45	4.44	4.45
	NTCP	Heart	0.00E+00	0.00E+00	0.00E+00	0.00E+00	0.00E+00
Esophagus		1.12E-02	1.27E-02	1.23E-02	1.21E-02	1.25E-02	
Spinal Cord		1.14E-04	1.78E-04	1.51E-04	1.31E-04	2.21E-04	
Lungs		1.02E-02	1.04E-02	1.07E-02	1.07E-02	1.07E-02	

Table G.14. DVH parameters for Patient-14

	Parameter	Volume	TPS <sub>PB</sub>	TPS <sub>CCC</sub>	MC <sub>H2O</sub>	MC <sub>DM</sub>	MC <sub>DW</sub>
Targets	D <sub>min</sub>	GTV	68.33	66.83	67.18	64.03	67.68
		CTV	67.38	66.43	66.28	62.73	66.83
		PTV	66.73	62.88	64.78	62.18	65.38
	D <sub>max</sub>	GTV	76.38	73.48	73.68	73.63	76.53
		CTV	76.68	73.48	74.08	74.83	76.88
		PTV	77.73	73.48	74.08	74.83	77.18
	D <sub>mean</sub>	GTV	71.54	70.42	70.32	69.90	70.73
		CTV	71.86	70.36	70.48	69.98	71.01
		PTV	71.96	70.14	70.41	69.90	71.05
	D <sub>93%</sub>	GTV	69.58	68.68	68.88	68.48	69.33
		CTV	69.73	68.38	68.73	68.03	69.28
		PTV	69.53	67.93	68.38	67.08	69.08
	HI	GTV	11%	9%	9%	14%	13%
CTV		13%	10%	11%	17%	14%	
PTV		15%	15%	13%	18%	17%	
CI	PTV	42%	46%	43%	44%	42%	
OARs	D <sub>max</sub>	Heart	3.88	4.68	4.58	4.48	4.58
		Esophagus	55.03	54.33	54.83	54.73	55.28
		Spinal Cord	49.13	50.33	49.88	48.03	53.03
	D <sub>33%</sub>	Heart	1.33	1.23	1.28	1.28	1.38
		Esophagus	23.03	23.98	23.78	23.58	23.98
		Spinal Cord	25.43	26.28	25.88	25.63	26.43
	D <sub>67%</sub>	Heart	0.83	0.63	0.73	0.73	0.73
		Esophagus	2.38	3.08	2.98	2.93	2.93
		Spinal Cord	2.88	3.43	3.18	3.13	3.28
	V <sub>20Gy</sub>	Lungs	0.14	0.14	0.14	0.14	0.14
	V <sub>30Gy</sub>	Lungs	0.12	0.12	0.12	0.12	0.12
	D <sub>mean</sub>	Lungs	10.33	10.20	10.58	10.54	10.55
	EUD	Heart	1.00	0.98	1.04	1.04	1.09
		Esophagus	12.65	13.51	13.27	13.15	13.39
		Spinal Cord	5.53	7.82	7.48	7.41	7.68
		Lungs	10.12	10.07	10.44	10.41	10.42
	NTCP	Heart	0.00E+00	0.00E+00	0.00E+00	0.00E+00	0.00E+00
Esophagus		4.11E-02	4.47E-02	4.33E-02	4.25E-02	4.44E-02	
Spinal Cord		2.83E-03	3.43E-03	3.16E-03	2.41E-03	5.31E-03	
Lungs		3.69E-02	3.59E-02	3.86E-02	3.84E-02	3.84E-02	



Table G.15. DVH parameters for Patient-15

	Parameter	Volume	TPS <sub>PB</sub>	TPS <sub>CCC</sub>	MC <sub>H2O</sub>	MC <sub>DM</sub>	MC <sub>DW</sub>
Targets	D <sub>min</sub>	GTV	67.93	65.03	67.08	64.78	67.28
		CTV	67.03	61.43	64.43	63.68	64.78
		PTV	64.43	56.93	58.58	59.73	59.68
	D <sub>max</sub>	GTV	76.23	73.83	75.08	74.68	78.53
		CTV	77.33	74.48	75.73	75.23	78.83
		PTV	77.68	74.53	76.23	76.18	78.88
	D <sub>mean</sub>	GTV	72.40	70.59	71.50	70.96	72.10
		CTV	72.33	70.25	71.29	70.64	72.07
		PTV	72.18	69.82	70.98	70.30	71.88
	D <sub>93%</sub>	GTV	71.13	68.98	70.08	69.38	70.38
		CTV	70.58	67.93	69.28	68.23	69.63
		PTV	69.48	66.63	68.08	67.18	68.58
	HI	GTV	11%	12%	11%	14%	16%
		CTV	14%	19%	16%	16%	19%
		PTV	18%	25%	25%	23%	27%
CI	PTV	52%	58%	54%	56%	52%	
OARs	D <sub>max</sub>	Heart	16.13	11.58	10.48	10.23	11.28
		Esophagus	69.88	67.88	70.38	70.73	70.93
		Spinal Cord	50.78	50.78	52.28	52.48	54.93
	D <sub>33%</sub>	Heart	2.03	2.43	2.23	2.18	2.38
		Esophagus	66.18	64.03	65.13	64.53	65.83
		Spinal Cord	34.63	35.78	35.88	35.53	36.58
	D <sub>67%</sub>	Heart	1.08	1.03	1.13	1.13	1.23
		Esophagus	7.63	6.63	6.43	6.33	6.48
		Spinal Cord	2.93	3.13	2.98	2.93	3.03
	V <sub>20Gy</sub>	Lungs	0.40	0.41	0.41	0.41	0.41
	V <sub>30Gy</sub>	Lungs	0.26	0.26	0.27	0.26	0.26
	D <sub>mean</sub>	Lungs	18.25	18.12	18.43	18.39	18.43
	EUD	Heart	1.61	1.82	1.78	1.76	1.91
		Esophagus	34.53	33.65	34.21	33.94	34.58
		Spinal Cord	10.03	10.21	9.66	9.55	9.81
		Lungs	18.11	17.99	18.30	18.25	18.30
	NTCP	Heart	0.00E+00	0.00E+00	0.00E+00	0.00E+00	0.00E+00
		Esophagus	4.51E-01	4.26E-01	4.45E-01	4.38E-01	4.57E-01
Spinal Cord		2.57E-02	2.43E-02	2.98E-02	2.79E-02	3.56E-02	
Lungs		1.37E-01	1.34E-01	1.41E-01	1.40E-01	1.41E-01	

## APPENDIX H: ILLUSTRATIONS FOR THE DVH PARAMETER COMPARISONS

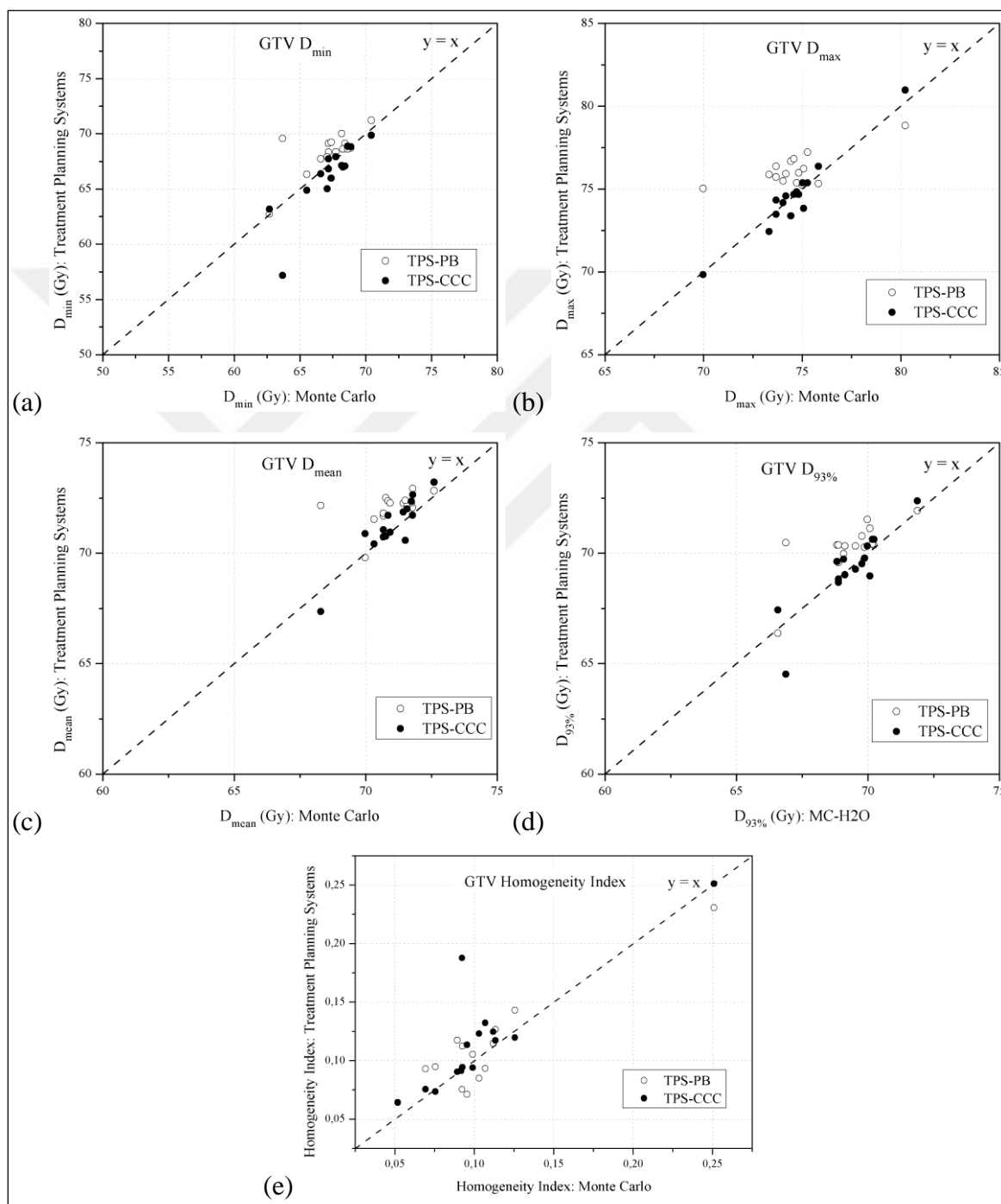


Figure H.1. Comparisons between  $MC_{H_2O}$  and TPSs for GTV: (a)  $D_{\min}$ , (b)  $D_{\max}$ , (c)  $D_{\text{mean}}$ , (d)  $D_{93\%}$ , (e) HI

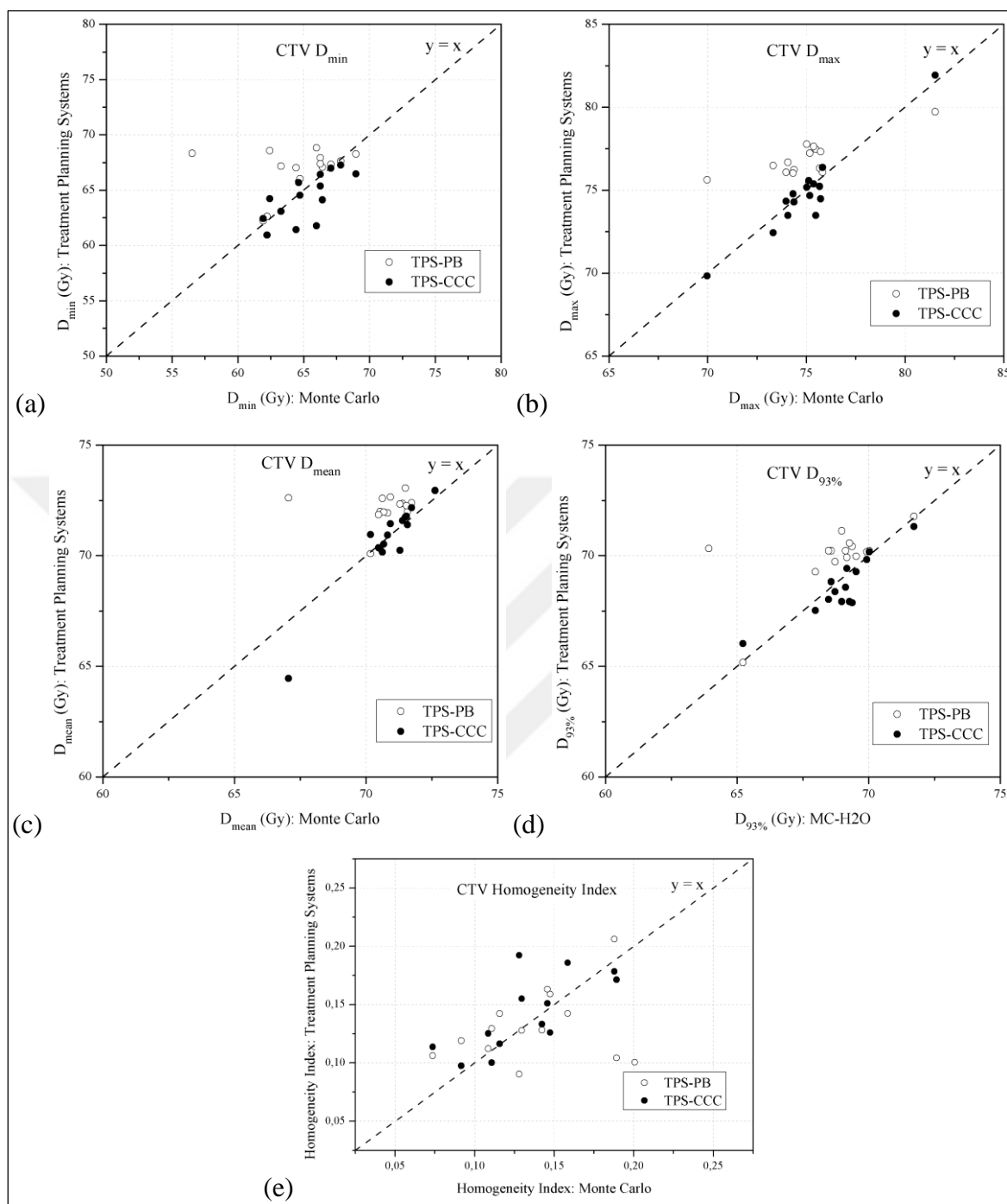


Figure H.2. Comparisons between  $MC_{H2O}$  and TPSs for CTV: (a)  $D_{\min}$ , (b)  $D_{\max}$ , (c)  $D_{\text{mean}}$ , (d)  $D_{93\%}$ , (e) HI

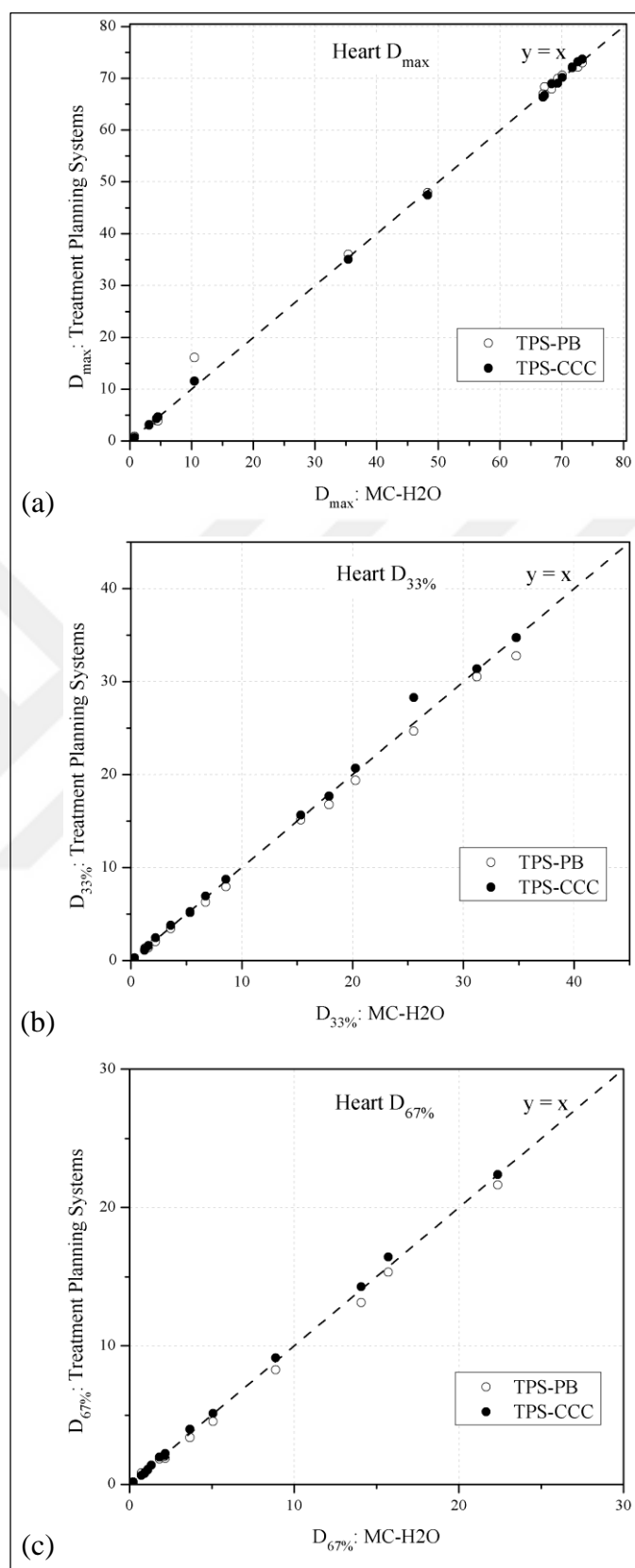


Figure H.3. Comparisons between  $MC_{H2O}$  and TPSs for Heart: (a)  $D_{max}$ , (b)  $D_{33\%}$ , (c)  $D_{67\%}$

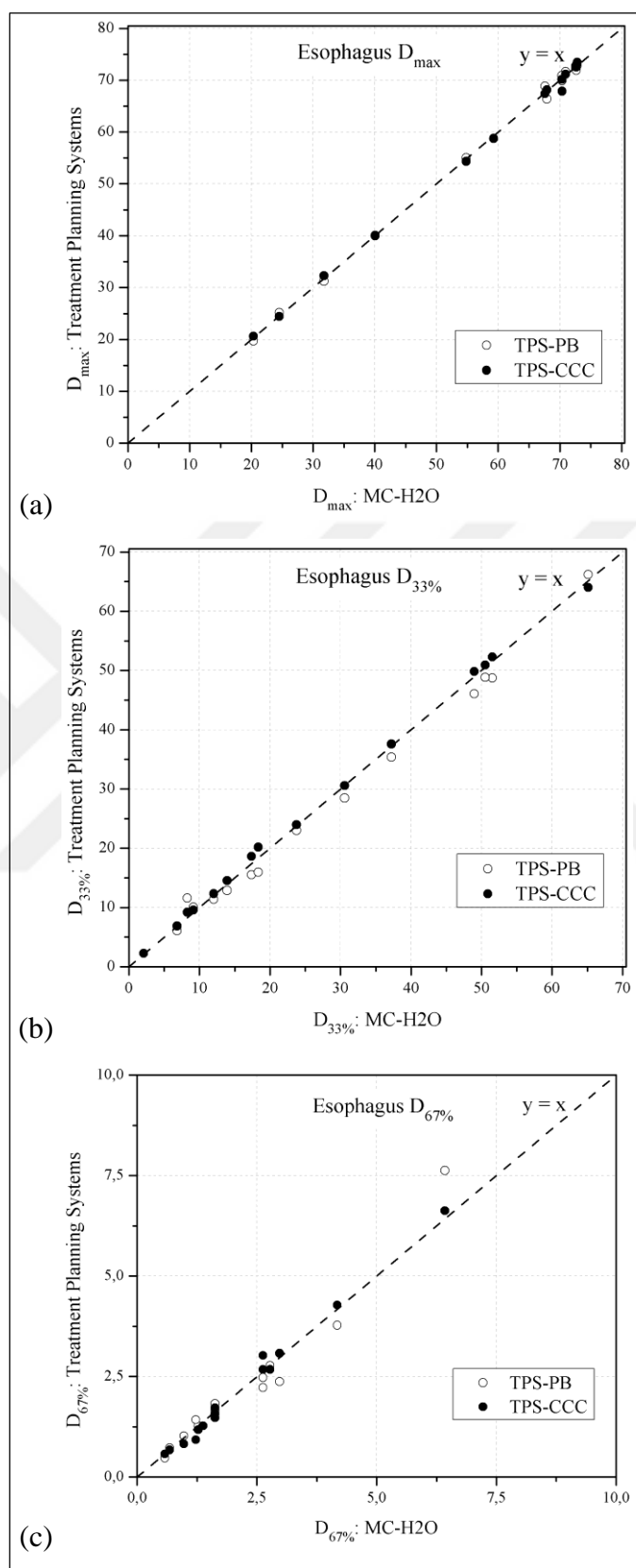


Figure H.4. Comparisons between MC<sub>H<sub>2</sub>O</sub> and TPSs for Esophagus: (a)  $D_{max}$ , (b)  $D_{33\%}$ ,  
(c)  $D_{67\%}$

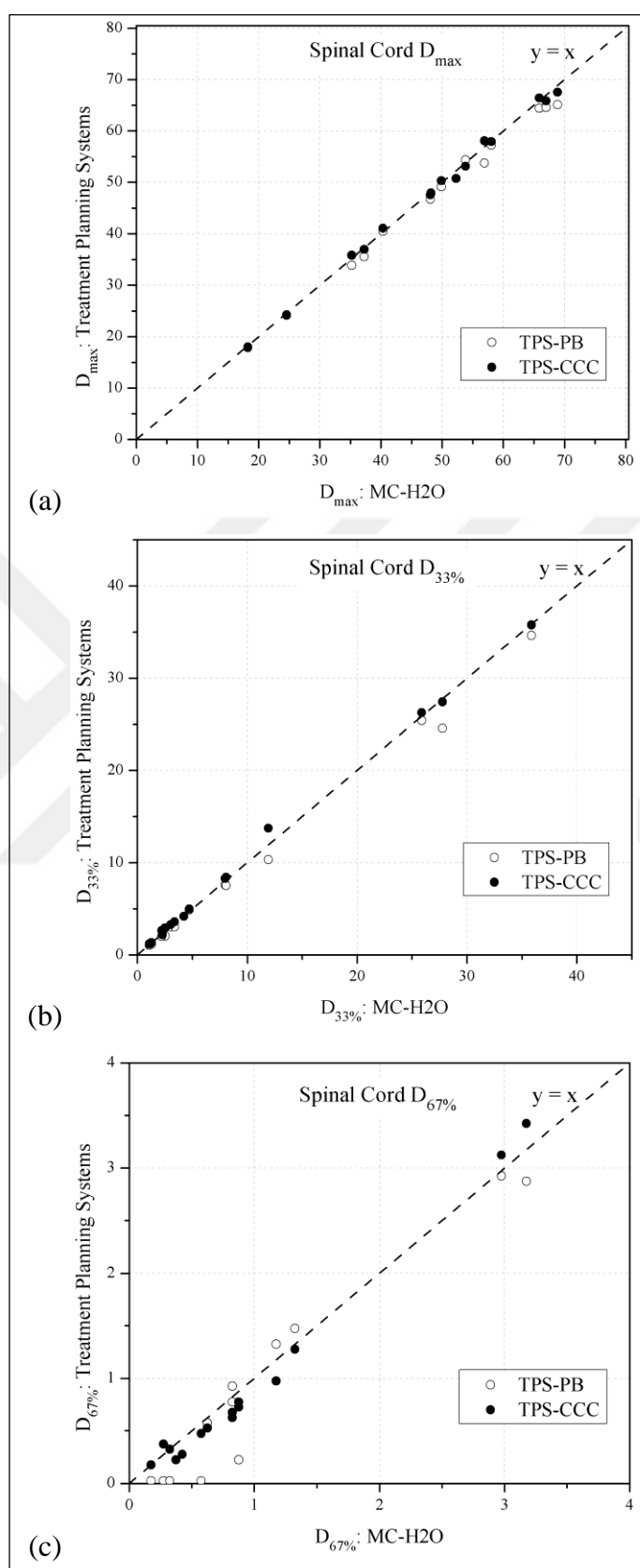


Figure H.5. Comparisons between  $MC_{H2O}$  and TPSs for Spinal Cord: (a)  $D_{max}$ , (b)  $D_{33\%}$ ,  
(c)  $D_{67\%}$

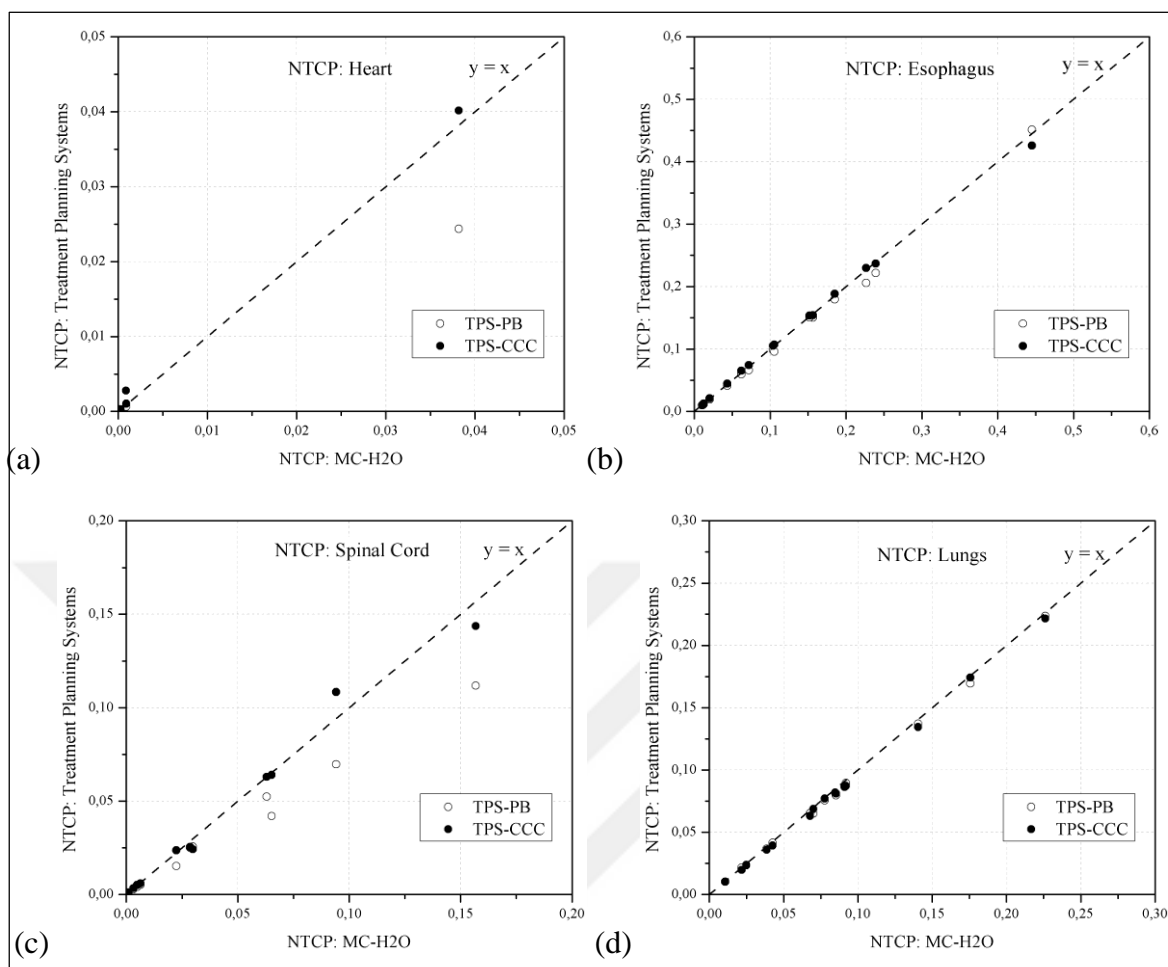


Figure H.6. Comparisons between MC<sub>H2O</sub> and TPSs for NTCP (a) Heart, (b) Esophagus, (c) Spinal Cord, (d) Lungs

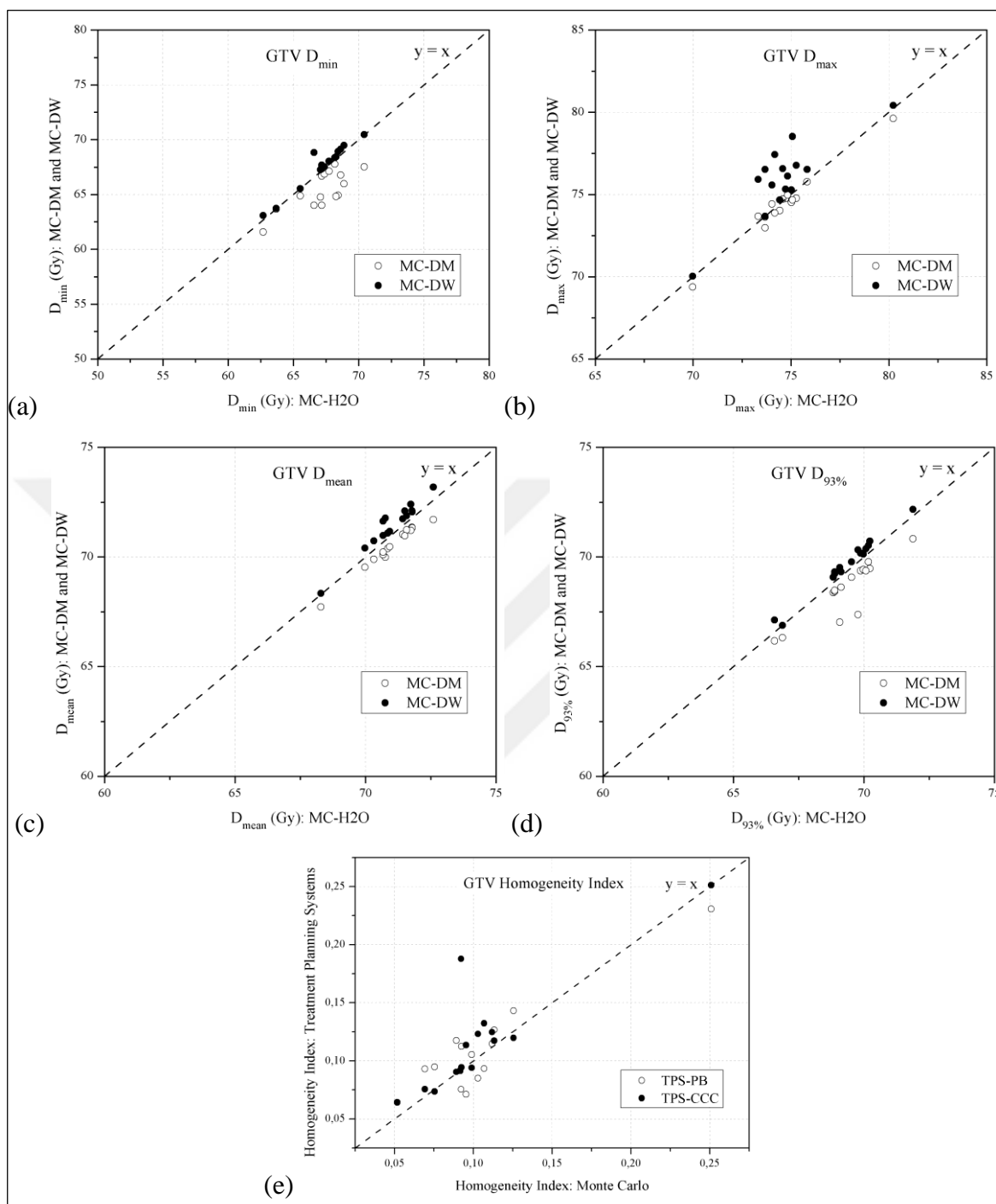


Figure H.7. Comparisons between  $MC_{H2O}$  and the other MC calculations for GTV:

(a)  $D_{\min}$ , (b)  $D_{\max}$ , (c)  $D_{\text{mean}}$ , (d)  $D_{93\%}$ , (e) HI



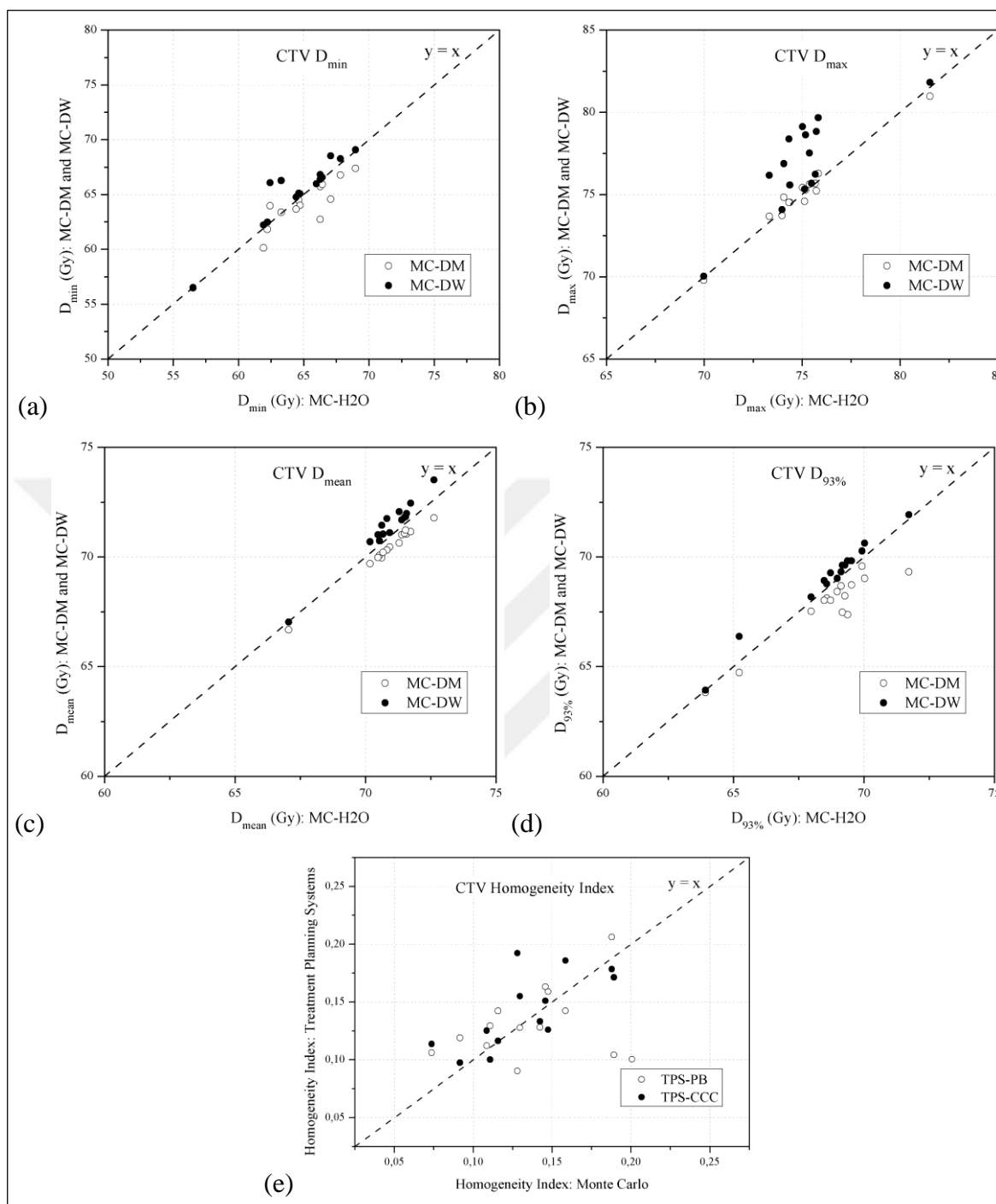


Figure H.8. Comparisons between  $MC_{H2O}$  and the other MC calculations for CTV:

(a)  $D_{\min}$ , (b)  $D_{\max}$ , (c)  $D_{\text{mean}}$ , (d)  $D_{93\%}$ , (e) HI

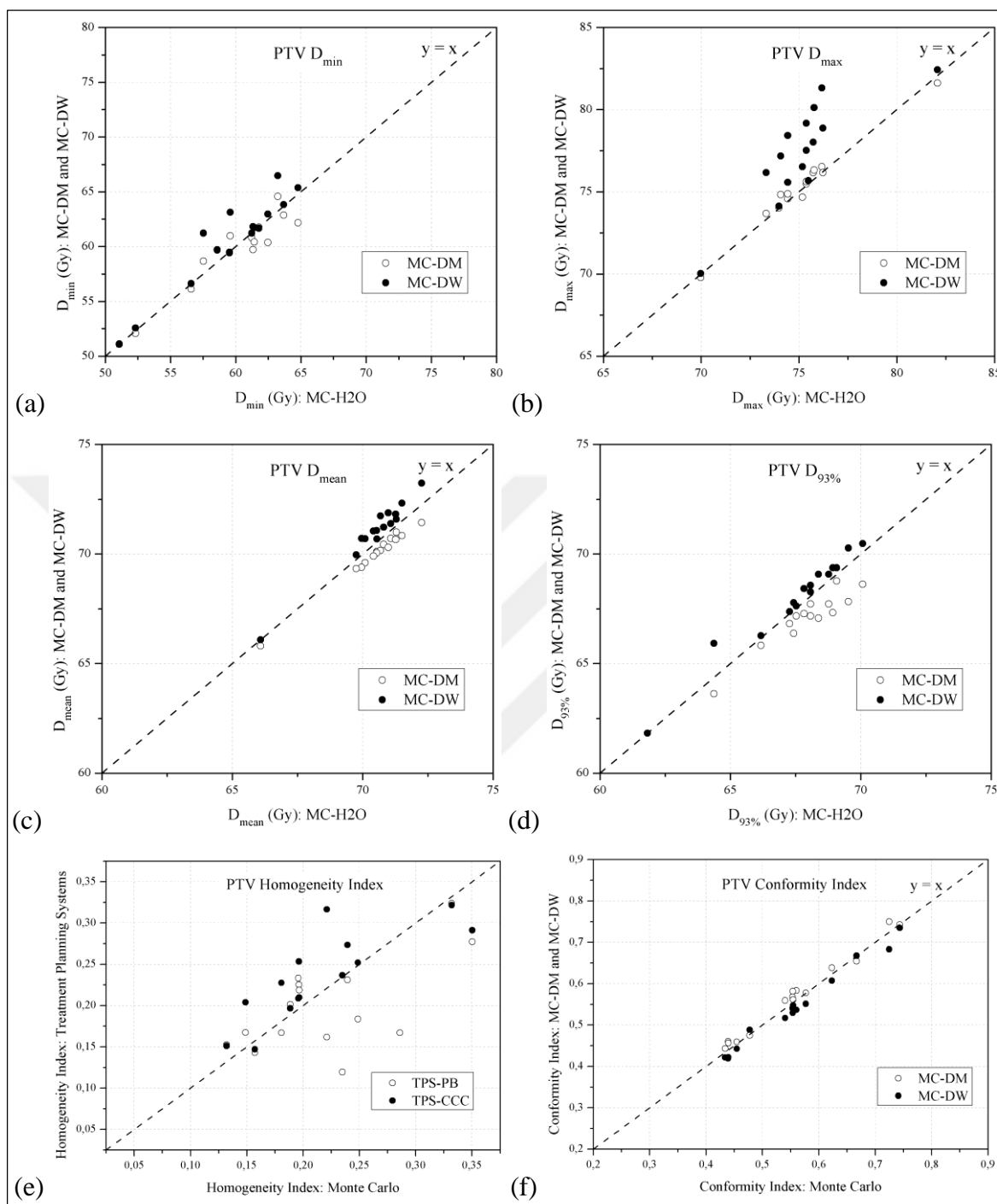


Figure H.9. Comparisons between  $MC_{H_2O}$  and the other MC calculations for CTV:

(a)  $D_{\min}$ , (b)  $D_{\max}$ , (c)  $D_{\text{mean}}$ , (d)  $D_{93\%}$ , (e) HI, (f) CI

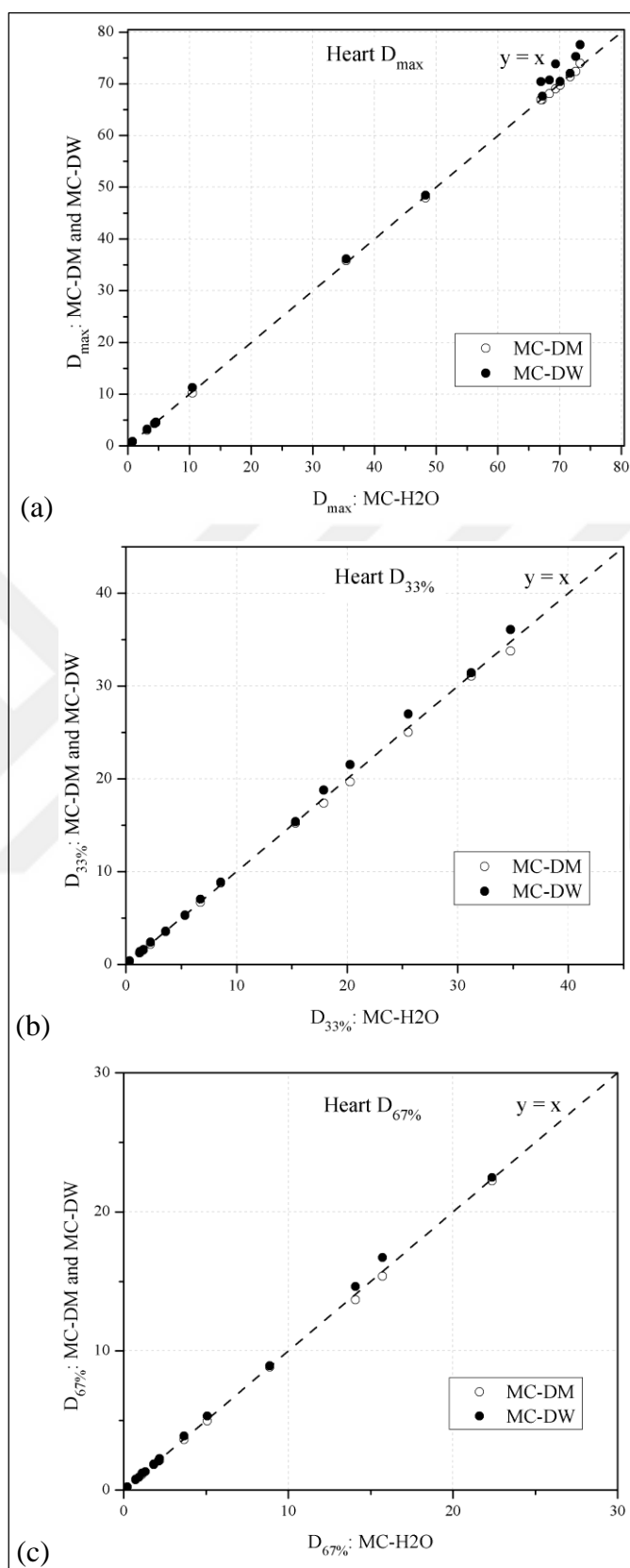


Figure H.10. Comparisons between  $MC_{H2O}$  and the other MC calculations for Heart:

(a)  $D_{max}$ , (b)  $D_{33\%}$ , (c)  $D_{67\%}$

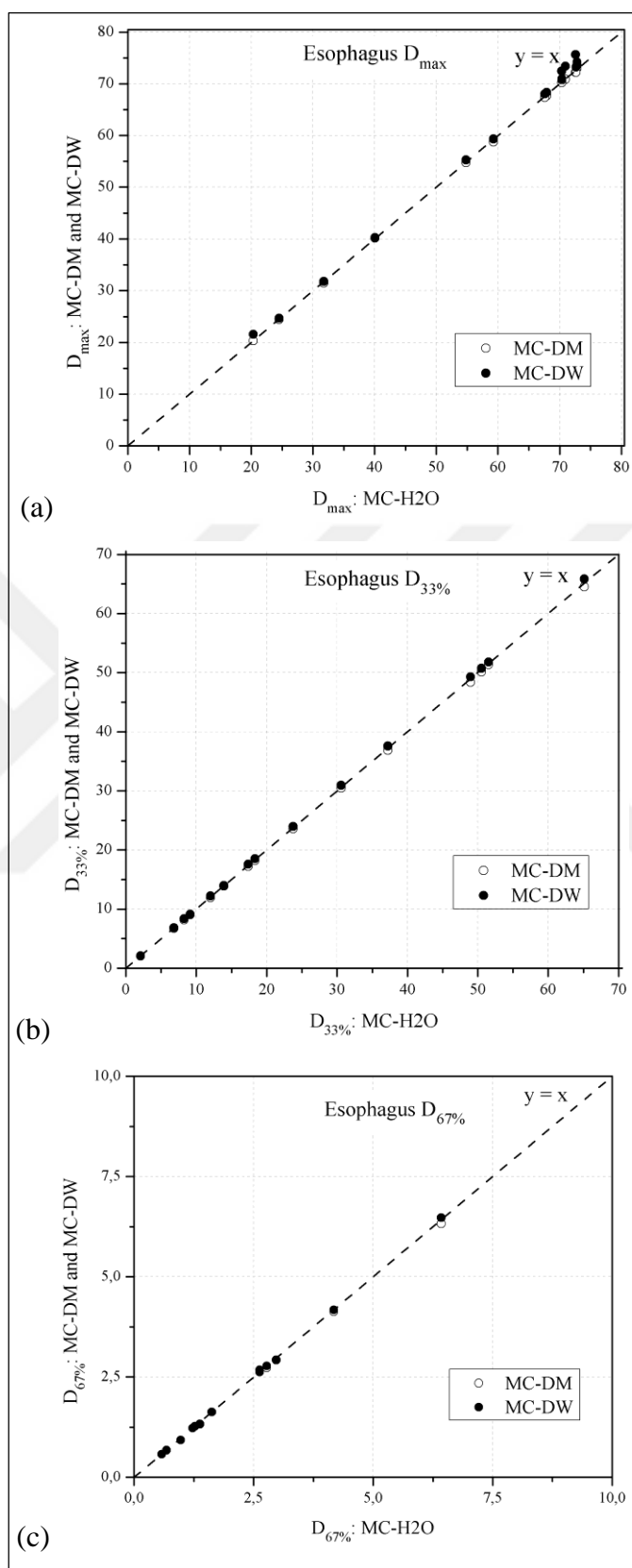


Figure H.11. Comparisons between  $MC_{H2O}$  and the other MC calculations for Esophagus:

(a)  $D_{max}$ , (b)  $D_{33\%}$ , (c)  $D_{67\%}$

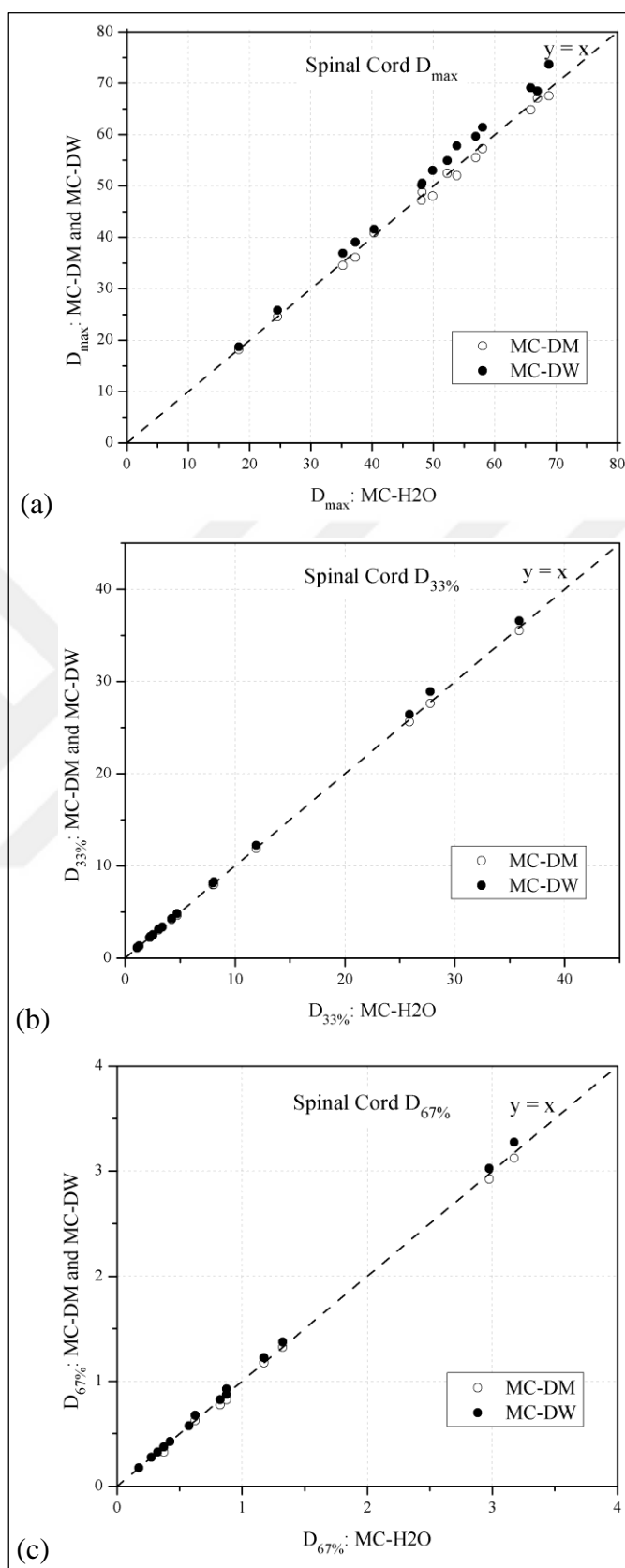


Figure H.12. Comparisons between MC<sub>H<sub>2</sub>O</sub> and the other MC calculations for Spinal Cord:

(a)  $D_{\max}$ , (b)  $D_{33\%}$ , (c)  $D_{67\%}$

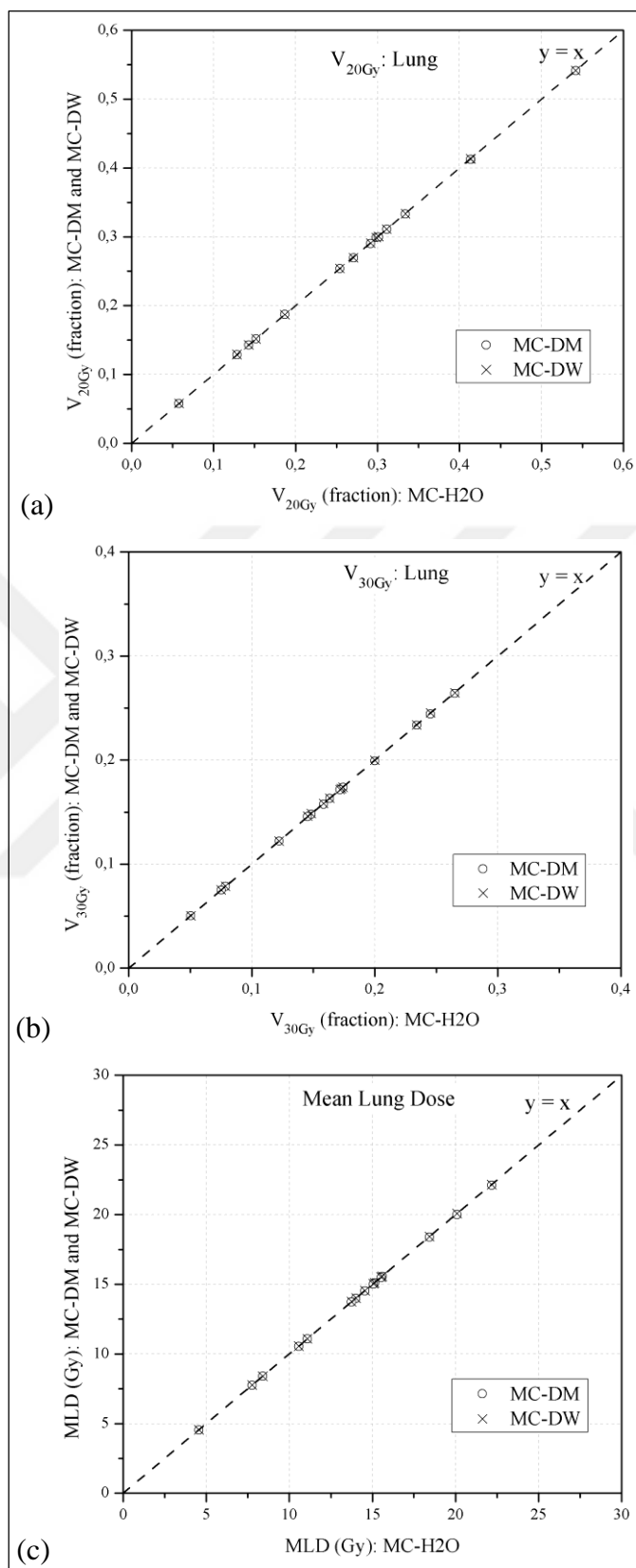


Figure H.13. Comparisons between  $\text{MC}_{\text{H2O}}$  and the other MC calculations for Lungs:

(a)  $V_{20\text{Gy}}$ , (b)  $V_{30\text{Gy}}$ , (c) MLD

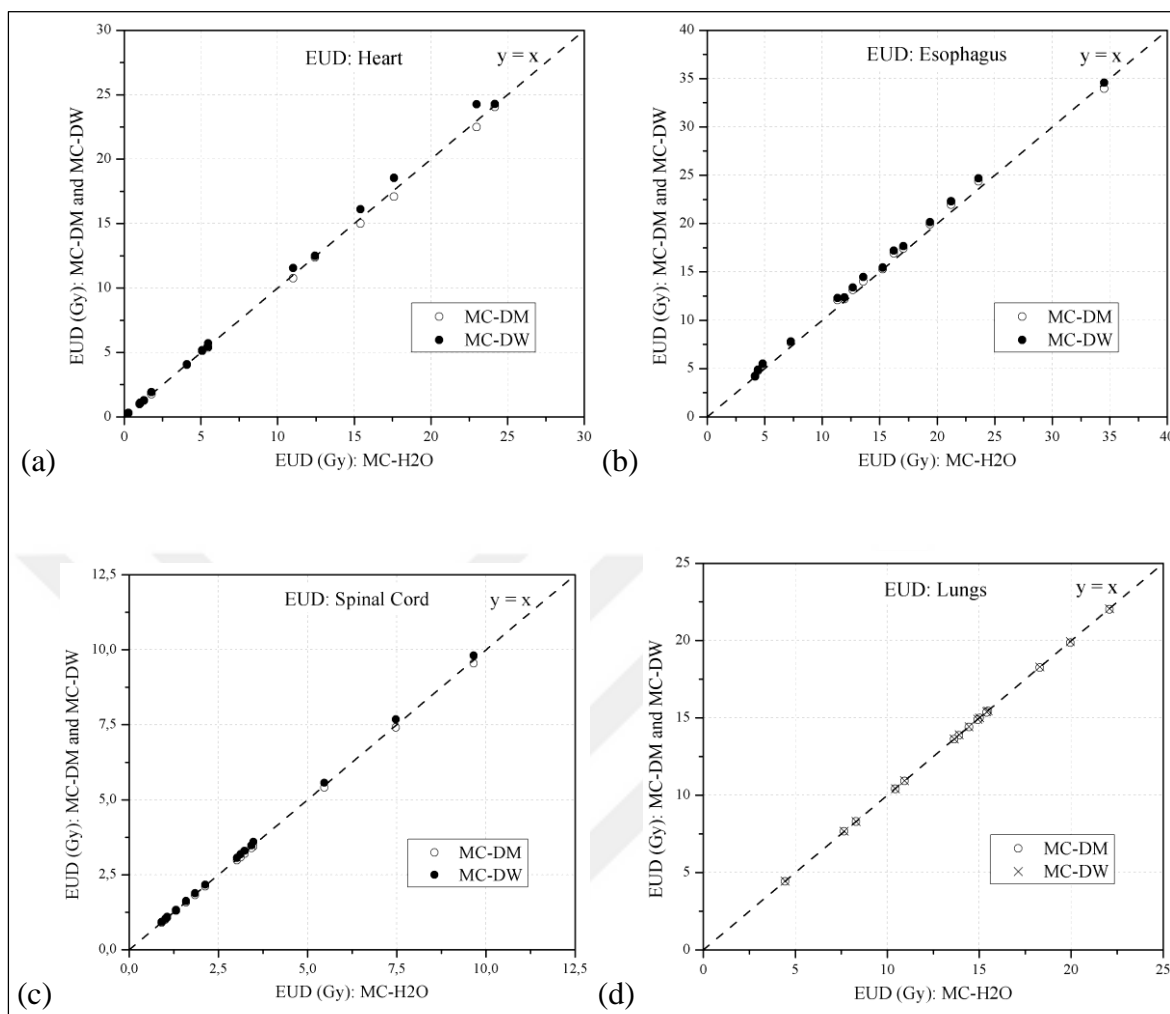


Figure H.14. Comparisons between  $MC_{H_2O}$  and the other MC calculations for EUD  
 (a) Heart, (b) Esophagus, (c) Spinal Cord, (d) Lungs

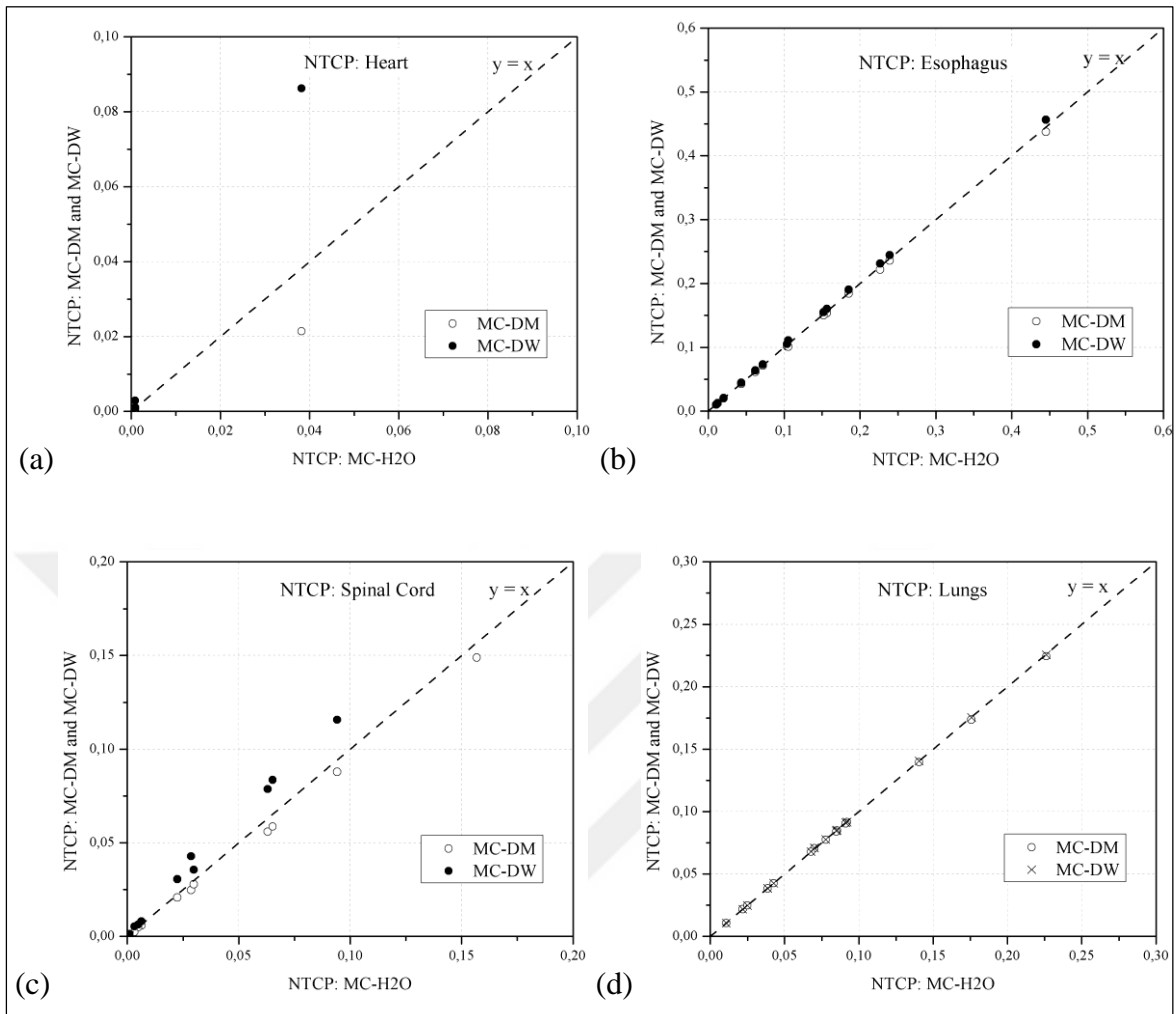


Figure H.15. Comparisons between  $MC_{H_2O}$  and the other MC calculations for NTCP  
 (a) Heart, (b) Esophagus, (c) Spinal Cord, (d) Lungs